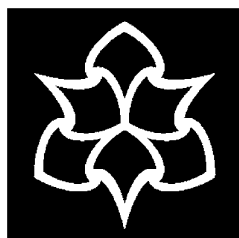


DESIGNING AND FABRICATING NOVEL
SCREEN PRINTED ELECTROCHEMICAL
CONFIGURATIONS



**Manchester
Metropolitan
University**

Jonathan Peter Metters

DESIGNING AND FABRICATING NOVEL
SCREEN PRINTED ELECTROCHEMICAL
CONFIGURATIONS

Jonathan Peter Metters

*Submitted in partial fulfilment of the
requirements of Manchester Metropolitan
University for the degree of Doctor of
Philosophy*

2013

*School of Science and the Environment
Division of Chemistry and Environmental
Science
Manchester Metropolitan University*

In loving memory of Stella Nuttall

31st October 1926 – 22nd August 2013

ABSTRACT

This thesis reports the design and fabrication of novel never before reported screen printed electrochemical devices. Chapters 1 and 2 of this thesis give an overview of the relevant fundamental electrochemical concepts with which this thesis is concerned. Additionally Chapter 2 focuses on the technique of screen printing upon which this thesis is focused on with a detailed overview not only of the screen printing process, but also its current prevalence within the field of electrochemistry with particular attention paid towards the development of novel screen printed electrode configurations.

Chapter 3 reports modified electrodes presenting the first examples of noble metal and carbon nanotube modified screen printed electrodes which are evaluated and benchmarked towards target analytes and the current literature. Again, simplification of analytical protocols is sought through the production of screen printed sensors using screen printing technology rather than alternative techniques such as drop-coating and electroplating.

The final part of this thesis explores electrode geometry and substrate composition (described in Chapters 4 and 5) in order to impart improvements and greater understanding in the mass transport characteristics in order to lead to significant improvement in the electroanalytical sensing features of the devised sensors. In the case of substrate composition the role of the underlying substrate, a fundamental component concerning screen printing is explored with different potential substrate materials being trialled and compared to the commonly utilised polyester substrate with regards to the effects of mechanical force upon the electrochemical performance of the sensors.

The primary focus of this thesis is to investigate and evaluate the development and fabrication of both existing and new screen printed electrochemical sensing platforms through the interrogation of existing sensors and their potential applications and the development of novel and unique sensor geometries and materials. The objectives of this study are described in greater detail below.

Objectives:

- 1) Investigate the modification of the pre-existing screen printed sensor through the utilisation of newly fabricated screen printed inks.
- 2) Design, fabricate and characterise screen printed sensors which, through the use of intuitive electrode geometries provide new insights into electrochemical behaviour and application of screen printed sensors with particular interest into the development of micro-sized sensors.
- 3) Investigate the role played by the substrate upon which the screen printed sensor is fabricated through the development of sensors using different substrate materials, with focus upon the resilience and robust nature of sensors devised intended for electroanalytical purposes.

ACKNOWLEDGMENTS

I think it is only right that I first express my deepest gratitude to Dr Craig E. Banks, my research supervisor, not least for gifting me the opportunity to undertake this project, but also for his continued and unfaltering support and guidance throughout its duration. I further extend my sincere gratitude to both Dr Dimitrios K. Kampouris and Dr Rashid O. Kadara. Dimitrios has afforded me a great deal of not only his time, but also his extensive knowledge over the course of the project, while Rashid having initially taught me the art of screen printing, has continued to offer his expertise in this technical field in the form of guidance when required.

Importantly, I must not forget those who have accompanied me upon this journey: fellow members of the Banks Research Group. Through the good days, the bad days and the even worse days the camaraderie within the group has played a huge role in the research outcomes I have attained. One member of the group, Dale, has taken each step by my side, joining me on this journey from day one - whilst undertaking his own research project - and is not just a lab-mate but one of my closest friends and as such I have felt privileged to share this experience with him.

As the old saying goes “last, but not least” I wish to express my eternal gratitude to my family; my Mother and Father Susan and Jon Metters and my two sisters Charlotte and Lucy Metters whose continued support, love and resilience to my moods has known no boundaries! It is essential that I also extend this thanks to my Nanna and Grandpa Stella and Bernard Nuttall who have helped raise me and provide me with the morals and values I possess today. Finally I would like to extend even further still my thanks to the remainder of the very close-knit family which I am fortunate enough to be a part of; my grandma, aunties, uncles and cousins who have all played their own important roles in helping me achieve what I have to date. It is unto each of them, as only proper, I dedicate this thesis.

CONTENTS

Abstract	I
Aims and Objectives	II
Acknowledgments.....	III
List of Tables.....	1
List of Schemes	1
List of Figures.....	1
Abbreviations	15
Chapter 1	18
Electrochemistry	18
1.1 Fundamental Concepts In Electrochemistry.....	18
1.1.1 Electrochemistry.....	18
1.1.2 Faradaic Processes.....	21
1.1.3 Mass Transport	23
1.1.4 Reactions Controlled By The Rate of Electron Transfer.....	26
1.1.5 Potential Step/Sweep Based Experiments.....	27
1.1.6 Cyclic Voltammetry.....	29
1.1.7 Chronoamperometry	31
1.1.8 Square-Wave Voltammetry.....	33
1.1.9 Interpreting Data	33
1.1.10 Electroanalysis.....	38
1.1.11 Benchmarking The Fabricated Screen Printed Devices	40
1.2 Electrode Materials	43
1.2.1 Graphite.....	44
1.2.2 Pyrolytic Graphite.....	48
1.2.3 Carbon Nanotubes	49
1.2.4 Boron Doped Diamond	51
1.2.5 Glassy Carbon.....	52

1.2.6 Metal Electrodes.....	53
Chapter 2.....	55
Screen Printing Technology For Electrochemical Applications	55
2.1 Screen Printed Electrodes Employed for Electroanalytical Applications.....	56
2.1.1 Sensor Fabrication.....	57
2.1.2 Fundamental Understanding of Screen Printed Electroanalytical Sensors.....	60
2.1.3 Metal Oxide Modified Screen Printed Electrodes.....	67
2.1.4 The Improvement of Mass Transport Through Intuitive Sensor Design.....	71
Chapter 3.....	81
Coplanar Macro Electrodes: Economical Modification For Enhanced Electroanalytical Sensing.....	81
3.1 Gold Screen Printed Electrodes.....	82
3.1.1 Introduction.....	82
3.1.2 Experimental	86
3.1.3 Results and Discussion.....	89
3.1.4 Conclusions.....	100
3.2 Platinum Screen Printed Electrodes.....	101
3.2.1 Introduction.....	101
3.2.2 Results and Discussion.....	104
3.2.3 Conclusions.....	116
3.3 Single-Walled Carbon Nanotube Screen Printed Electrodes: A Comparative Study	118
3.3.1 Introduction.....	118
3.3.2 Results And Discussion	123
3.3.3 Conclusions.....	143
Chapter 4.....	145
Electrode Geometry.....	145
4.1 Recessed Electrodes: Can Screen Printing Technology Facilitate The Development of Novel Electrode Geometries?.....	146
4.1.1 Introduction.....	146
4.1.2 Experimental	148
4.1.3 Results and Discussion.....	152

4.1.4 Conclusions.....	173
4.2 Mass Transport Control: A Screen Printed Microelectrode Array.....	175
4.2.1 Introduction.....	175
4.2.2 Results and Discussion.....	178
4.2.3 Conclusions.....	195
4.3 Microband Screen Printed Electrodes	197
4.3.1 Introduction.....	197
4.3.2 Results and Discussion.....	200
4.3.3 Conclusions.....	214
4.4 Screen Printed Microband Electrodes: Reducing The Microscopic Size.....	216
4.4.1 Introduction.....	216
4.4.2 Results and Discussion.....	218
4.4.3 Conclusions.....	231
4.4.3 Screen Printed Microband Electrodes: Reducing The Microscopic Size - Limitations	232
Chapter 5	235
Substrate Selection: An often Overlooked Parameter?	235
5.1 Traditional Polyester-based Substrates Versus Paper-Based Alternatives: A New Outlook On Substrates For Use in Electroanalysis	236
5.1.1 Introduction.....	236
5.1.2 Experimental	238
5.1.3 Results and Discussion.....	240
5.1.4 Conclusions.....	253
5.2 Traditional polyester-based Substrates Versus Paper-Based Alternatives: Flexibility Versus Stability	255
5.2.1 Introduction.....	255
5.2.2 Results and Discussion.....	257
5.2.3 Conclusions.....	278
Chapter 6.....	279
Conclusions and Future Work.....	279
6.1 Overall Conclusions.....	279

6.2 Suggestions For Future Work.....	281
6.4 Appendices.....	286
6.4.1 Appendix I.....	286
6.4.2 Appendix II.....	287
References	289
Relevant Publications Arising From This Thesis	319

LIST OF TABLES

1. Table 3.1 A summary of electrochemical reports for the detection of chromium (VI).
2. Table 4.1 A summary of electrochemical reports for the detection of nitrite.
3. Table 4.2 A summary of electrochemical reports for the detection of NADH.
4. Table 6.1 A comparison of the theoretical and experimental currents arising from utilisation of the laser ablated arrays of different electrode separations (50, 100 and 150 μm).

LIST OF SCHEMES

1. Scheme 3.1 Proposed mechanism for the electrochemical oxidation/reduction of capsaicin.
2. Scheme 4.1 Proposed mechanism for the electrochemical oxidation/reduction of β -nicotinamide adenine dinucleotide.

LIST OF FIGURES

1. Figure 1.1 A) A typical experimental set-up showing the reference electrode (saturated calomel electrode), the working electrode (edge-plane pyrolytic graphite electrode) and the counter electrode (platinum rod) immersed into an electrolyte solution. B) A simple electronic schematic equivalent to the electrochemical cell. A commercial potentiostat is required for the running of electrochemical experiments.
2. Figure 1.2 The three modes of mass transport towards an electrode surface.
3. Figure 1.3 Concentration profiles for potential step-based experiments over various times.
4. Figure 1.4 Voltage (potential) – time excitation signal utilised in cyclic voltammetric experiments.
5. Figure 1.5 Typical cyclic voltammogram for a reversible redox process, where E_{Pa} and E_{Pc} correspond to the potential values at which the maximum anodic and cathodic peak currents (I_{Pa} and I_{Pc} , respectively) are recorded.
6. Figure 1.6 Chronoamperometric experiment: A) potential-time waveform; B) change of concentration gradient; C) resulting current-time response.

7. Figure 1.7 Examples of cyclic voltammograms for a quasi-reversible (A/dotted) and irreversible (B/dash-dot) redox processes. The solid line represents a typical voltammogram for a reversible process.
8. Figure 1.8 An example of shifting peak potentials as a result of increasing scan rate.
9. Figure 1.9 A typical calibration plot constructed to determine the theoretical limit of detection using experimental data.
10. Figure 1.10 Schematic of sp^2 hybridised structure of graphite (free 2p orbitals shown).
11. Figure 1.11 Schematics of hexagonal and rhombohedral graphite stacking arrangements.
12. Figure 1.12 Schematic of a zig-zag (left) and arm-chair (right) graphitic crystal formations.
13. Figure 1.13 Schematic representation of graphene.
14. Figure 1.14 Image of a HOPG electrode.
15. Figure 1.15 Graphical Depictions of a) graphene sheet b) SWNT and c) MWNT.
16. Figure 1.16 Glass carbon 'ribbon' network where L_a is the Intraplanar Microcrystalline Size and L_c is the Interplanar Microcrystalline Size.
17. Figure 2.1 A schematic (cross-sectional) representation of the process of screen printed manufacturing of electrodes, outlining the basic processes involved.
18. Figure 2.2 SEM images of the screen-printed electrochemical platforms. Figures A and C display the bare unmodified electrode surface alongside that of a 40 % (M_B/M_I) modified (B and D) and 80 % (M_B/M_I) (E) electrochemical platforms.
19. Figure 2.3 Plot of heterogeneous electron transfer rate constant (k_{edge}^0) as a function of % (M_B/M_I).
20. Figure 2.4 Cyclic voltammetric profiles (A) obtained in 1 mM potassium ferrocyanide in 1 M KCl using the standard electrochemical platform (solid line) with that of a bespoke electrochemical platform (dashed line). Scans recorded at 100 mV s^{-1} vs. SCE. SEM images of the copper plated standard (B) and bespoke (C) screen printed electrochemical platforms.
21. Figure 2.5 Schematic representations of the diffusional zones at micro- and nano-electrode ensembles.
22. Figure 2.6 Simulated concentration profiles with isoconcentration contour lines over a microelectrode array representing the five main categories of diffusion modes: (I) planar diffusion layers on individual microdisk; (II) mixed diffusion layers on

- individual microdisk; diffusion mode between planar and hemispherical diffusion; (III) hemispherical diffusion layers on individual microdisk; (IV) mixed diffusion layers; diffusion mode of partial overlapping of adjacent diffusion layers; (V) planar diffusion layer over the entire microelectrode array; diffusion mode of complete overlapping of individual diffusion layers. In the scale bar next to the figure, the red colour represents the bulk concentration and the blue colour represents zero concentration. The second scale bar represents a relative concentration scale for the contour lines. Typical CVs of the each category are shown at the right.
23. Figure 2.7 Screen printed chips with gold (a) electrode structures. The black spots (d) represent the signals observed on chips after enzyme induced silver deposition. SEM images show the ultra-structure of gold (b, c) electrodes.
 24. Figure 2.8 (A) An alternating layer-by-layer pattern structure of the SPUME (a disposable screen-printed edge band carbon ultramicroelectrode) assembly. (B) Cross-sectional diagram of a typical SPUME with a built-in three-electrode configuration.
 25. Figure 3.1 Typical SEM images of the gold screen printed macro electrode at increasing magnifications; x250 (A), x2500 (B) and x5000 (C).
 26. Figure 3.2 EDX analysis of the AuSPE, determining the working surface to consist of 4.73 % oxygen, 14.15 % carbon and 81.12 % gold.
 27. Figure 3.3 Typical cyclic voltammetric curves resulting from additions of chromium (III) over the range of 100 to 1600 mM into 0.1 M KOH using the AuSPE. The dotted line is the response of the AuSPE in the absence of any chromium (III). Scan rate: 50 mV s^{-1} . Dashed arrow signifies direction of scan.
 28. Figure 3.4 Typical calibration plot resulting from additions of Chromium (III) into 0.1 M KOH (as shown in figure 3.3) using the AuSPE.
 29. Figure 3.5 Electrochemical reduction of 100 mM chromium (VI) in 0.05 M H_2SO_4 using the AuSPEs recorded over the scan rate range of 10 to 600 mV s^{-1} (vs. SCE). Dashed arrow signifies direction of scan.
 30. Figure 3.6 Typical linear sweep voltammetric profiles resulting from the electrochemical reduction of chromium (VI) in 0.05 M H_2SO_4 using an AuSPE over the range of 10 to 1600 mM. Scan rate: 50 mV s^{-1} . Dashed arrow signifies direction of scan.
 31. Figure 3.7 A typical calibration plot resulting from additions of chromium (VI) into 0.05 M H_2SO_4 using the AuSPE as shown in figure 3.6.

32. Figure 3.8 A typical calibration plot resulting from additions of chromium (VI) over the range of 10 to 1300 μM into canal water samples. Scan Rate: 50 mV s^{-1} .
33. Figure 3.9 Typical SEM image of the platinum screen printed electrode.
34. Figure 3.10 EDAX analysis of the platinum screen printed electrode.
35. Figure 3.11 Electrochemical oxidation and reduction of 1 mM potassium hexachloroiridate in 0.1 M KCl using the PtSPEs recorded over the scan rate range of 5 to 200 mV s^{-1} (*vs.* Ag/AgCl). Dashed arrow signifies direction of scan.
36. Figure 3.12 A typical cyclic voltammogram recorded in 0.1 M H_2SO_4 using a platinum screen printed electrode. Scan rate: 100 mV s^{-1} . Dashed arrow signifies direction of scan.
37. Figure 3.13 A) Typical cyclic voltammetric responses resulting from additions of hydrazine into a phosphate buffer using the PtSPE. Scan rate: 50 mV s^{-1} . B) A typical calibration plot resulting from additions of hydrazine over the range of 50 to 500 μM . Dashed arrow signifies direction of scan.
38. Figure 3.14 Typical chronoamperometric measurements resulting from the electrochemical oxidation of hydrazine in a phosphate buffer using a PtSPE over the range of 50 to 500 μM . Measurements were taken at a potential of + 0.5 V (*vs.* Ag/AgCl).
39. Figure 3.15 An overlay of typical responses through addition of hydrazine in 'ideal' conditions (phosphate buffer solution) (circles) and into a canal water sample (triangles) over the range of 50 to 500 μM . Scan rate: 50 mV s^{-1} .
40. Figure 3.16 Typical cyclic voltammetric responses resulting from additions of hydrogen peroxide into a phosphate buffer using the PtSPE. Scan rate: 50 mV s^{-1} . Inset: The calibration plot corresponding to the voltammetric peak arising at + 0.35 V over the range 100 to 1000 μM hydrogen peroxide. Dashed arrow signifies direction of scan.
41. Figure 3.17 Typical chronoamperometric measurements resulting from additions of hydrogen peroxide into a phosphate buffer over the range of 100 to 1000 μM using the PtSPE. Measurements were taken at a potential of + 0.35 V (*vs.* Ag/AgCl). Inset: The corresponding calibration plot.
42. Figure 3.18 Schematic representations of the two types of diffusional process that can occur at carbon nanotube modified electrode.
43. Figure 3.19 A schematic representation of the fabrication procedure of the SW-SPE.

44. Figure 3.20 SEM analysis of the SW-SPE at x15,000 (A) and x30,000 (B) magnification. Additionally (C) and (D) depict SEM analysis of the underlying carbon electrode (unmodified SPE) prior to screen printing the SW-CNTs at x15,000 and x30,000 magnification respectively
45. Figure 3.21 XPS analysis of the SW-SPE.
46. Figure 3.22 XPS analysis of the DS-SW-SPE (A) and DS-MW-SPE (B).
47. Figure 3.23 Cyclic voltammetric measurements obtained using the unmodified SPE (solid line), the SW-SPE (dashed line), DS-SW-SPE (dotted line) and the DS-MW-SPE (dot-dash line) in a pH 7.4 phosphate buffer solution. Scan rate: 100 mV s⁻¹. Dashed arrow signifies direction of scan.
48. Figure 3.24 Typical cyclic voltammograms resulting from increasing scan rates in 1 mM potassium ferrocyanide (II) and 0.1 M KCl using (A) a standard SPE, (B) the SW-SPE, (C) the DS-SW-SPE and (D) the DS-MW-SPE. Scan rates: 10, 25, 50, 75, 100, 200, 400 mV s⁻¹. Dashed arrow signifies direction of scan.
49. Figure 3.25 SEM analysis of the working electrode surface of the DS-SW-SPE (A) and DS-MW-SPE (B) at x20,000 magnification.
50. Figure 3.26 EDAX analysis of the working electrode surface of the DS-SW-SPE (A) and DS-MW-SPE (B). The DS-SW-SPE was determined (semi-quantitatively) to contain: 92.04 % carbon, 5.90 % oxygen, 2.01 % chlorine and 0.05 % sulphur, while the DS-MW-SPE was determined to contain: 92.36 % carbon, 5.56 % oxygen, 2.01 % chlorine and 0.07 % sulphur.
51. Figure 3.27 Typical cyclic voltammograms recorded in 600 μM dopamine in a pH 7.4 phosphate buffer solution at the unmodified SPE (solid line), SW-SPE (dashed line), DS-SW-SPE (dotted line) and DS-MW-SPE (dot-dash line). Scan rate: 100 mV s⁻¹. Dashed arrow signifies direction of scan.
52. Figure 3.28 Typical cyclic voltammograms recorded in 1 mM hydrazine in a pH 7.4 phosphate buffer solution at the unmodified SPE (solid line), SW-SPE (dashed line), DS-SW-SPE (dotted line) and DS-MW-SPE (dot-dash line). Scan rate: 100 mV s⁻¹. Dashed arrow signifies direction of scan.
53. Figure 3.29 Typical calibration plots arising from additions of hydrazine (100 – 1000 μM) into a pH 7.4 phosphate buffer solution at the unmodified SPE (pentagons), SW-SPE (circles), DS-SW-SPE (triangles) and DS-MW-SPE (square).

54. Figure 3.30 The first (solid line) and second (dashed line) scans using cyclic voltammetry at 5 μM capsaicin in a pH 1 buffer using the standard SPE. Scan rate: 100 mV s^{-1} . Dashed arrow signifies direction of scan.
55. Figure 3.31 The effect of accumulation time upon the observed voltammetric profiles. Scan rate: 50 mV s^{-1} . Dashed arrow signifies direction of scan.
56. Figure 3.32 Typical cyclic voltammograms obtained in 35 μM capsaicin in a pH 1 buffer solution at an unmodified SPE (solid line), the SW-SPE (dashed line), DS-SW-SPE (dotted line) and the DS-MW-SPE (dot-dash line). Scan rate: 100 mV s^{-1} . Dashed arrow signifies direction of scan.
57. Figure 3.33 Typical calibration plots for the addition of capsaicin (5 – 50 μM) at a standard carbon screen printed sensor (triangles), SW-SPE (pentagons), DS-SW-SPE (circles) and DS-MW-SPE (squares) upon the first cyclic voltammetric scan. The peak height is recorded using the oxidation peak (Peak I; see figure 3.30). Scan rate: 100 mV s^{-1} .
58. Figure 4.1.1 A single recessed screen printed electrode (drSPE; working area: 500 μm) (A), an image of the drSPE obtained using an optical microscope (x5 magnification) (B), SEM analysis of the drSPE working electrode at x1000 magnification (D).
59. Figure 4.2 Typical cyclic voltammetric responses observed through scan rate studies using the drSPE in 1 mM hexaammine-ruthenium (III) chloride/ 0.1 M KCl. Scan rates: 5 – 400 mV s^{-1} . Dashed arrow signifies direction of scan.
60. Figure 4.3 Typical cyclic voltammetric responses (A) and the corresponding calibration plot (B) resulting from additions over the range 10 to 90 μM of NADH into a phosphate buffer (pH 7) using the drSPE. Scan rate: 50 mV s^{-1} . Dashed arrow signifies direction of scan.
61. Figure 4.4 An overlay of typical current density calibration plots resulting from cyclic voltammetric measurement of additions of NADH into a phosphate buffer over the range of 10 to 90 μM using the drSPE (squares) versus a standard 3 mm diameter coplanar SPE (circles).
62. Figure 4.5 Typical cyclic voltammetric responses (A) and the corresponding calibration plot (B) resulting from additions of nitrite into a phosphate buffer (pH 7) using the drSPE; additions were made over the range 100 to 1000 μM . Scan rate: 50 mV s^{-1} . Dashed arrow signifies direction of scan.

63. Figure 4.6 An overlay of typical current density calibration plots resulting from cyclic voltammetric measurement of additions of nitrite into a phosphate buffer over the range of 100 to 1000 μM using the drSPE (circles) versus a standard 3 mm diameter SPE (squares).
64. Figure 4.7 An overlay of typical current density calibration plots resulting from cyclic voltammetric measurement of additions of nitrite into a phosphate buffer (squares) and a canal water sample (circles) over the range of 100 to 1000 μM using the drSPE.
65. Figure 4.8 Typical cyclic voltammetric responses observed through scan rate studies using the prSPE in 1 mM potassium hexachloroiridate (III) / 0.1 M KCl. Scan rates: 5 – 200 mV s^{-1} . Dashed arrow signifies direction of scan.
66. Figure 4.9 A) Typical cyclic voltammetric responses resulting from additions of hydrazine into a phosphate buffer (pH 7) (dotted line) at the PtdrSPE; additions made over the range 50 to 500 μM . Scan rate: 50 mV s^{-1} . Dashed arrow signifies direction of scan. B) Typical current density calibration plots measured using cyclic voltammetry for the oxidation of hydrazine, arising from increasing concentrations at the PtdrSPE (squares) and PtSPE (triangles).
67. Figure 4.10 Typical current density calibration plots arising from chronoamperometric measurement (+ 0.35 V, 120 seconds) of hydrogen peroxide arising from increasing concentrations using the PtdrSPE (squares) and PtSPE (circles).
68. Figure 4.11 A representation of a two sides of the prSPE showing the modes of edge and point diffusion.
69. Figure 4.1.12 SEM of the prSPE working electrode (x1,000 magnification).
70. Figure 4.13 A) Typical cyclic voltammetric responses observed through scan rate studies using the prSPE in 1 mM hexaammine-ruthenium (III) chloride/ 0.1 M KCl. Scan rates: 5 – 400 mV s^{-1} . B) Comparison between the drSPE (solid line) and prSPE (dashed line) scan rates (of 5 and 10 mV s^{-1}) in 1 mM hexaammine-ruthenium (III) chloride / 0.1 M KCl. Dashed arrow signifies direction of scan.
71. Figure 4.14 A) Typical square wave cathodic stripping voltammetry ($E_{dep} = + 0.9 \text{ V}$ (vs. SCE), 120 s) resulting from additions of manganese (II) into a 0.1 M sodium acetate solution. B) An overlay of typical calibration plots resulting from additions of manganese (II) into a 0.1 M sodium acetate solution over the range of 73 to 504 nM at the drSPE (diamonds) and prSPE (squares) ($N = 7$).

72. Figure 4.15 A schematic representation of the SPMA fabricated entirely through screen printing technology.
73. Figure 4.16 Photograph of the carbon (left image) and gold (right image) SPMA (A). An optical microscope image of the carbon SPME (B). Typical SEM images of the carbon SPMA at x140 (C) and x1000 magnification (D).
74. Figure 4.17 Cyclic voltammetric response arising from the carbon SPMA recorded in 1 mM hexaammine-ruthenium (III) chloride / 0.1 M KCl. Scan rates: 5 - 200 mV s^{-1} . Dashed arrow signifies direction of scan.
75. Figure 4.18 Typical cyclic voltammetric responses obtained using the carbon SPMA (solid line) and a single electrode from the carbon SPMA (dotted line) in 1 mM hexaammine-ruthenium (III) chloride / 0.1 M KCl. Scan rate: 5 mV s^{-1} . Dashed arrow signifies direction of scan.
76. Figure 4.19 Linear sweep voltammograms recorded following the addition of acetaminophen into a pH 7 phosphate buffer solution (dotted line) over the concentration range 10 – 1000 μM using the carbon SPMA (A). Typical corresponding calibration plots using the carbon SPMA (squares) and a single electrode from the carbon SPMA (circles) (B). Scan rate: 5 mV s^{-1} . Dashed arrow signifies direction of scan.
77. Figure 4.20 Linear sweep voltammograms recorded following the addition of dopamine hydrochloride into a pH 7 phosphate buffer solution (dotted line) over the concentration range 50 – 500 μM using the carbon SPMA (A). Typical corresponding calibration plots using the carbon SPMA (squares) and a single electrode from the carbon SPMA (circles) (B). Scan rate: 5 mV s^{-1} . Dashed arrow signifies direction of scan.
78. Figure 4.21 Cyclic voltammograms recorded following the addition of nitrite into a pH 7 phosphate buffer solution (dotted line) over the concentration range 10 – 100 μM using the carbon SPMA (A). Typical corresponding calibration plots using the carbon SPMA (squares) and a single electrode from the carbon SPMA (circles) (B). Scan rate: 5 mV s^{-1} . Dashed arrow signifies direction of scan.
79. Figure 4.22 Linear sweep voltammograms recorded following the addition of chromium (VI) into a 0.05 M H_2SO_4 solution (dotted line) over the concentration range 10 – 100 μM using the gold SPMA (A). Typical corresponding calibration plots

- using the gold SPMA (squares) and a single electrode from the carbon SPMA (circles) (B). Scan rate: 5 mV s^{-1} . Dashed arrow signifies direction of scan.
80. Figure 4.23 An overlay of typical corresponding calibration plots resulting from additions of chromium (VI) made into both an 'ideal' $0.05 \text{ M H}_2\text{SO}_4$ solution (squares) and a canal water sample (circles). Scan rate: 5 mV s^{-1} .
81. Figure 4.24 Optical and Scanning Electron Microscopy images of the bSPE. A: An optical microscopic image of the screen printed band electrode, B: SEM x50 magnification of the bSPE working area tip, C: SEM x140 magnification of the bSPE working area tip, D: SEM x750 magnification of the bSPE working area tip.
82. Figure 4.25 Typical cyclic voltammetric responses observed through scan rate studies using the bSPE at A: 1 mM potassium ferrocyanide in 0.1 M KCl and B: 1 mM hexaammine-ruthenium (III) chloride in 0.1 M KCl . Dashed arrow signifies direction of scan.
83. Figure 4.26 Typical cyclic voltammetric responses and their corresponding calibration plots resulting from additions of NADH into a pH 7 phosphate buffer using the bSPE; additions over the range A: 1 to $10 \text{ }\mu\text{M}$ and B: 10 to $100 \text{ }\mu\text{M}$. Scan rate: 50 mV s^{-1} . Dashed arrow signifies direction of scan.
84. Figure 4.27 An overlay of typical current density calibration plots resulting from additions of NADH into a pH 7 phosphate buffer over the range of 1 to $100 \text{ }\mu\text{M}$ using the bSPE (diamonds) versus a standard 3 mm diameter SPE (circles).
85. Figure 4.28 A schematic representation of convergent diffusion (A) and linear diffusion (B) at μbSPEs which arise from cutting with scissors.
86. Figure 4.29 Calibration plots resulting from additions of NADH in a pH 7 phosphate buffer, over the range 1 to $40 \text{ }\mu\text{M}$ at three separate μbSPE .
87. Figure 4.30 Peak potential dependence on solution pH for oxidation of $100 \text{ }\mu\text{M}$ nitrite on a bSPE over the pH range 1 to 12 using the bSPEs.
88. Figure 4.31 A typical calibration plot corresponding to the addition of nitrite over the range of 10 to $700 \text{ }\mu\text{M}$ at the bSPE using cyclic voltammetry. Scan rate: 50 mV s^{-1} .
89. Figure 4.32 Optical and Scanning Electron Microscopy images of the $50 \text{ }\mu\text{m}$ graphite-50bSPE. A: An optical microscopic image of the screen printed band electrode, B, C, D: SEM magnification of the bSPE working area.
90. Figure 4.33 Dependence of the peak current on the voltammetric scan rate obtained in 1 mM hexaammine-ruthenium (III) chloride / 0.1 M KCl using the graphite-50bSPE.

91. Figure 4.34 Cyclic voltammetric traces obtained in 1 mM hexaammine-ruthenium (III) chloride / 0.1 M KCl) using the graphite-50bSPE (solid line) and graphite-100bSPE (dashed line). Scan rate: 5 mV s^{-1} . Dashed arrow signifies direction of scan.
92. Figure 4.35 Image of the graphite-50bSPE arrays, left $N = 4$ and right $N = 3$.
93. Figure 4.36 Typical cyclic voltammetric traces obtained in 1 mM hexaammine-ruthenium (III) chloride / 0.1 M KCl) using the graphite-50bSPE (solid line) and at arrays of graphite-50bSPE; $N = 3$ (dashed line) and $N = 4$ (dotted line). Scan rate: 5 mV s^{-1} . Dashed arrow signifies direction of scan.
94. Figure 4.37 A) Typical cyclic voltammograms arising from additions of NADH in to a pH 7.4 buffer using the graphite-50bSPE. Scan rate: 5 mV s^{-1} . Dashed arrow signifies direction of scan. B) A corresponding calibration plot from A) over the range studied ($1 - 10 \text{ }\mu\text{M}$) NADH.
95. Figure 4.38 SEM images of the $50 \text{ }\mu\text{m}$ gold-50bSPE working area.
96. Figure 4.39 Typical cyclic voltammetric responses observed through scan rate studies ($5 - 200 \text{ mV s}^{-1}$) using the gold-50bSPE at 1 mM hexaammine-ruthenium (III) chloride in 0.1 M KCl. Dashed arrow signifies direction of scan.
97. Figure 4.40 A) Typical cyclic voltammograms arising from additions of chromium (VI) in to 0.05 M H_2SO_4 using the gold-50bSPE. Scan rate: 5 mV s^{-1} . Dashed arrow signifies direction of scan. B) A corresponding calibration plot from A) over the range studied ($1 - 10 \text{ }\mu\text{M}$) chromium (VI).
98. Figure 5.1 Typical cyclic voltammograms comparing the response in 1 mM ferrocyanide (II) in 0.1 M KCl using a standard SPE (solid line), IP-SPE (dashed line) and RP-SPE (dotted line). Scan rate: 50 mV s^{-1} . Dashed arrow signifies direction of scan.
99. Figure 5.2 An image demonstrating the ultra flexible and robust nature of the IP-SPE (A) and typical SEM images of the sensor at increasing magnifications; x18 (B), x400 (C) and x3000 (D).
100. Figure 5.3 Typical SEM images of the paper-based electrodes screen printed upon different paper substrates; A) RP-SPE and B) FP-SPE at a magnification of x35, whilst C) and D) show the RP-SPE and FP-SPE at an increased magnification of x1000.
101. Figure 5.4 Typical cyclic voltammograms resulting from increasing scan rates (mV s^{-1}) at the IP-SPE in 1 mM potassium ferrocyanide (II) and 0.1 M KCl (A), 1 mM

hexaammine-ruthenium (III) chloride in 0.1 M KCl (B), 1 mM potassium hexachloroiridate in 0.1 M KCl (C) and 1mM TMPD in 0.1 M KCl (D). Scan rate range in all cases: 5 – 200 mV s⁻¹. Dashed arrow signifies direction of scan.

102. Figure 5.5 The effect of immersion time in solution upon the observed cyclic voltammetric response using a single IP-SPE in 1 mM potassium ferrocyanide / 0.1 M KCl with scans carried out at 5 minute intervals. The first scan at 0 minutes is depicted using a dotted line. Scan rate: 50 mV s⁻¹. Dashed arrow signifies direction of scan. Inset: Corresponding plot of peak height versus immersion time.

103. Figure 5.6 A) Typical cyclic voltammograms arising from additions of NADH in to a pH 7 buffer using the IP-SPE. Scan rate: 100 mV s⁻¹. Dashed arrow signifies direction of scan. B) Corresponding calibration plots over the range studied (10 – 100 μM) NADH using the IP-SPE (squares) and standard SPE (circles).

104. Figure 5.7 A) Typical cyclic voltammograms arising from additions of nitrite in to a pH 7 buffer using the IP-SPE. Scan rate: 100 mV s⁻¹. Dashed arrow signifies direction of scan. B) Corresponding calibration plots over the range studied (100 – 1000 μM) nitrite using the IP-SPE (circles) and standard SPE (squares).

105. Figure 5.8 Typical calibration plots resulting from the addition of nitrite into a pH 7 buffer using a single IP-SPE for the entire concentration range (circles) and a new IP-SPE (squares) for each concentration. Scan rate: 100 mV s⁻¹.

106. Figure 5.9 Typical calibration plots corresponding to additions of nitrite into a pH 7 buffer solution (squares) and canal water solution (circles) using the IP-SPE. Scan rate: 100 mV s⁻¹.

107. Figure 5.10 Photographs of: (A) The standard polymer-based screen printed electrode (standard-SPE) (left), the sellotape coated paper-based screen printed sensor (ps-SPE) (middle) and the clear nail varnish coated paper-based screen printed sensor (pv-SPE) (right). The contortion angles of 45 and 90 degrees utilised throughout this investigation are shown in (B) and (C) respectively.

108. Figure 5.11 The effect of contortion time on the resistivity observed at various electrodes when contorted at angles of 45 (circles) and 90 (triangles) degrees. (A): standard-SPE; (B) ps-SPE; (C) pv-SPE. The data points (circles and triangles) represent the average response ($N = 3$) with the error bars representing the standard deviation.

109. Cyclic voltammetric responses obtained at standard-SPE contorted at angles of (A): 45 and (B): 90 degrees, recorded in 1 mM ferrocyanide (II) / 1 M KCl. Contortion times of 60 (dashed line), 10 (dash-dotted line), 5 (dotted line) and 0 minutes (solid line) were utilised for each of the SPEs. Scan rate: 100 mV s⁻¹. Dashed arrow signifies direction of scan. Also shown is the effect of contortion time for the two angles upon voltammetric peak-to-peak separation (ΔE_P): 45 degrees (squares) and 90 degrees (circles).
110. Figure 5.13 Cyclic voltammetric responses for ps-SPE contorted at angles of (A): 45 and (B): 90 degrees, recorded in 1 mM ferrocyanide (II) / 1 M KCl. Contortion times of 60 (dashed line), 10 (dash-dotted line), 5 (dotted line) and 0 minutes (solid line) were utilised for each of the SPEs. Scan rate: 100 mV s⁻¹. Dashed arrow signifies direction of scan. Also shown is the effect of contortion time for the two angles upon peak-to-peak separation (ΔE_P): 45 degrees (squares) and 90 degrees (circles).
111. Figure 5.14 Cyclic voltammetric responses for pv-SPE contorted at angles of (A): 45 and (B): 90 degrees, recorded in 1 mM ferrocyanide (II) / 1 M KCl. Contortion times of 60 (dashed line), 10 (dash-dotted line), 5 (dotted line) and 0 minutes (solid line) were utilised for each of the SPEs. Scan rate: 100 mV s⁻¹. Dashed arrow signifies direction of scan. Also shown is the effect of contortion time for the two angles upon peak-to-peak separation (ΔE_P); 45 degrees (squares) and 90 degrees (circles).
112. Figure 5.15 The effect of contortion time for the two angles upon peak-to-peak separation (ΔE_P): 45 degrees (squares) and 90 degrees (circles), in a solution of 1 mM hexaamine-ruthenium (III) chloride / 0.1 M KCl when utilising the standard-SPE (A), ps-SPE (B) and pv-SPE (C). Scan rate: 100 mV s⁻¹.
113. Figure 5.16 Cyclic voltammetric responses for standard-SPE contorted at angles of (A): 45 and (B): 90 degrees, recorded in 100 μ M NADH in pH 7 phosphate buffer. Contortion times of 60 (dashed line), 10 (dash-dotted line), 5 (dotted line) and 0 minutes (solid line) were utilised for each of the SPEs. Scan rate: 100 mV s⁻¹. Dashed arrow signifies direction of scan. Also shown is the effect of contortion time for the two angles upon the voltammetric peak potential (E_P): 45 degrees (squares) and 90 degrees (circles).
114. Figure 5.17 Cyclic voltammetric responses for ps-SPE contorted at angles of (A): 45 and (B): 90 degrees, recorded in 100 μ M NADH in pH 7 phosphate buffer. Contortion times of 60 (dashed line), 10 (dash-dotted line), 5 (dotted line) and 0 minutes (solid

- line) were utilised for each of the SPEs. Scan rate: 100 mV s^{-1} . Dashed arrow signifies direction of scan. Also shown is the effect of contortion time for the two angles upon the voltammetric peak potential (E_p): 45 degrees (squares) and 90 degrees (circles).
115. Figure 5.18 Cyclic voltammetric responses for pv-SPE contorted at angles of (A): 45 and (B): 90 degrees, recorded in $100 \mu\text{M}$ NADH in pH 7 phosphate buffer. Contortion times of 60 (dashed line), 10 (dash-dotted line), 5 (dotted line) and 0 minutes (solid line) were utilised for each of the SPEs. Scan rate: 100 mV s^{-1} . Dashed arrow signifies direction of scan. Also shown is the effect of contortion time for the two angles upon the voltammetric peak potential (E_p): 45 degrees (squares) and 90 degrees (circles).
116. Figure 5.19 SEM images of the conductive track of a carbon screen printed electrodes on polyester substrates (A and B) and a paper based substrate (C and D, prior to coating with nail varnish or sellotape), following 60 minutes contorted at an angle of 45 degrees at magnifications of x25 and x85.
117. Figure 5.20 The effect of numerous and consecutive contortions to an angle of 45 degrees on voltammetric peak current (I_p), in a solution of 1 mM potassium ferrocyanide (II) / 0.1 M KCl when utilising the standard-SPE (squares), ps-SPE (circles) and pv-SPE (triangles). Scan rate: 100 mV s^{-1} .
118. Figure 5.21 The effect of numerous and consecutive contortions to an angle of 45 degrees on voltammetric peak current (I_p), in a solution of $100 \mu\text{M}$ NADH in a pH 7 phosphate buffer solution when utilising the standard-SPE (squares), ps-SPE (circles) and pv-SPE (triangles). Scan rate: 100 mV s^{-1} .
119. Figure AI.1 3-dimensional analysis of a standard screen printed sensor (top image) and profile analysis (bottom image). Analysis performed by: Dr Walter Perrie, School of Engineering, University of Liverpool.
120. Figure AII.1 Typical SEM images depicting the laser ablated graphite microelectrode arrays with different electrode separations of: A) $50 \mu\text{m}$, B) $100 \mu\text{m}$ and C) $150 \mu\text{m}$.
121. Figure AII.2 Typical cyclic voltammetric responses observed through scan rate studies ($5 - 200 \text{ mV s}^{-1}$) at the laser ablated graphite microelectrode arrays with different electrode separations of: A) $50 \mu\text{m}$, B) $100 \mu\text{m}$ and C) $150 \mu\text{m}$ in 1 mM hexaammine-ruthenium (III) chloride in 0.1 M KCl.
122. Figure AII.3 A comparison of typical cyclic voltammograms obtained at the laser ablated graphite microelectrode arrays with different electrode separations of: $50 \mu\text{m}$

(dashed line), 100 μm (solid line) and 150 μm (dotted line) in 1 mM hexaammine-ruthenium (III) chloride in 0.1 M KCl. Scan rate: 5 mV s^{-1} .

ABBREVIATIONS

AuSPE	Gold screen printed macro electrode
BDDE	Boron-doped diamond
BPPG	Basal-plane pyrolytic graphite
bSPE	Screen printed microband electrode
CE	Counter electrode
CNT	Carbon nanotube
CV	Cyclic voltammetry
CVD	Chemical vapour deposition
drSPE	Carbon disc-shaped shallow recessed screen printed electrode
EDAX	Energy-dispersive X-ray spectroscopy
EIS	Electrochemical impedance spectroscopy
E_p	Peak potential
EPA	Environmental Protection Agency
EPPG	Edge-plane pyrolytic graphite
FIA	Flow injection analysis
FP-SPE	Filter paper-based screen printed electrode
GCE	Glassy carbon electrode
HOPG	Highly ordered pyrolytic graphite
ICP-AES	Inductively coupled plasma atomic emission spectroscopy
IR	Infra-red

I_p	Peak current
IP-SPE	Inkjet paper-based screen printed electrode
k^0	Electron chemical rate constant
LOD	Limit of detection
M_B	Mass of binder
M_I	Mass of ink
MWCNT	Multi-walled carbon nanotube
RE	Reference electrode
RP-SPE	Ruled pad paper-based screen printed electrode
RSD	Relative standard deviation
prSPE	Pentagon-shaped shallow recessed screen printed electrode
ps-SPE	Paper-based screen printed electrode (sellotape)
PtdrSPE	Platinum disc-shaped shallow recessed screen printed electrode
PtSPE	Platinum screen printed macro electrode
pv-SPE	Paper-based screen printed electrode (varnish)
SCE	Saturated calomel electrode
SEM	Scanning electron microscope
SPE	Screen printed electrode
SPMA	Screen printed microelectrode array
SPUME	Screen printed ultramicro electrode
SWCNT	Single-walled carbon nanotube
SWSPE	Screen printed single-walled carbon nanotube electrode

TEM	Transmission electron microscope
WE	Working electrode
WHO	World Health Organisation
XRD	X-ray diffraction
μ bSPE	Ultramicroband electrode
50bSPE	50 μ m Screen printed microband electrode

1.1 FUNDAMENTAL CONCEPTS IN ELECTROCHEMISTRY

1.1.1 ELECTROCHEMISTRY

Electroanalytical techniques are concerned with the interaction between electricity and chemistry, specifically the measurements of electrical quantities, such as current, potential, or charge, and their relationship to chemical parameters.^{1, 2} The field of electrochemistry encompasses a plethora of different phenomena (*e.g.* electrophoresis and corrosion), devices (electrochromic displays, electroanalytical sensors, batteries, and fuel cells), and technologies (the electroplating of metals and the large-scale production of aluminum and chlorine) which fulfil a virtually limitless number of applications many of which people encounter on a daily, if not hourly basis albeit in most cases unwittingly.

In contrast to many chemical measurements that involve bulk solutions, electrochemical processes take place at the electrode-solution interface.³ Electrochemical techniques can be broadly divided in to two sub-sets; potentiometric and potentiostatic measurements. This differentiation is owing to the electrical signal used for quantification for each. Both techniques depend upon the presence of at least two electrodes (conductors) and a contacting sample (electrolyte) solution within the system; the electrochemical cell.³ The surface of the electrode represents the junction between an ionic conductor and an electronic conductor.¹ The two minimum electrodes which must be present to allow for the formation of the electrochemical cell are termed the working electrode and the reference electrode. The working electrode is that which responds to the target analyte(s), whereas the reference electrode maintains a constant potential (that is, independent of the properties of the solution). Electrochemical cells can be classified as electrolytic (consuming energy from an

external source) or galvanic (producing electrical energy). Controlled-potential (potentiostatic) techniques deal with the study of charge-transfer processes at the electrode-solution interface based on dynamic (no zero current) situations; this is the section of electrochemical techniques with which this thesis is concerned. In such potentiostatic conditions, the electrode potential is used to drive an electron-transfer reaction, where the resulting current is measured which reflects the rate at which electrons are transferred across the electrode-solution interface. This is effectively "electron pressure", forcing a chemical species to either gain or lose an electron (reduction and oxidation respectively).³ The advantages of using controlled-potential techniques include high sensitivity and selectivity towards electroactive species where extremely low limits of detection (nanomolar) can be achieved with very small sample volumes (5 - 20 μL) (an often critical operational parameter with respect to real world applications of an analytical protocol), in addition to the extensive array of electrode materials now available, permitting the assay of unusual sample environments.^{3,4}

For the case of potentiostatic techniques it is common practise to employ a third electrode known as the auxiliary or counter electrode. When a three electrode cell is used to perform electroanalytical measurements, the auxiliary electrode in combination with the working electrode, forms a circuit *via* the sample solution over which current is measured. In such cases the potential of the auxiliary electrode is not of concern and as such not monitored but is adjusted so as to balance the reaction occurring at the working electrode. Importantly, this configuration allows the potential of the working electrode to be measured against the reference electrode without compromising the stability of the reference electrode by passing current over it.³ Shown in figure 1.1 is a typical experimental set-up where the three electrode system is being utilised. The reference electrode can be a Ag/AgCl or a Saturated Calomel Electrode (SCE) which can either be commercially obtained or fabricated within the

laboratory. The counter electrode should be a non-reactive high surface area electrode such as platinum or carbon and the working electrode can be a plethora of configurations and compositions. This approach is simplified using screen printed electrodes where all the electrodes are on one single, disposable strip (see later).

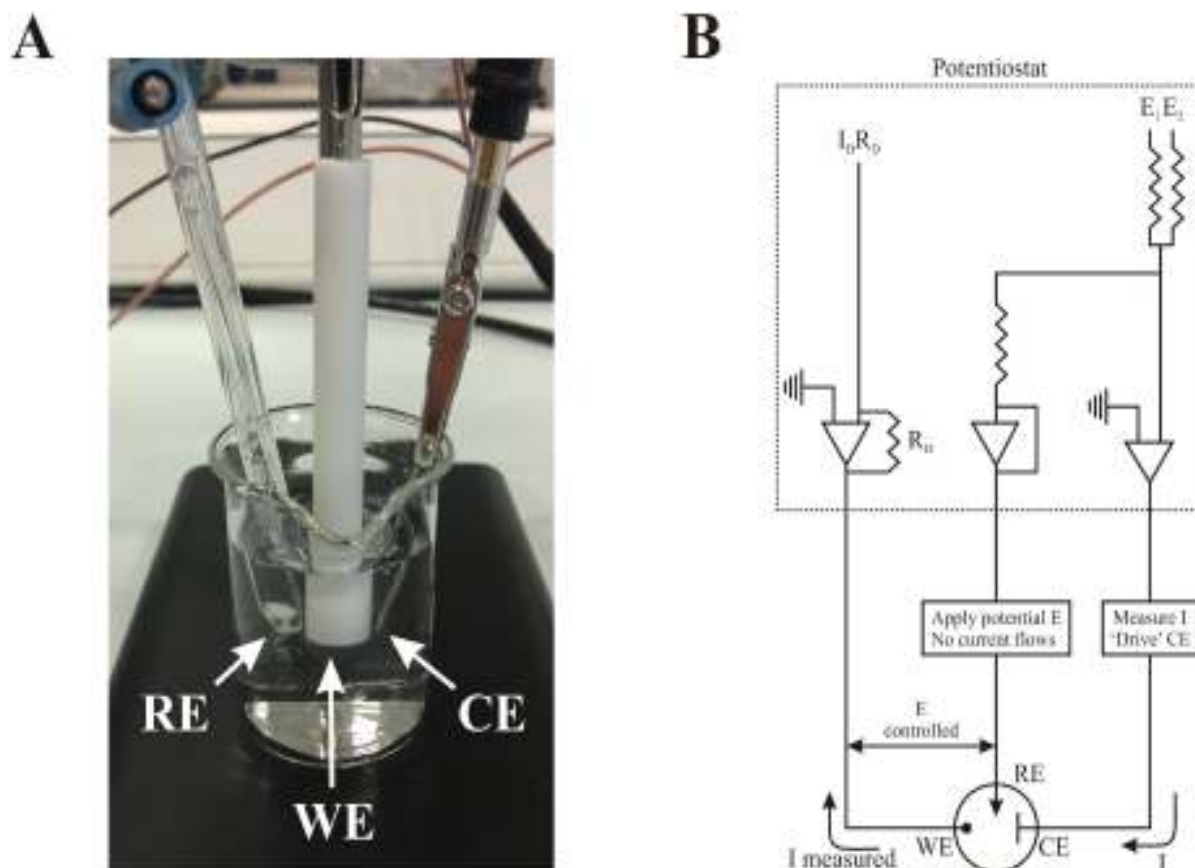


Figure 1.1 A) A typical experimental set-up showing the reference electrode (saturated calomel electrode), the working electrode (edge-plane pyrolytic graphite electrode) and the counter electrode (platinum rod) immersed into an electrolyte solution. B) A simple electronic schematic equivalent to the electrochemical cell. A commercial potentiostat is required for the running of electrochemical experiments.

1.1.2 FARADAIC PROCESSES

The intention of controlled-potential electro-analytical experiments is to obtain a current response that is dependent upon the concentration of the target analyte.³ This is achieved by recording the transfer of electron(s) during the redox process of the analyte²:



where O and R are the oxidised and reduced forms, respectively, of the redox couple. This reaction will occur in a potential region that makes the electron transfer thermodynamically or kinetically favourable. Within systems that are controlled by the law of thermodynamics, the potential of the electrode can be used to establish the concentration of the electroactive species [$C_o(0, t)$ and $C_R(0, t)$ where C_o and C_R simply represent the concentration of the oxidised and reduced forms, respectively] at the surface (distance from surface ($x = 0$) at time (t) according to the *Nernst equation*^{1-3, 5}:

$$E = E^o + \frac{2.3RT}{nF} \log \frac{C_o(0, t)}{C_R(0, t)} \quad (1.2)$$

At standard conditions (298 K):

$$E = E^o + \frac{0.059}{n} \log \frac{C_o(0, t)}{C_R(0, t)} \quad (1.3)$$

where E is the potential at which the peak is truly measured, E^o is the standard potential for the redox reaction, R is the universal gas constant ($8.314 \text{ J K}^{-1} \text{ mol}^{-1}$), T is the temperature (in Kelvin), n is the number of electrons transferred in the reaction, and F is the Faraday constant ($96,485.33 \text{ C mol}^{-1}$). Alternatively the *Nernst equation* can be expressed as:

$$E = E^o + (RT/nF) \ln(a_p / a_R) \quad (1.4)$$

where a_p and a_R are the standard activities of the products and reactants respectively.

For systems with negative E^o values, the oxidised reactants tend to be reduced thus the forward reaction (*i.e.* reduction) becomes more favourable. The current produced, resulting

from the change in oxidation state of the electroactive species is termed the Faradaic current because it obeys Faraday's law (that is the reaction of 1 mole involves a change of $n \times 96,485.33$ C). The Faradaic current is a direct measure of the rate of redox reaction. The resulting current-potential plot, known as a *voltammogram*, is a display of current signal (y axis) versus the excitation potential (x axis). The exact shape and magnitude of the voltammetric response is governed by the processes involved in the electrode reaction. The total current is the summation of the Faradaic currents for the sample and blank solution, as well as the non-Faradaic charging background current.^{2,4}

The reaction route undertaken at the electrode can be quite complicated, sometimes involving a sequence of different phases. The rate of such a reaction is determined by the slowest step in the sequence. Simple reactions involve only the mass transport of the electroactive species to the electrode's surface, the electron transfer across the interface, and the transport of the product back to the bulk solution. More complex reactions involve additional chemical and surface reactions that precede or follow the actual electron transfer. The overall rate of the reaction, and thus the measured current, is related to and may be limited by the mass transport of the reactant and/or the rate of electron transfer. As would be expected the slowest process will be the rate-determining step. Determining whether a given reaction is controlled by the mass transport or the rate of electron transfer depends on the type of compound being measured and the experimental conditions employed (these include electrode material, media, operating potential, mode of mass transport and time scale etc.). It is therefore apparent that the rate determining step of a given system may depend on the potential range under investigation. If the overall reaction is governed solely by the rate at which the electroactive species reaches the electrode's surface (*i.e.* a facile electron transfer), the current is said to be mass-transport limited. Such reactions are called Nernstian or reversible, because they obey thermodynamic relationships.

1.1.3 MASS TRANSPORT

As has been highlighted, mass transport or the rate of transport of an analyte of interest to the electrode-solution interface can also effect or even dominate the overall reaction rate. Considering this, it is apparent that mass transport is a major contributing factor towards electrochemical processes. Typically mass transport arises from three different modes²:

- *Diffusion* – the spontaneous movement of particles under the influence of concentration gradient (*i.e.* from regions of high concentration to regions of lower concentrations), aimed at minimizing concentration differences.
- *Migration* – movement of charged particles along an electric field (*i.e.* the charge is carried through the solution by ions according to their transference number).
- *Convection* – transport to the electrode by a gross physical movement, such as stirring or flow of the solution with rotation or vibration of the electrode (*i.e.* forced convection) or attributed to density gradients (*i.e.* natural convection).

These modes of mass transport are illustrated in figure 1.2.

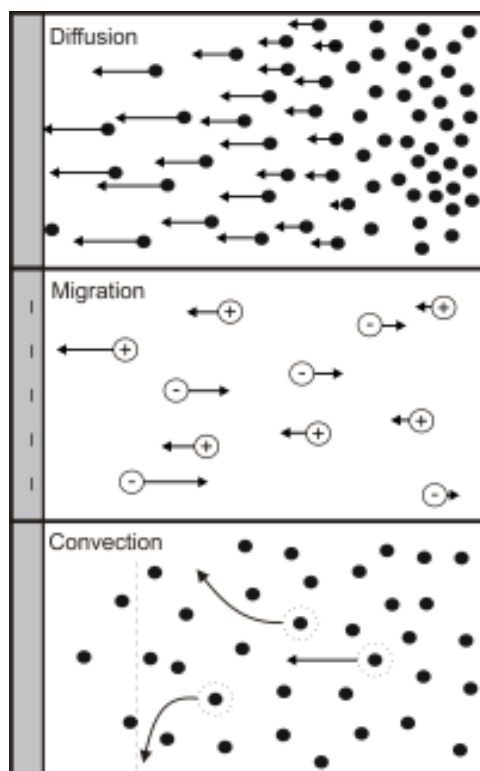


Figure 1.2 The three modes of mass transport towards an electrode surface.

Another important concept relating to electrochemical processes is flux (J). The flux is the measure of the rate of mass transport at a fixed point. It is defined as the number of molecules penetrating a unit area of an imaginary plane in a unit of time, and has the units of $\text{mol cm}^{-2} \text{s}^{-1}$. The flux to the electrode surface is described mathematically by a differential equation, known as the *Nernst-Planck equation* given here for one dimension²:

$$J(x, t) = -D \frac{\partial c(x, t)}{\partial x} - \frac{zFDc(x, t)}{RT} \frac{\partial \phi(x, t)}{\partial x} + c(x, t) V(x, t) \quad (1.5)$$

where D is the diffusion coefficient ($\text{cm}^2 \text{s}^{-1}$, D typically ranges between 10^{-5} and $10^{-6} \text{cm}^2 \text{s}^{-1}$), $\partial c(x, t)/\partial x$ is the concentration gradient (at distance x and time t), $\partial \phi(x, t)/\partial x$ is the potential gradient, z and $c(x, t)$ are the charge and concentration respectively of the electroactive species, and $V(x, t)$ is the hydrodynamic velocity (in the x direction) in aqueous media. The current (i) is directly proportional to the flux^{1-3, 5}:

$$i = -nFAJ \quad (1.6)$$

where n is the number of electrons transferred per molecule and A is the area of the electrode.

As shown by equation (1.5), the situation is relatively complex when the three modes of mass transport take place simultaneously. This impediment makes it particularly difficult to relate the current to the analyte concentration. The situation can be simplified significantly by suppressing the electromigration or convection, through the addition of surplus salt or the use of a quiescent solution respectively. Under these conditions, the movement of the electroactive species is limited solely by diffusion. The reactions that transpire at the surface of the electrode produce a concentration gradient adjacent to the surface, thus resulting in a diffusional flux. Consequently, equations prevailing over diffusion processes are applicable to many electrochemical procedures.

Fick's first law illustrates how the rate of diffusion adjacent to the surface (*i.e.* the flux) is directly proportional to the slope of the concentration gradient⁵:

$$J(x,t) = -D \frac{\partial c(x,t)}{\partial x} \quad (1.7)$$

Combining equations (1.6) and (1.7) yields a general expression for the current response⁵:

$$i = -nFAD \frac{\partial c(x,t)}{\partial x} \quad (1.8)$$

Therefore, the current (at any time) is proportional to the concentration gradient of the electroactive species. As shown by the above equation, the diffusional flux is time dependant.

Such dependence is described by Fick's second law (for linear diffusion)⁵:

$$\frac{\partial c(x,t)}{\partial t} = D \frac{\partial^2 c(x,t)}{\partial x^2} \quad (1.9)$$

This equation mirrors the rate of change with time to the concentration between parallel planes at points x and $(x + dx)$ (which is equal to the difference in flux at the two planes). Fick's second law is valid when assuming the condition that the parallel planes are perpendicular to the direction of diffusion. In contrast, for the case of diffusion towards a

spherical electrode (where the lines are not quite parallel but are perpendicular to segments of the sphere), Fick's law has the form⁵:

$$\frac{\partial c}{\partial t} = D \left(\frac{\partial^2 c}{\partial r^2} + \frac{2}{r} \frac{\partial c}{\partial r} \right) \quad (1.10)$$

where r is the distance from the electrode. Overall, Fick's 2nd law describes the flux and the concentration of the electroactive species as a function of position and time.

1.1.4 REACTIONS CONTROLLED BY THE RATE OF ELECTRON TRANSFER

Reactions with sufficiently fast mass transport, [those controlled by the rate of electron transfer ($O + ne^- \xrightleftharpoons[k_f]{k_b} R$)] display a different current-potential relationship to those discussed previously for mass transport-controlled reactions. The actual electron transfer step involves transfer of the electron between the conduction band of the electrode and a molecular orbital of O or R . The rate of the forward (oxidation) reaction, V_f , is given by:

$$V_f = k_f C_R(0, t) \quad (1.11)$$

while the reversed (reduction) reaction, V_b is given by:

$$V_b = k_b C_O(0, t) \quad (1.12)$$

where k_f and k_b are the forward and backward electrochemical rate constants respectively. These constants are dependent on the operating potential according to the following expressions²:

$$k_f = k^0 \exp[-\alpha nF(E - E^0)/RT] \quad (1.13)$$

$$k_b = k^0 \exp[(1 - \alpha)nF(E - E^0)/RT] \quad (1.14)$$

where k^0 is the electrochemical rate constant and α is the transfer coefficient. The value of k^0 (in cm s^{-1}) reflects the reaction between the chosen electrode material and the particular

reactant. The value of α (typically between 0.3 and 0.6) reflects the symmetry of the free energy curve with respect to the reactants and products. For symmetric curves α will be close to 0.5. Overall, equations (1.13) and (1.14) indicate that changing the applied potential influences k_f and k_b exponentially. Thus positive and negative potentials speed up the formation of oxidation and reduction products, respectively. For oxidation, the energy of the electrons found in the donor orbital in R must be equal to or higher than the energy of the electrons in the electrode. Conversely, for reduction, the energy of the electrons found in the electrode must be higher than the electrons in the receptor orbital of R .

1.1.5 POTENTIAL STEP/SWEEP BASED EXPERIMENTS

Potential step or sweep based experiments consider the effects in terms of current monitored, arising from the potential of the working electrode which is swept from a potential value V_1 to a second potential value V_2 . The rate at which the potential is swept over this potential range (V_1 to V_2) is known as the scan rate and is measured in Vs^{-1} . For macro electrodes the electrode potential is typically swept at rates within the range of 5 mV s^{-1} to 10^2 Vs^{-1} .²

The current-time relationship of such potentiostatic experiments can be explained through the resulting concentration-time profiles.^{2, 3} The region within which the solution is depleted of reactants (O in this case) is known as the *diffusion layer*, its thickness is given by δ . The concentration gradient is sharp at first, with a thin diffusion layer. As the time period increases, the diffusion layer expands, resulting in a decrease in the concentration gradient (see figure 1.3). The slope of the concentration gradient is given by $(C_o(b,t) - C_o(0,t))/\delta$ where $C_o(b,t)$ and $C_o(0,t)$ are the bulk and surface concentrations of O respectively. The change in the slope, and hence the resulting current, is due to changes of both $C_o(0, t)$ and δ .²

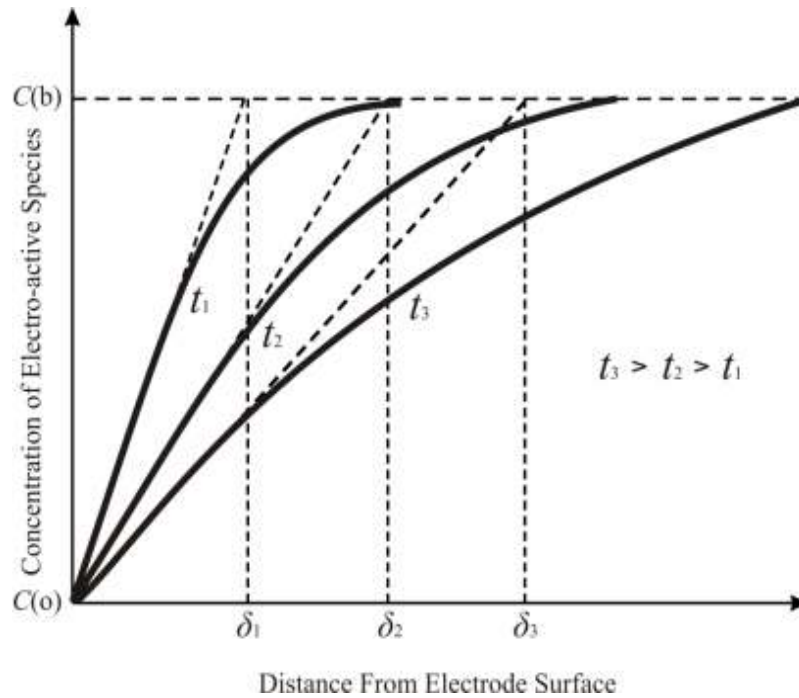


Figure 1.3 Concentration profiles for potential step-based experiments over various times.

As the scanned potential approaches the standard potential (E^O) of the redox couple, the surface concentration rapidly changes in accordance with the Nernst equation (equation 1.15). At a potential (E) equal to E^O the concentration ratio is balanced ($C_o(0,t)/C_R(0,t) = 1$). At further negative potentials (> 59 mV) than E^O , $C_R(0,t)$ is present at 10 fold excess ($C_o(0,t)/C_R(0,t) = 1/10$, $n = 1$). The decrease in $C_o(0,t)$ is allied with an increase in the diffusion layer thickness, dominating the change in the slope after $C_o(0,t)$ approaches zero, resulting in a peak-shaped voltammogram. The current decrease (within a time-dependent concentration profile) is proportional to the square root of time, described by the *Cottrell* equation¹⁻³:

$$i(t) = \frac{nFAD_oC_o(b)}{(\pi D_o t)^{1/2}} + \frac{nFAD_oC_o(O)}{r} \quad (1.15)$$

with $(\pi D_o t)^{1/2}$ corresponding to the diffusion layer thickness. Under constant stirring, the bulk concentration can be maintained at distance δ , hence, the concentration-distance profile

becomes solely dependent on the change in surface concentration ($C_o(\theta, t)$) and no longer influenced by the surface electron transfer reaction.

1.1.6 CYCLIC VOLTAMMETRY

Linear sweep voltammetry as described above where the potential range of swept from V_1 to V_2 can be extended so that when the potential reaches the value V_2 , the direction of sweep is reversed and the electrode potential is scanned back to the original value, V_1 . Cyclic voltammetry is the most extensively used technique for acquiring qualitative information about electrochemical reactions and is used extensively in this thesis. It tends the rapid identification of *redox* potentials distinctive to the electroactive species, providing considerable information about the thermodynamics of a redox process, kinetics of heterogeneous electron-transfer reactions, coupled electrochemical reactions or adsorption processes. Cyclic voltammetry consists of scanning (linearly) the potential of the working electrode using a triangular potential wave form (figure 1.4).

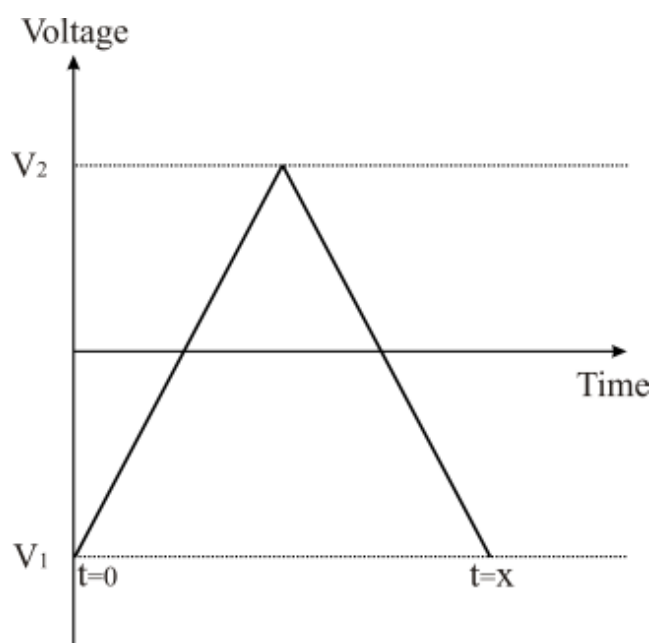


Figure 1.4 Voltage (potential) – time excitation signal utilised in cyclic voltammetric experiments.

Depending on the information sought, either single or multiple cycles can be performed. For the duration of the potential sweep, the potentiostat measures the resulting current that arises *via* the applied voltage (potential). The plot of current versus potential (voltage) is termed a 'cyclic voltammogram'. A cyclic voltammogram is complex and dependent on time along (scan rate) with many other physical and chemical properties. An illustration of a typical (reversible) redox couple is shown in figure 1.5. Assuming only O is present initially, a negative potential scan is selected for the first half-cycle, originating from a potential where no reduction transpires. As the applied potential advances towards the characteristic E^O for the redox process (unique to each process), the cathodic current increases until a peak is reached. Once the potential region (or window) in which the reduction process arises is traversed, the direction of the sweep potential is reversed. In this stage of the scan, R molecules (generated in the first phase of the sweep) that accumulate near the surface of the electrode are re-oxidised back to O , resulting in an anodic (current) peak. The magnitude of peaks which arise are commonly known as the peak current/height or I_p (as shown in figure 1.5).³ The peak potential commonly termed E_p and height seen on the reverse scan ($V_2 - V_1$) when observing redox probes as is exhibited in figure 1.5 give indication as to the reversibility of the redox couple.

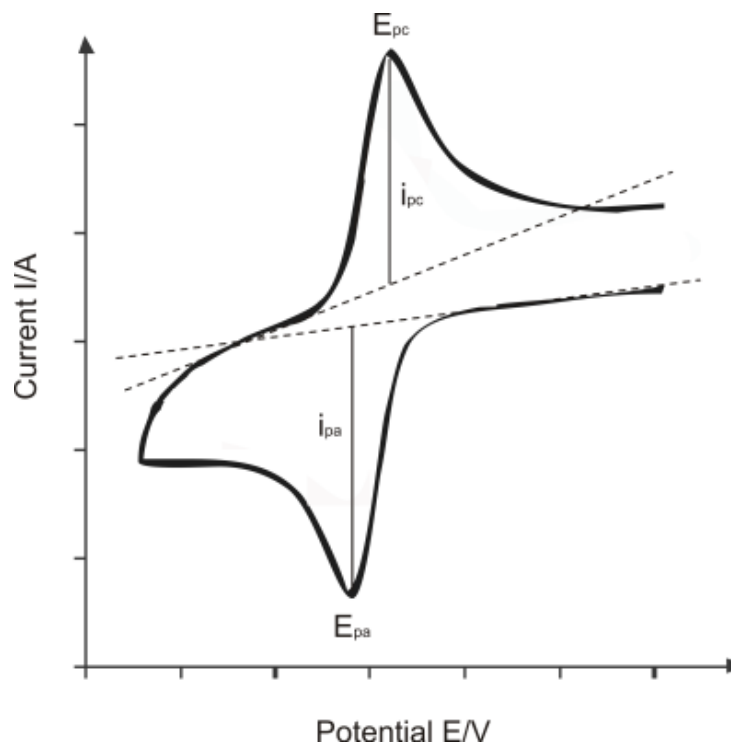


Figure 1.5 Typical cyclic voltammogram for a reversible redox process, where E_{pa} and E_{pc} correspond to the potential values at which the maximum anodic and cathodic peak currents (i_{pa} and i_{pc} , respectively) are recorded.

The characteristics of the peaks distinguished in a cyclic voltammetry are attributed to diffusion layers that occur near the electrode's surface (see earlier). The resulting current peaks are thus reflections of the continuous change in the concentration gradient with time. Therefore, increased peak current can be attributed to the achievement of diffusion control, while the current drop (beyond the peak) exhibits a $t^{-1/2}$ dependence (independent of the applied voltage/potential). Thus the reversal current displays a similar shape to the forward reaction.³

1.1.7 CHRONOAMPEROMETRY

The electrochemical technique of chronoamperometry involves stepping the potential applied to the working electrodes initially held at a value at which no Faradaic reaction

occurs before jumping to a potential at which the surface concentration of the electroactive species is zero (figure 1.6A) where the resulting current time dependence is recorded (figure 1.6C).³

The mass transport process throughout this process is solely governed by diffusion, and as such the current-time curve reflects the change in concentration at the electrode's surface. This involves the continuing growth of the diffusion layer associated with the depletion of reactant, thus a decrease in the concentration gradient is observed as time progresses (figure 1.6B). The current decay with time is given by the *Cottrell equation* mentioned previously (equation (1.15)).³

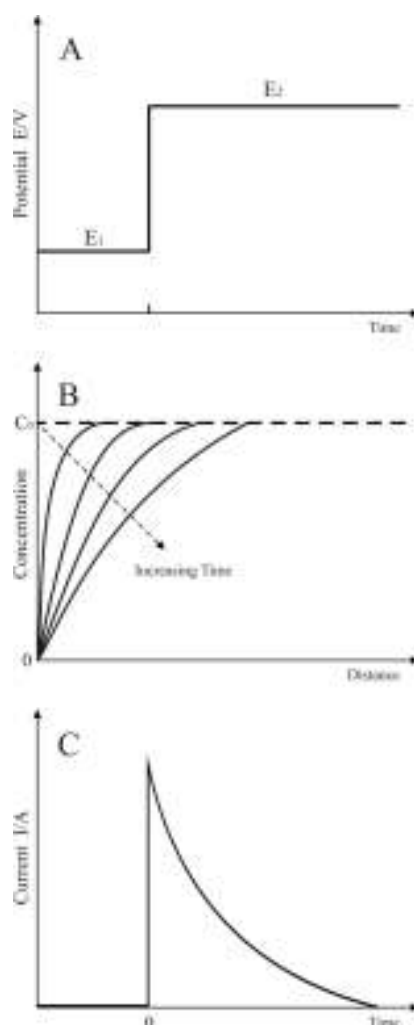


Figure 1.6 Chronoamperometric experiment: A) potential-time waveform; B) change of concentration gradient; C) resulting current-time response.

1.1.8 SQUARE-WAVE VOLTAMMETRY

Square-wave voltammetry is a large-amplitude differential technique in which a symmetrical waveform is superimposed onto a base staircase potential. The current is sampled twice during each square-wave sample, the first at the end of the forward pulse (t_1) and the other at the end of the reverse scan (t_2). The large amplitude grants the reverse pulse the capacity to sources the inverse reaction of the product formed during the forward pulse.³

The difference between the forward and reverse measurements is plotted versus the base staircase potential. The resulting peak shaped voltammetry is symmetrical about the half-wave potential, with the peak current directly proportional to the concentration. The outstanding sensitivity offered via this technique arises from the fact that the net current is a measurement of the difference between the forward and reverse currents and thus larger than its discrete components. Coupled with the diminished influence of the charging background current, extremely low limits of detection (approaching $1 \times 10^{-8} \text{ mol L}^{-1}$) can be attained. In addition, the current produced from dissolved O_2 is subtracted, thus there is no need to degas prior to experimental measurement.³

1.1.9 INTERPRETING DATA

The cyclic voltammogram is characterised by several key parameters. The two peak currents (I_p) and peak potentials (E_p) (observed visually), provide the basis for the diagnostic analysis of the voltammetric response. (See figure 1.5)

The peak current for a reversible redox couple is given by the Randles–Ševčík equation^{1, 2, 5, 6}:

$$I_p = 0.4463 \left(\frac{F^3}{RT} \right)^{1/2} n^{3/2} AD^{1/2} C v^{1/2} \quad (1.16)$$

where I_p is the voltammetric peak current, F is the Faraday constant, A is the electrode area (in cm^2), D is the diffusion coefficient of the analyte (in $\text{cm}^2 \text{s}^{-1}$), v is the applied scan rate (in V s^{-1}), C is the concentration of the electro-active species (in mol cm^{-3}) and n is the number of electrons transferred in the electrochemical process. Accordingly, the current is directly proportional to the concentration (useful for electroanalysis - see later) and increases with the square root of the scan rate. The ratio of forward-to-reverse current peaks should be equivalent for a simple reversible couple. However, the peak ratios can be strongly affected by chemical reactions coupled with the redox system. Peak currents (or heights), are normally measured by extrapolating the preceding baseline current.

The position (or potential) of the peaks (E_p) is related to the standard potential of the redox process. The formal potential for a reversible system is centred between $E_{p,a}$ and $E_{p,c}$ ⁴:

$$E^O = \frac{E_{p,a} + E_{p,c}}{2} \quad (1.17)$$

The peak separation (at 298 K) is given by:

$$\Delta E_p = 2.218 \frac{RT}{F} \quad (1.18)$$

Accordingly, a fast one electron process should exhibit a ΔE_p of 57 mV at 298 K. Note both peak potentials are independent of scan rate. For multiple electron transfer (reversible processes) the voltammogram will contain several discrete peaks if the E^O values of the individual processes are consecutively higher and distinctly separated. When a redox reaction is slow, or coupled with a chemical reaction, the situation changes significantly. It is these 'non-ideal' processes that are frequently of greatest chemical interest, for which the diagnostic power of cyclic voltammetry is most useful.

For an irreversible system (those with slow electron exchange), the individual peaks are reduced in magnitude and widely separated. Totally irreversible systems are characterised by a shift in the peak potential (see figure 1.7)^{3, 4}:

$$E_p = E^O - \frac{RT}{\alpha n' F} \left[0.78 - \ln \left(\frac{k^0}{D^{1/2}} \right) + \ln \left(\frac{\alpha n' F v}{RT} \right)^{1/2} \right] \quad (1.19)$$

where α is the transfer coefficient, v is the applied voltammetric scan rate and n' is the number of electrons involved in the charge-transfer step. As such, E_p occurs at potentials higher than E^O , with the over potential related to k^0 (the electrochemical rate constant) and α ; the voltammogram becomes increasingly 'drawn out' as αn is decreased.

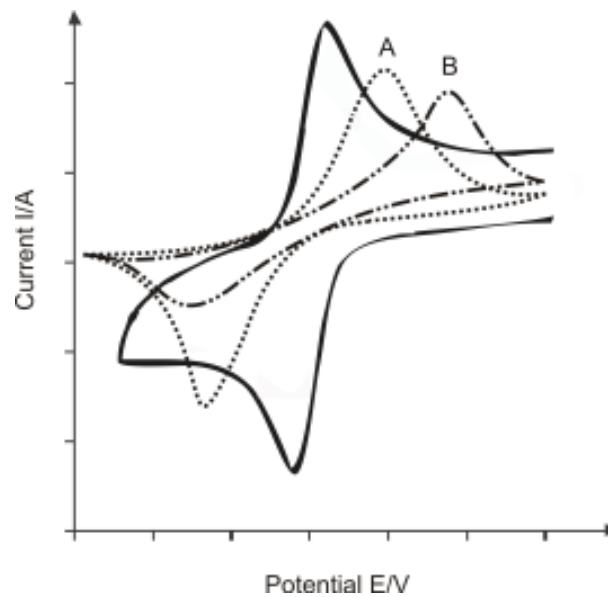


Figure 1.7 Examples of cyclic voltammograms for a quasi-reversible (A/dotted) and irreversible (B/dash-dot) redox processes. The solid line represents a typical voltammogram for a reversible process.

The peak current in this irreversible case (at standard conditions) is given by²:

$$I_p = 2.99 \times 10^5 n (an_a)^{1/2} ACD^{1/2} v^{1/2} \quad (1.20)$$

where n is the total number of electrons transferred and an is the number of electrons involved in the charge-transfer step, as mentioned above. Assuming a value of 0.5 for α , the reversible-to-irreversible current peak ratio is 1.27; thus the resulting peak current for the irreversible process is approximately 80 % of that attained for the reversible system.

Quasi-reversible processes are controlled *via* both charge transfer and mass transport. The rate of the electron kinetics is measured *via* the electron chemical rate constant (k^0), whilst the rate of mass transport is measured by the mass transport coefficient:

$$m_T = \frac{D}{\delta} \quad (1.21)$$

where δ is the diffusion layer thickness, and as discussed earlier, is dependent on time (t) according to²:

$$\delta \sim \sqrt{6Dt} \quad (1.22)$$

$$t \sim \frac{RT}{Fv} \quad (1.23)$$

The distinction between fast and slow electrode kinetics relates to the dominant rate of mass transport given by²:

$$k^0 \gg m_T \text{ (reversible)} \quad (1.24)$$

$$k^0 \ll m_T \text{ (irreversible)} \quad (1.25)$$

The transition limits between a system that is reversible and irreversible can be defined through the parameter Λ ³:

$$\Lambda = \frac{k^0}{\left(\frac{FDv}{RT}\right)^{1/2}} \quad (1.26)$$

Three classifications of systems at stationary macro electrodes (at 298 K, assuming $\alpha \sim 0.5$) are evident:

Reversible	$\Lambda \geq 15$	$\Lambda \geq 0.3 v^{1/2} \text{ cm s}^{-1}$
Quasi-reversible	$15 > \Lambda > 10^{-3}$	$0.3 v^{1/2} > k^0 > 2 \times 10^{-5} v^{1/2} \text{ cm s}^{-1}$
Irreversible	$\Lambda \leq 10^{-3}$	$k^0 \leq 2 \times 10^{-5} v^{1/2} \text{ cm s}^{-1}$

These conditions show that reversible and irreversible behaviour observed for a given electrochemical rate constant is dependent on the applied scan rate. At sufficiently fast scan rates, at least in principle, all processes can appear electrochemically irreversible (figure 1.8).

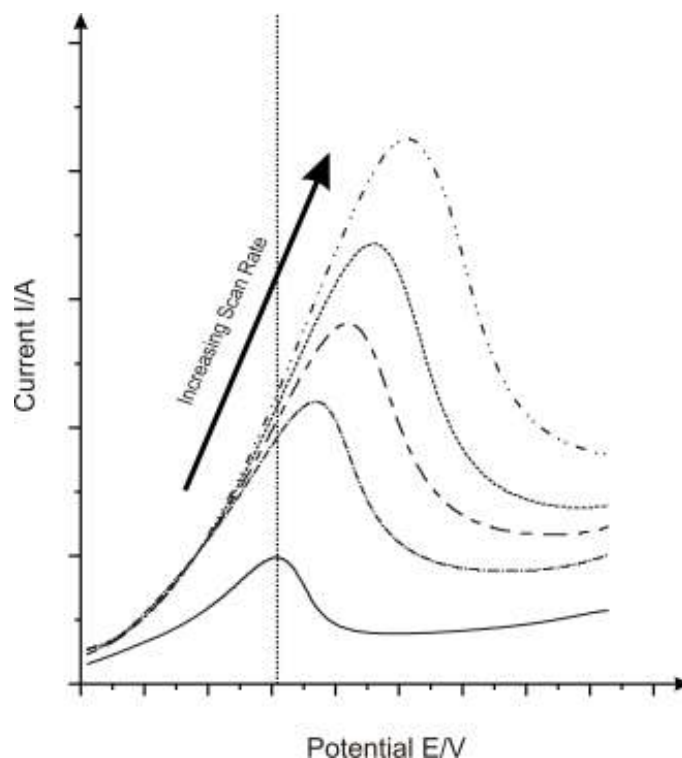


Figure 1.8 An example of shifting peak potentials as a result of increasing scan rate.

Cyclic voltammetry offers an indispensable tool for the determination of the experimental electrochemical rate constant. Numerical calculations developed by Nicholson provide a basis for calculating the electrochemical rate constant (k^0) via the peak separation potential ($\Delta E_p = E_{p,a} - E_{p,c}$) observed during cyclic voltammetric analysis. The Nicholson method is routinely used to estimate the observed standard heterogeneous electron transfer rate for quasi-reversible systems using the following equation⁷:

$$\psi = k^0 [\pi D n v F / (RT)]^{-1/2} \quad (1.27)$$

where ψ is the kinetic parameter, D , the diffusion coefficient, n , the number of electrons involved in the process, F , the Faraday constant, v , the scan rate, R , the gas constant, and T

the temperature. The kinetic parameter, ψ is tabulated as a function of peak-to-peak separation (ΔE_p) at a set temperature (298 K) for a one-step, one electron process (where $\alpha = 0.5$). The function of (ΔE_p), which fits Nicholson's data, for practical usage (rather than producing a working curve) is given by⁸:

$$\psi = (-0.6288 + 0.021X)/(1 - 0.017X) \quad (1.28)$$

where $X = \Delta E_p$ is used to determine ψ as a function of ΔE_p from the experimentally recorded voltammetry. From this, a plot of ψ against $[\pi D n \nu F / (RT)]^{-1/2}$ is produced graphically (see equation (1.27)) allowing the standard heterogeneous rate transfer constant, k^0 to be readily determined.

1.1.10 ELECTROANALYSIS

Voltammetric techniques such as those discussed within this Chapter are frequently applied in analysis; the main focus of this thesis. Potential step techniques such as those considered earlier, particularly cyclic voltammetry find wide applications in analytical electrochemistry and are naturally compatible with digitally based potentiostats utilised for potentiostatic measurements.

When considering the utilisation of cyclic voltammetry for electroanalysis as has been defined earlier, the current arising from the electrochemical reactions taking place at the electrode-solution interface is of paramount interest. The voltammetric peak (height) arising at a particular voltammetric potential (E_p) from the oxidation or reduction of the analyte of interest is known as the I_p . In a typical electrochemical system, for example when considering the redox probe potassium ferrocyanide (II) it would be expected that an increase in the analyte concentration would result in an increase in the observed voltammetric peak height. The concentration range over which this relationship between the recorded voltammetric peak height and analyte concentration is linear is known as the “analytical

linear range". Simply, this is the concentration range over which a particular increment in the analyte concentration will give an equally, fixed increment in the observed voltammetric peak height. Outside of this linear range the dynamics of the relationship between the two parameters change and as such the expected voltammetric peak height cannot easily be deduced for a given concentration. As shown earlier, the peak current (I_p) is proportional to the analyte concentration (see equation (1.20)) where the analytical signal is "amplified" by 2.99×10^5 . As such this is the origins as to why electrochemistry is such a sensitive analytical tool.

Equally important when considering the utilisation of electrochemical techniques for analytical purposes is the pH of the solution in which the analyte and electrodes reside. At certain pHs for example electrochemical measurement of analytes is not possible, for example generally the determination of metals *via* electrochemical means in alkaline solutions is not feasible. Furthermore the pH of a solution can dictate or affect the potential (E_p) at which a voltammetric peak occurs, if protons are involved in the mechanism.

One avenue for improved electrochemical performance in relation to electroanalysis is the working electrode utilised within the electrochemical cell. With this in mind new electrode materials or substrates are constantly being reported in the literature with each piece of research hoping to unveil the next generation of electrode material. Additionally the electrode material utilised can yield beneficial electrochemical characteristics for the sensing of key analytes if correctly employed which ensures that a common theme within the field of electrochemistry is the modification of existing electrode materials or in some cases development of a completely new electrode material; such is the case with graphene currently.

1.1.11 BENCHMARKING THE FABRICATED SCREEN PRINTED DEVICES

The main thrust of this thesis is to push the boundaries of screen printed technology to produce novel, never-before-reported electrochemical devices. In order to evaluate these fabricated screen printed platforms target analytes are studied with an electroanalytical context in order to benchmark the electrochemical devices with the current literature in order to discover the potential benefits and limitations of the given sensor. Note that target analytes which have been well-characterised and studied in relation to not only their electrochemical determination, but also generic analytical monitoring have been purposely chosen to allow such benchmarking and in turn evaluation of the proposed electrochemical devices.

The two key parameters that are utilised extensively and routinely within the literature to benchmark and evaluate electrochemical devices in terms of their electroanalytical merits are: analytical linear range and statistical limit of detection (LOD). Consequently these two tools of evaluation are used extensively in later Chapters (3 - 5). Note that it is not the thrust of this thesis to extensively explore the electroanalytical performance/merits of the devices described herein, but rather demonstrate that such designs are feasible and of merit in terms of the current state-of-the-art.

For clarity the linear range is defined as the concentration range over which an increase in the analyte concentration present within a given solution results in a proportional increase in the electrochemical signal recorded. Linearity is measured and rationalised through the monitoring of the coefficient of determination, commonly denoted as R^2 . In statistics, the R^2 value indicates how well data points fit a line or curve. The extent of linearity is determined through the value determined for the R^2 value which can range from 0 to 1, with 1 describing complete linearity over the entire data range. When considering the coefficient of determination in relation to experimental data, as is the case within this thesis, it would be unexpected to achieve an R^2 value of 1, but rather one in the range of 0.96 to

0.99, which would be sufficient to support the conclusion that the analytical performance of a given sensor was linear over the range studied for a particular analyte.

The limit of detection (LOD) is defined as the minimum value of the signal from the species being measured that is significantly different from the blank signal. Although there is some discussion on this point, the vast majority of the electroanalytical literature available utilises this concept to benchmark proposed electrochemical systems/sensors. Here the determined limit of detection is determined based upon its calculation from calibration plots on three times the standard deviation of the y -residuals. Thus, the intercept of the linear plot, $y = a + bx$, is the blank value of the response $y_B (= a)$, and the limit of detection for x corresponds to the y -value for $y = y_B + 3s_B$, where s_B is the standard deviation of the y -residuals from the line of best fit. A software package (Origin®) is used to provide the value of s_B directly. The limit of detection is then $(3s_B/b)$ as shown in figure 1.9.

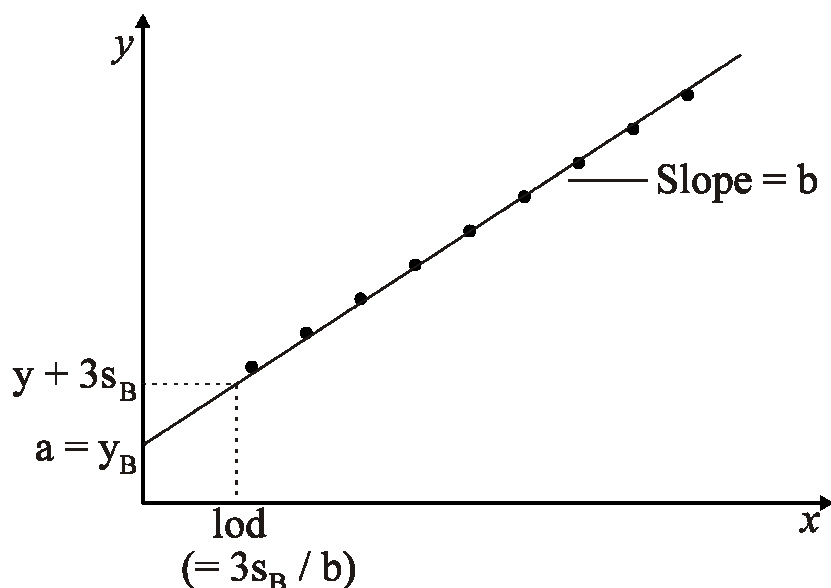


Figure 1.9 A typical calibration plot constructed to determine the theoretical limit of detection using experimental data.

It is important to note that the limit of detection is a theoretical value and as such, not always a definitive value. However, such a determination is required to allow the

benchmarking of electrochemical systems against the current literature. Some thought concerning this method for determining detection limits reveals a potential weakness, which is of great importance. If the calibration plot is of high quality, then s_B will be very small leading to an extremely low detection limit. In practice this limit may never be reached due to limitations of the experimental procedure or the instrumentation (noise and drift at low signal levels), apart from any chemical interferences. However, this approach to produce LODs is common place in the literature to benchmark one's electrochemical system.

1.2 ELECTRODE MATERIALS

The material selected for use as a working electrode can enhance or hinder the desirable characteristics sought by researchers since all electrochemical processes take place at the working electrode surface.² Electronic conductors used as electrodes are metals, rarely metal oxides, various forms of carbon and also rarely some polymers.⁴

Carbon is a highly utilised electrode material due to its many attributes which include being readily available, cheap (depending on its form), easily modified and chemically inert. Carbon electrodes are made of various materials, such as graphite of spectral purity, glassy carbon, graphite powder with liquid or solid binders, carbon fibres, highly oriented pyrolytic graphite (HOPG), carbon nanotubes, boron-doped diamond and titanium carbide, tending the hardest, highest strength and highest surface area respectively of any materials commonly found. It presents varying properties depending on its allotropic form, many of which are under intense research, such as carbon nanotubes or graphene.

The choice of material used for the working electrode also depends on the system being electrochemically investigated. Elemental metals can be highly reactive, undergoing electrochemical processes, forming oxides which limit their electrical conductivity. Typically gold or platinum are commonly favoured, though their high cost often makes them unfavourable.

An alternative and often more cost-effective material utilised within as a solid electrode within electrochemistry is the carbon based electrode. Carbon based electrodes are now widely used in electroanalysis because they offer a wide potential window, low background current; rich surface chemistry, low cost and chemical inertness. Unfortunately, electron transfer rates observed at carbon surfaces are often slow when compared to traditionally employed metal electrodes. The electron transfer rate is strongly affected by the orientation of the carbon surface. Although all (frequently encountered) carbon electrode

materials share the same rudimentary six-membered aromatic ring and sp^2 bonding, each holds relatively different densities of edge and basal-plane amid their surface which is of fundamental importance. The edge orientation is more reactive towards electron transfer and adsorption processes than the graphite basal-plane.^{9, 10} Thus, materials with different edge-to-basal ratios can exhibit significantly different electron transfer kinetics for a given redox analyte. The most commonly exploited carbon materials are described below.^{9, 10}

1.2.1 GRAPHITE

The low cost and ease of manipulation of graphite has established its use as an electrode material in electrochemistry. Hybridisation of the carbon atom changes the crystal structure of the material. In the case of sp^2 hybridisation, the carbon atom remains with one free electron in the 2p orbital. Each of the sp^2 hybridised orbitals then combines with other hybridised atoms/orbitals to form a series of planar hexagonal structures (figure 1.10). The free delocalised orbital is orientated perpendicular to this plane. Thus the electron can move easily from one side of the carbon atom layer to the other but cannot easily move from one layer to the other. This phenomenon makes the material anisotropic.^{9, 10}

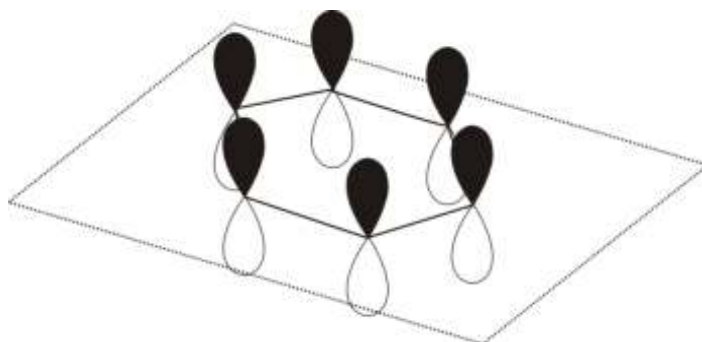


Figure 1.10 Schematic of sp^2 hybridised structure of graphite (free 2p orbitals shown).

Graphite is comprised of a series of parallel planar layers, termed basal-planes. Graphite has a perfect (defect free) hexagonal, crystallographic structure (shown below) and

should not be confused with other graphitic materials. The stacking of the basal-plane occurs in two ordered structures, hexagonal or rhombohedral. The most commonly found stacking order is hexagonal (or alpha) with a –ABABAB– sequence, superimposing the carbon atoms of alternating basal-planes as shown in figure 1.11.^{9, 10}

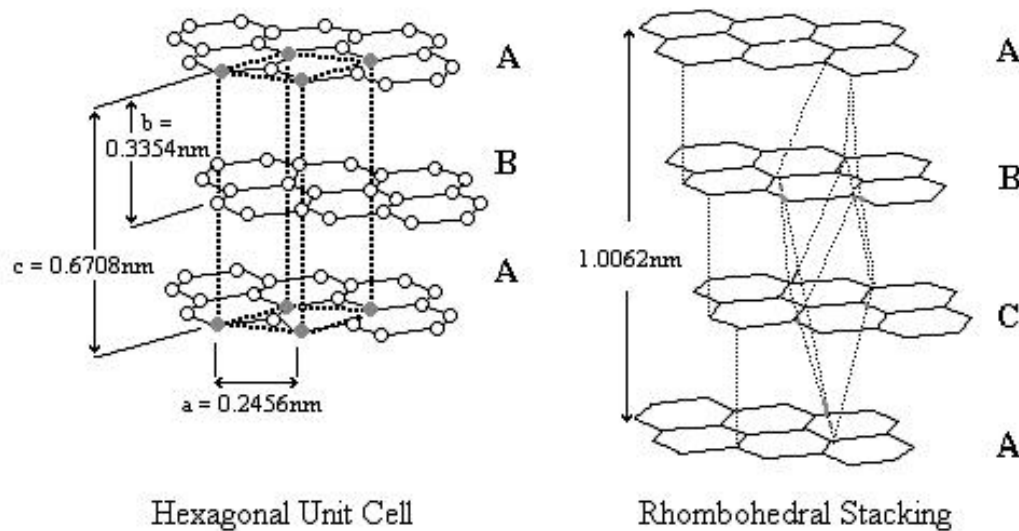


Figure 1.11 Schematics of hexagonal and rhombohedral graphite stacking arrangements, adapted from reference ⁹.

A rhombohedral structure (figure 1.11) displays a –ABCABC– stacking order, thus the carbon atoms of every third basal layer are superimposed. This type of structure is not found in a pure form but in a blend with the hexagonal arrangement. The rhombohedral configuration converts to the hexagonal form, which is thermodynamically more stable, after heat treatment (over 1300 °C).⁹

The significant difference between the two structures is found in the distance between the basal layers (C_o), 0.6708 nm and 1.0062 nm for hexagonal and rhombohedral systems respectively. No direct overlap of carbon atoms between adjacent layers is found in either structure.⁹

The graphitic crystal (basal) layer has two faces (zig-zag or arm-chair), depending on the orientation of the basal layer (figure 1.12); these two configurations display different electron conductivities (important for carbon nanotubes (described later)).

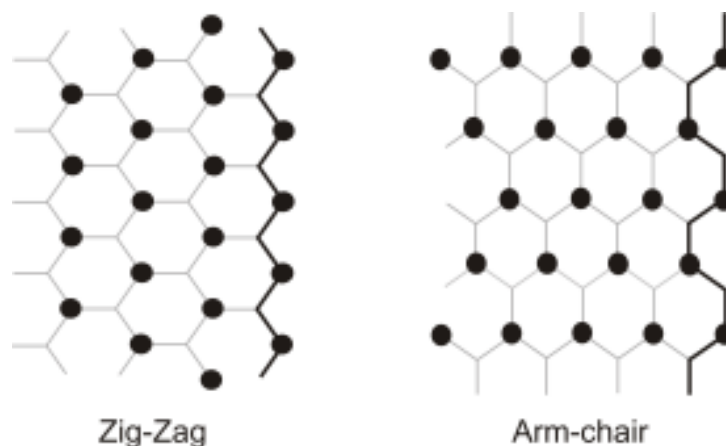


Figure 1.12 Schematic of a zig-zag (left) and arm-chair (right) graphitic crystal formations.

In line with the basal-plane is what researchers have termed the ‘edge-plane’. The edge-plane is formed *via* the termination sites found around the perimeter of the basal-plane layers. Basal and edge-plane sites exhibit significantly different surface energies (0.11 J/m^2 and 5 J/m^2 respectively). Thus, the reaction rate at the edge-plane sites is considerably faster than that found at the basal-plane. This parameter is important when constructing or tailoring a graphite electrode for a specific system. Evidently, for processes that require fast electro-catalytic reactions, the working surface area should contain an elevated percentage of edge-plane-like sites/defects. Concurrently, the reverse is true for systems favourable to slow electro-catalytic processes. Edge-plane and basal-plane pyrolytic-graphite electrodes (EPPG and BPPG respectively) are fashioned from highly-ordered pyrolytic-graphite (HOPG). The HOPG surface consists of islands of basal-plane graphite, surrounded by nano bands of edge-plane sites, which lie parallel to the surface. Defects along the surface occur in the form of steps exposing the edges of the graphite layers. Graphite’s layered structure tenders low

resistivity along the plane (~ 2.5 to $5 \times 10^{-6} \Omega \cdot \text{m}$), conversely through (perpendicular to) the plane, resistivity values approach close to $3000 \times 10^{-6} \Omega \cdot \text{m}$. This consequently results in electrodes, consisting entirely of edge-plane *viz* an edge-plane pyrolytic-graphite electrode, displaying a near reversible voltammogram, while an electrode consisting mostly of basal-planes will show irreversible behaviour; it should be noted that this is highly dependent on the percentage of edge-plane exposed.⁹

It is also important to highlight the recent and rapidly growing prevalence for the favouring and utilisation of the nano-material graphene (figure 1.13). Graphene, a single atomic layer thick two-dimensional carbon nanomaterial, has been reported to possess spectacular physical, chemical, and electrical properties,¹¹⁻¹³ and has consequently received enormous interest from a plethora of scientific disciplines into the exploration and exploitation of its unique properties.^{12, 13} One area of particular interest where graphene has had significant impact is electrochemistry, where it has been widely used as an electrode material within a variety of sensing and energy related devices, claiming superior electrochemical performances when compared to traditional noble metals and various fullerene based electrode materials, such as graphite and carbon nanotubes. At present graphene has been incorporated within electrochemical sensors acting as a modifier that is deposited, typically by drop coating, upon an electrode surface such as a carbon or metal-based electrode.

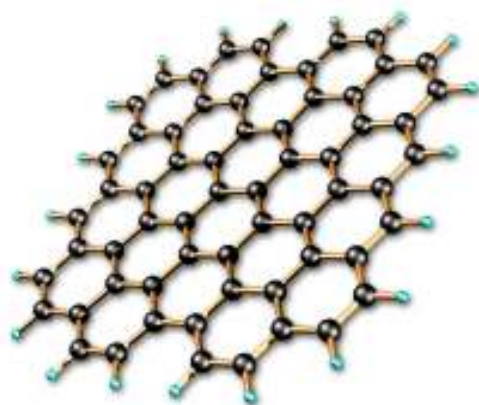


Figure 1.13 Schematic representation of graphene.

1.2.2 PYROLYTIC GRAPHITE

Pyrolytic graphite is a unique form of graphite produced *via* chemical vapour deposition (CVD). An organic precursor, such as methane, typically contained within hydrogen (or a similar mixture), flows through a gas chamber. Inside is a preheated substrate where the methane is deposited on its surface and slowly decomposed into continuously growing layers of carbon *via* the following reaction scheme: methane \rightarrow benzene \rightarrow poly-aromatic hydrocarbons \rightarrow carbon. This material is consequently heat treated at 2500 °C, reordering the crystal structure into its final form. Depending on the temperature and pressure applied, pyrolytic graphite can take three different forms: columnar, laminar and isotropic. Isotropic pyrolytic graphite displays a reduced size in the basal-plane's surface area, with greater interlayer spacing when compared to the other forms. The layered pyrolytic graphite is then cut. The orientation of the material determines the electro-catalytic properties, fashioning an electrode surface consisting of either basal (basal-plane pyrolytic graphite, or BPPG) or edge (edge-plane pyrolytic graphite, or EPPG) like sites. EPPG electrodes display enhanced electro-catalytic properties (fast electron transfer reactions, lower overpotentials *etc*) compared to the same electrode material with a basal-plane orientation (BPPG). Typically in electrochemical measurements, a body allegedly capable of increasing the electro-catalytic response of the working electrode's surface is initially tested on a BPPG orientated electrode. The analyte is deposited on the basal-plane-like surface of the BPPG electrode prior to electrochemical analysis. When the current response from the modified BPPG is augmented in comparison to its typically electrochemical spectra (approaching or even surpassing that of an EPPG electrode), the newly incorporated material is deemed to have enhanced the electro-catalytic behaviour of the working electrode's surface (since BPPG itself exhibits slow electro-catalytic behaviour). An example of a HOPG electrode is shown in figure 1.14

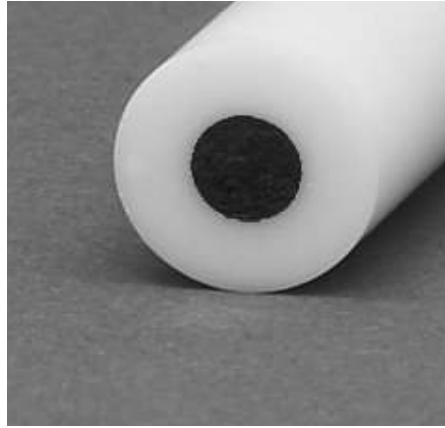


Figure 1.14 Image of a HOPG electrode.

1.2.3 CARBON NANOTUBES

A carbon nanotube (CNT) is conceptually a single dimensional, micrometer scale graphene sheet (single layer of graphite), rolled into a cylinder of nano-scale diameter, crowned with a spherical fullerene (fullerenes are zero dimensional enclosed cage-like carbon structures). Pairing a nano-scale diameter with a micro- to centimetre length yields CNT structures with remarkable aspect ratios. Extensive published literature is available on the synthesis and structural conformations of CNTs.¹⁴ The sidewalls of CNTs, have a hexagonal sp^2 conformation; however, the degree of curvature witnessed at carbon nanotubes is not limited to a single dimension. The stronger sp^3 bonding characteristics found at the nanotube reduce the strain energy at the walls and render the carbons less susceptible to chemical modification and rearrangement than spherical fullerene structures.

CNTs typically exist in three main forms; single-walled nanotubes, double-walled nanotubes and multi-walled nanotubes. Isolated single-walled nanotubes (SWNTs), typically of small diameters, can display metallic, semi-metallic or semiconducting characteristics subject to the orientation of the hexagonal carbon lattice. Typically, in high yield synthesis techniques, the nanotube adopts the metallic arm-chair structural conformation.

Double-walled and multi-walled nanotubes (MWNTs) share many of the properties of bulk SWNTs as the coupling across the 0.34 nm interlayer is weak (figure 1.15). Unlike SWNT, MWNTs display semiconducting characteristic akin to bulk graphite.

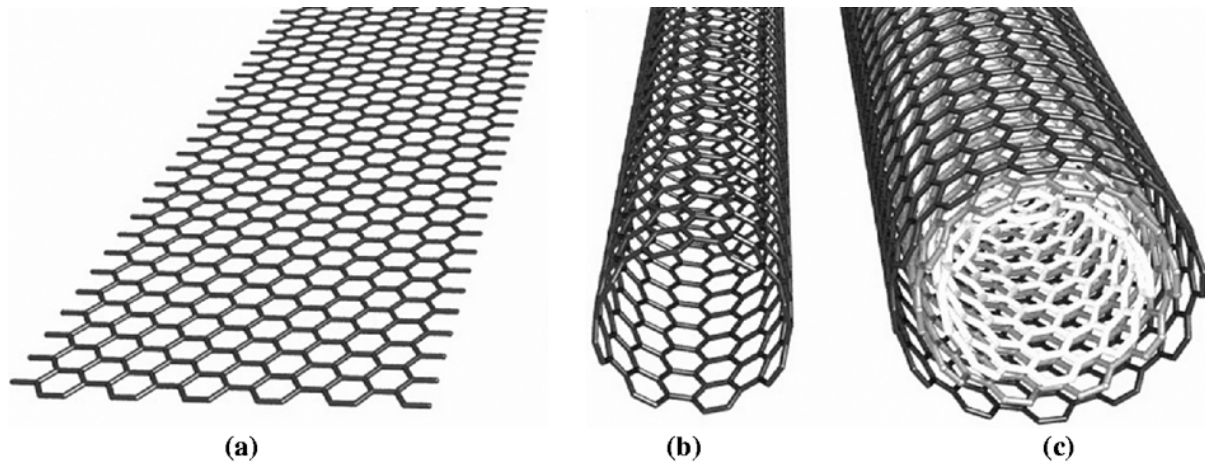


Figure 1.15 Graphical Depictions of a) graphene sheet b) SWNT and c) MWNT. Figure reproduced from reference ¹⁴.

Strong attraction forces between the nanotubes complicates purification and manipulation processes. The tightly bundled conformation and poor dispersal observed at CNTs in both polar and non-polar solvents is credited to these forces, often requiring physical dispersion processes, such as sonication, to produce a uniform mixture.

SWNTs and MWNTs obtained commercially are replete with defects, metal impurities and physical dissimilarities. Thus, these discrepancies between samples convolute research, having a substantial impact on the commercial application of CNTs. As such, the application of CNTs draws upon its bulk properties, like high surface area, rather than single nanotube characteristics such as high conductivity.

The bonding arrangement of fullerenes and nanotubes offer unique conductive, optical and thermal properties, tendering auspicious characteristics for applications within the electronic industry. Tuneable band gaps, high stability, remarkable current transport

capability, low ionization potential, and efficient field emission are among the most desirable electronic characteristics of SWNTs. A vast amount of these properties occur *via* the electron flow confinement in one-dimensional nanotubes. The electronic behaviour observed at nanotubes is strongly coupled to chirality, diameter, length, and the number of concentric tubules. Metallic SWNTs act akin to quantum wires, with electron confinement in the radial direction as mentioned previously, quantizing the conduction bands into discrete energy levels. Electrons are transported *via* resonant tunnelling through these discrete electron states in the nanotube, delocalized over an extended length of the nanotube. This spatial extension of charge not only bolsters conductivity and current capability, but also diminishes the impact of defects occurring along the nanotube sidewalls.

1.2.4 BORON DOPED DIAMOND

The boron-doped diamond electrode (BDDE) is a commonly employed tool within electrochemistry. The BDDE does not interact or bind with organic compounds, the by-products are not absorbed onto its surface during the redox reaction that occur at its surface, leaving it unpolluted and available for further redox reactions of further electroactive species present in solution. Boron-doped diamond is a tough, stable (does not form oxides) material, resistant to most chemicals. The reason for these distinctive characteristics lies in the BDDE structure.

Carbon atoms have a $1s^2, 2s^2, 2p^2$ electron configuration in the ground state. Once these atoms bond together in a diamond structure (similar to methane), the following electron configuration is present: $1s^2$ and four $2sp^3$ (hybrid orbitals). This raises the energy state of the electrons in the carbon atom, stabilised *via* the bonds found in the structure. The resulting hybridisation is the formation of four strong covalent bonds with an additional four carbon atoms (each sharing two electrons). The four sp^3 valence electrons of the hybrid carbon

atoms, in conjunction with a small atom size results in a strong covalent bond. This is enhanced as four of the six electrons found at the carbon atom formulate bonds.

Diamond is one of the best known electrical insulators, making it a poor candidate as an electrode material. Conversely its high strength, stability and chemical resistance make it ideal. This only occurs when the diamond is a pure crystal. The presence of impurities or defects diminishes these optimum properties. Thus doping diamond with metal impurities alters its electrical properties (increasing conductivity). Boron has a similar atom size to carbon and is a known electron acceptor, due to electron deficiencies found in its outer shell. To provide adequate conductivity, doping of the diamond electrode ranges from 10^{19} to 10^{21} atoms/cm³. The resulting electrode, as mentioned previously has a wide operating potential window (~ -1.35 to $+2.3$ V versus a normal hydrogen electrode), low background currents and stability in aggressive media.

1.2.5 GLASSY CARBON

Glassy carbon offers unique properties compared to other types of carbon materials. Essentially non-porous, it offers low permeability, while free from surface defects and containing little or no impurities. These characteristics are attributed to the organic precursor (polymer) from which it is produced. The crystallite arrangement is random (no long-range order) making the material isotropic and produces a 'ribbon' like structure (figure 1.16). The aromatic rings are twisted and cross linked with covalent bonds, producing variable bond energies and thus the existence of sp^2 and sp^3 structures. The partial diamond structure (sp^3) is believed to give the glassy carbon its high strength and hardness. It is for this reason that this material is not easily graphitised (converted to graphite under high temperatures) and is highly resistant to chemical attack.

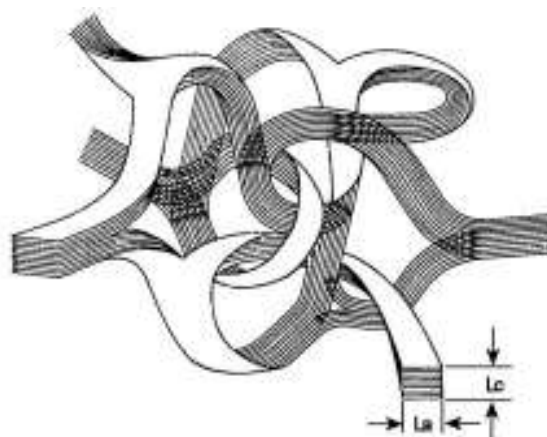


Figure 1.16 Glass carbon 'ribbon' network where L_a is the Intraplanar Microcrystalline Size and L_c is the Interplanar Microcrystalline Size. Figure reproduced from reference ¹⁵.

1.2.6 METAL ELECTRODES

A wide variety of metal electrodes are available for use in electroanalysis including platinum, gold, nickel, and palladium, with platinum and gold being the most commonly used. Metal electrodes can come in either bulk or thin-film form. Such electrodes exhibit fast electron-transfer kinetics for many redox systems and can be utilised over a large anodic range. The cathodic window for some metal electrodes, such as platinum, is more limited due to hydrogen evolution. However, metal electrodes are prone to exhibiting features or peaks associated with the formation and reduction of surface oxides which is also associated with background currents. Such films strongly affect the rate kinetics of the electrode reaction which if not controlled can result in problems with reproducibility. This is less problematic in non-aqueous media. Gold electrodes, compared to that of a platinum electrode, are more inert and therefore less prone to surface contamination and/or the formation of surface oxides films.⁴

As is the case with carbon-based electrode materials bulk platinum and gold electrodes can be prepared for use by mechanical polishing. In order to achieve the most rapid electron transfer kinetics, it is vital to polish under ultraclean conditions. The electrode

should be polished using successively smaller sizes of alumina on a smooth glass plate, typically using deagglomerated alumina powders (ranging in sizes from 1.0 down to 0.05 μm) slurried in ultra-pure water making a paste.^{1, 4} In addition to the mode of mechanical polishing for metal electrodes alternatives such as heat treatment, solvent cleaning, laser activation and electrochemical polarisation are on occasion utilised through these vary in cost and practicality with mechanical polishing being the most commonly utilised mode of electrode preparation. Based on the above, graphite-based screen printed electrodes are also useful electrode materials; these are explored in the next Chapter.

CHAPTER 2

SCREEN PRINTING TECHNOLOGY FOR ELECTROCHEMICAL APPLICATIONS

The main thrust of this thesis is concerned with the implementation of screen printing technology for the fabrication of screen-printed electrodes. Consequently this Chapter introduces these novel electrodes and overviews both recent and fundamental literature utilising such electrodes as sensors.

The origins of screen printing technology (for general purposes), date as far back as 2500 B.C. reported to be utilised by the Egyptians and Greeks.¹⁶ Modern day techniques utilised for screen printing are closely related to work in 1907 by Samuel Simon (Manchester, UK) who utilised a fabric printing system in which the designs were produced from stencils drawn onto bolting cloth stretched on frames with the printing operation made with a brush across the mesh.¹⁶ Consequently, in 1920 Albert Kosloff gave a demonstration in Berlin of screen printing on paper using a wooden frame stretched with bolting cloth which supported a stencil and on which a rubber-bladed squeegee was used to print the ink through the stencil. Shortly afterwards, Kosloff emigrated to the USA and there became one of the pioneers of the process. Though the ethos of screen printing remains the same, its applications and the equipment used has, and continues to evolve, greatly offering ever increasing potential applications; one such newly developed application being for the fabrication of screen printed electrodes.¹⁶

2.1 SCREEN PRINTED ELECTRODES EMPLOYED FOR ELECTROANALYTICAL APPLICATIONS

Screen printed electrodes have been utilised within many notable pieces of work without the additional pre-treatment or modification of the electrodes used. The ability to achieve highly sensitive electrochemical responses without the requirement of further modification to the screen printed electrodes is clearly desirable with the reduced pre-treatment/modification improving the potential commercial development of such work, where minimum costs and ease of production are essential. Screen printed electrodes have the following inherent advantages: *i)* reduction of the so called ‘memory’ effect where the electrode ‘remembers’ the last analysis and through surface contamination will affect the next measurement; *ii)* being cost effective (when mass produced) to become one-shot usage; *iii)* exhibiting suitable electron transfer properties to replace expensive noble metal electrodes; unique and exciting designs can be realized such as allowing the measurement of multiple analytes from one single sample; facile incorporation of electro-catalysts into the bulk of the screen printed sensor or deposition upon its surface.

Screen printed derived sensors have ease of use, scale of economies, are disposable in nature and require a reduced volume of the analyte (~ microlitres) making them a natural choice in sensing applications over conventional (solid) carbon electrodes and other fabrication approaches due to screen printing’s adaptability. It is likely that new directions in this area will include the use of a range of nanomaterials to improve electron transfer processes yet being completely scalable in terms of fabrication whilst also pushing towards smaller and well-defined geometries which have applications in screen printed microelectrode arrays and ‘lab on a chip’ approaches with the overall ethos of simpler, cheaper, disposable, scalable and ease of use. As has been highlighted, screen printed sensors offer great longevity with abundant potential future applications. There are many advantages

of using screen printed electrodes over conventional carbon based electrodes and it is therefore expected that many more reports will be published where screen printed sensors are employed, both without modification “as-is” and through novel and advantageous modification.

2.1.1 SENSOR FABRICATION

The fundamental principles for all forms of graphic reproduction are the same. In simple terms, a quantity of ink or other viscous compound is spread and deposited in a film of controlled pattern and thickness. In the case of screen printing this entails squeezing ink through a gauze or mesh onto a surface beneath. To allow for the effective printing of a desired design there are five prerequisites;

- i.* a screen, comprising a frame upon which is stretched a mesh,
- ii.* a photo stencil of the required design upon the mesh,
- iii.* a squeegee, comprising a flexible, resilient blade,
- iv.* an ink or paste (these terms are used interchangeably),
- v.* a secure base on which to position the component to be printed,

Although machinery for the process of screen printing to produce the desired product is not essential (akin to t-shirt printing), in most cases, particularly for the fabrication of electrochemical sensors the utilisation of commercial machines is common practise. Such machines are favoured due to the advantages offered, such as: improved repeatability of print cycle, improved reproducibility and a faster rate of output.

As figure 2.1 shows, during the printing process the screen is located just above the substrate to be printed so that it is accurately placed to deposit the print (ink) in the desired position. Contrary to common belief the screen is not brought into contact with the substrate as this would result in the screen being pulled away in an uncontrolled manner after printing

causing the print to be spoilt and most importantly reducing the reproducibility of the process. Contact between the screen and the substrate is in fact a result of the squeegee moving across the screen, applying pressure to the screen as it does so. The action of the squeegee results in the ink being pushed through the screen (within the defined open areas) thus the desired pattern is formed, with the surplus ink being removed by the edge of the squeegee. The mesh should peel away from the surface immediately behind the squeegee, leaving all the ink that was in the mesh deposited on the printing surface.

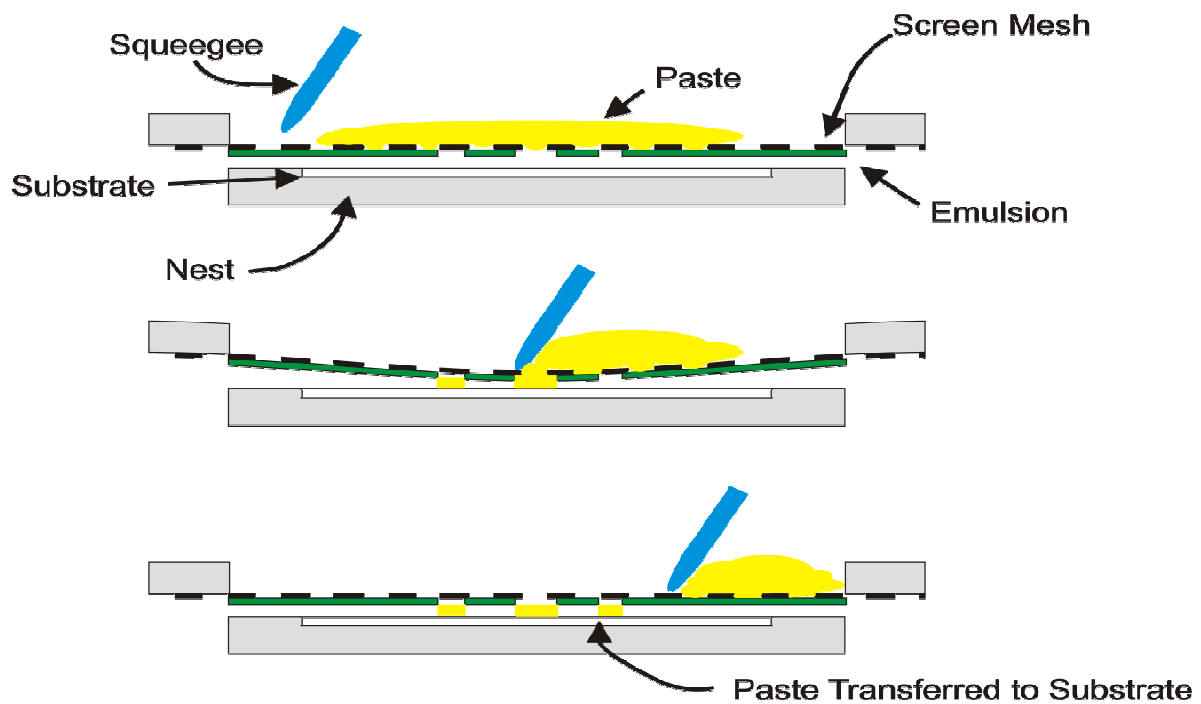


Figure 2.1 A schematic (cross-sectional) representation of the process of screen printed manufacturing of electrodes, outlining the basic processes involved.

When considering the technique of screen printing in greater depth with regards to the fabrication of electrochemical sensors parameters such as the screen, squeegee and inks possess paramount importance. The ink is generally considered the most critical participant in the process of screen printing, though this is debatable. Nonetheless it is important that the ink utilised and its properties are given full consideration to minimise any negative contribution which may arise through this parameter. During the print process the ink

undergoes five steps: *i*) the flood stroke, *ii*) the squeegee stroke, *iii*) mesh coming out of the ink, *iv*) levelling and *v*) slumping. During these steps the ideal performance would consist of *i*) flooding which gives a full, but light coverage of the stencil area with no drip-through, *ii*) minimum amount of pressure required to force the ink through the mesh allowing for improved lifespan of both the mesh and squeegee, *iii*) mesh coming away from the ink with the minimum effort so printing is possible with minimum snap-off (preferably zero snap-off) to minimise distortion, *iv*) levelling takes place very quickly to ensure no mesh marks remain and *v*) there is very little slumping so the print and lines comprising it are as close to the original as possible. The requirements for levelling and slumping are somewhat contradictory as a high viscosity is required to reduce slumping but this slows down levelling which can result in mesh marks remaining in the final cured sensor. Fortunately however levelling theory shows that high viscosities remain, in most cases suitable, for printing as levelling times should be very short for a well-designed ink.¹⁷

As has been alluded to, the screen utilised and in particular the mesh from which the screen is composed is a critical parameter for consideration, particularly when screen printing intricate or detailed designs. An array of mesh types exist with a range of highly specific parameters including mesh thread diameter, mesh thread thickness and open area (%). When selecting a mesh for a specific application various parameters require consideration. The mesh opening must be large enough for at least three of the ink or paste particles to pass through at any one given time, removing the potential of the mesh becoming blocked. Similarly, the amount of paste which can be deposited, upon the substrate of choice, is a factor of mesh thickness multiplied by the percent of open area. If a thinner deposit is required, a thinner mesh and/or smaller open area percentage must be used. Additional wet deposit is achieved by using a thicker mesh or by increasing the emulsion thickness, or build-up. Note however, the final dried, reflowed or fired thickness depends on the composition of

the paste, its volatile content and the sintering characteristics of the particles, but control of this final value always begins with the wet deposit. Additionally, the pattern or print tolerances must be 3 times larger than either the wire diameter or the mesh knuckle, where wires cross over each other. Wire size affects the proper development of the pattern, as well as the flow of the ink or paste around the wire.¹⁷

The final critical technical aspect of the screen printing process involves squeegee selection. Typically a contact angle with the screen of 60° is selected, as this has been determined within the industry to be the most effective contact angle. The shape and angle of the squeegee however can be altered to suit the needs of the operator. Some printers will round the squeegee with a small radius to get more ink deposit. However, the most effective, and the best shearing edge is still a 90 degree or a straight edge profile. This owing to the fact that a squeegee which has a round or tapered edge has a tendency to lose sharpness or cutting edge. Further to this a rounded squeegee fails to successfully shear or transfer the ink over the screen, but rather in such instances the blade now spears the ink across the screen. This principle is portrayed well when considering the screen after printing using such a squeegee, where it would be expected that a thicker ink deposit than required or desired would remain upon the surface of the screen after the passing of the squeegee.¹⁷

2.1.2 FUNDAMENTAL UNDERSTANDING OF SCREEN PRINTED ELECTROANALYTICAL SENSORS

As mentioned earlier, inks consist of graphite particles, polymer binder and other additives which are utilised for dispersion, printing and adhesion tasks. The exact ink formulation is regarded by the manufacturer as proprietary information and it has been shown that differences in ink composition *e.g.* type, size or loading of graphite particles and in the printing and curing conditions can strongly affect the electron transfer reactivity and overall analytical performance of the resulting carbon sensors.¹⁸⁻²⁰

Screen printed electrochemical sensors provide excellent platforms for modification with a variety of nano-particles and structurally related materials requiring no pre-treatment such as electrode polishing or electrochemical pre-treatment *via* electro-deposition, as is common with other electrode materials. While these electrodes find widespread usage, the fundamental understanding of the electrochemical reactivity at these electrodes has been seldom studied. Notable work by Sljukić *et al* has demonstrated that the mass transport at a macro screen printed electrode can be beneficially improved through the application of power ultrasound.²¹ The application of ultrasound has the benefit of not only increasing the mass transport of the target analyte through convection but also can remove surface active species which would otherwise hinder the electroanalytical measurement through surface passivation.^{22, 23} Using a redox probe to explore the effect of surface changes on the application of ultrasound it was found that an improvement in the heterogeneous rate constant was evident. This increase in the magnitude of the voltammetric peaks likely reflects the ‘roughening’ of the surface of the screen printed electrode from either cavitation, or high mass transport, or a combination of both processes; which likely removes constituents of inks covering carbon particles and thus increases the overall effective surface area of the electrode,²³ suggesting that the levels of graphite / carbon and other ink constituents (such as the binder) are key parameters to the electrodes performance.

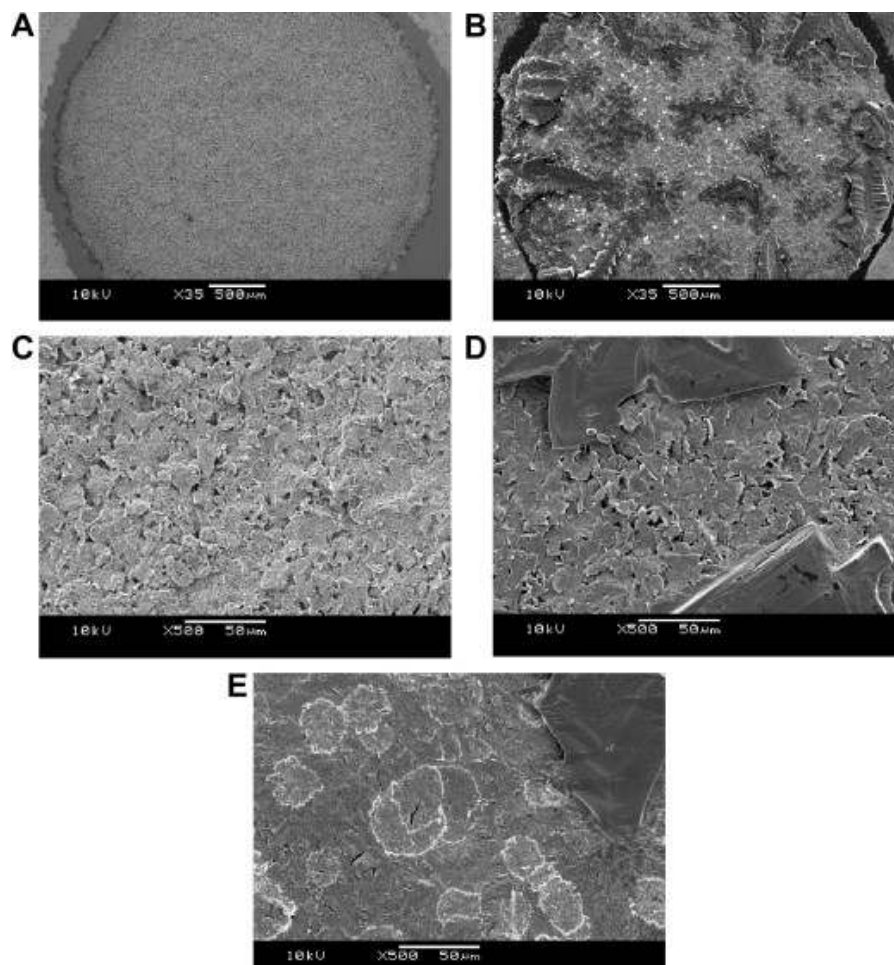


Figure 2.2 SEM images of the screen-printed electrochemical platforms. Figures A and C display the bare unmodified electrode surface alongside that of a 40 % (M_B/M_I) modified (B and D) and 80 % (M_B/M_I) (E) electrochemical platforms. Figure reproduced from reference.²⁴

Choudhry *et al*²⁴ has for the first time explored the role of the polymeric binder used in electrode fabrication *via* screen printing. It was demonstrated that a dramatic effect on the electrode's morphology is evident as the amount of polymeric binder is dramatically increased, as depicted in figure 2.2; polymeric domains are readily formed which are clearly identifiable in figure 2.2 (D and E). The effect on the voltammetric response from increasing the amount of binder was evaluated using an inner-sphere electron transfer redox probe. Figure 2.3 depicts the analysis of the voltammetric peak-to-peak separations indicating that the heterogeneous electron transfer rate (k_{edge}^0) constant decreases as the polymer binder is

increased, which is represented as % M_B/M_I , where M_B and M_I are the mass of the binder and the ink, respectively. The global coverage of edge plane sites of the electrode surface was found to decrease from 5.5 % to 0.3 % for the range of 0 – 80 % (M_B/M_I) respectively, indicating that the electron transfer characteristics can be tailored from that of edge plane-like, to that of basal plane-like in nature.²⁴ This has significant impact in fundamental electrochemistry, for example, when one is studying the electron transfer dynamics of say, metal nanoparticles, there is the need to have no contributions from the underlying electrode in order to study the electrochemical response of the metal nanoparticles, this is usually achieved with a basal plane electrode fabricated from highly ordered pyrolytic graphite (which consequently has slow electron transfer kinetics) but has the drawbacks of being expensive and requiring renewal each time; the use of a basal plane like electrode which is disposable and cost effective therefore has clear advantages. The cyclic voltammetric response ($I-E$), observed at screen printed electrochemical platforms arises from various contributions which can be described by the following:

$$I - E_{SPE} = \beta[I - E_{basal}] + \gamma[I - E_{binder}] + \varepsilon[I - E_{edge}] \quad (2.1)$$

It has been shown that due to non-linear diffusion over an electrode surface the individual contributions of edge and basal plane graphite do not scale with relative areas.²⁵ In equation (2.1) β , γ and ε are complicated functions that take into account the relative areas and sizes of the materials comprising the electrode as well as the contribution from non-linear diffusion. It has been conveniently demonstrated for electroactive species with diffusion coefficients of $\sim 1 \times 10^{-6} \text{ cm}^2 \text{ s}^{-1}$ and greater, that there is no contribution from basal plane.²⁵ Additionally the demonstration that the polymeric formulation used within ink formulations is electrochemically inert (see figures 2.2 and 2.3)²⁴ and does not contribute to the cyclic voltammetric response allows for a convenient methodology for modifying the electrochemical reactivity of screen printed electrochemical platforms, and consequently

equation (2.1) reduces to equation (2.2) conveniently describing cyclic voltammetry ($I-E_{SPE}$) at screen printed electrodes:²⁴

$$I - E_{SPE} = \varepsilon[I - E_{edge}] \quad (2.2)$$

indicating that screen printed electrodes depend on the global coverage of edge plane like-sites/defects. This work clearly contributes to the understanding that the binder/ink has a detrimental effect on the voltammetric performance and also confirming that edge plane sites are the likely origin of electron transfer (see above).

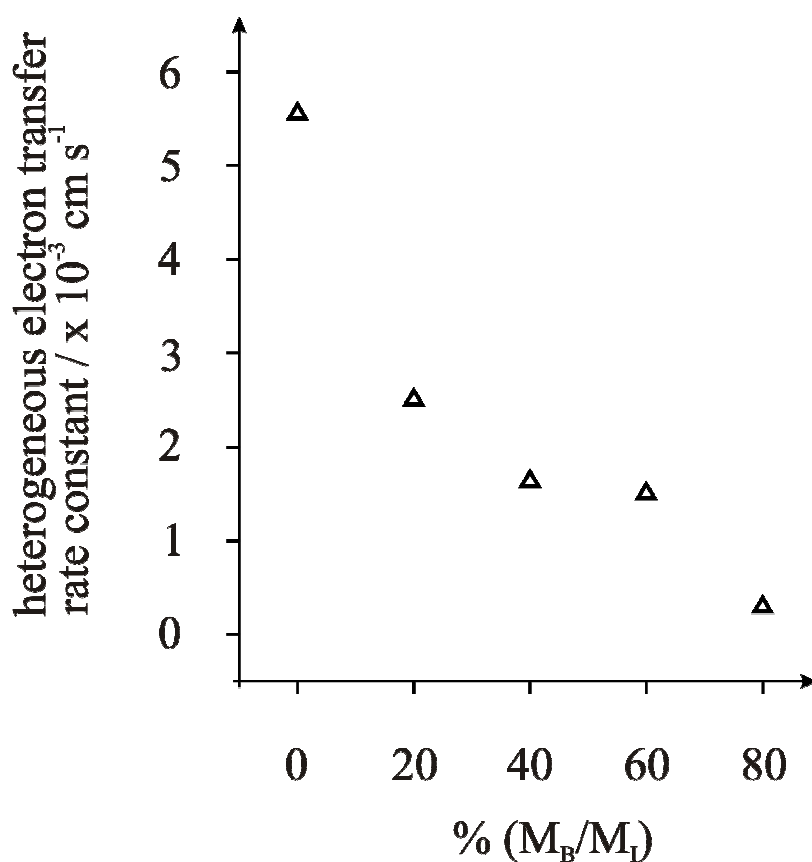


Figure 2.3 Plot of heterogeneous electron transfer rate constant (k_{edge}^0) as a function of % (M_B/M_I).

Figure reproduced from reference.²⁴

The ability to tailor the electrode surface's electron transfer properties has clear analytical implications. Figure 2.4 compares the voltammetric performance of a standard unmodified screen printed electrode with that of a polymeric modified screen printed

electrode where a clear difference is observed; the former has fast electron transfer while the latter has slow electron transfer; copper plating these two screen printed electrodes has a clear distinction in the copper metal morphology. Choudhry *et al* have shown that this can be beneficially utilised for the electrolytic modification of various electro-catalytic metals where the bespoke electrode surface acts as a micron-sized template.²⁴ Note that the modification utilises less metal and hence has a clear cost implication, especially where precious materials are used, but also has the beneficial viewpoint of creating a metal ensemble. The term ensemble is used to indicate that the spacing between each metal deposit, *viz* metal domain is not uniform, as in the case of arrays.²⁶ When an ensemble is used over that of an electrolytically modified macro electrode a dramatic change in the mass transport prevails facilitating low detection limits and improvements in the analytical performance even though only a fraction of the electrode surface is covered.

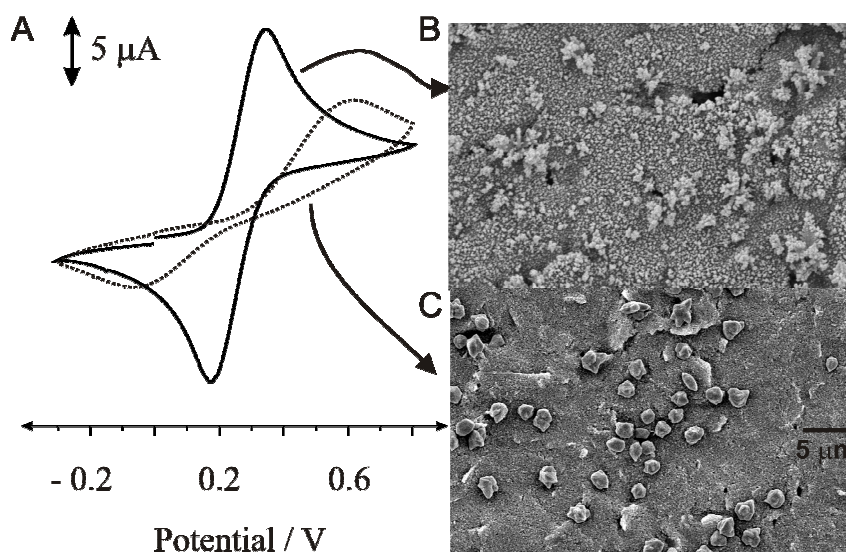


Figure 2.4 Cyclic voltammograms (A) obtained in 1 mM potassium ferrocyanide in 1 M KCl using the standard electrochemical platform (solid line) with that of a bespoke electrochemical platform (dashed line). Scans recorded at 100 mV s^{-1} vs. SCE. SEM images of the copper plated standard (B) and bespoke (C) screen printed electrochemical platforms. Reproduced from Reference²⁷.

For example Choudhry *et al*²¹ have shown that the bespoke screen printed electrodes could be electrolytically modified with palladium which is electro-catalytic towards the electrochemical oxidation of hydrazine where the underlying (unmodified) electrode exhibits slow electron transfer. An average palladium particle size of 2.7 μm was found possible where the screen printed electrode substrates act as a template for the deposition of the target metal. This equates to a global coverage of only 0.27 (where 1.0 indicates a fully covered electrode surface). The electrochemical performance towards hydrazine was explored where a limit of detection of $\sim 9 \mu\text{M}$ was found to be possible which compared well with nanoparticle modified electrodes, even though only 27 % of the surface was modified! Clearly the mass transfer from employing a microdomain electrode, over that of a macro electrode, is highly beneficial and acts akin to a nanoparticle modified electrode.²¹

In the case of the nucleation of metal deposits on screen printed electrodes, the deposition and stripping mechanisms in terms of nucleation processes are important when quantifying metals at screen printed electrodes; the authoritative work of Honeychurch *et al*²⁸ and Brainina *et al*²⁹ is highly recommended. Honeychurch *et al* has shown that the redox behaviour of lead is not as straight forward as one would first think, as during the stripping step two or three peaks could be observed, which was attributed to the heterogeneity of the screen printed electrode surface, where deposition occurs in a competitive nature and the target metal deposits onto favourable active sites as a monolayer. As deposition proceeds, these sites are depleted and the process becomes competitive between metal deposition on unoccupied bare electrode sites or on already deposited metal.²⁸

Recently Choudhry *et al*³⁰ have shown that when an electrochemical modification designed for producing nickel nanoparticles on boron-doped diamond is explored using a standard screen printed electrode, the observed resulting nickel morphology is actually microrod like. The production of such structures requires complicated fabrication strategies

(non-electrochemical) and this is the first example of producing such structures electrochemically; the change in deposit morphology from using a boron-doped diamond electrode to a screen printed electrode is due to the differing nucleation dynamics, allowing new and exciting structures to be derived. These nickel microrods were shown to be analytically useful towards the sensing of alcohols.

Other fundamental work on understanding screen printed sensors has been to explore surface oxygen functionalities residing on the electrode surface. Zen *et al*³¹ have reported on a ‘pre-anodized’ screen printed electrode for the detection of a range of target analytes. This has the most beneficial effect on the simultaneous sensing of ascorbic acid, dopamine and uric acid where on a standard screen printed electrode only broad and overlapping voltammetric peaks are observed while for the case of the pre-anodized screen printed electrodes, three distinguishable signals are readily observed which, using Raman and XPS, was found to be due to an increment of carbon-oxygen species residing on the graphite surface and/or surface reorientation through the generation of edge plane sites³² which we interpret as likely through the removal of the ink from edge plane like sites/defects on the graphite. This work has been extended for application in the direct electron transfer to glucose oxidase³³ and for the sensing of lincomycin.³¹

2.1.3 METAL OXIDE MODIFIED SCREEN PRINTED ELECTRODES

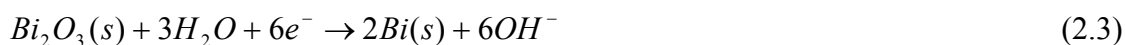
As mentioned in the above section mediator bulk modified screen printed electrodes have been the backbone of sensors towards portable and de-centralised testing which are also easily mass produced and consequently have scales of economy. Modification of the electrode surface with electro-catalytic metals is a common approach, such as decoration or through the use of metallic screen printed inks producing film modified screen printed electrodes,³⁴ while another approach is to incorporate metallic electro-catalysts into a carbon

paste electrode which is an aspect which has been extensively explored.³⁵⁻³⁷ However, this methodology suffers from drawbacks indentified above. Wu *et al*³⁸ have utilised ruthenium oxide which is commonly used in resistive pastes for screen printing and demonstrated this towards the sensing of ascorbic acid which provided an analytical output of 0 – 4 mM with little interference from uric acid and hydrogen peroxide.³⁸ This work has been extended for example for the determination of hydrogen peroxide and with enzymatic modification for sensing hypoxanthine and glucose, whilst also being applied to food analysis.³⁹ Along these lines we have reported the bulk modification of screen printed electrodes with copper oxide for carbohydrate sensing,⁴⁰ nickel oxide for hydroxide detection⁴¹, manganese oxide for nitrite, oxygen and ascorbic acid,⁴² and finally bismuth oxide.⁴³

This last application of using bismuth oxide is particularly interesting as modifying an electrode substrate with bismuth is well documented to improve the electroanalytical performance and can act akin to a mercury modified electrode yet having negligible toxicity.⁴⁴⁻⁴⁷ Since this pioneering work, by Wang and co-workers, the use of bismuth modified electrodes has been greatly expanded. Recent prominent examples include lead in human blood,⁴⁸ zinc and cadmium *via* sono-electroanalysis,⁴⁹ sensing of Escherichia Coli,⁵⁰ aminosalicylate drugs,⁵¹ indium,⁵² and metallothionein.⁵³ In these examples bismuth modified electrodes are usually prepared *via ex situ* or *in situ* electrodeposition. This approach involves careful preparation of the electrode surface between samples and to eliminate this preparative step, the use of disposable screen printed electrodes as underlying electrode substrates have been reported.⁵⁴ Towards simplifying the electrochemical methodology further, bismuth-powder modified carbon paste electrodes⁵⁵ have been reported as well as bismuth nanopowder modified electrodes, where the bismuth nanopowder is immobilised with Nafion.^{55, 56} Hwang *et al* have recently reported the screen printing of a

bismuth oxide layer onto a screen printed electrode surface which is then electrochemically reduced *ex situ* in sodium hydroxide to produce a bismuth film.⁴⁷

To generate a truly disposable mass produced sensor, bismuth oxide has been reported⁵⁷ rather than modifying the surface *in situ* via the addition of a bismuth salt or *ex situ*, where it is electrochemically deposited in an external solution, bismuth oxide is incorporated into the bulk of the screen printed electrode such that when the potential is held sufficiently negative, bismuth oxide at the electrode surface is electrochemically reduced forming bismuth metal:



The electrochemical deposition of target species preferentially occurs on the bismuth metal surface, in comparison to the underlying graphite surface, allowing for enhanced sensing in the case of target metals; alloy formation beneficially assists. On the anodic sweep, the *in situ* formed Bi(s) should maintain until at sufficiently high potentials when the following transition will occur:



such an approach alleviates the need for *ex situ* bismuth film plating or *in situ* bismuth film formation greatly simplifying the analytical protocol.^{47, 57}

Bismuth domains act as a preferential nucleation site which, due to the nature of electrode fabrication, are randomly distributed across the electrode surface such that each bismuth microdomain has its own diffusional zone and due to the reduced spacing of the microdomains and partial diffusional overlap of diffusion zones, the mass transport is akin to that observed at a macroelectrode made entirely from bismuth, yet has a very low coverage.⁵⁸ The advantages of mimicking a bismuth film macroelectrode are that similar analytical performances can be obtained with a cheap, easily mass produced disposable electrode which does not require *ex situ* or *in situ* plating of bismuth.⁴⁷

In the majority of cases, bulk modified screen printed electrodes, where micron sized particles of the electro-catalytic metal are incorporated into the electrode, we find that these modified screen printed electrodes act analytically similar to that of a nanoparticle modified carbon electrode. The pertinent question here is, *why is this the case?*

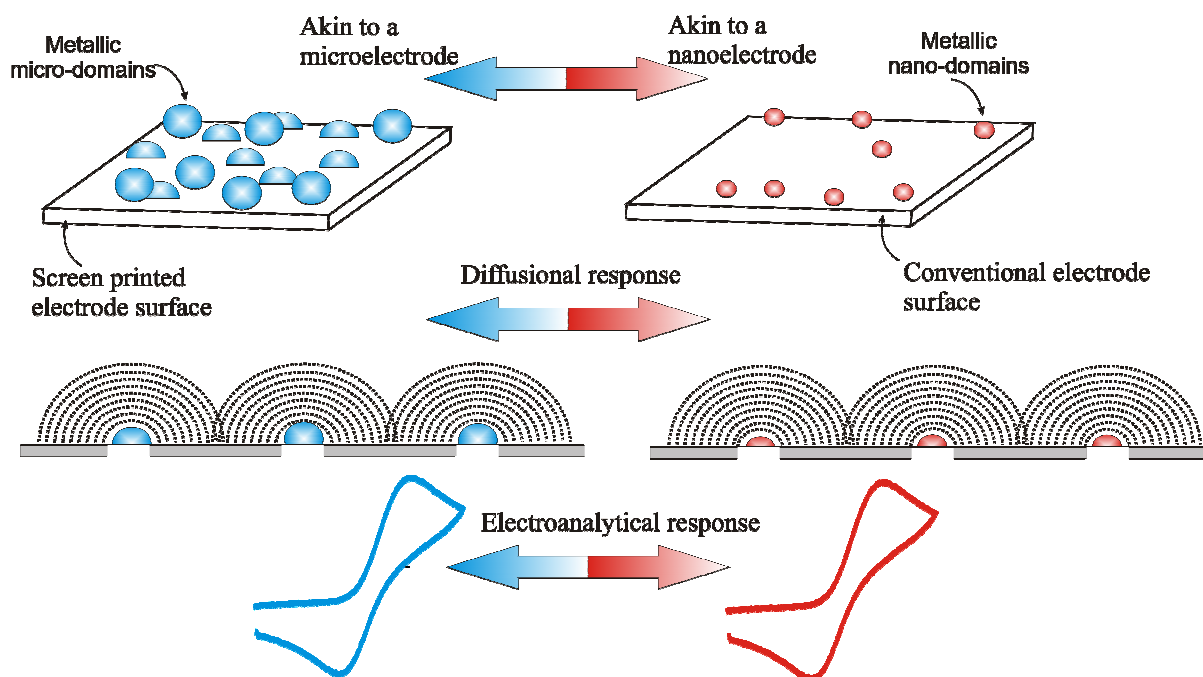


Figure 2.5 Schematic representations of the diffusional zones at micro- and nano-electrode ensembles.

The reason can be found by considering the diffusion zones at each electrode surface *viz* either the nano- or micron- particles. Figure 2.5 depicts a schematic representation of the diffusional zones at microelectrode and nanoparticle ensembles. It is clear that the same parameters apply here as in the case of microelectrode arrays, such that the distance between the particles is the key factor. Again, diffusion zones will build up at each electrode, in this case the micro- or nano- particles and due to no regular spacing, diffusional overlap occurs at a substantial degree at modest scan rates resulting in essentially the same voltammetric profiles observed at the microelectrode arrays. The degree of overlap is important, and if the overlap is not significant the ensemble has faster mass transport and hence improves electro-

analytical performance over that of a heavily overlapping diffusional regime. The voltammetric responses observed are identical due to the fact that the diffusional profiles are similar, indicating that a nanoparticle modified electrode for use in analysis does not always confer enhancements in electroanalysis. Thus, it is clear that in going from a micro- to nanoparticle size ensemble is not always beneficial since close neighbouring nanoparticles will heavily overlap acting akin to a micro-particle of the same geometric area.⁵⁹ The advantageous approach of our methodology, as described above, is that any metallic oxide can be readily incorporated, allowing a true platform technology.

2.1.4 THE IMPROVEMENT OF MASS TRANSPORT THROUGH INTUITIVE SENSOR DESIGN

Microelectrodes are exploited in electrochemistry due to their increased temporal resolution and current densities, reduced ohmic drop and charging currents, and high Faradaic to capacitive current ratios. However, micro electrodes have current ranges in the nanoamp to picoamp range, and are usually engulfed beneath electrochemical noise precluding useful measurements. The solution to this problem lies in using an array of microelectrodes where single microelectrodes are wired in parallel, with each electrode independent; radial diffusion dominates the mass transport, generating a signal which is many orders of magnitude larger. Microelectrode arrays are increasingly used in electrochemistry and especially in electroanalytical applications where they facilitate lower detection limits and exhibit greater sensitivities in comparison to macroelectrodes, and consequently research is dedicated to designing new types and variations.²⁰ The analytical signal in the form of the (limiting) current is defined as⁶⁰:

$$I_L^{Planar} = 4zFDCr \quad (2.5)$$

for a co-planar electrode array, where z is the number of electrons transferred, F is the Faraday constant, D is the diffusion coefficient, C is the concentration, r is the radius of the

microdisc comprising the array. In order to amplify the response, if we have a surface with many microelectrodes, hence an array, we have:

$$I_L^{Planar} = 4zFDCrN \quad (2.6)$$

where N is the total number of microelectrodes making up the array. Consequently, the current is multiplied by the number of electrodes comprising the array and will transform a nano-amp signal into a micro-amp one (or larger depending on N) which is easier to monitor and utilises the benefits of a microelectrode (improved mass transport, low background currents *etc.*) and ultimately improves the limit of detection and analytical range. However, one has to ensure that the electrodes did not communicate with each other, that is, they do not diffusively interact. An elegant paper by Guo and Linder has shown what the expected voltammetric profile is at differing levels of diffusional interaction, which is depicted in figure 2.6.⁶⁰

Related to co-planar microelectrodes/arrays, if the electrode is not completely flat with the insulating surface, a recessed or inlaid disc is apparent. Due to the nature of recessed electrodes, at slower scan rates the transition from diffusional independence (sigmoidal response) to diffusional dependence (peak shaped response) is extended over that possible at planar microelectrode arrays due to the time required for the diffusion layer to reach the edge of the recess. Thus, it should be easier to achieve a sigmoidal response at a recessed microelectrode array over a planar microelectrode array which has the same disc size, geometry, distance between neighbouring electrodes, and the total number of electrodes comprising the array. The advantages are greater sensitivity, increased current density, and an improved signal to noise ratio⁶¹ allowing enhanced electroanalytical sensing.^{20, 62}

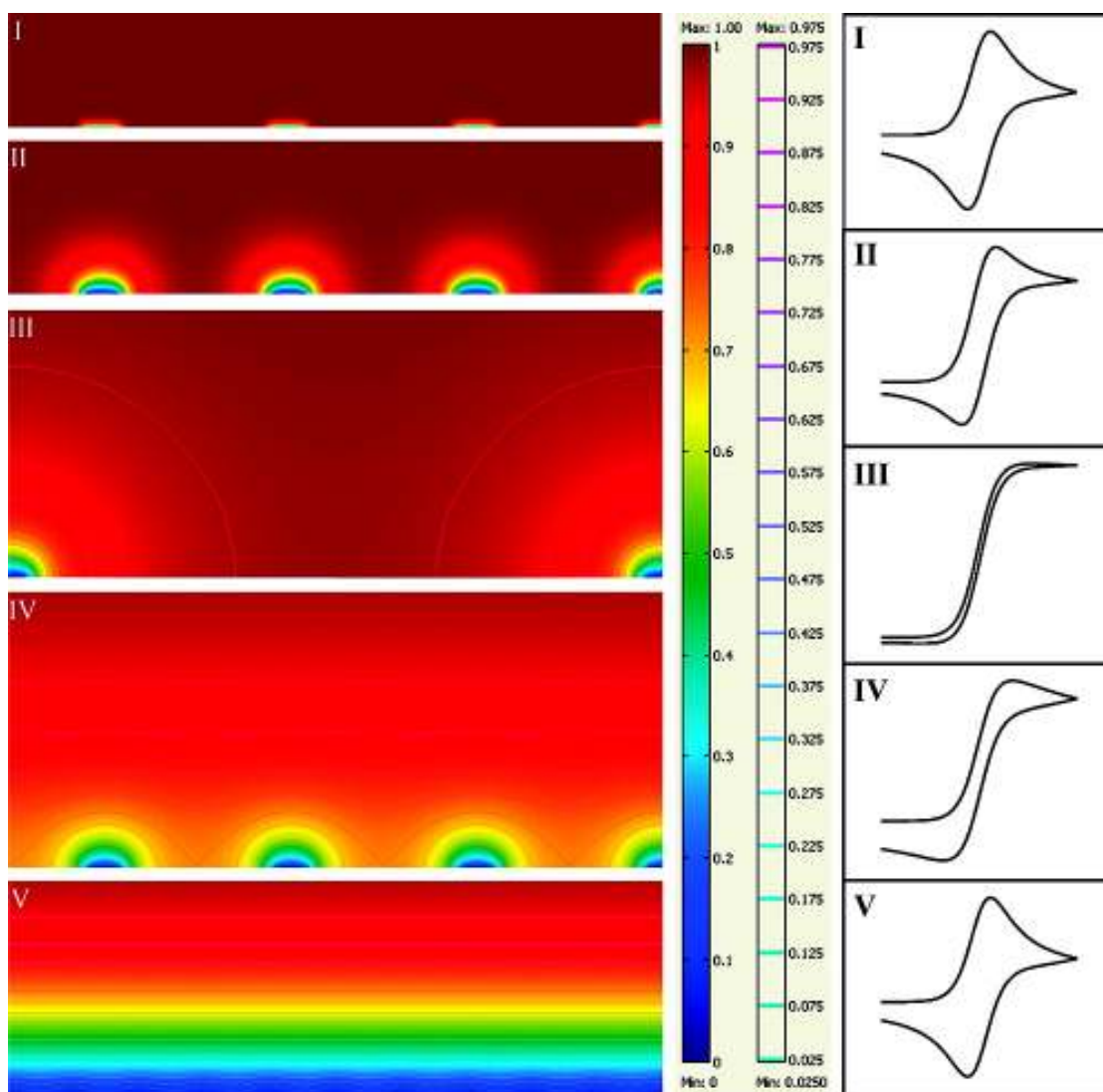


Figure 2.6 Simulated concentration profiles with isoconcentration contour lines over a microelectrode array representing the five main categories of diffusion modes: (I) planar diffusion layers on individual microdisk; (II) mixed diffusion layers on individual microdisk; diffusion mode between planar and hemispherical diffusion; (III) hemispherical diffusion layers on individual microdisk; (IV) mixed diffusion layers; diffusion mode of partial overlapping of adjacent diffusion layers; (V) planar diffusion layer over the entire microelectrode array; diffusion mode of complete overlapping of individual diffusion layers. In the scale bar next to the figure, the red colour represents the bulk concentration and the blue colour represents zero concentration. The second scale bar represents a relative concentration scale for the contour lines. Typical CVs of the each category are shown at the right. Figure reproduced from reference ⁶⁰.

One approach towards screen printed microelectrode arrays has reported the coating of screen printed electrodes with polymeric films. These are then subjected to sonochemical ablation producing a random ensemble of microelectrodes, albeit with a large size distribution,²⁰ which are also irregularly shaped and distorted which is likely to hamper reproducibility between sensors from the same batch.^{63, 64} Another approach is the screen printing of a carbon layer onto which an inert material is placed, which has been laser ablated to produce micron sized holes which expose the underlying screen printed carbon surface.⁶⁵ However, problems may be encountered between sealing the patterned material to the carbon layer leading to leakages. Other approaches involve patterning inert material *in situ* but can change the micro structure of the underlying carbon surface, ultimately affecting the electrochemical performance of the sensor. A novel new kind of microelectrode array based on femtosecond laser ablation and screen printing process was reported by Cugnet *et al*⁶⁶ which demonstrated enhanced diffusion behaviour and a greater mass-transport in comparison with macroelectrodes. These approaches, while noteworthy, are unlikely to be used in the mass production of microelectrode arrays.⁵⁷ An individually addressable array comprising eight electrodes of 1 mm diameter has been reported by Dock *et al*⁶⁷ made entirely by screen printing. It is evident that pushing the boundaries of screen printing is the only way for new and diverse electrochemical platforms to be produced *via* this technology.⁵⁷

Recently Kadara and co-workers have explored the fabrication of microelectrode arrays entirely *via* screen printing where a large carbon working is first printed. Onto this carbon layer a dielectric is printed which has predefined holes, as defined by the mesh screen, exposing the underlying carbon electrode in the form of carbon microelectrode arrays. It was found that the optimum printing allowed microdiscs with radii of $116 (\pm 6) \mu\text{m}$; attempts at smaller microelectrodes result in a large range of sizes and ill-defined geometries.²⁰ Due to the fabrication methodology, recessed microelectrodes are produced and in our recent case,

this is $\sim 4 \mu\text{m}$, equating to a shallow recessed microelectrode. If the number of microelectrodes on the array is known, the average disc radius, can be estimated from a single measurement of the limiting current. This should be the case due to the fabrication process *via* screen printing which defines the geometry and number of electrodes. However it was found that this was over-estimated with the error arising due to the diffusional overlap between neighbouring microelectrodes.

The electroanalytical utility of the screen printed electrode array was explored in relation to the sensing of manganese (II) allowing a limit of detection of $\sim 81 \text{ nM}$. Note that this was achieved using an array comprising 16 electrodes separated by $1250 \mu\text{m}$ from its nearest neighbour. A 6 microelectrode array was also constructed which has a separation of $2500 \mu\text{m}$ from its nearest neighbour and exhibited a detection limit of $\sim 64 \text{ nm}$. Both responses have significant analytical benefits over current literature in terms of both electrochemical and general analytical methodologies.

In comparison of the two shallow recessed microelectrode arrays, the 6 microelectrode array exhibits an improved sensitivity and wider linear range over the 16 microelectrode array. This is due to the distance between neighbouring electrodes being larger on the 6 microelectrode array than the 16 microelectrode array, where radial diffusion of the former is greater than on the latter. Based on these results the screen printed shallow microelectrode arrays clearly have beneficial analytical utility in comparison to conventional carbon electrodes.²⁰ Note that this has been demonstrated for the sensing of lead in river samples at the EC Dangerous Substance Directive (76/464/EEC)⁶⁸ and for the detection of nitrite in river water samples where Khairy *et al*⁶⁹ demonstrated a protocol which was deemed feasible for the sensing of levels indicated by the World Health Organisation. The disposable nature and low cost of the sensor offers an economical and portable screening tool for nitrite.

Other work by Kadara *et al*⁷⁰ reported the fabrication of disposable and flexible screen printed microelectrodes characterized with microscopy and cyclic voltammetry. The advantages presented by the fabricated electrodes included: reduced expenditure and cleaning processes as each of the microelectrodes are designed to be disposable; the removal of the requirement of cleaning stages, but also pre-treatment between analyses allows for much more efficient and rapid analysis of samples; the work also boasted exceptional detection limits with the screen printed electrodes providing comparable detection limits to that obtained in the literature at insonated boron-doped diamond electrodes.⁷⁰

Elegant work by Ball *et al*⁷¹ highlighted the concept of coupling screen printing and laser micromachining technology in order to fabricate a nanovial with “built-in” working and reference electrodes. A nanolitre cell was created through the incorporation of both mechanisms which successfully simplifies manipulations necessary for small volume experiments. Additionally the ease of manipulation of both screen printing and laser micromachining techniques allows for a wide array of applications in electrochemistry in ultra-small environments in the future.

Other notable reports of using screen printing for adventurous designs have been reported by Schüler *et al*⁷² who explored the fabrication of DNA-chips. Figure 2.7 shows one such chip fabricated using a gold paste screen printed onto glass. This methodology offers a cost efficient alternative for the production of chips with electrode structures as needed for an electrical chip-based DNA detection.⁷²

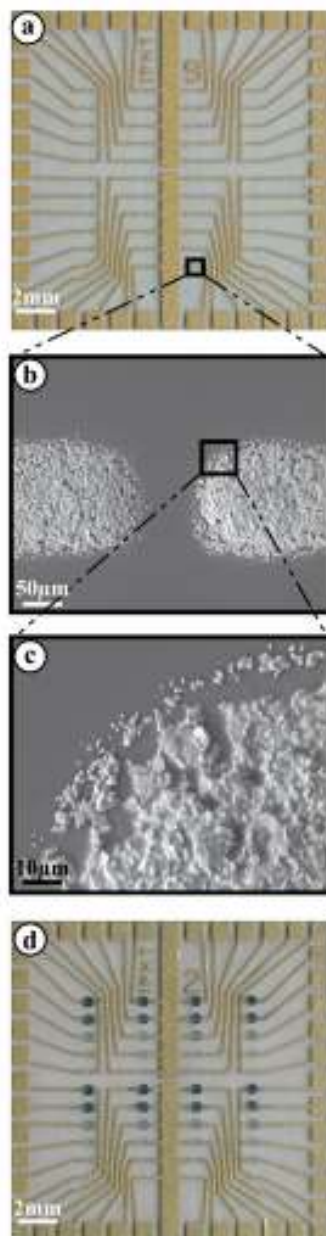


Figure 2.7 Screen printed chips with gold (a) electrode structures. The black spots (d) represent the signals observed on chips after enzyme induced silver deposition. SEM images show the ultra-structure of gold (b, c) electrodes. Reproduced from Reference⁷².

Electrodes of dimensions lower than millimetre size with diffusion limited processes have attracted considerable interest among electrochemists. Their unique electrochemical properties have been used in many applications preferable to electrodes of conventional size.⁷³ Zen and his group⁷³⁻⁷⁵ have developed edge band ultra-microelectrodes (SPUME),

building upon initial work by Craston and co-workers,⁷⁶ where the electrode is built up as shown in figure 2.8. Through slicing the edge of the working electrode a band-type ultramicroelectrode is formed and can easily be ‘renewed’ after use by cutting the edge off. The length of the band-type ultramicroelectrode can be varied in the range of 0.18 -1.35 mm with a width of $\sim 20 \mu\text{m}$.⁷³ This electrode configuration has been extended and explored in flow injection analysis for the sensing of nitrite in lake and ground waters,^{77, 78} and has recently been modified with platinum nanoparticles for the amperometric sensing of carbon monoxide⁷⁹ and formaldehyde.⁸⁰

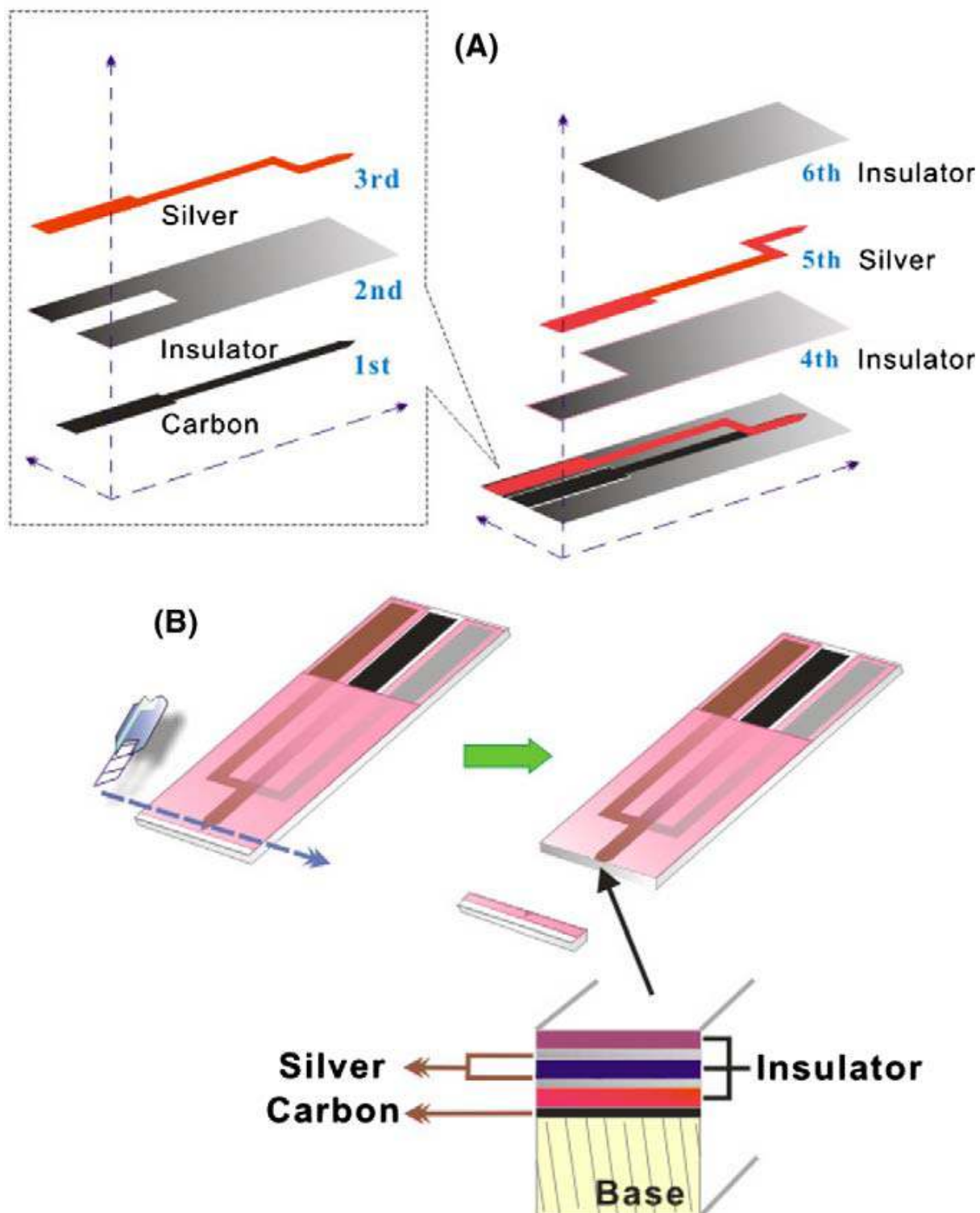


Figure 2.8 (A) An alternating layer-by-layer pattern structure of the SPUME (a disposable screen-printed edge band carbon ultramicroelectrode) assembly. (B) Cross-sectional diagram of a typical SPUME with a built-in three-electrode configuration. Reproduced from Reference⁷³.

This novel design has been extended by Hart and his group using water based inks containing cobalt phthalocyanine for the sensing of lactate,⁸¹ toxins⁸² and glucose.⁸³ Other advantageous designs involve the fabrication of wall-jet screen printed ring disk electrodes which, compared to traditional methods of fabrication, such designs are inexpensive and due to the disposable nature, do not suffer from extensive pre-treatment in the form of electrode polishing.^{74, 75} Additionally such electrodes could be modified with nano- and micro- sized electro-catalytic particles or produced using metallic inks.

Last, notable designs from Karousos *et al*⁸⁴ have been shown where carbon fibre matting (and foils) are trapped between alternating layers of insulating polymer, where a hole is created through the centre of the laminate exposing the conductive carbon – each layer effectively forming a microtube type electrode within the wall of the hole which serves as a 3-dimensional detection well with the volume of the sample controlled through the manipulation of the well diameter. The bottom carbon layer is left intact and acts as a counter electrode. One major advantage of this type of methodology is the step-wise assembly of the various layers such that pre-patterned layers can be created and then laminated – as is necessary when adding the base (counter) electrode layer.⁸⁴ This work has been shown to be useful where the base fibre mat is modified with copper oxide, where the sample permeates and selectively removes ascorbate. Whilst the methodology doesn't strictly involve screen printing (but rather pad printing), this approach can be readily adapted for mass production using screen printing technology with the detection well volume readily tailored to specific applications.

CHAPTER 3

COPLANAR MACRO ELECTRODES: ECONOMICAL MODIFICATION FOR ENHANCED ELECTROANALYTICAL SENSING

In this Chapter the validity of electrode modification is considered with specific relation to screen printed sensors. As has been highlighted within previous Chapters (for example Chapter 2), electrode modification has long gathered great interest as is well documented within the literature; in some instances with modification being employed unnecessarily. Such modifications often involve the method of drop-coating where the modifier, for example nanoparticles, is deposited upon the electrode surface prior to use. Other methods for the modification of electrodes include electrochemical deposition where the underlying electrode material is coated with a metallic film comprising the chosen metal, such as copper or gold. Critically however such protocols for the modification of electrodes intended for use within electroanalysis generally require preparatory steps which result in electrodes which can be unstable and complex in their development whilst offering limited reproducibility and uniformity between sensors due to this nature of fabrication. One proposed method for the alleviation of such problems is the modification of sensors, in this instance co-planar graphite screen printed electrodes, is the screen printing of the desired modification upon the surface of the electrode at hand.

This Chapter considers the potential application of newly formulated noble metal inks for the modification of co-planar graphite screen printed electrodes, investigating the scope for the utilisation of these electrodes for the sensing of analytes of interest.

3.1 GOLD SCREEN PRINTED ELECTRODES

Section 3.1 contains published work^[1] which explores, for the first time, the modification of co-planar graphite screen printed electrodes with a micron particle sized gold ink applied *via* screen printing techniques. The intended novelty and benefit of such an electrode would undoubtedly be the alleviation for the requirement of modification prior to use; an essential factor when considering the utilisation of a sensor within the field of practise whilst also ensuring the large scale production of the sensor is possible. This sensor is the first instance in which a gold screen printed macro electrode is evaluated towards the sensing of chromium (III) and (VI), two key analytes with the latter being of great importance for application into water quality control.

3.1.1 INTRODUCTION

As is the case with many heavy metals, there is a keen interest in the monitoring of chromium (III) and (VI).⁸⁵ Although chromium (III) possess no significant threat, being relatively harmless, it maintains an important biological role.⁸⁶ In contrast, chromium (VI) poses a great environmental threat, being around 100 – 1000 times more toxic than chromium (III).⁸⁷ This increased hazardous status is attributed to the high oxidation potential and World Health Organisation (WHO) recommends chromium (VI) to be limited to 0.05 mg L⁻¹ (0.17 mM) within groundwater.⁸⁸ Due to the previously discussed imposed restrictions relating to chromium (VI) levels within water, areas of industry such as plating industries, cooling towers, timber treatment, leather tanning, wood preservation and steel manufacturing require sensitive and reliable techniques to monitor anthropogenic chromium pollution in ground water.^{89, 90}

¹ J. P. Metters, R. O. Kadara and C. E. Banks, *Analyst*, 2013, **137**, 896.

Currently available techniques for the detection of chromium (VI) fall in to two distinct categories; direct and indirect detection. Chromatography,^{91, 92} extraction,^{93, 94} and co-precipitation^{95, 96} are techniques used to obtain or determine chromium (VI) which all require prior separation; increasing detection costs, time and accessibility. Each of the indirect methods also suffer from chromium (III) interference, often found in relatively high concentrations within natural samples.⁹⁷ Direct detection of chromium (VI) can be achieved through spectrophotometric techniques boasting limits of detection of ~ 0.85 mM though no studies have reported the possible effects of interferences upon the detection of chromium (VI).⁹⁸⁻¹⁰⁰ In addition to spectrophotometric techniques, electrochemical methods facilitate the direct and rapid detection of chromium (VI) even within samples considered to contain excessive concentrations of chromium (III), thus highlighting the robust nature of the electrochemical techniques towards chromium (VI) detection. Table 3.1 highlights the various different electrochemical strategies utilised for the detection of chromium (VI). Limits of detection for chromium (VI) far below WHO guidelines have been reported through the use of electrochemical methods, such as 0.01 and 0.032 mM at sol-gel modified glassy carbon¹⁰¹ and mercury thin-film¹⁰² electrodes respectively, however, as is exposed within table 3.1 many of the electrochemical techniques require an additional pre-treatment phase prior to analysis, such as potential cycling, film and nanoparticle formation.

Screen printed electrodes offer further advantages for the detection of such environmentally important analytes due to their scales of economy, ease of fabrication, facile modification and disposable nature.¹⁰³ The application of screen printed electrodes towards the detection of chromium species is not widely reported. Elegant work by Hallam *et al* demonstrated the applicability of screen printed electrodes towards the detection of chromium (VI), in this case using solely a graphite based screen printed electrode.¹⁰⁴ Other work has focused on the detection of chromium through modification of a screen printed

electrode with metallic nano-particles such as that reported by Arcos-Martinez and co-workers,¹⁰⁵ while bismuth film modified electrodes have been exploited by Lawrence *et al* for catalytic adsorptive stripping of chromium (VI),²² though such techniques still require a period of pre-treatment.^{105, 106} A further example of the application of modified screen printed electrodes for the sensing of chromium (VI) involves the formation of a poly-L-histidine film upon the electrode surface, which, though boasting a low limit of detection of 0.046 mM, still suffers from the requirement of a pre-treatment phase to allow for the production of the poly-L-histidine film.¹⁰⁷

Although such studies utilising screen printed electrodes have been reported, this is the first instance in which a gold screen printed macro electrode is evaluated towards the sensing of chromium (III) and (VI). The novelty of this is also highlighted by the fact that the electrode requires no prior pre-treatment in the form of potential cycling which is required in the case of gold macroelectrodes in order to form the required gold oxide surface. Within this section the electrochemical detection of both chromium (III) in alkaline and chromium (VI) in acidic conditions are studied through the novel application of gold screen printed macro electrodes, with the detection of chromium (VI) being trialled within an environmentally relevant sample (canal water), whilst other known interferences, Fe (III), Ni (II) and Cu (II) were also shown to have little effect upon the analytical method.

Electrode	Linear Range (μM)	Limit of Detection (μM)	Comments	Reference
Gold macro	20 to 2000	4.5	Detection in the presence of known interferences	¹⁰⁸
Gold nanoparticle modified screen	θ	0.4	Electrochemical deposition pre-treatment was	¹⁰⁵

printed			required for the formation on the nanoparticle modified surface	
Silver nanoparticle modified screen printed	θ	0.85	Electrochemical deposition pre-treatment was required for the formation on the nanoparticle modified surface	¹⁰⁵
Gold nanoparticle modified indium tin oxide	5 to 100	2	Gold nanoparticles induced through electrodeposition	¹⁰⁹
World Health Organisation Recommendation: 0.17 μ M				
Gold nanoparticle modified screen printed	0.03 to 17	0.015	Nanoparticles introduced through electrodeposition	¹¹⁰
Graphite screen printed	0.34 to 3.4	0.065		¹⁰⁴
Sol-gel modified glassy carbon	0.04 to 1.35	0.01	Pre-treatment to allow formation of electrodeposited sol-gel film followed by 12h curing in an oven	¹⁰¹
Mercury thin film electrode	0.01 to 0.6	0.032	Electrodeposition of a mercury film performed prior to analysis	¹⁰²
Poly(4-vinylpyridine) coated platinum	0.1 to 10	θ	Pre-treatment required for the formation of the thin film	¹¹¹

θ = Information not supplied.

Table 3.1 A summary of electrochemical reports for the detection of chromium (VI).

3.1.2 EXPERIMENTAL

All chemicals used were of analytical grade and were used as received without any further purification from Sigma-Aldrich. The specific chemicals utilised relevant to the analysis described within this Chapter included: potassium dichromate, chromium (III) chloride hexahydrate, hydrazine hydrate, hydrogen peroxide (30 % in water) and dihydrocapsaicin. All solutions were prepared with deionised water of resistivity not less than 18.2 Ω cm. All solutions (unless stated otherwise) were vigorously degassed with nitrogen to remove oxygen prior to analysis. Additionally all solutions contained 0.1 M KCl acting as an electrolyte, unless otherwise stated.

Voltammetric measurements were carried out using a μ -Autolab III (Eco Chemie, The Netherlands) potentiostat/galvanostat and controlled by Autolab GPES software version 4.9 for Windows XP. Screen-printed carbon macro electrodes (SPEs) which have a 3 mm diameter working electrode were fabricated in-house with appropriate stencil designs using a DEK 248 screen printing machine (DEK, Weymouth, UK).

The critical operating parameters of the screen printing machine consisted of print and flood speeds of 92 mm/s and 96 mm/s respectively, a print gap of 0.88 mm and printing pressure of 8.0 Kg. The screen meshes utilised for each of the layers comprising the sensors were sourced from MCI Screens Ltd¹¹² with the design parameters including a mesh number of 77/195 cm/inch, mesh material of: polyester, mesh opening of 77 μ m and a mesh thread diameter nominal of 48 μ m. The squeegees utilising for each of the printed layers were positioned at an angle of 60° comprising a straight edged, polyurethane 60 durometer blade.

For the fabrication of the screen-printed sensors, firstly, a carbon-graphite ink formulation (Product Code: C2000802P2; Gwent Electronic Materials Ltd, UK), was screen-printed onto a polyester (Autostat, 250 micron thickness) flexible film (denoted throughout as standard-SPE). This layer was cured in a fan oven at 60 degrees for 30 minutes. Next a

silver/silver chloride reference electrode was included by screen printing Ag/AgCl paste (Product Code: C2040308D2; Gwent Electronic Materials Ltd, UK) onto the polyester substrates. Finally, a dielectric paste (Product Code: D2070423D5; Gwent Electronic Materials Ltd, UK) was then printed onto the polyester substrate to cover the connections. After curing at 60 degrees for 30 minutes the screen-printed electrodes are ready to be used (as is explored within Chapter 3).

Finally, in the case of the electrodes considered within this Chapter a further layer was economically screen printed upon the 3 mm carbon-based working electrode surface. In the case of the gold modified screen printed electrodes (section 3.1) a gold polymer paste consisting of a mixture of powder and dendritic gold with particles size in the range of low micrometres (82 % gold) (Product Code: C2041206P2; Gwent Electronic Materials Ltd, UK) working electrode was printed on top of the carbon working electrode surface. In the same fashion a platinum polymer paste comprising dendritic platinum (83 - 87 %) with particles sizes in the low micrometers range (Product Code: C2050804D9; Gwent Electronic Materials Ltd, UK) was screen printed on top of the carbon working electrode surface for the fabrication of the platinum modified screen printed electrodes (section 3.2). In the case of the two noble metal inks utilised the manufactures stipulate that the metal form utilised for the fabrication of the inks is the relevant oxide form which hold potential uses for electrochemical applications. As identified in references^{85,192, 193} gold oxide is the basis of electrocatalysis for the analyte chromium (VI). Hence, later we find that since the gold utilised herein is in the form of a gold oxide, the need to make gold oxide, usually *via* potential cycling, is alleviated.

In the case of the single-walled carbon nanotube modified electrodes (section 3.3), for the final modification of the electrode, a commercially purchased single-walled carbon nanotube ink was printed upon the pre-existing working electrode surface, covering the

defined working electrode finally producing the screen printed single-walled carbon nanotube electrodes (3 mm diameter geometry). The ink utilised for the fabrication of the carbon nanotube layer was purchased from Southwest Nanotechnologies, USA. The carbon nanotubes utilised within the ink are synthesised by the CoMoCAT process.¹¹³ Information from the ink supplier states that whilst the ink contains ‘carbon as a single-walled nanomaterial’ (0.1 %), metallic impurities still remain within the ink including oxides of silicon, molybdenum and cobalt (< 15 ppm). Additional noted ingredients within the ink include 2-aminobutane (60 - 95 %), water (0.5 - 15 %) and co-solvents (5 - 40 % alcohols). The ink was mechanically stirred prior to use allowing for a shear rate of $\sim 10 \text{ s}^{-1}$ resulting in an ideal ink viscosity of 3.37 Pa.s.¹¹³

For comparative purposes when examining the potential of the screen printed single-walled carbon nanotube electrodes commercially available single-walled and multi-walled carbon nanotube modified screen printed electrodes were also utilised; sourced from Dropsens (Spain) which are produced exclusively on ceramic substrates.¹¹⁴ The graphite working screen printed surface is 4 mm in diameter, which are modified with single- (DRP-110SWCNT) or multi-walled (DRP-110CNT) carbon nanotubes containing approximately 5 % of carboxylic groups.¹¹⁴ The diameter of the carbon nanotubes is reported to be approximately 10 nm, with an average length of 1 – 2 μm .¹¹⁴ Further details about disposable single- and multi-walled carbon nanotube screen printed sensors can be obtained from the supplier’s website.¹¹⁴ The method of incorporating the carbon nanotubes within the carbon-based screen printed sensor is not defined by the manufacturer resulting in reduced clarity whether the nanotubes were simply deposited upon the surface after the screen printing process, or incorporated within screen printing inks or the use of a novel nanotube ink as is the case in this study.

Canal water was sampled at the edge of the canal bank (Rochdale Canal, Oxford Road, Manchester, UK) and collected in a polycarbonate bottle which was washed three times with canal water before being taken back to the laboratory. The sample was stored at room temperature and used within a day of sampling. For determination of chromium (VI) the water sample was simply acidified with H_2SO_4 to a concentration of 0.05 M before electroanalytical measurements were commenced, whilst modification to pH 7 using a phosphate buffer was necessary for the determination of hydrazine.

Scanning electron microscope (SEM) images and surface element analysis were obtained with a JEOL JSM-5600LV model. X-ray photoelectron spectroscopy (XPS, K-Alpha, Thermo Scientific) was used to analyse the electrode surface. All spectra were collected using Al-K radiation (1486.6 eV), monochromatized by a twin crystal monochromator, yielding a focused X-ray spot with a diameter of $400\mu\text{m}$, at $3\text{ mA} \times 12\text{ kV}$. The alpha hemispherical analyser was operated in the constant energy mode with survey scan pass energies of 200 eV to measure the whole energy band and 50 eV in a narrow scan to selectively measure the particular elements. Thus, XPS was used to provide the chemical bonding state as well as the elemental composition of the filter surface. Charge compensation was achieved with the system flood gun that provides low energy electrons and low energy argon ions from a single source.

3.1.3 RESULTS AND DISCUSSION

Characterisation of gold screen printed macro electrodes

Gold screen printed macro electrodes (denoted throughout as AuSPE) were fabricated as detailed in the Experimental section (3.1.2) with a working electrode consisting of gold ink printed onto an underlying graphite based screen printed electrode. Note that in this case, the expensive gold material is economically utilised but it could be the case that the connecting

legs are constructed of the same material. Inspection of the AuSPE using SEM, as depicted in figure 3.1, reveals a ‘granular’ structure is observed consisting of gold micro particles held together with a polymeric formulation. Energy-dispersive X-ray (EDAX) analysis (see figure 3.2) was performed on the AuSPE surface with typical values, using the semi-quantitative technique, revealing the surface to consist of 4.73 % oxygen, 14.15 % carbon and 81.12 % gold. The oxygen content arises due to the gold being in an oxide formation¹¹⁵ and interestingly the carbon and oxygen content arises due to the use of a polymeric binder in the ink formulation. Note that the percent of gold is in excellent agreement with that of the original ink formulation from the commercial suppliers (see Experimental section (3.1.2)).

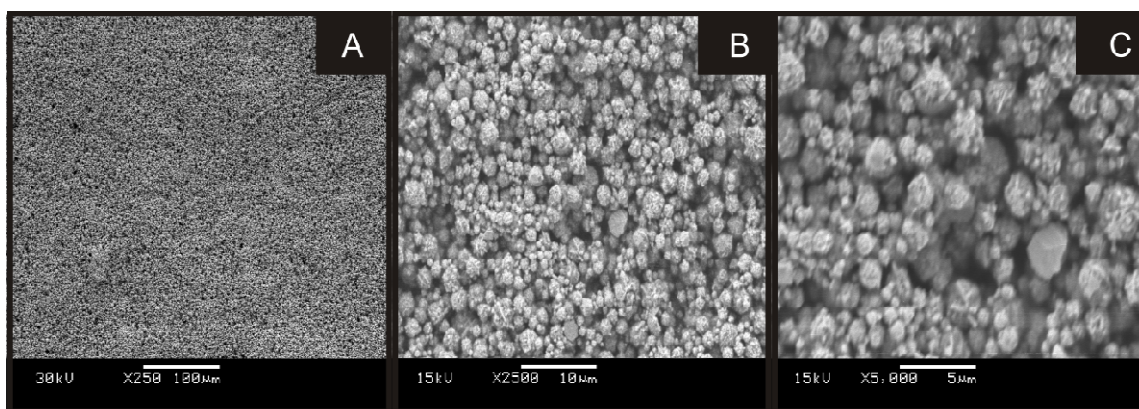


Figure 3.1 Typical SEM images of the gold screen printed macro electrode at increasing magnifications; x250 (A), x2500 (B) and x5000 (C).

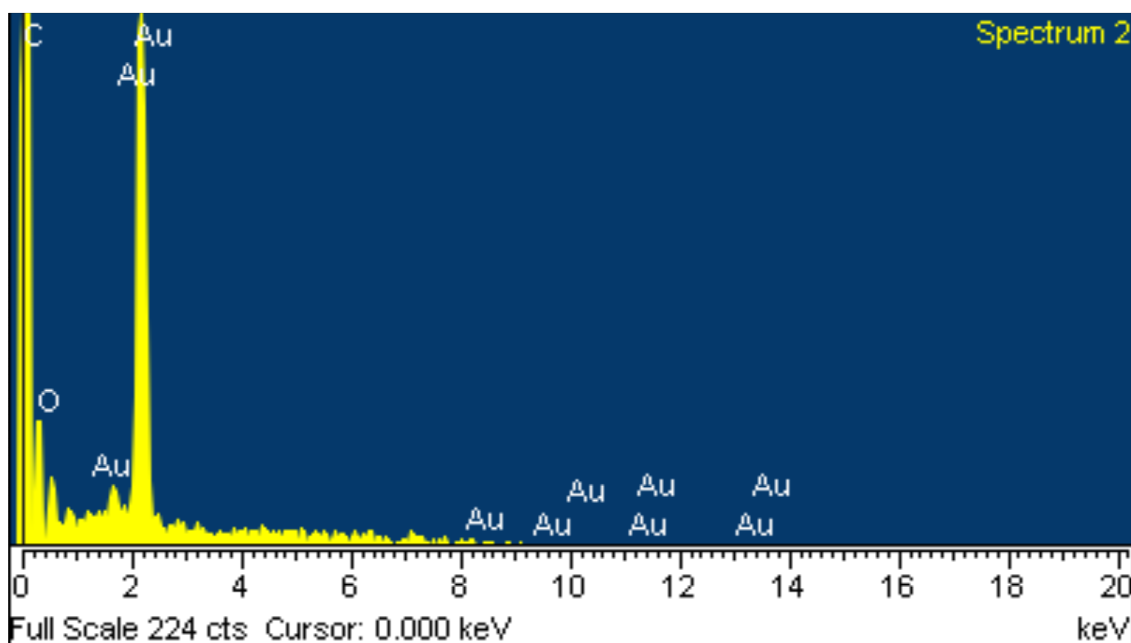


Figure 3.2 EDX analysis of the AuSPE, determining the working surface to consist of 4.73 % oxygen, 14.15 % carbon and 81.12 % gold.

The AuSPEs were first electrochemically characterised using the redox probe potassium ferrocyanide. Firstly scan rate studies were performed using the AuSPE in 1 mM potassium ferrocyanide with 0.1 M KCl, where observation of voltammetric peak height, plotted as peak current (I_p) against square root of the applied scan rate over the range 10 – 600 mV s^{-1} was found to be linear ($I_p / \mu\text{A} = 1.0228 \mu\text{A}/(\text{Vs}^{-1})^{1/2} + 1.8234 \mu\text{A}$), suggesting a diffusional rather than a surface controlled process. The electron transfer rate constant, k^0 , for the process was determined using the Nicholson method⁷ with an electron transfer rate constant of $1.5 \times 10^{-4} \text{ cm s}^{-1}$ consequently deduced. It was noted that this is less than previous reports utilising gold polycrystalline macroelectrodes ($\sim 0.01 \text{ cm s}^{-1}$).^{116, 117} In terms of the deduced electron transfer rate constant, this is of course relative to the rate of mass transport to the electrode surface,^{118, 119} based on the analysis by Matsuda and Ayabe.¹²⁰ The transition between reversible and irreversible limits in terms of electron transfer can be determined by the parameter, ψ :

$$\psi = \frac{k^0}{\left(\frac{FDv}{RT}\right)^{-1/2}} \quad (3.1)$$

where the reversible range is $\psi > 15$ and quasi-reversible $15 > \psi > 10^{-3}$. Using the electron transfer rate constant deduced (see above) along with a literature diffusion coefficient of $6.5 \times 10^{-6} \text{ cm}^2 \text{ s}^{-1}$ in 0.1 M KCl,¹²¹ it is found in the experimental case, over the range of scan rates employed, that overall the electrochemical process can be described as quasi-reversible. The electro-active area of the AuSPE was calculated using the following equation for quasi-reversible electrochemical processes:¹²²

$$I_p = (2.65 \times 10^5) n^{3/2} A C_0 D^{1/2} v^{1/2} \quad (3.2)$$

Where n is total number of electrons transferred in the electrochemical process, D is the diffusion coefficient, C_0 is the bulk concentration of the analyte, A is the electrode area and v is the applied voltammetric sweep scan rate. The electrode area was estimated to be 0.71 cm^2 compared to a geometric area of 0.071 cm^2 which conforms with SEM images (figure 3.1) suggesting that the surface of the gold macro electrode is one of a porous nature; note that this porosity, is not so substantial to result in thin layer voltammetric behaviour as seen for other electrode surfaces.¹⁰⁴

Electroanalytical sensing of chromium (III)

Attention is next turned to exploring the electroanalytical performance of the AuSPE towards the sensing of chromium (III). The direct oxidation of chromium (III) is well reported at solid electrodes; gold macro electrodes,⁸⁵ smooth and platinised platinum microelectrodes¹²³ and metal oxide electrodes.¹²⁴ More recently, the detection of chromium (III) in pharmaceutical compounds at pH 8 has been explored though the development of an analytical procedure based on natural and synthetic diamond paste electrodes.¹²⁵

Previous reports by Compton *et al* have reported the electrochemical oxidation of trivalent chromium at boron doped-diamond, glassy carbon and polycrystalline gold macroelectrodes, determining that only good quality voltammetric responses were possible at a gold electrode in solutions of pH greater than 12.⁸⁵ Such observations have been explained by the “enhanced activity” of gold electrodes in alkaline conditions, attributed to the formation of some kind of oxygen containing species, namely hydrous gold oxide; consequently based on this elegant report, 0.1 M KOH was adopted as the model solution.⁸⁵

126

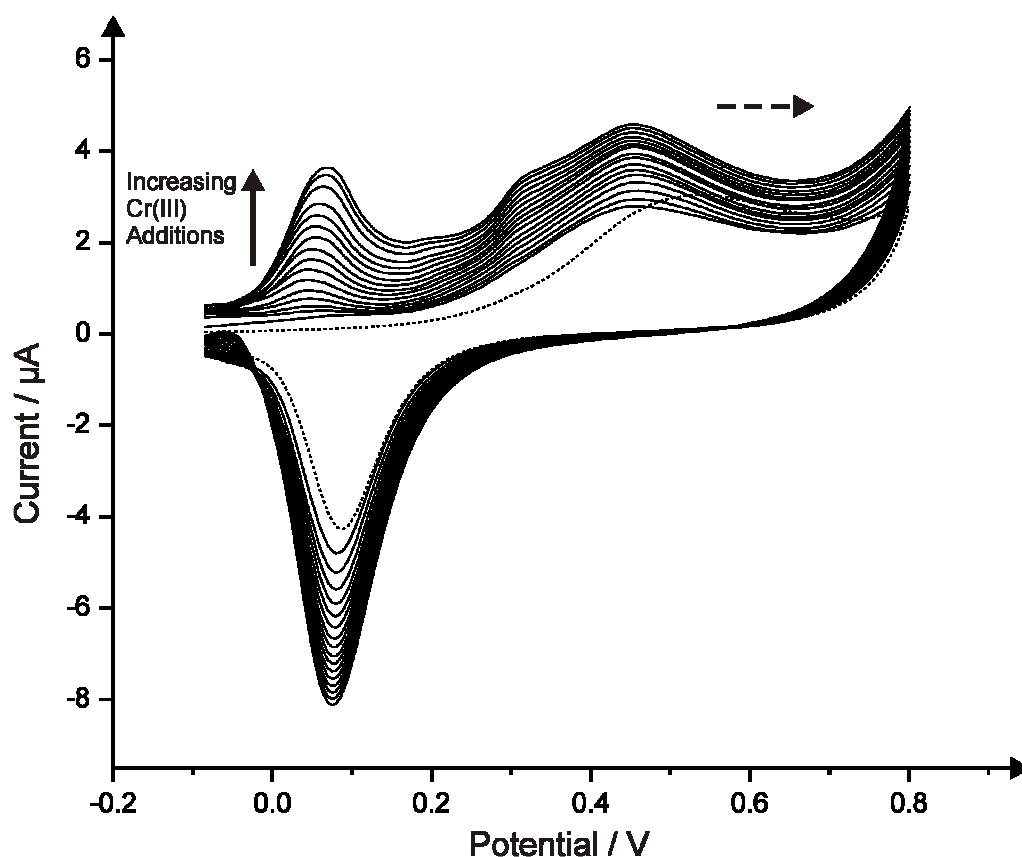


Figure 3.3 Typical cyclic voltammetric curves resulting from additions of chromium (III) over the range of 100 to 1600 μM into 0.1 M KOH using the AuSPE. The dotted line is the response of the AuSPE in the absence of any chromium (III). Scan rate: 50 mV s^{-1} . Dashed arrow signifies direction of scan.

The electroanalytical sensing of chromium (III) was first explored with cyclic voltammetry using the AuSPEs. Figure 3.3 depicts typical cyclic voltammetric responses resulting from additions of chromium (III) in to a solution of 0.1 M KOH⁸⁵ over the range of 100 to 1600 μM . Clearly prior to additions of trivalent chromium, an oxidation peak at $\sim + 0.45 \text{ V}$ (*vs.* SCE) is evident using the AuSPEs. This response is consistent with previous literature reports utilising polycrystalline gold macro electrodes⁸⁵ which has been reported to be due to the formation of an anodic oxide film upon the electrode surface. A further, new, chromium (III) concentration dependant oxidation peak is observed at $\sim + 0.075 \text{ V}$ (*vs.* SCE).⁸⁵ Analysis of the peak height observed at $\sim + 0.075 \text{ V}$ versus chromium (III) additions is depicted in figure 3.4 where a linear response over the range of 100 μM to 1000 μM is evident, after which a slight deviation from linearity can be seen, though peak currents continue to increase with increasing chromium (III) concentration. From this calibration plot a limit of detection towards the sensing of chromium (III) was calculated (using 3σ in line with section 1.1.11) to correspond to 38.8 μM . This compares favourably to reports by Compton *et al*⁸⁵ using a polycrystalline gold macro electrode, though other reports have claimed lower limits of detections of 8.9 and 0.032 μM at ion selective poly(vinyl chloride) membrane¹²⁷ and multi-walled carbon nanotube polyvinylchloride electrodes.¹²⁸ When attempting to determine the analytical applicability of such studies it is important to note that WHO guideline values for chromium (III) and (VI) are not provided as individual parameters, but rather as a guideline value for total chromium.¹²⁹ As a practical measure, a limit of 0.17 μM for total chromium is suggested which is considered to be unlikely to give rise to significant risks to health and has been retained as a provisional guideline value until additional information becomes available to set separate values for chromium (III) and (VI).¹²⁹ Thus it is clear that the detection limit of the sensors and those previously reported^{127,}

¹²⁸ would likely need to be considerably reduced to be of analytical importance in terms of meeting the WHO guidelines.

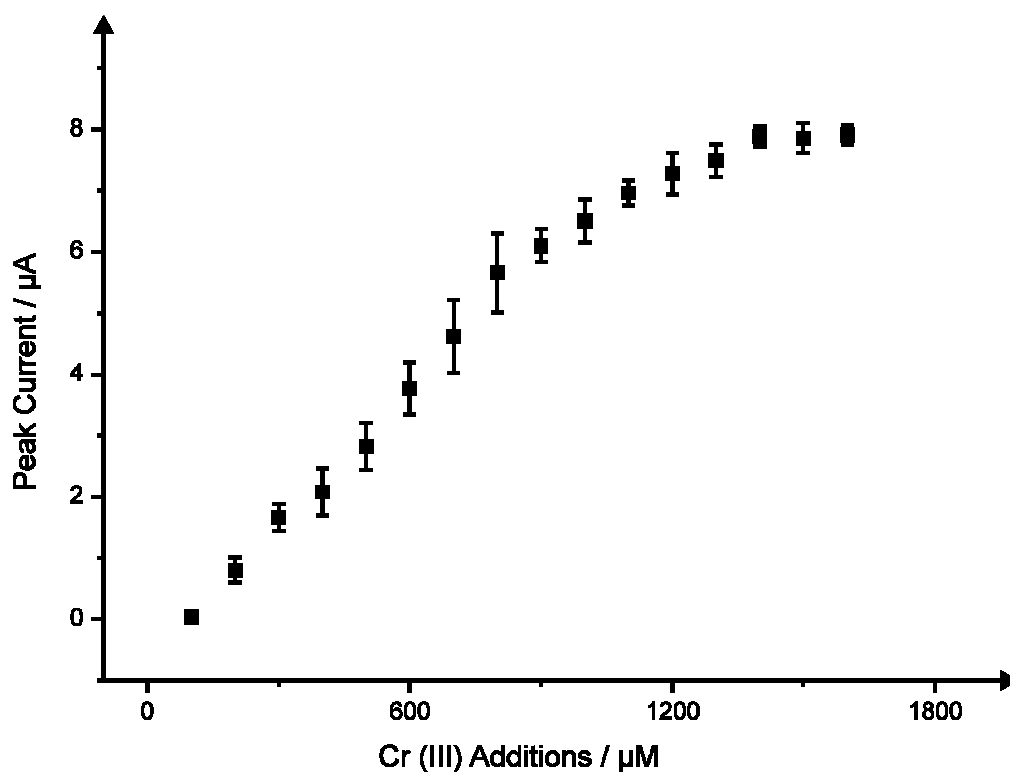


Figure 3.4 Typical calibration plot resulting from additions of chromium (III) into 0.1 M KOH (as shown in figure 3.3) using the AuSPE.

Interestingly, Compton *et al* showed that gold oxide was essential for good electrocatalysis to occur, that is, a cleaned polycrystalline gold exhibited a poor response towards the electrochemical oxidation of chromium (III) until gold oxide was formed *via* extensive potential cycling.⁸⁵ The AuSPEs fabricated and utilised within the present study alleviate the need for any such pre-treatment, as the gold used within the electrode construction is gold oxide, hence offering a significant advantage over existing techniques allowing a simplified analytical protocol.

Electroanalytical sensing of chromium (VI)

Consideration of the electroanalytical reduction of 100 mM chromium (VI) using the AuSPE in 0.05 M H₂SO₄ was next turned to. Note that the electrolyte H₂SO₄ was preferred over HCl as reported in previous studies due to potential problems when using HCl for the detection of chromium (VI).¹⁰⁴ Hallam *et al*¹⁰⁴ elegantly explored the potential of the electrochemical reduction wave attributed to the electrochemical reduction of chlorine, as in agreement with previous work,¹³⁰ suggesting that in HCl, the electrochemical reduction of chromium (VI) may not actually be that as suggested previously¹³¹ but in fact an indirect methodology.

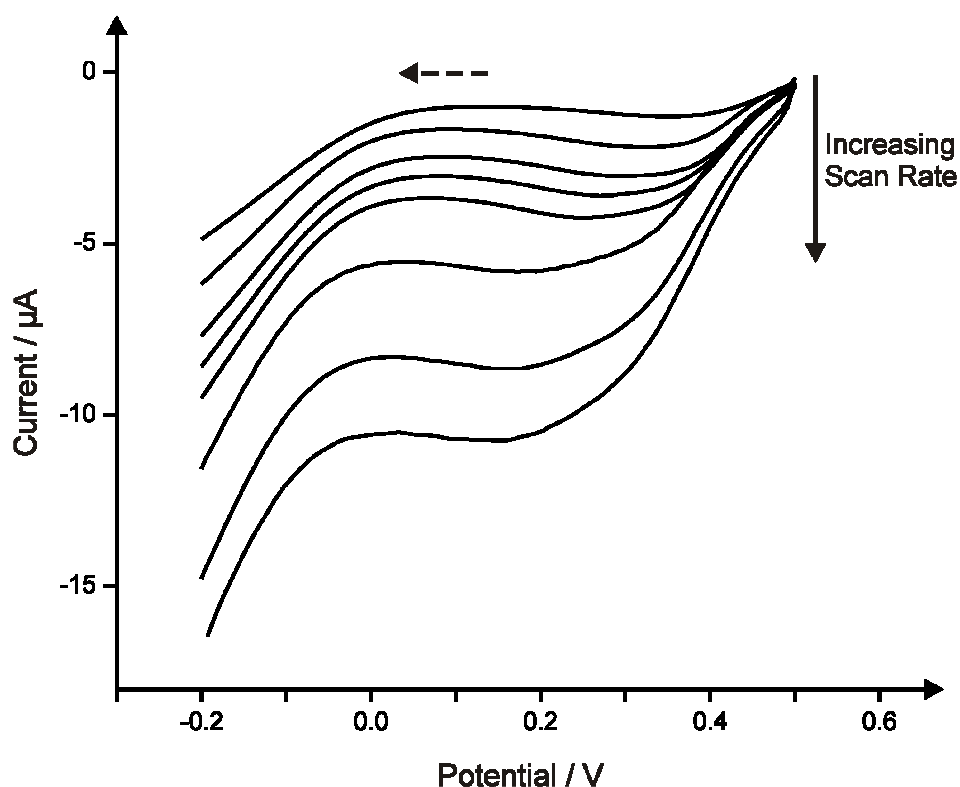


Figure 3.5 Electrochemical reduction of 100 mM chromium (VI) in 0.05 M H₂SO₄ using the AuSPEs recorded over the scan rate range of 10 to 600 mV s⁻¹ (vs. SCE). Dashed arrow signifies direction of scan.

Figure 3.5 depicts the observed voltammetric response utilising the AuSPE where an electrochemical reduction wave shifts to more negative potentials upon increasing the scan

rate, indicating an irreversible electrochemical reaction. The corresponding plot of peak current against square root of scan rate (10 – 600 mV s^{-1}) was found to be linear ($I_p / \mu\text{A} = 0.42\mu\text{A}/(\text{Vs}^{-1})^{1/2} + 0.0144\mu\text{A}$; $R^2 = 0.99$; $N = 8$), suggesting a diffusional rather than a surface controlled process.

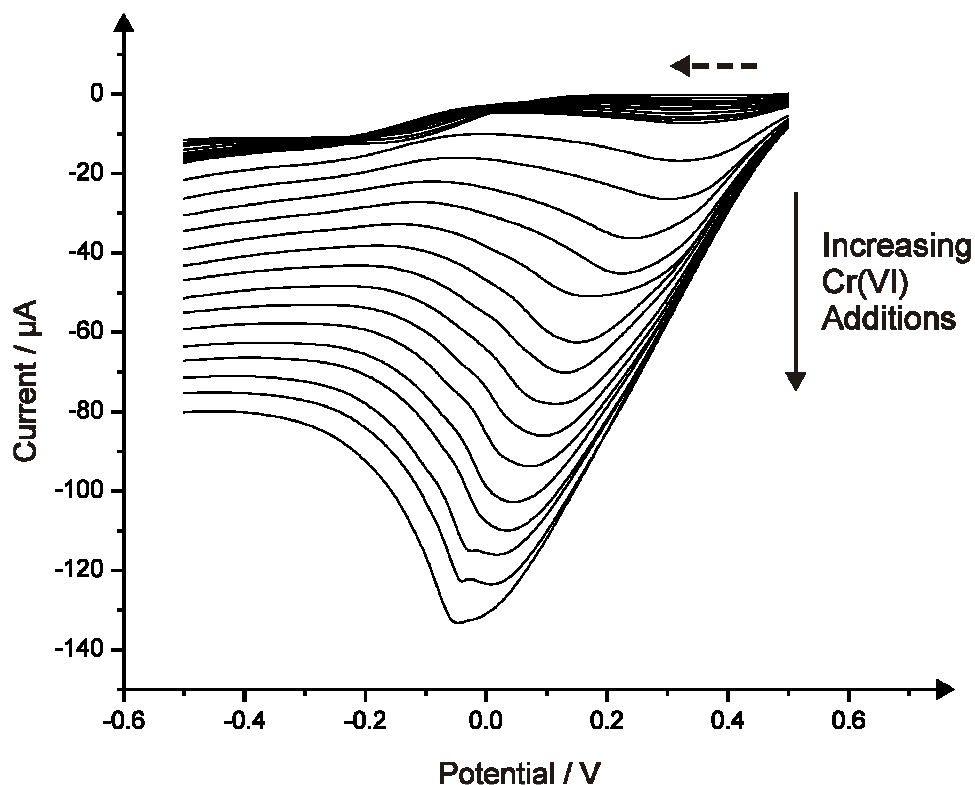


Figure 3.6 Typical linear sweep voltammetric profiles resulting from the electrochemical reduction of chromium (VI) in 0.05 M H_2SO_4 using an AuSPE over the range of 10 to 1600 μM . Scan rate: 50 mV s^{-1} . Dashed arrow signifies direction of scan.

The application of the AuSPE was trialled towards the detection of chromium (VI) over a broad concentration range. Figure 3.6 depicts typical linear sweep voltammograms for the electrochemical reduction of chromium (VI) using the AuSPE in 0.05 M H_2SO_4 over a concentration range of 10 to 1600 μM . As is easily distinguishable, with increased chromium (VI) concentration an increased reduction peak current (μA) is observed at the AuSPE. Further analysis of such data demonstrates a strong, reliable correlation between the concentration of chromium (VI) and the determined reduction peak height (figure 3.7). The

AuSPE was seen to exhibit linearity over the entire concentration range observed and as shown in figure 3.7. The % Relative Standard Deviation was found to correspond to 5.8 % ($N = 3$). Consequently a limit of detection for chromium (VI) was calculated (using 3σ in line with section 1.1.11) to correspond to $4.4 \mu\text{M}$. The experimentally determined limit of detection for chromium (VI) at an AuSPE, although not offering detection below the WHO recommendation, does exhibit analytical limits very close to that of a polycrystalline gold macro electrode.¹⁰⁸ Note that as can be observed in table 3.1, the detection limit derived at the AuSPE deviates from that observed at nanoparticle modified electrodes. The analytical response could likely be improved *via* producing an array of AuSPE, as has been reported for graphite electrodes.¹⁰³

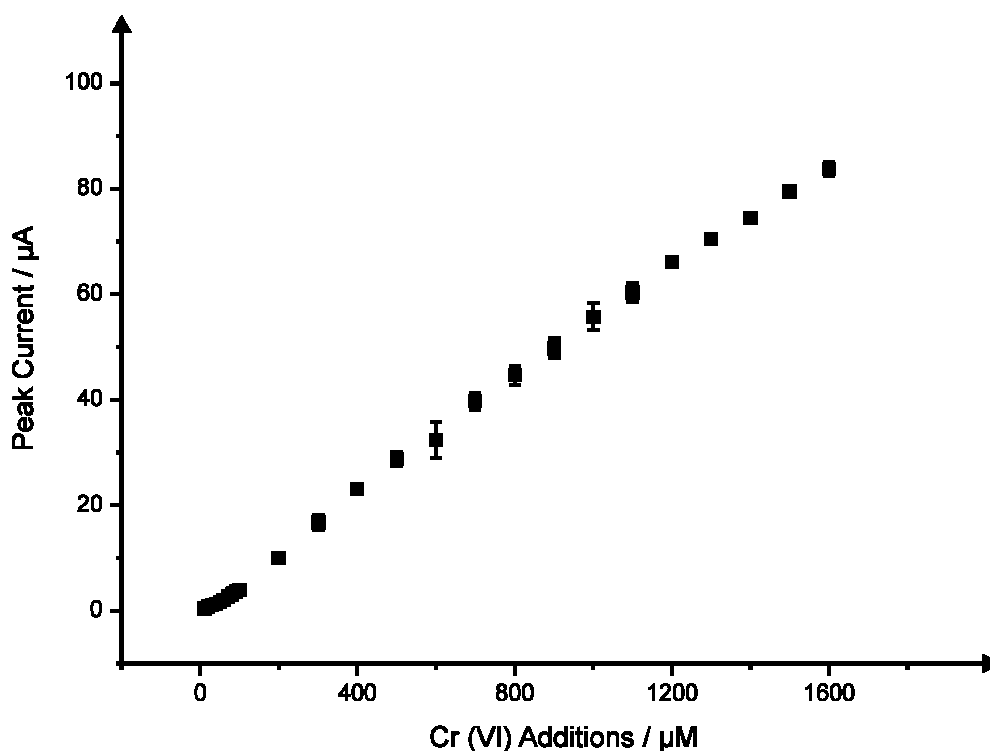


Figure 3.7 A typical calibration plot resulting from additions of chromium (VI) into $0.05 \text{ M H}_2\text{SO}_4$ using the AuSPE as shown in figure 3.6.

The analytical applicability of the AuSPEs was examined through the attainment of plots of chromium (VI) reduction peak current against concentration of chromium (VI) added

in both the absence, and presence of known, previously determined water interferences.¹³² Copper (II), nickel (II) and iron (III) were each introduced to the solutions at a concentration of 250 μM with additions of chromium (VI) then being carried out. The resulting plots of the corresponding plot of peak (I_p) current against concentration of chromium (VI) were determined to be, $(I_p / \mu\text{A} = 6.63 \times 10^{-2} \mu\text{A} / \mu\text{M} + 1.61 \mu\text{A}; R^2 = 0.99; N = 10)$, $(I_p / \mu\text{A} = 5.74 \times 10^{-2} \mu\text{A} / \mu\text{M} + 1.31 \times 10^{-1} \mu\text{A}; R^2 = 0.98; N = 10)$ and $(I_p / \mu\text{A} = 1.24 \times 10^{-2} \mu\text{A} / \mu\text{M} + 11.53 \mu\text{A}; R^2 = 0.60; N = 10)$ for copper (II), nickel (II) and iron (III) respectively, highlighting little variation amongst samples with possible interferences and that obtained under ideal conditions ($0.0541 \mu\text{A}/\mu\text{M}^{-1}$); note that only iron (III) was found to significantly deviate at levels of 250 μM . Such observations would suggest that using the AuSPE under the current parameters, the detection of chromium (VI) is independent of environmental factors, and thus accordingly this AuSPE can be used for the electroanalytical detection of chromium (VI) in environmental samples.

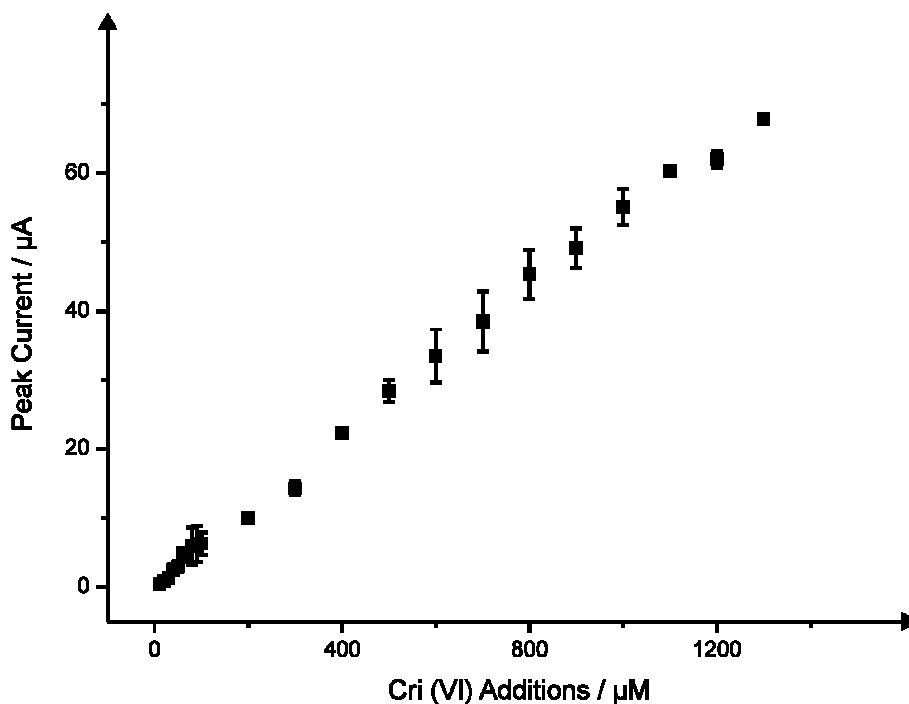


Figure 3.8 A typical calibration plot resulting from additions of chromium (VI) over the range of 10 to 1300 μM into canal water samples. Scan Rate: 50 mV s^{-1} .

In order to assess the true viability of the AuSPEs for the sensitive detection of chromium (VI) in environmental samples, additions of chromium (VI) were made to a solution of canal water (sourced and pre-treated as reported in the Experimental section (3.1.2)). Low level additions of chromium (VI) in the μM range were once more made to an acidified canal water sample (10 to 1300 mM) as depicted in figure 3.8 through a plot of peak height (μA) vs. chromium (VI) concentration. Admirable linearity was observed over the entire concentration range, even within a true environmental sample which potentially contained numerous potential contaminants. When comparing the calculated slope of the calibration graph, $0.0529 \mu\text{A}/\mu\text{M}^{-1}$ with that corresponding to additions in ideal analytical samples as previously discussed with a slope of $0.0541 \mu\text{A}/\mu\text{M}^{-1}$, it is clear that the fabricated AuSPE boasts encouraging sensitivity even within difficult, real world samples, further highlighting the potential environmental applications of the AuSPEs.

3.1.4 CONCLUSIONS

The application of novel, disposable, single-shot gold screen printed macro electrodes has been explored and evaluated their analytical performance towards the sensing of chromium (III) and (VI). In addition the AuSPE was found to exhibit competitive limits of detection for both chromium (III) and (VI) at $38.8 \mu\text{M}$ and $4.4 \mu\text{M}$ respectively comparing well with current literature reports. The response of the electrode to addition of chromium (VI) was found to be independent of common environmental interferences such as Ni and Cu.

An important point to note is the potential recyclable nature of the AuSPEs due to their fabrication and additionally the surface is in the form of gold oxide which, in the cases where this is used as an electro-catalyst towards target analytes, alleviates the need for potential cycling as is the case when polycrystalline gold electrodes are utilised.

3.2 PLATINUM SCREEN PRINTED ELECTRODES

Continuing with the observations and conclusions from the previous section where gold modified screen printed sensors were fabricated and implemented towards the sensing of chromium species a sensor, fabricated using the same screen printing technology was produced comprising a platinum modified working electrode surface. Within this section, this electrode, the first of its kind, is electrochemically characterised with experiments to determine the potentially useful analytical applications of the sensor being explored. This section contains work which has been published.^[2]

3.2.1 INTRODUCTION

The transition from the electrochemical development systems into the field is a perilous journey. One tried and tested approach for electro-analytical based sensors is through the use of screen printed electrodes which has helped the implementation of electrochemical biosensors for the sensing of glucose in blood used globally by diabetics.¹³³ The technique of screen printing is a well-established process producing disposable and cost effective electrodes that can be utilised in electrochemical sensors and biosensors with many academic research groups and industrial enterprise's producing new and advantageous electrode configurations.¹⁰³

The most commonly utilised screen printed electrodes are constructed of graphite where a commercially purchased ink consisting of graphite and carbon black particles with a polymeric binder and solvents are screen printed onto a suitable substrate which is then cured at a suitable temperature.^{103, 134} Many advantageous geometric designs have been reported¹⁰³ and new electrodes of different compositions have been produced such as graphite electrode consisting of prussian blue^{135, 136} and cobalt phthalocyanine¹³⁷ mediators utilised in

² J. P. Metters, F. Tan, R. O. Kadara and C. E. Banks, *Anal. Methods*, 2012, **4**, 1272.

biosensors, metal oxides,^{104, 138-143} carbon nanotubes^{144, 145} modified screen printed electrodes and gold^{109, 146, 147} and silver¹⁴⁶ nanoparticles modified electrode fabricated *via* electrochemical formation. Similarly other screen printed electrodes comprising entirely gold have been reported.¹⁴⁸⁻¹⁶⁴

It is important to note that in these configurations the whole geometric working electrode comprises the noble metal rather than being modified later. As described in the previous section the fabrication of gold screen printed electrodes applied towards the sensing of highly toxic chromium (VI)⁸⁵ and biologically important chromium (III)¹⁶⁵ highlighting the facile reduction and oxidation of each analyte respectively. Interestingly the electro-analytical sensing of chromium (VI), gold oxide surfaces are highly desired and typically gold macro electrodes need to be potential cycled to induce the formation of gold oxide^{146, 166} but in the case of the gold screen printed electrode, this requirement is alleviated due to the gold electrode surface consisting of predominantly gold oxide alleviating the requirement of the pre-treatment. The economical use of the noble metal also acts to ensure that a low cost sensor is feasible without the sensitivity of the electrode being compromised. With the ultimate objective of a screen printed sensor being to ensure facile monitoring of key analytes, such developments which ensure to keep pre-treatments such as potential cycling to a minimum are of great interest!

There are very few literature reports concerning the fabrication of platinum screen printed electrodes;^{136, 167, 168} consequently herein is described the fabrication and characterisation of platinum screen printed electrodes which are critically evaluated in regards their response towards the important target analytes hydrazine and hydrogen peroxide. It is noted that hydrazine an increasingly important industrial molecule utilised within rocket fuel and missile systems and corrosive inhibitors, in addition to the ever expanding fuel cell development.¹⁶⁹ The need for facile detection of hydrazine is further

compounded with the knowledge that it is a neurotoxin and molecule which is found to have carcinogenic and mutagenic effects.^{170, 171}

Reports have detailed the sensing of hydrazine including methods based on flow injection analysis (FIA),^{172, 173} ion chromatography,¹⁷⁴ chemiluminescence and various types of spectroscopy.¹⁷⁵⁻¹⁷⁷ However, the processes involved in many of these methods are extremely complex, and the linear ranges are relatively narrow and have low precision. Fortunately, electrochemical techniques offer the opportunity for portable, cheap and rapid methodologies. Platinum is one such electrode which has been successfully utilised for the sensing of hydrazine, offering faster electrode kinetics over that of the traditional, more sluggish carbon based electrodes. Drawbacks to the use of a traditional platinum electrode evidently centre on the expense and uneconomical nature of such materials.

Similarly hydrogen peroxide is of importance acting as a common intermediate in both environmental and biological systems and is a product of the oxidation of glucose by Glucose oxidase.¹⁷⁸ As such the investigation of its detection is of interest and has had substantial attention, with the application of various techniques such as chemiluminescence,¹⁷⁹ oxidimetry¹⁸⁰ and electrochemistry.¹⁸¹⁻¹⁸³

Although a handful of studies describing the fabrication and application of platinum screen printed electrodes have been reported, this is the first instance in which a platinum screen printed electrode is evaluated towards the sensing of hydrazine and hydrogen peroxide. The novelty of this approach is also highlighted by the fact that the electrode requires no prior pre-treatment in the form of potential cycling. Within the present study the electrochemical detection of both hydrazine and hydrogen peroxide in neutral conditions are studied through the novel application of platinum screen printed electrodes.

Characterisation of the Platinum Screen Printed Electrodes

Platinum screen printed electrodes (denoted throughout as PtSPE) were fabricated as detailed in the Experimental section (3.1.2) with a working electrode consisting of platinum ink screen printed onto an underlying graphite based screen printed electrode. Note that in this case, the expensive platinum material is parsimoniously utilised but it could be the case that the connecting legs are constructed of the same platinum material. Figure 3.9 depicts SEM characterisation of the PtSPE revealing a non-uniform surface which consists of platinum microparticles held together with a polymeric formulation. Energy-dispersive X-ray (EDAX) analysis (see figure 3.10) was conducted on the PtSPE revealing through semi-quantitative determination that the surface to consist of 4.00 % oxygen, 8.15 % carbon and 87.85 % platinum. This individually determined amount of platinum is consistent with the specifications of the commercially purchased original ink formulation (see Experimental section (3.1.2)). It is surmised that the oxygen content arises due to the platinum being in an oxide formation and likely the carbon content arises due to the use of a polymeric binder in the ink formulation. Note EDAX cannot prove that the oxygen content is due to the platinum oxide or a constituent from the ink such as the binder. As the latter is proprietary information and the former is readily identified *via* electrochemistry and additionally the suppliers information which stipulates that a platinum oxide is utilised it is highly likely that the final surface consists of a platinum oxide.

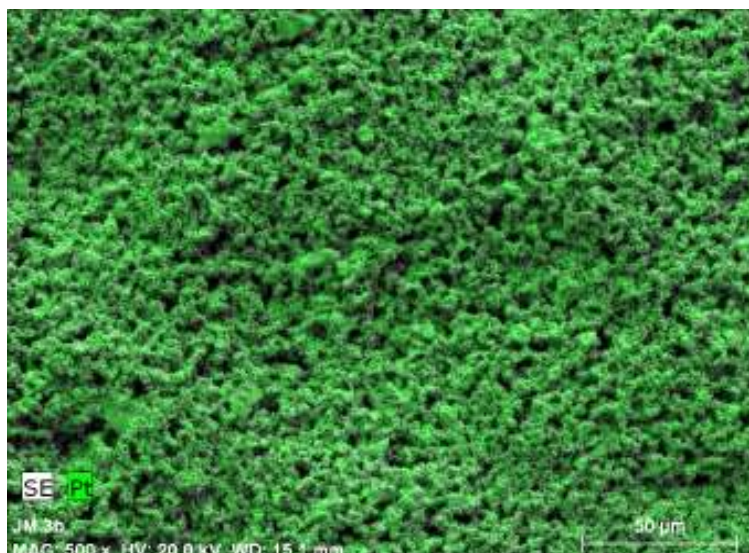


Figure 3.9 Typical SEM image of the platinum screen printed electrode.

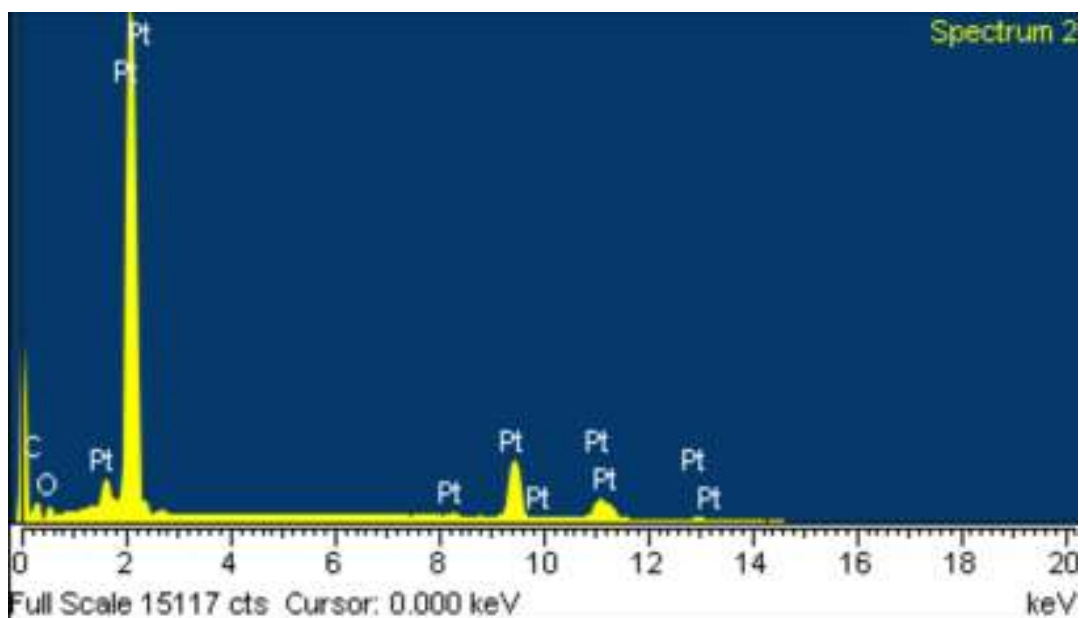


Figure 3.10 EDAX analysis of the platinum screen printed electrode.

The PtSPEs were first electrochemically characterised using the redox probe potassium hexachloroiridate. Firstly, scan rate studies were performed using the PtSPE in 1 mM potassium hexachloroiridate with 0.1 M KCl (see figure 3.11), where observation of voltammetric peak height, plotted as peak current (I_p) against square root of the applied scan rate over the range 5 – 200 mV s^{-1} was found to be linear ($I_p / \mu\text{A} = 49.96 \mu\text{A} / (\text{Vs}^{-1})^{1/2} + 1.14 \mu\text{A}$; $R^2 = 0.98$; $N = 8$) confirming a diffusional process.

The electron transfer rate constant, k^0 , for the process was determined using the Nicholson method;⁷ using a literature diffusion coefficient value of $8.3 \times 10^{-6} \text{ cm}^2 \text{ s}^{-1}$ (reported in 0.2 M KCl)¹⁸⁴ the electron transfer rate constant was estimated to correspond to $1.4 \times 10^{-3} \text{ cm} \text{ s}^{-1}$. Such a value is relative to the rate of mass transport to the electrode surface and using the analysis of Matsuda and Ayabe¹⁸⁵ (see equation 4.1). Using the electron transfer rate constant deduced (see above) along with the literature diffusion coefficient for potassium hexachloroiridate (IV), for the experimental case, over the range of scan rates employed, that overall the electrochemical process can be described as quasi-reversible. The electro-active area of the PtSPE can be estimated using equation (1.20) to be 0.1 cm^2 compared to a geometric area of 0.071 cm^2 ; this response suggests that the platinum electrode surface is slightly porous in agreement with SEM images (see figure 3.9), but is not substantially porous that thin layer voltammetric behaviour is observed. In addition, the intra-reproducibility (that is within the same batch of sensors) of the PtSPE was determined through repeat analysis in potassium hexachloroiridate (IV) where an RSD of 9.05 % ($N=5$) was determined. The PtSPE electrode was also explored in 0.1 M H_2SO_4 , and as shown in figure 3.12, in the anodic scan, a single peak is observed at $\sim -0.3 \text{ V}$ (vs. Ag/AgCl) with a further peak seen in the cathodic scan, which appeared at $\sim -0.17 \text{ V}$ (vs. Ag/AgCl) which can be likely attributed to the adsorption and desorption of hydrogen as observed on polycrystalline platinum surface.^{186, 187}

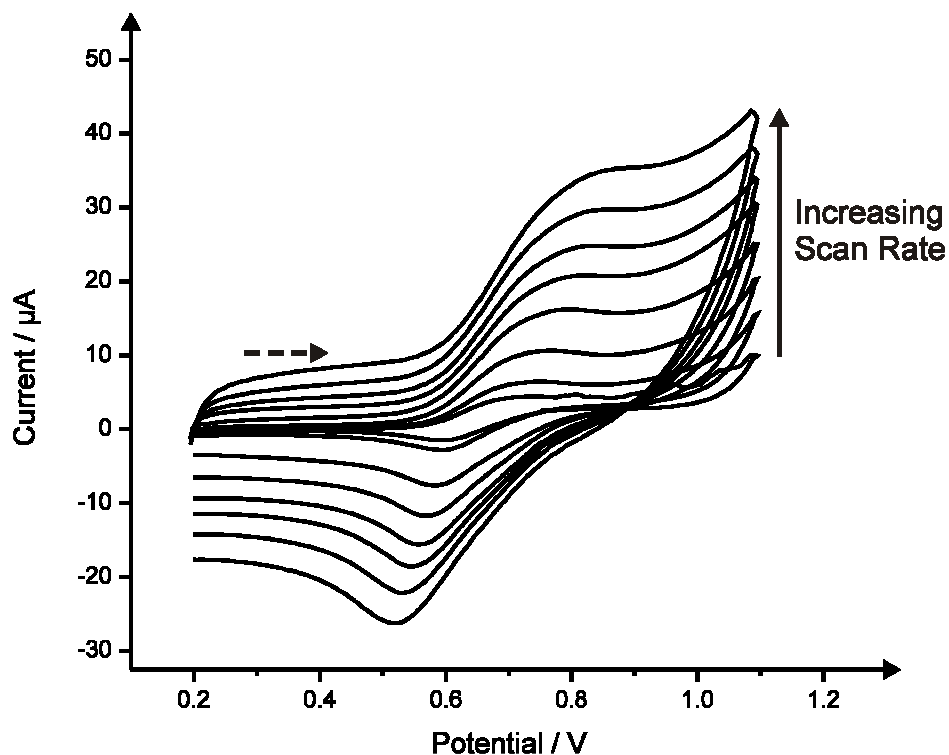


Figure 3.11 Electrochemical oxidation and reduction of 1 mM potassium hexachloroiridate in 0.1 M KCl using the PtSPEs recorded over the scan rate range of 5 to 200 mV s^{-1} (vs. Ag/AgCl). Dashed arrow signifies direction of scan.

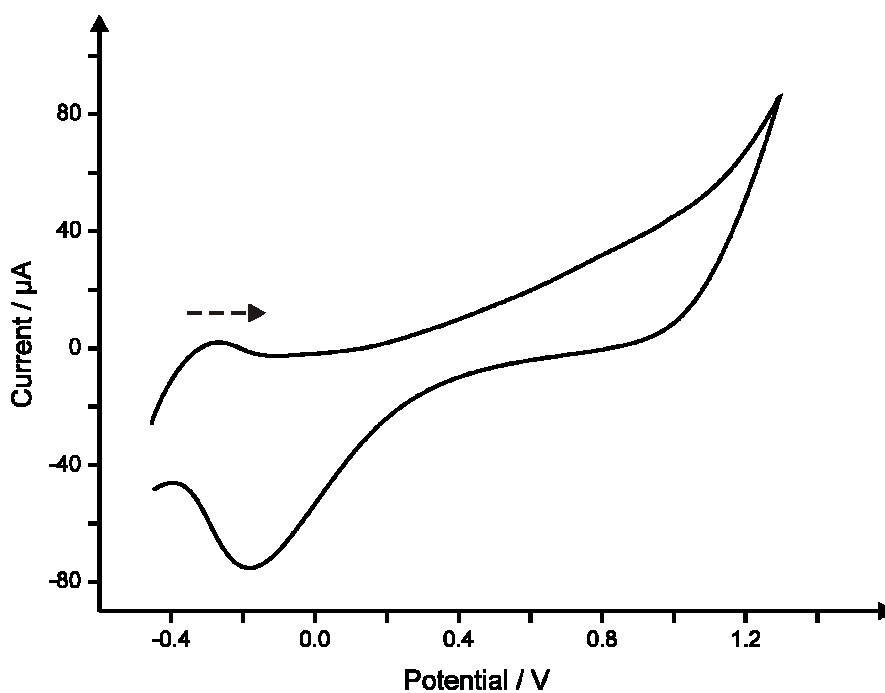


Figure 3.12 A typical cyclic voltammogram recorded in 0.1 M H₂SO₄ using a platinum screen printed electrode. Scan rate: 100 mV s^{-1} . Dashed arrow signifies direction of scan.

Electroanalytical Sensing of Hydrazine

Following the characterisation of the novel platinum based sensors, their application towards the detection of the important analyte, hydrazine was trailed. Initial cyclic voltammetric measurements for the sensing of hydrazine were obtained, as shown in figure 3.13, where an oxidation wave corresponding to the electrochemical oxidation of hydrazine in a phosphate buffer of pH 7 was evident at a potential of $\sim + 0.7$ V (*vs.* Ag/AgCl). A reduction wave can also be observed at $\sim - 0.25$ V (*vs.* Ag/AgCl), presumed to be the reduction of the oxide based platinum present within the electrode. Additions of hydrazine into the pH 7 PBS were made where the magnitude of the voltammetric peak height is observed to grow with increasing additions, as shown in figure 3.13A. Analysis of these voltammetric profiles are presented in figure 3.13B where a plot of the voltammetric peak height (oxidation) versus hydrazine concentration which is seen to demonstrate linearity over the entire concentration range of 50 to 500 μ M ($I_p / A = 1.0 \times 10^{-7} A / \mu M + 3.0 \times 10^{-6} A; R^2 = 0.98; N = 10$). A limit of detection (using 3σ in line with section 1.1.11) was found to correspond to 0.15 μ M; clearly this is a theoretical result rather than a practical one (as discussed within section 1.1.10). The analytical range of 50 to 500 μ M was selected as it is recommended that Limit tests for hydrazine in pharmaceuticals suggest that it should be in the low ppm range; concentrations encompassed by the selected analytical range.¹⁸⁸ The use of chronoamperometry was explored where the potential was held at a value of + 0.5 V (*vs.* Ag/AgCl), selected due to the observed oxidation potential of hydrazine at the PtSPE through earlier cyclic voltammetric analysis, for a period of 120 s in a phosphate buffer of \sim pH 7 with additions of hydrazine being made. Figure 3.14 demonstrates a calibration plot ($I_p / A = 2.0 \times 10^{-8} A / \mu M + 7.0 \times 10^{-7} A; R^2 = 0.97; N = 10$) obtained using the PtSPE using chronoamperometric techniques, which highlights the ability of the electrochemical technique, combined with the novel PtSPE to facilitate improved

sensitivity and detection of hydrazine with measurements within the concentration range 50 to 500 μM and a detection limit (using 3σ in line with section 1.1.11) calculated to be 0.12 μM ; once again, in reality this level is unlikely to be practically achievable but is required to benchmark against current literature (see later).

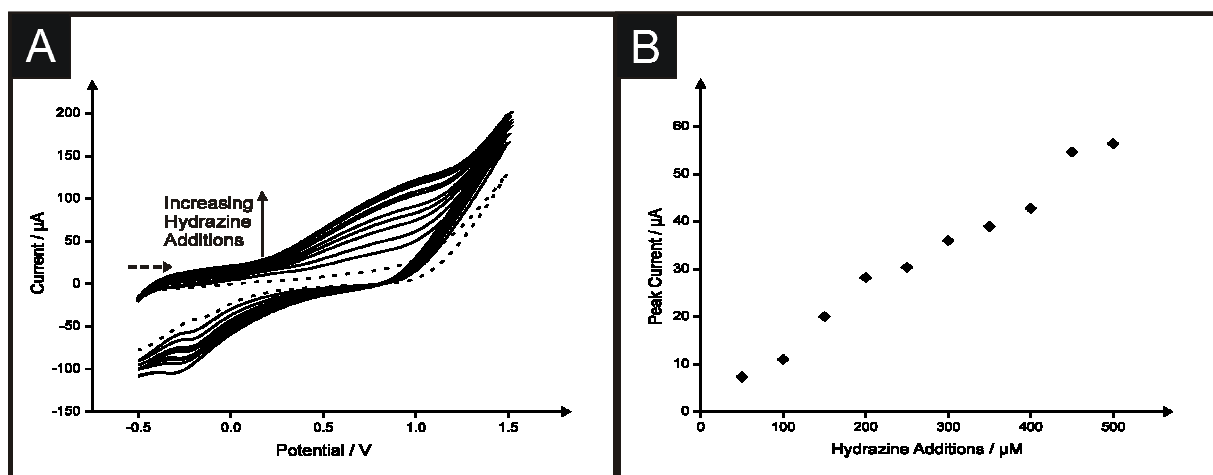


Figure 3.13 A) Typical cyclic voltammetric responses resulting from additions of hydrazine into a phosphate buffer using the PtSPE. Scan rate: 50 mV s^{-1} . B) A typical calibration plot resulting from additions of hydrazine over the range of 50 to 500 μM . Dashed arrow signifies direction of scan.

In an attempt to test the applicability of the PtSPE towards the detection of hydrazine in a true sample, additions of hydrazine were made into a sample of canal water (sourced and pre-treated as reported in the Experimental section (3.1.2)). Low level additions of hydrazine (over the range 50 to 500 μM) were made into the sample of canal water as depicted in figure 3.15 through a plot of peak height (μA) vs. hydrazine concentration. Though there is an apparent reduction in the sensitivity of the PtSPE towards the detection of hydrazine within canal water when compared with that in ‘ideal’ conditions, likely due to interferents within the sample, it is clearly evident that the proposed PtSPE is still viable in such a potentially complex sample media.

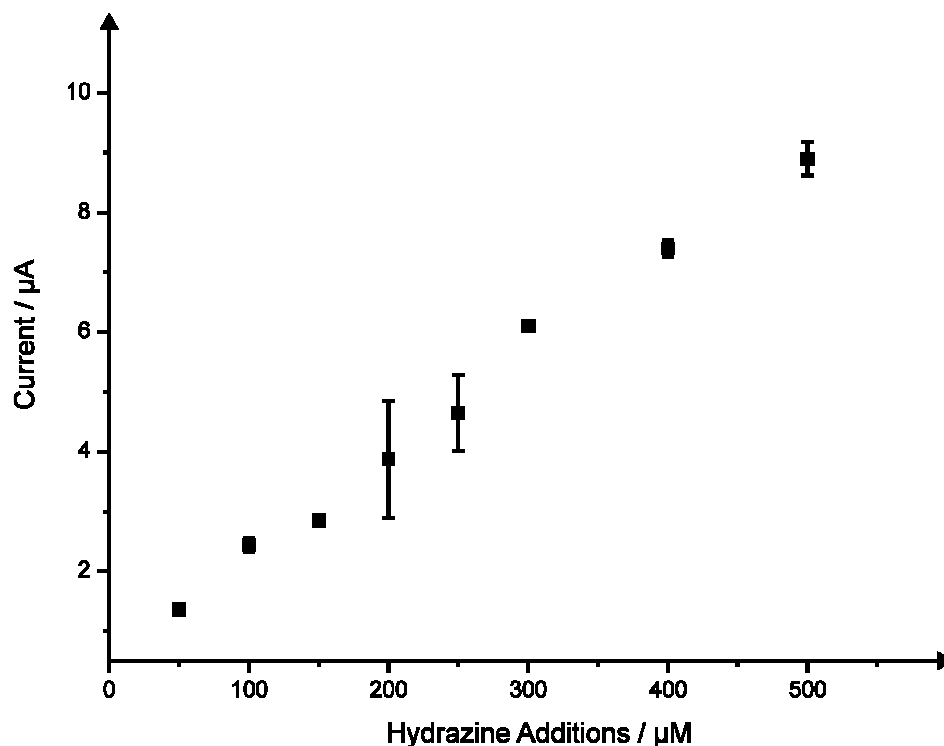


Figure 3.14 Typical chronoamperometric measurements resulting from the electrochemical oxidation of hydrazine in a phosphate buffer using a PtSPE over the range of 50 to 500 μM . Measurements were taken at a potential of + 0.5 V (vs. Ag/AgCl).

Both analytical responses using cyclic voltammetry and chronoamperometry are found to be competitive to previous studies relating to hydrazine such as that by Compton *et al*¹⁸⁹ who report upon the sensing of hydrazine using iron (III) oxide graphite composite electrodes which is shown to boast a detection limit of 1.2 μM hydrazine, which is seen to be close to that determined at the PtSPE, though as with many traditional electrodes, there was a requirement for polishing between measurements. Similarly a traditional gold macro electrode modified through the application of an iron phthalocyanine film has been utilised for the sensing of hydrazine and although admirable detection limits of 11 μM for hydrazine are determined extensive preparatory steps are seen to be required in order to form the electrocatalytic film upon the gold surface.¹⁹⁰ A low limit of detection of 1 μM was reported by Nakagaki *et al*¹⁷⁷ using a carbon paste electrode modified with copper porphyrin with

linearity observed over the range 5 – 60 μM hydrazine. Though such low operation detection (5 μM) and limits of detection are desirable, electrode preparation is in this case, somewhat of a drawback due to the extensive fabrication procedures, though the easily renewable surface offered by a paste electrode is undoubtedly an advantage of the methodology.¹⁷⁷ A highly novel approach towards the sensing of hydrazine was reported by Wang and co-workers¹⁹¹, with double-stranded DNA being applied to a carbon paste electrode enabling part-per-billion hydrazine level detection. Though the ingenuity of the sensor and reported detection limits cannot be called into question, as with previous studies, the requirement for modification of the electrode is an undeniable drawback, as is the requirement for reaction time waiting periods of up to 10 minutes.¹⁹¹ An interesting study by Batchelor-McAuley and colleagues¹⁹² provides a comparison between the use of palladium nanoparticle modified boron-doped diamond electrode and a palladium plated boron-doped diamond microdisc array with the nanoparticle modified electrode providing a detection limit for hydrazine of 2.6 μM and the array enhancing the detection with a low limit of detection of 1.8 μM .

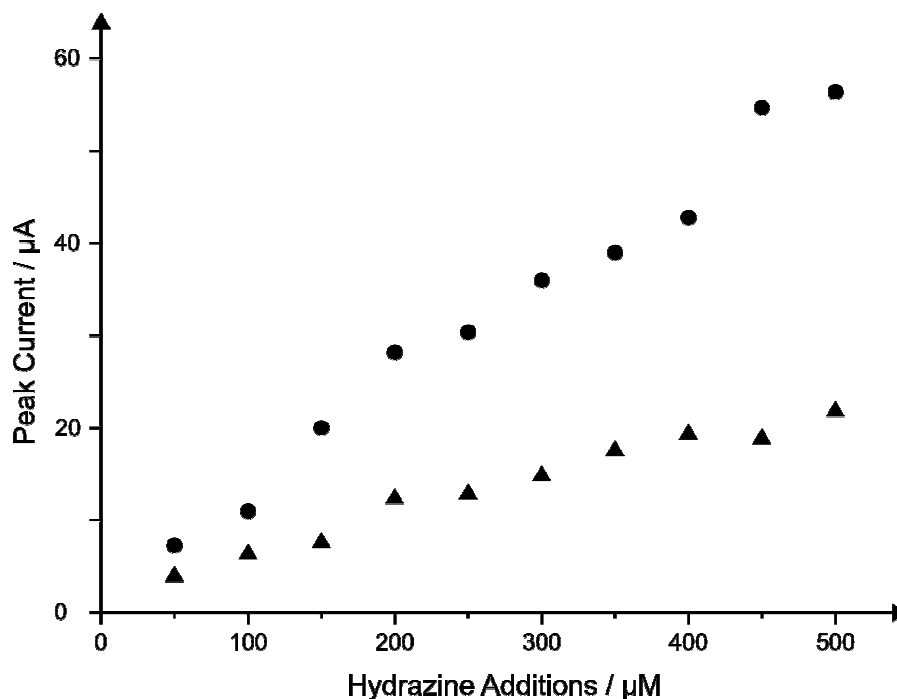


Figure 3.15 An overlay of typical responses through addition of hydrazine in 'ideal' conditions (phosphate buffer solution) (circles) and into a canal water sample (triangles) over the range of 50 to 500 μM . Scan rate: 50 mV s^{-1} .

Although each of the studies discussed allow for the sensing of hydrazine at low μM concentrations, as is found to be the case when utilising the PtSPE, many also require extensive preparatory stages, or pre-treatments prior to use. Such requirements are negated through the use of the PtSPE, which is also not found to compromise the low detection limits. Interestingly, the PtSPE has an inherent advantage over that of platinum microelectrodes, where Aldous and Compton^{193, 194} demonstrate that variable results can be achieved which is greatly dependant on the history of the electrode with optimal results observed at oxidised platinum surfaces; extensive pre-treatment in the form of potential cycling^{65, 66} needs to be applied to ensure generation of the platinum oxide but in the case of the PtSPE, such a step is negated since the platinum is in the form of an oxide upon the screen printed surface greatly simplifying the analytical protocol.

To further test the potential utilisation of the PtSPEs towards the sensing of analytes of great interest, the sensing of the biologically important analyte, hydrogen peroxide was next pursued.

Electroanalytical Sensing of Hydrogen Peroxide

First the applicability of the PtSPE was explored through cyclic voltammetric measurement in a phosphate buffer of \sim pH 7 with additions of hydrogen peroxide. Figure 3.16 highlights the successful reduction of hydrogen peroxide at \sim + 0.35 V (*vs.* Ag/AgCl) which is seen, as demonstrated through the corresponding calibration plot (figure 3.16, inset) to be concentration dependant and linear of the range 100 to 1000 μ M ($I_p / \mu A = 0.022 \mu A / \mu M - 1.37 \mu A; R^2 = 0.95; N = 10$). With a limit of detection (using 3σ in line with section 1.1.11) calculated to be 0.24 μ M. A redox peak couple can also be observed at \sim - 0.1 and 0 V (*vs.* Ag/AgCl) for the reduction and oxidation of the platinum species present within the PtSPE respectively. Note that the majority of electrochemical methods report the electrochemical oxidation of hydrogen peroxide at relatively high positive potentials which can also oxidise other substances leading to interfering currents.^{195, 196}

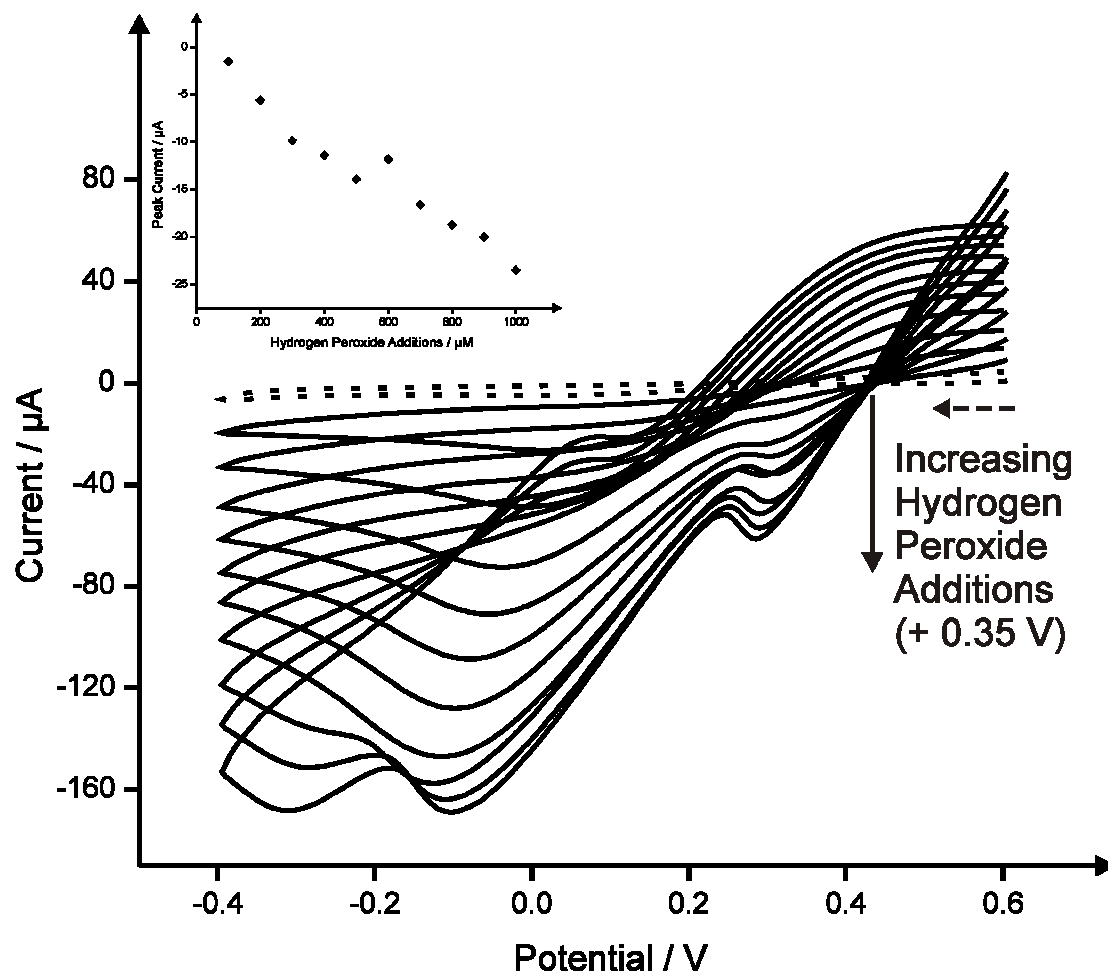


Figure 3.16 Typical cyclic voltammetric responses resulting from additions of hydrogen peroxide into a phosphate buffer using the PtSPE. Scan rate: 50 mV s^{-1} . Inset: The calibration plot corresponding to the voltammetric peak arising at $+ 0.35 \text{ V}$ over the range 100 to $1000 \text{ }\mu\text{M}$ hydrogen peroxide. Dashed arrow signifies direction of scan.

Attention was turned towards exploring the chronoamperometric measurements for the reduction of hydrogen peroxide with the potential of the electrode being maintained at $+ 0.35 \text{ V}$ (vs. Ag/AgCl) for a period of 120 seconds, with additions of hydrogen peroxide being made as shown in figure 3.17. A corresponding plot of hydrogen peroxide concentration versus final current (at 120 seconds) (figure 3.17, inset) demonstrates good linearity over the entire analytical range of 100 to $1000 \text{ }\mu\text{M}$ hydrogen peroxide ($I_p / \mu\text{A} = -5.23 \times 10^{-9} \mu\text{A} / \mu\text{M} - 5.40 \times 10^{-6} \mu\text{A}$; $R^2 = 0.96$; $N = 10$), with a detection limit

(using 3σ in line with section 1.1.11) found to correspond to 0.14 μM , improving on that obtained, as discussed earlier, using purely cyclic voltammetric measurements. Previous reports on the detection of hydrogen peroxide have included the use of; cobalt (II) hexacyanoferrate modified glassy carbon electrode¹⁹⁷, sol-gel modified glassy carbon and aluminium electrode modified with manganese hexacyanoferrate¹⁹⁸ allowing a detection limits of 0.06 μM , 0.5 μM and 0.2 μM respectively. Clearly the response of the PtSPE is competitive suggesting its analytical utility. As discussed in relation to the sensing of hydrazine, other electrode configurations allow for a lower limit of detection for hydrogen peroxide than that determined at a PtSPE, though none are found to offer the stability, lack of pre-treatment (in the form of techniques such as potential cycling or chemical treatment) and ease of use facilitated through the PtSPE.

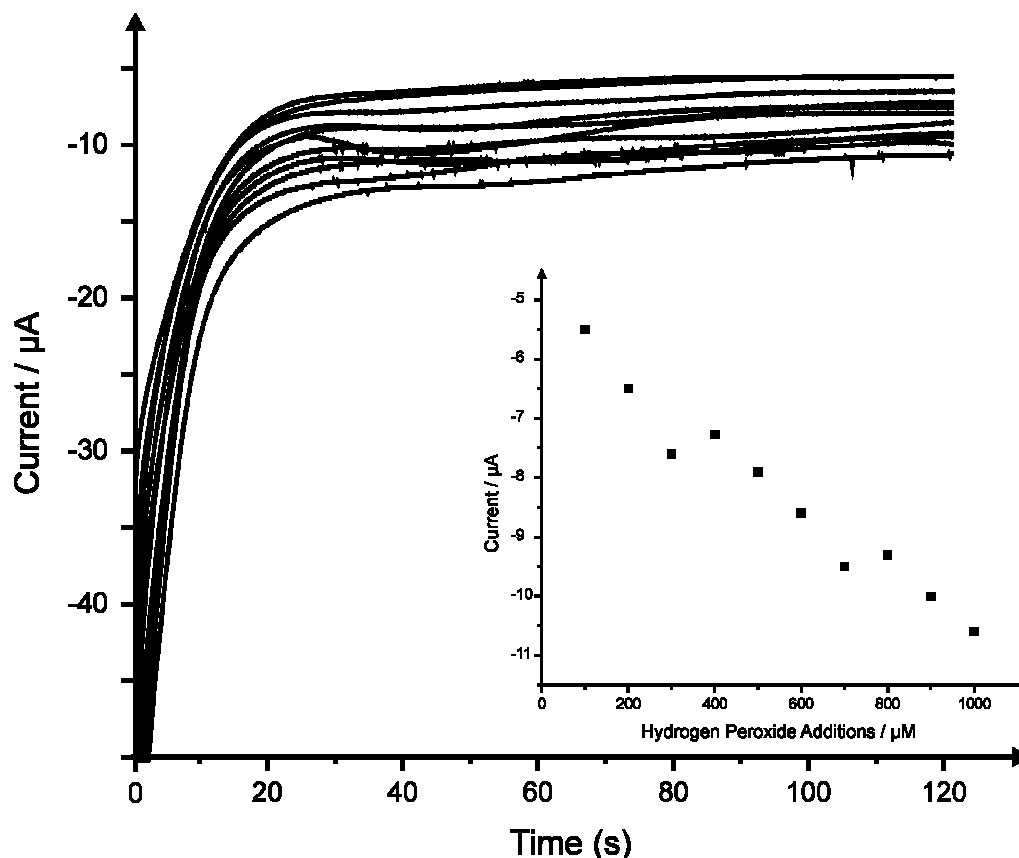


Figure 3.17 Typical chronoamperometric measurements resulting from additions of hydrogen peroxide into a phosphate buffer over the range of 100 to 1000 μM using the PtSPE. Measurements were taken at a potential of + 0.35 V (vs. Ag/AgCl). Inset: The corresponding calibration plot.

3.2.3 CONCLUSIONS

The application of novel, disposable, single-shot platinum screen printed electrodes has been described with the analytical performance of the sensors explored towards the sensing of hydrazine and hydrogen peroxide which is found to exhibit analytically useful linear ranges and limits of detection compared to existing methodologies. The added benefit of such sensors is that the platinum resides as an oxide which is beneficial for the electrochemical determination of hydrazine^{193, 194} since the need to produce platinum oxides *via* extensive potential cycling on platinum electrodes is alleviated greatly simplifying the

analytical protocol offering an electrochemical sensor which is not only disposable and simplistic in design, but also requires no prior preparation or pre-treatment.

3.3 SINGLE-WALLED CARBON NANOTUBE SCREEN PRINTED ELECTRODES: A COMPARATIVE STUDY

The bulk of this Chapter so far has considered the incorporation of noble metals (gold and platinum) within the screen printed electrode fabrication process for the production of modified co-planar macro sensors. These sensors have been determined, as is described, to offer competitive analytical performance when compared with alternative electrochemical configurations and also differing analytical techniques outside the realms of electrochemistry, whilst importantly offering a greatly simplified protocol over the array of techniques available for such applications.

This section builds upon these findings and the utilisation of novel screen printing inks for the development of new, previously unreported sensors through the development of a co-planar single-walled carbon nanotube modified screen printed macro electrode. Described within in published work^[3] which investigates the application of carbon nanotubes; a highly topical electrode material for the development of disposable screen printed sensors. Again, as with sections 4.1 and 4.2, it is hoped that such a method of electrode modification will allow for a truly reproducible and reliable modification and in turn sensor.

3.3.1 INTRODUCTION

Carbon nanotubes (CNTs) are molecular-scale tubes of graphitic carbon which are reported to boast outstanding, and in some cases unrivalled, properties.¹⁹⁹ These two-dimensional nanostructures are reported to be amongst the stiffest and strongest fibres known to man, and have remarkable electronic properties along with many other unique and beneficial characteristics¹⁹⁹ and consequently there has been intensive research activity in their applications such as field emission displays^{200, 201}, hydrogen storage vehicles,²⁰²⁻²⁰⁴

³ J. P. Metters, M. Gomez-Mingot, J. M. Iniesta, R. O. Kadara and C. E. Banks, *Sens. Actuators, B*, 2013, **177**, 1043.

atomic-force and scanning tunnelling microscope tips,^{205, 206} nanoelectronics,²⁰⁷⁻²¹⁰ optoelectronics²¹¹ and within composites.²¹²

Single-walled carbon nanotubes (SWCNT) are effectively one single rolled up sheet of graphene with either open or closed ends, depending on the fabrication methodology, and possess outstanding strength, exhibit a very large surface area per unit mass and have unique optical properties.²¹³ The structure of individual graphene tubes are defined by the unit cell reactors where the open ends may have ‘zig-zag’, ‘arm-chair’ and ‘chiral’ geometries.^{199, 214} Multi-walled carbon nanotubes (MWCNT) are coaxial assemblies of graphene cylinders and have dimensions ranging from 2 to 30 nm in diameter and are several microns in length.²¹⁵

Many sensor based products capitalising on the beneficial attributes of the incorporation of CNTs have been reported including those for ultrasensitive detection of carbon monoxide, ammonia, nitrous oxide, and other gases, as well as point-of-care monitoring for glucose and asthma.²¹⁶ One prevalent application of carbon nanotubes is within the field electrochemical sensors.²¹⁷⁻²²² Initially carbon nanotube based electrodes received great plaudits due to their apparent excellent electro-activity and resultant electro-catalytic behaviour. Numerous literature reports can be found demonstrating the improved electron transfer at carbon nanotube modified electrodes over their unmodified counterparts.²¹⁷⁻²²² It is however key to note that although for many years carbon nanotubes were thought to be ‘electro-catalytic’, it is now widely accepted that the origin of electron transfer at carbon nanotubes is at the open end of the nanotubes and along the tube axis where defect sites exist both at which electron transfer is reported to be anomalously faster than that of the pristine side walls of the nanotube.^{223, 224} Other work has shown that in the case of CVD grown carbon nanotubes, metallic impurities reside which can dominate the electrochemical response rather than the carbon nanotube itself such that false claims of electro-catalysis towards target analytes are claimed.²²⁵⁻²³¹ Additionally it has been shown

that the metallic impurities between batches can significantly vary suggesting that these impurities are a major limitation for nanotubes when used as the basis of sensors.^{199, 223, 232} Note that these impurities are trapped within graphene layers of the nanotube wall and to 'purify' the nanotube as so to exclude the metallic impurities is requiring extensive treatment. A common approach applied in the literature is an acid wash and it has been shown that this does not leave the nanotube free from impurities largely due to that the fact that the kinetics of dissolution of many metal oxides and carbides even in concentrated mineral acids can be very slow and also since the connecting graphitic layers need to be broken and hence destroys the nanotube structure.^{199, 233} This may be circumvented by using carbon nanotubes that are produced *via* a solid state process which does not require any metallic catalyst producing high purity carbon nanotubes;²³⁴ such nanotubes have been used in the electroanalytical sensing of nicotine in artificial saliva²³⁵ and hydrogen peroxide.²³⁶ Interestingly nanographite impurities have also been reported to potentially dominate the electrochemical response of carbon nanotubes towards select analytes.²³⁷ Another important consideration is the oxygenated species residing at the edge plane like-sites / defects of the carbon nanotubes; it is well known that electrochemically active species may have favourable or detrimental interactions with surface oxygenated species.^{199, 223}

When utilising CNTs in electrochemical applications there are two main approaches: (i) immobilisation of the chosen nanomaterials onto an electrode surface, or (ii) growth of carbon nanotube arrays on a substrate, such as chemical vapour deposition, with the use of the nanotube arrays as the electrode itself.¹⁹⁹ In the case of (i), this is the most common approach and generally involves dispersing the chosen carbon nanotubes into a non-aqueous media followed by agitation from an ultrasonic bath to disperse the nanomaterials and then an aliquot is extracted and placed onto the desired working electrode with the solvent evaporating leaving the nanomaterials immobilised.¹⁹⁹ This procedure has the drawback that

the immobilisation of the nanomaterial may not be reproducible with surface stability potentially being an issue; both limitations will detrimentally contribute to analytical performance of carbon nanotube modified sensors fabricated in this manner.

Since the end of the open tubes and defects along the tube axis are the origin of electron transfer, the amount of these sites greatly dictates the electrochemical performance of the constructed nanotube sensor. This means that the position of the voltammetric signal corresponding from the electrochemical species will shift in the voltammetrically accessible voltammetric window from high potentials to lower potentials depending on the amount of edge plane like – sites/defects.^{224, 238} This will occur of course up to a point such that the carbon nanotubes residing on the electrode surface start to form a porous surface and such the mass transport of the target analyte changes. Compton and co-workers have reported on the change from purely semi-infinite diffusion to that of thin layer type behaviour.²³⁹ Figure 3.18 depicts a schematical representation and as the amount of nanomaterials is immobilised upon the surface a porous film results changing the diffusional process; in addition to semi-infinite diffusion the contribution from thin layer diffusion becomes significant, altering the observed voltammetric signal giving the false impression of electro-catalysis.²³⁹

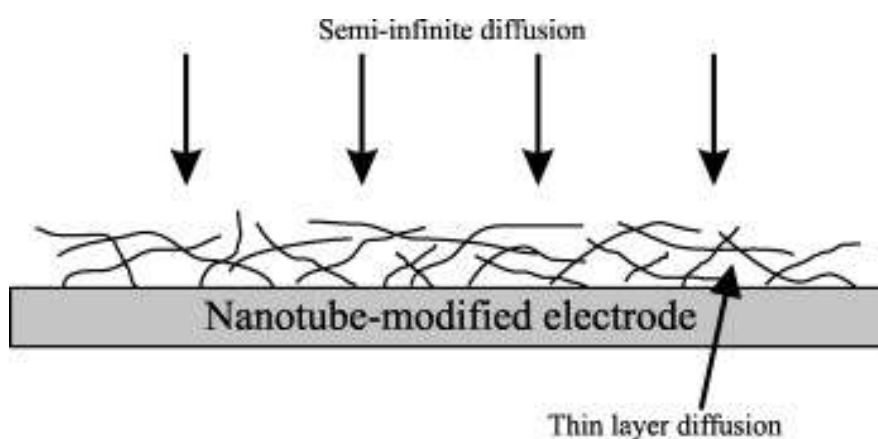


Figure 3.18 Schematic representations of the two types of diffusional process that can occur at carbon nanotube modified electrode. Reprinted from Ref²³⁹ with permission from Elsevier.

Another approach is that reported by Wang *et al* who demonstrated that multi-walled CNT-based inks could be produced allowing the fabrication of screen printed carbon nanotube sensors upon alumina ceramic substrates, which were utilised for the sensing of NADH, catechol and potassium ferrocyanide (II).²⁴⁰ The advantages of the screen printed CNT sensor were reported to be the ability to have a well-defined surface morphology, whilst maintaining mechanical stability (with good resistance to mechanical abrasion), and exhibiting higher electrochemical reactivity (compared to conventional carbon strips);²⁴¹ such an approach alleviates the need for prior modification of the electrode surface with carbon nanotubes. Further to this screen printing offers the well reported and established attributes of offering low costs sensors which are readily modified and tailored to suit the needs of the end user offering true potential for commercial applications.²⁴² Following this pioneering work of Wang²⁴⁰, commercially available single- and multi-walled carbon nanotube screen printed electrodes upon ceramic substrates have been made available with researchers exploring these towards a range of analytes such as lactate and glucose,²⁴³ polyphenols,^{244, 245} dopamine,²⁴⁶ capsaicin,²⁴⁷ hesperidin²⁴⁸ and monitoring DNA hybridisation²⁴⁹ to name just a few. Other screen printed electrodes incorporating carbon nanotubes have additionally been reported by Li and co-workers towards the sensing of dopamine *via* cyclic voltammetry using multi-walled carbon nanotube screen oriented electrodes modified through the immobilisation of lactase with silica spheres on the surface of the working electrode.²⁵⁰ Further to this Li described the utilisation of differential pulse voltammetry using a screen printed multi-walled carbon nanotube electrode array for the sensitive detection of dopamine, hydroquinone and catechol reporting limits of detection of 0.337, 0.289 and 0.369 μM , respectively.²⁵¹ The screen printed sensors fabricated by Li *et al*^{250, 251} used different mass proportions of multi-walled carbon nanotubes/carbon paste which was then screen printed upon the surface of the working electrode of the carbon-based screen printed sensor.

Within the present study the first example of novel screen printed single-walled carbon nanotube electrodes upon flexible polyester substrates which are electrochemically characterised and the electroanalytical performance of the sensors trialled towards the detection of model analytes is described. Additionally, the screen printed single-walled carbon nanotube electrodes are contrasted with commercially available alternatives and are shown to be particularly useful for sensing capsaicin down to low micromolar levels.

3.3.2 RESULTS AND DISCUSSION

Fabrication of the Screen Printed Single-Walled Carbon Nanotube Electrodes

Screen printed single-walled carbon nanotube electrodes (denoted throughout as SW-SPE) were fabricated as detailed in the Experimental Section (3.1.2) with a working electrode consisting of single-walled carbon nanotube ink screen printed onto an underlying graphite based screen printed electrode (see figure 3.19).

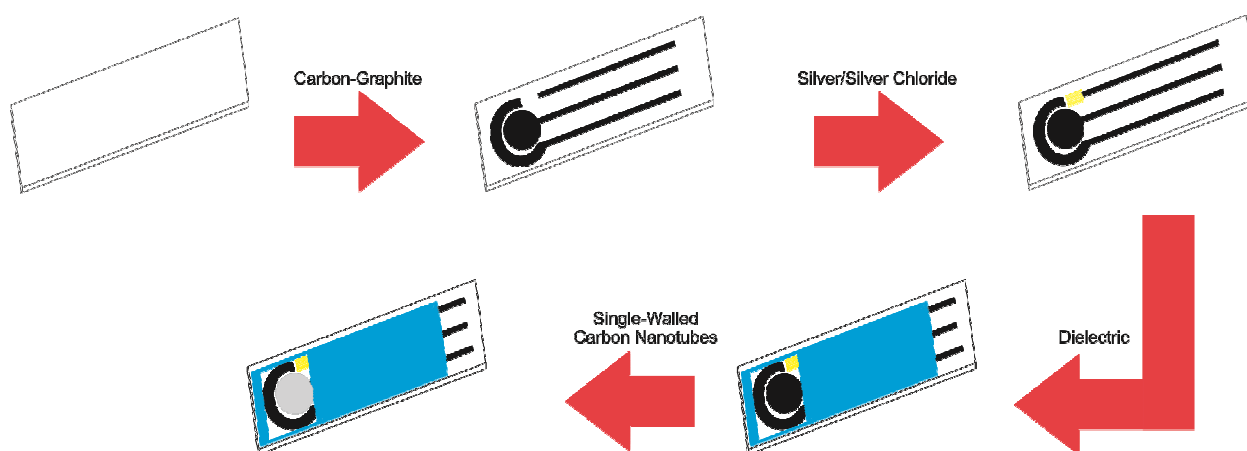


Figure 3.19 A schematic representation of the fabrication procedure of the SW-SPE.

Figures 3.20A and B depict SEM analysis of the single-walled carbon nanotube ink where the presence of a mesh of single-walled carbon nanotubes is clear. Also illustrated in figure 3.20 C and D is the surface of the unmodified SPE, prior to the screen printing of the carbon nanotube ink layers. Clearly there is a clear difference in surface morphology between

the unmodified graphite working electrode surface and the carbon nanotube modified surface with the single-walled carbon nanotubes being readily visible in figure 3.20A and B. XPS analysis of the SW-SPE revealed impurities present within the ink, as shown in figure 3.21. Fluoride was found to be present in abundance (as high as 12 %) along with nitrogen (0.7 %), molybdenum (0.3 %), sulphide (0.9 %), chloride (6 %) and also oxygen (6 %) with the carbon content determined to be to be 75 %. Analysis of the XPS de-convoluted spectra reveals 65 % of the carbon (C1) content corresponds to 285.5 eV; characteristic of graphitic groups, C-O, C=O, aromatic bonds and CF, CN bonds and 10% at 287.1 eV, which corresponds to a satellite or C-O and -C=O . The oxygen content resulted to be 5 % of O1s at 533 eV which is in agreement with C-O and C=O bonds.

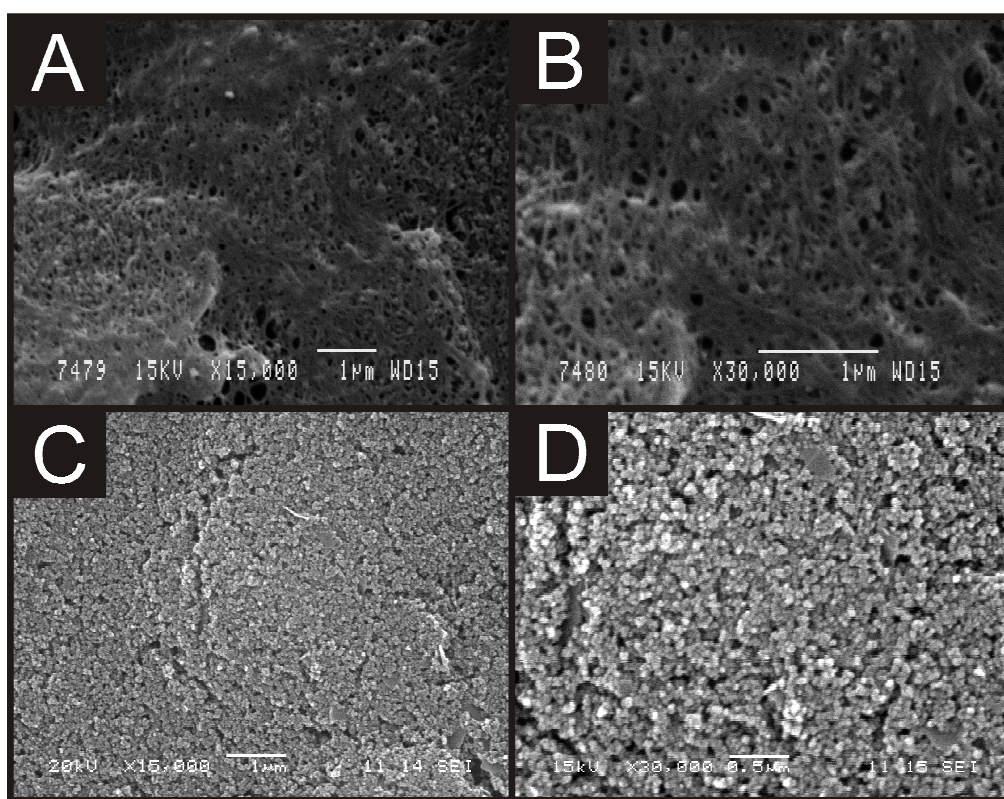


Figure 3.20 SEM analysis of the SW-SPE at x15,000 (A) and x30,000 (B) magnification. Additionally (C) and (D) depict SEM analysis of the underlying carbon electrode (unmodified SPE) prior to screen printing the SW-CNTs at x15,000 and x30,000 magnification respectively.

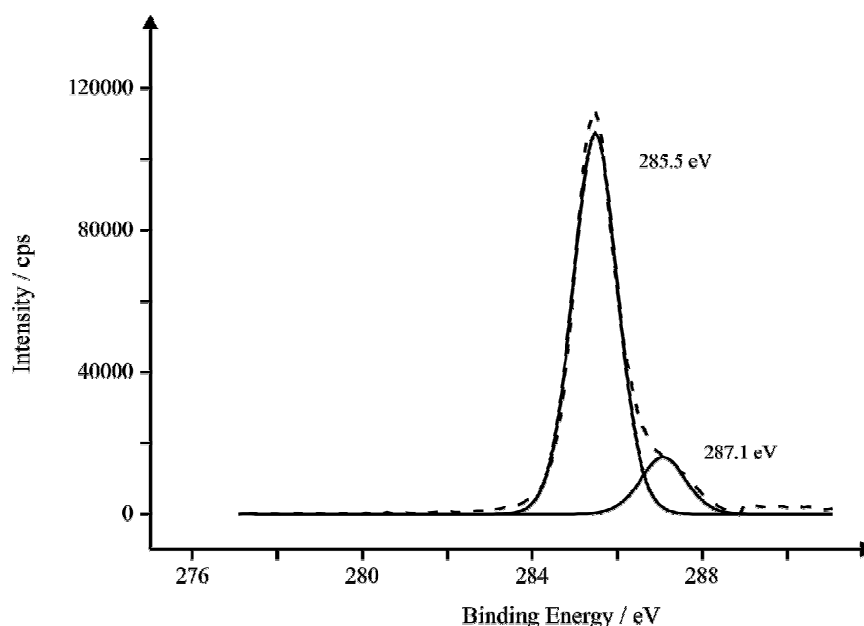


Figure 3.21 XPS analysis of the SW-SPE.

In contrast XPS analysis of the DS-SW-SPE revealed 76 % of the carbon (C1s) content (58 %) corresponding to 285 eV which is characteristic of graphitic groups, 5 % at 286 eV and 13 % at 286.8 eV which corresponds to -C-O and -C=O. The oxygen content (8 %) resulted to be 3 % of O1s at 532 eV which corresponds to the groups -OH, a 4 % at 533.3 eV and 0.4 % at 534.5 eV which correspond respectively to oxygenated groups such as C=O and C-O bonds; see figure 3.22A. Further to this analysis of the XPS de-convoluted spectra obtained for the DS-MW-SPE reveals 80 % of the carbon (C1s) content (61 %) corresponding to 284.8 eV and a 7 % at 285.8 eV, which is characteristic of graphitic groups from -C-C- and -C-H- bonds, and a 12 % at 286.6 eV which corresponds to C-O and C=O. The oxygen content (7 %) resulted to be 2 % of O1s at 531 eV which corresponds to the groups -OH, a 4 % at 533 eV and 8 % at 534.8 eV which correspond respectively to oxygenated groups such as -C=O and -C-O bonds (figure 3.22B).

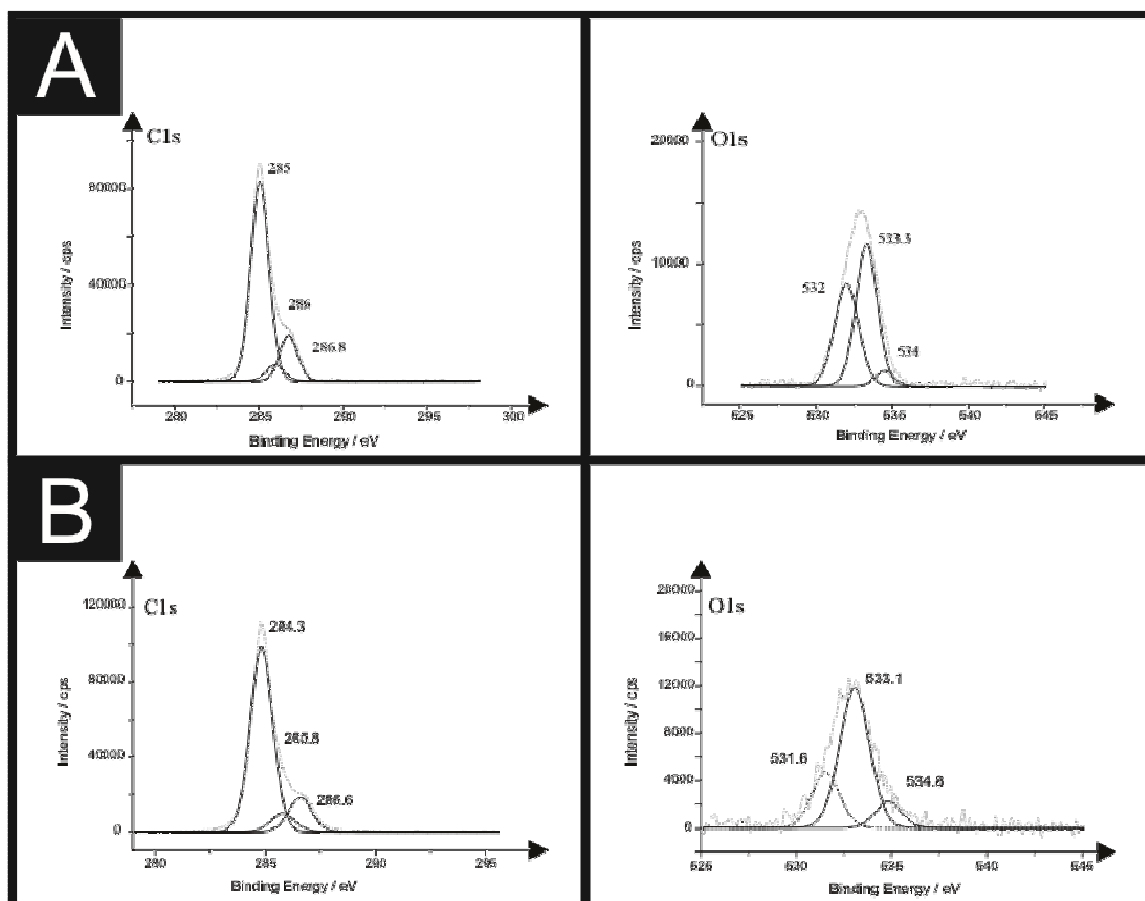


Figure 3.22 XPS analysis of the DS-SW-SPE (A) and DS-MW-SPE (B).

The presence of catalysts used within the fabrication process of CVD grown carbon nanotubes has been studied previously.²⁵²⁻²⁵⁴ Molybdenum is just one of these many catalysts, as are cobalt and nickel. Often, as discussed in the introduction, these catalysts can remain within the carbon nanotubes and in certain circumstances, can contribute to the observed electrochemical activity. As is discussed above, the ink utilised for the fabricated of the SW-SPEs was determined through XPS analysis to contain molybdenum; such findings were expected given the fabrication process¹⁴ of the single-walled CNTs used in the ink (see Experimental section). It is clear that, the presence of such metallic impurities could potentially affect the electrochemically activity and applicability of the sensors, and in turn raise questions as to whether observed responses, or electro-catalytic behaviour can truly be attributed to the carbon nanotubes or the catalyst impurities. The electrochemical activity of

molybdenum has been reported to exhibit an electrochemical oxidation peak at ~ 0.0 V (vs. Ag/AgCl) in a pH 7.4 buffer solution.²⁵⁵ As part of control experiments, cyclic voltammetry was performed in blank solutions, as shown later, for example in figure 3.23, which appear to exhibit no pertinent electrochemical activity of the metallic impurities under the chosen experimental conditions.

The electrochemical working regions of each of the sensors fabricated and utilised was determined through cyclic voltammetric measurement over a large potential range at a scan rate of 100 mV s^{-1} in a pH 7.4 phosphate buffer solution. Figure 3.23 demonstrates the improved operating potential range offered at the standard SPE and SW-SPE over the two carbon nanotube Dropsens sensors.

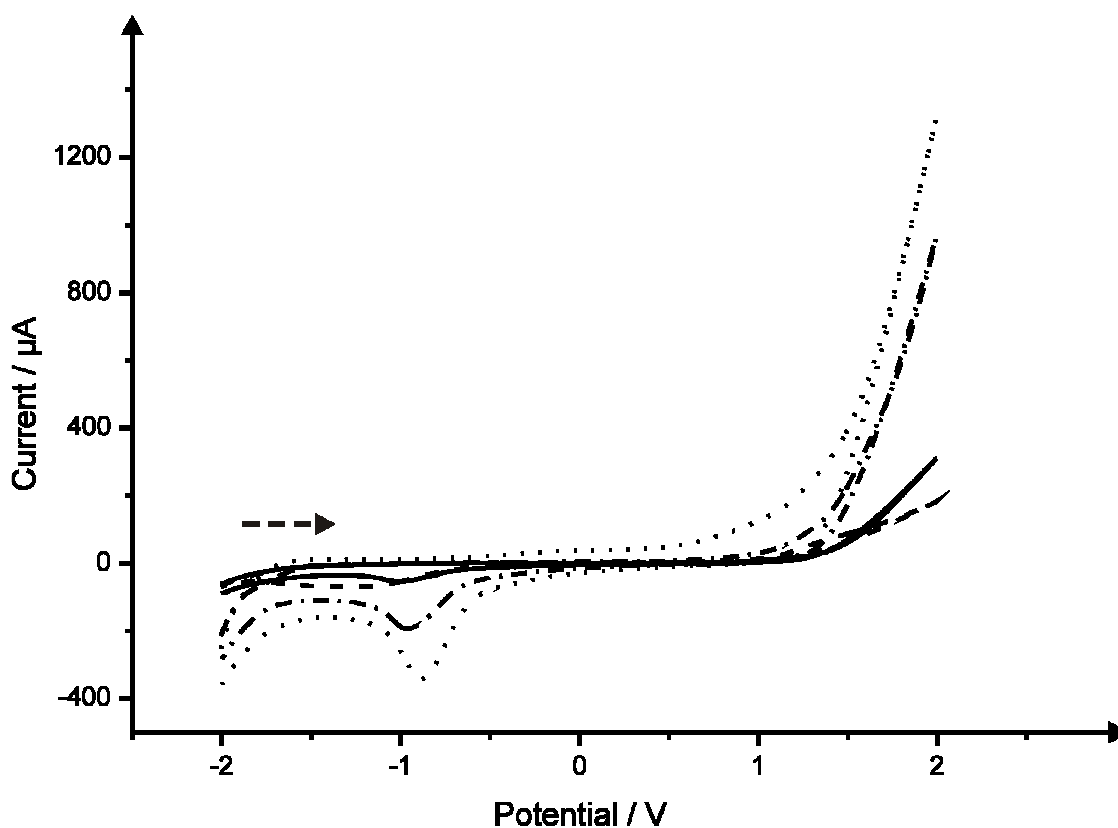


Figure 3.23 Cyclic voltammetric measurements obtained using the unmodified SPE (solid line), the SW-SPE (dashed line), DS-SW-SPE (dotted line) and the DS-MW-SPE (dot-dash line) in a pH 7.4 phosphate buffer solution. Scan rate: 100 mV s^{-1} . Dashed arrow signifies direction of scan.

Characterisation of the Screen Printed Single-Walled Carbon Nanotube Electrodes

Electrochemical characterisation was first carried out utilising well-established outer-sphere and inner-sphere redox probes, namely potassium ferrocyanide (II) and hexaammine-ruthenium (III) chloride respectively. Figure 3.24A depicts cyclic voltammograms obtained in 1 mM potassium ferrocyanide (II) / 0.1 M KCl studied at the SW-SPE over a range of voltammetric scan rates. Observation of voltammetric peak height, plotted as peak current (I_p) against square root of the applied scan rate over the range 10 – 400 mV s^{-1} was found to be linear ($I_p / \mu\text{A} = 1.82\mu\text{A}/(\text{V s}^{-1})^{1/2} + 0.49\mu\text{A}; R^2 = 0.98; N = 7$), suggesting a diffusional rather than a surface controlled process. Confirmation of the diffusional process dominating was compounded through cyclic voltammetric studies at the SW-SPE in 1 mM hexaammine-ruthenium (III) chloride / 0.1 M KCl from which a plot of peak current (I_p) against square root of the applied scan rate over the range 10 – 400 mV s^{-1} revealing a linear response ($I_p / \mu\text{A} = -2.54\mu\text{A}/(\text{Vs}^{-1})^{1/2} + 1.53\mu\text{A}; R^2 = 0.98; N = 7$). A plot of log scan rate versus log peak current at the SW-SPE was constructed confirming the presence of a semi-infinite diffusional process. Such a response indicates that the SW-SPE is not porous such that the contribution from thin-layer effects are realised.²³⁹

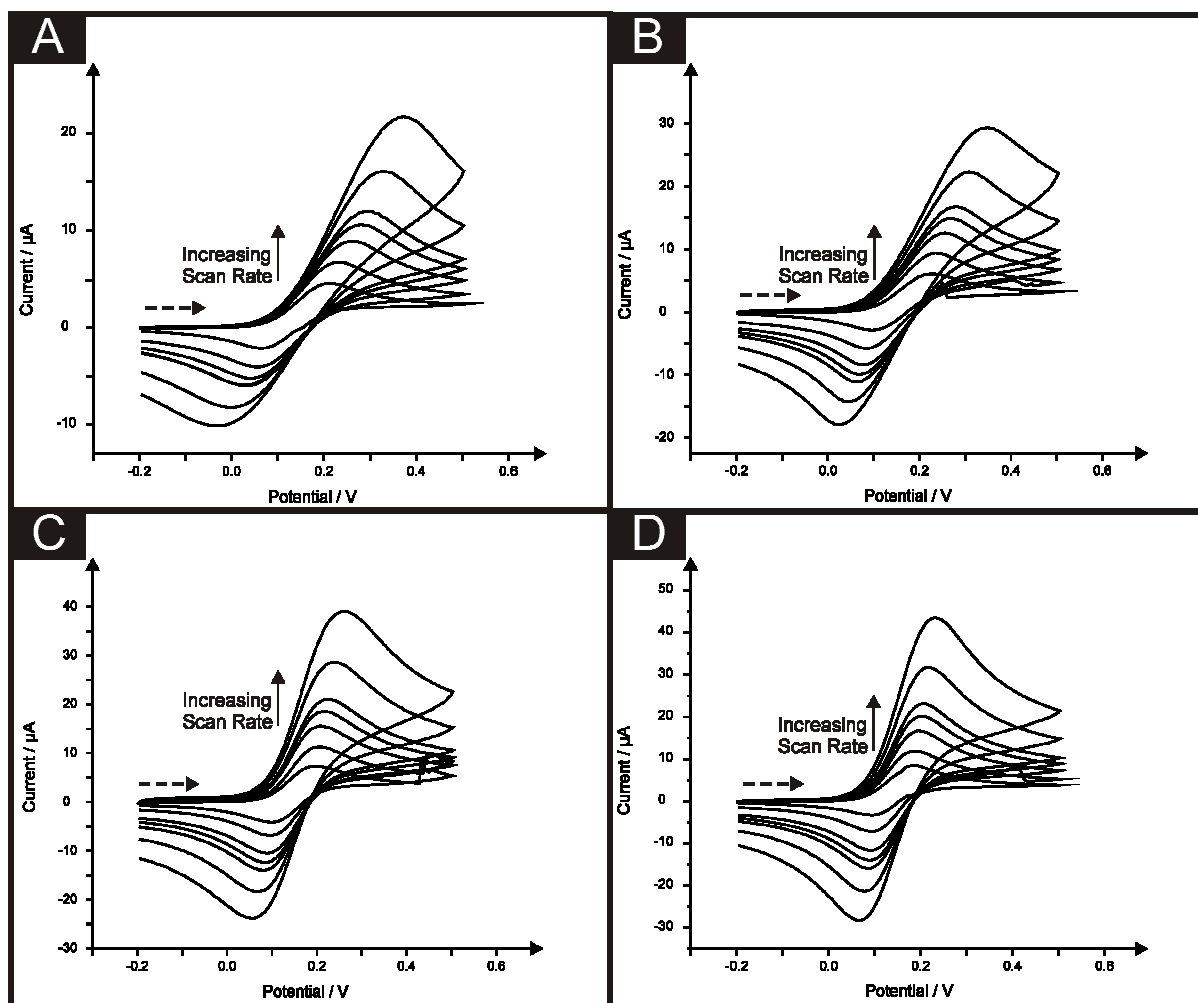


Figure 3.24 Typical cyclic voltammograms resulting from increasing scan rates in 1 mM potassium ferrocyanide (II) and 0.1 M KCl using (A) a standard SPE, (B) the SW-SPE, (C) the DS-SW-SPE and (D) the DS-MW-SPE. Scan rates: 10, 25, 50, 75, 100, 200, 400 mV s^{-1} . Dashed arrow signifies direction of scan.

The heterogeneous electron transfer rate constant, k^0 , was estimated at the SW-SPE and standard SPE when studied using the outer-sphere electron transfer probe potassium ferrocyanide (II). The Nicholson method is routinely used to estimate the observed standard heterogeneous electron transfer rate for quasi-reversible systems using equations (1.27 and 1.28) as is discussed in greater detail within Chapter 1. Using this approach, the heterogeneous electron transfer rate constant, k^0 of $1.1 \times 10^{-3} \text{ cm s}^{-1}$ was determined at the standard SPE comparing with a value of $1.4 \times 10^{-3} \text{ cm s}^{-1}$ deduced at the SW-SPE.

To impart further understanding of the role played by screen printed carbon nanotube based electrodes, electrochemical characterisation of commercially available carbon based screen printed carbon nanotube electrodes^{114114, 30} was also undertaken. Two types of commercially available electrodes were selected for use: Dropsens single-walled carbon nanotube screen printed electrodes (denoted throughout as DS-SW-SPE) and multi-walled carbon nanotube screen printed electrodes (denoted throughout as DS-MW-SPE). SEM images of these electrodes are presented in figure 3.25 along with EDAX analysis (figure 3.26). These commercially available carbon nanotube modified screen printed electrodes were first electrochemically characterised in the same manner as those fabricated in-house. Again the electrochemical redox probe potassium ferrocyanide (II) was utilised. As with the SW-SPE, a linear response ($I_p / \mu A = 1.31 \mu A / (V s^{-1})^{1/2} + 2.01 \mu A; R^2 = 0.97; N = 7$) through the plot of peak current (I_p) against square root of the applied scan rate over the range 10 – 400 $mV s^{-1}$ was determined at the DS-SW-SPE in 1 mM potassium ferrocyanide (II) / 0.1 M KCl (see figure 3.24C). A linear response was also achieved through the same plot using the DS-MW-SPE ($I_p / \mu A = 1.56 \mu A / (V s^{-1})^{1/2} + 2.57 \mu A; R^2 = 0.99; N = 7$) (figure 3.24D), providing confirmation of a diffusional process dominating. The gradient of a plot of log scan rate versus log peak current at the DS-SW-SPE and DS-MW-SPE which was constructed (gradients of 0.49 and 0.46 respectively) confirmed a semi-infinite diffusional process. Further to this, the electron transfer rate constant in potassium ferrocyanide (II) was also determined at the DS-SW-SPE and DS-MW-SPE to correspond to 9.3×10^{-3} and 5.5×10^{-2} $cm s^{-1}$ respectively. Clearly these exhibit more electrochemically reversible responses over that of the SW-SPE for the target analyte, likely due to the greater proportion of edge plane like-sites/defects residing on the carbon nanotubes used in the fabrication of the commercially available nanotube sensors.

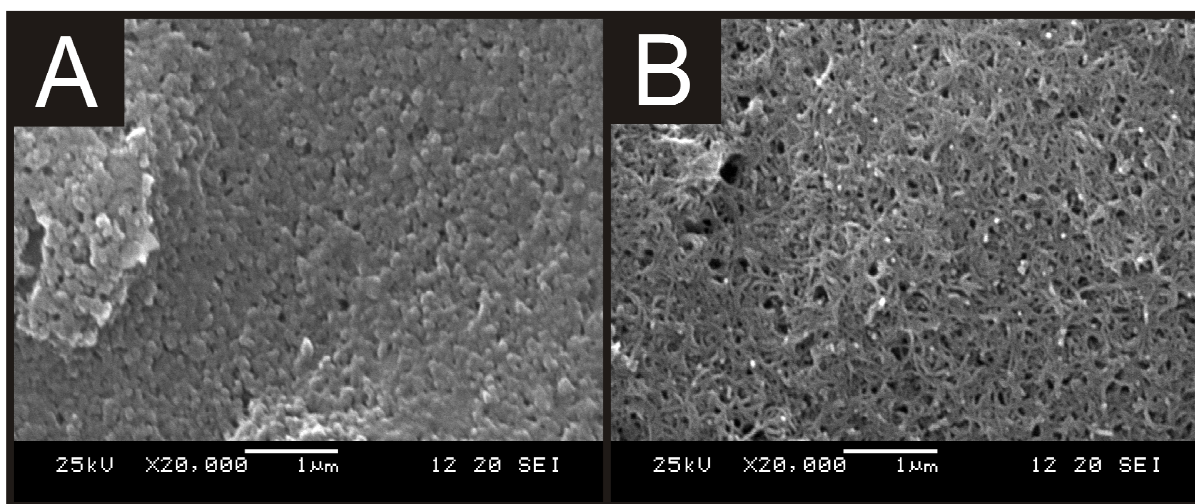


Figure 3.25 SEM analysis of the working electrode surface of the DS-SW-SPE (A) and DS-MW-SPE (B) at x20,000 magnification.

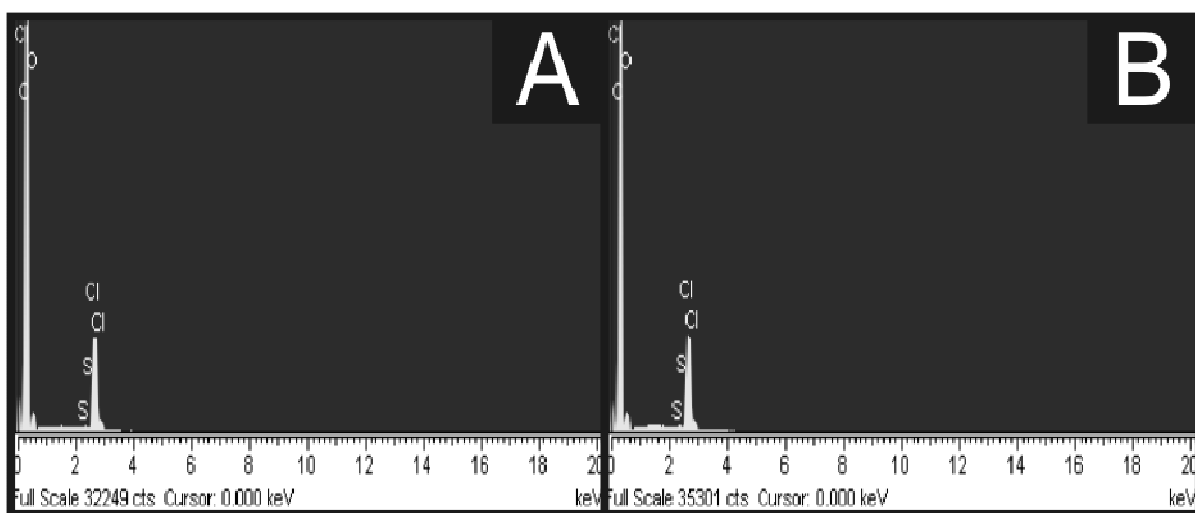


Figure 3.26 EDAX analysis of the working electrode surface of the DS-SW-SPE (A) and DS-MW-SPE (B). The DS-SW-SPE was determined (semi-quantitatively) to contain: 92.04 % carbon, 5.90 % oxygen, 2.01 % chlorine and 0.05 % sulphur, while the DS-MW-SPE was determined to contain: 92.36 % carbon, 5.56 % oxygen, 2.01 % chlorine and 0.07 % sulphur.

Next the fabricated sensors were electrochemically characterised using the electroactive analyte dopamine hydrochloride. First a solution of 600 μM dopamine hydrochloride / pH 7.4 phosphate buffer solution was used to explore the effect of scan rate upon the voltammetric response at the standard and SW-SPE. Scan rates over the range of 10 to 400 mV s^{-1} were selected with a linear response being determined at each of the sensors

(standard SPE: $I_p / \mu A = 1.87 \mu A / (V s^{-1})^{1/2} + 3.39 \mu A; R^2 = 0.99; N = 7$, SW-SPE: $I_p / \mu A = 2.07 \mu A / (V s^{-1})^{1/2} + 6.23 \mu A; R^2 = 0.99; N = 7$) suggesting a diffusional control process at each electrode surface. As depicted in figure 3.27, a peak-to-peak separation of 280 mV is found (scan rate: 100 mV s⁻¹) using the standard unmodified SPE, which is seen to reduce to 220 mV at the SW-SPE, suggesting that the presence of the single-walled carbon nanotubes produce a more electrochemically reversible response. Additionally, the SW-SPE is found to offer a greater peak height at a fixed dopamine hydrochloride concentration (600 μM) than that of a standard unmodified SPE at a given scan rate. Furthermore, inspection of figure 3.27 reveals that the Dropsens electrodes offer an improvement in the peak to peak separation over that of the SPE and SW-SPE with peak-to-peak separations of 57 and 60 mV for the DS-SW-SPE and DS-MW-SPE respectively. Also clearly depicted in figure 3.27 is the greatly improved peak current achieved when utilising the Dropsens electrodes compared to that of other sensors. Interestingly, comparison of the findings utilising the SPE and SW-SPE with the voltammetric response observed when using both the DS-SW-SPE and DS-MW-SPE highlights that a more electrochemically reversible response is observed by the commercially available Dropsens electrodes (*viz* figure 3.27). As with the SPE and SW-SPE, a linear response through the plot of square root of scan rate versus peak current was realised at both the DS-SW-SPE ($I_p / \mu A = 5.14 \mu A / (V s^{-1})^{1/2} + 0.51 \mu A; R^2 = 0.99; N = 7$) and DS-MW-SPE ($I_p / \mu A = 4.85 \mu A / (V s^{-1})^{1/2} + 3.16 \mu A; R^2 = 0.99; N = 7$). The effect of oxygenated species has been demonstrated for the sensing of dopamine hydrochloride indicating that carbonyl functionalities significantly dominate the electrochemical response, which likely accounts for the significant improvement in the response at the Dropsens sensors.²⁵⁶

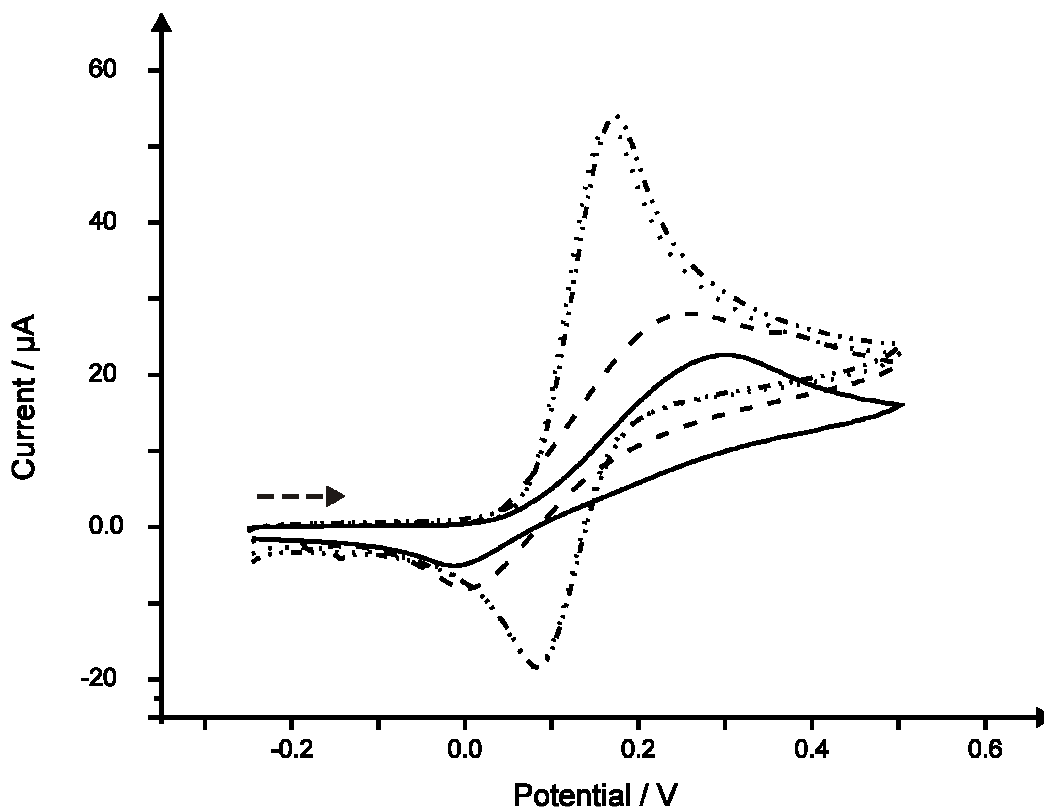


Figure 3.27 Typical cyclic voltammograms recorded in 600 μM dopamine in a pH 7.4 phosphate buffer solution at the unmodified SPE (solid line), SW-SPE (dashed line), DS-SW-SPE (dotted line) and DS-MW-SPE (dot-dash line). Scan rate: 100 mV s^{-1} . Dashed arrow signifies direction of scan.

Electroanalytical applications of the SWCNT-SPE

The electroanalytical applications of both the in-house fabricated unmodified carbon SPE, SW-SPE and the commercially available DS-SW-SPE and DS-MW-SPE were first explored towards the sensing of hydrazine. Hydrazine was selected as a model analyte due to its increasing importance and use within industrial systems including those relating to rocket fuels, corrosive inhibitors and the rapidly expanding fuel cell development.^{169, 170} Additionally, studies have demonstrated the substantial risks associated with hydrazine including its carcinogen and mutagenic effects but also neurotoxin capabilities.^{170, 171}

Initially, cyclic voltammetric measurements for the sensing of 1 mM hydrazine in a pH 7.4 phosphate buffer was observed at each of the screen printed sensors. Hydrazine was selected as it is highly active on metallic surfaces rather than that of carbon, thus allowing

metallic impurities to be observed.^{225, 226} As depicted in figure 3.28 the sensing of hydrazine is viable at each of the elected sensors. An improved peak current (I_p) is seen for the sensing of hydrazine upon the incorporation of a single-walled carbon nanotube layer (SW-SPE). The standard carbon SPE allows for the oxidation of hydrazine at a potential of $\sim + 1.08$ V (vs. Ag/AgCl) while the electrochemical oxidation is observed at the SW-SPE of $\sim + 1.05$ V (vs. Ag/AgCl). The effect of scan rate at using the screen printed sensors was determined in 1mM hydrazine / pH 7.4 phosphate buffer solution. Scan rates over the range of 10 to 400 mV s⁻¹ were selected with a linear response being determined at the standard SPE and carbon nanotube containing SW-SPE and commercially available DS-SW-SPE and DS-MW-SPEs through a plot of peak height (I_p) versus square root of scan rate (standard SPE: $I_p / \mu A = 3.20 \mu A / (V s^{-1})^{1/2} + 6.54 \mu A; R^2 = 0.95; N = 7$, SW-SPE: $I_p / \mu A = 3.37 \mu A / (V s^{-1})^{1/2} + 1.15 \mu A; R^2 = 0.98; N = 7$, DS-SW-SPE: $I_p / \mu A = 4.46 \mu A / (V s^{-1})^{1/2} + 1.23 \mu A; R^2 = 0.98; N = 7$ and DS-MW-SPE: $I_p / \mu A = 5.33 \mu A / (V s^{-1})^{1/2} + 4.71 \mu A; R^2 = 0.99; N = 7$) suggesting a diffusional control process at each.

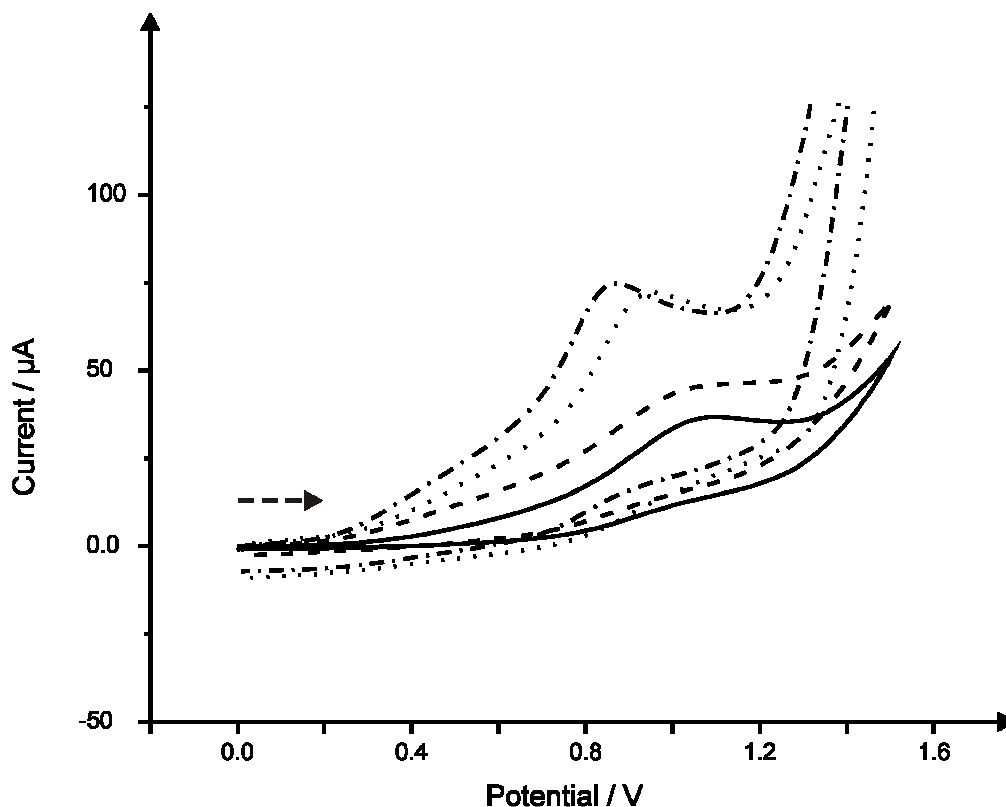


Figure 3.28 Typical cyclic voltammograms recorded in 1 mM hydrazine in a pH 7.4 phosphate buffer solution at the unmodified SPE (solid line), SW-SPE (dashed line), DS-SW-SPE (dotted line) and DS-MW-SPE (dot-dash line). Scan rate: 100 mV s^{-1} . Dashed arrow signifies direction of scan.

Interestingly the commercially available DS-SW-SPE offers an improvement for the oxidation of hydrazine through a reduction in the over-potentials as depicted in figure 3.28 where a voltammetric peak is observed at $\sim +0.9 \text{ V}$ (vs. Ag/AgCl) while the DS-MW-SPE exhibits a voltammetric peak at $\sim +0.8 \text{ V}$ (vs. Ag/AgCl). Although it would have originally been surmised that this enhanced electroanalytical performance was due to the presence of the carbon nanotubes, it could in fact be argued that the presence of a metallic impurities give rise to this improved voltammetry.²⁵⁷ Notably, it has previously been determined that the presence of a metal oxide, for example iron (II) oxide, could give rise to a reduction in the overpotential for the oxidation of hydrazine with electrochemical oxidation being observed at $\sim +0.4 \text{ V}$ (vs. SCE) in a pH 7.4 buffer.²³¹ EDAX analysis of the DS-MW-SPE and DS-SW-SPE (see figure 3.25) reveal the absence of any such metallic impurities. Thus it is likely that

the improvements are due to a greater proportion of edge plane like-sites/defects giving rise to the following order of electroactivity: DS-MW-SPE > DS-SW-SPE > SW-SPE > SPE.

Cyclic voltammetric measurements were then undertaken at increasing concentrations of hydrazine made into a pH 7.4 phosphate buffer solution over the range of 100 to 1000 μM at each of the screen printed electrodes. Figure 3.29 depicts the resulting calibrations plots for the addition of hydrazine at each of the screen printed electrodes (note error bars were not included as to avoid confusion on the detailed plot). When determining the effect of the presence of carbon nanotubes upon the screen printed electrodes fabricated in-house it is clear that little improvement in sensitivity ($I_p / \mu\text{A} = 3.64 \times 10^{-2} \mu\text{A} / \mu\text{M} + 1.61 \mu\text{A}; R^2 = 0.99; N = 10$) is offered at the SW-SPE over that of a standard SPE ($I_p / \mu\text{A} = 3.05 \times 10^{-2} \mu\text{A} / \mu\text{M} - 2.99 \mu\text{A}; R^2 = 0.98; N = 10$). An improvement is however observed through utilisation of the Dropsens electrodes with the DS-SW-SPE ($I_p / \mu\text{A} = 5.03 \times 10^{-2} \mu\text{A} / \mu\text{M} + 0.81 \mu\text{A}; R^2 = 0.9850; N = 10$) resulting in a greater peak height per given concentration of hydrazine over the in-house fabricated sensors (standard SPE and SW-SPE), with the DS-MW-SPE ($I_p / \mu\text{A} = 7.18 \times 10^{-2} \mu\text{A} / \mu\text{M} - 6.78 \mu\text{A}; R^2 = 0.96; N = 10$) yielding a further improvement. The determined limits of detection (using 3σ in line with section 1.1.11) for hydrazine were 92.9 μM , 53.7 μM , 31.6 μM and 40.1 μM at the standard SPE, SW-SPE, DS-SW-SPE and DS-MW-SPE respectively.

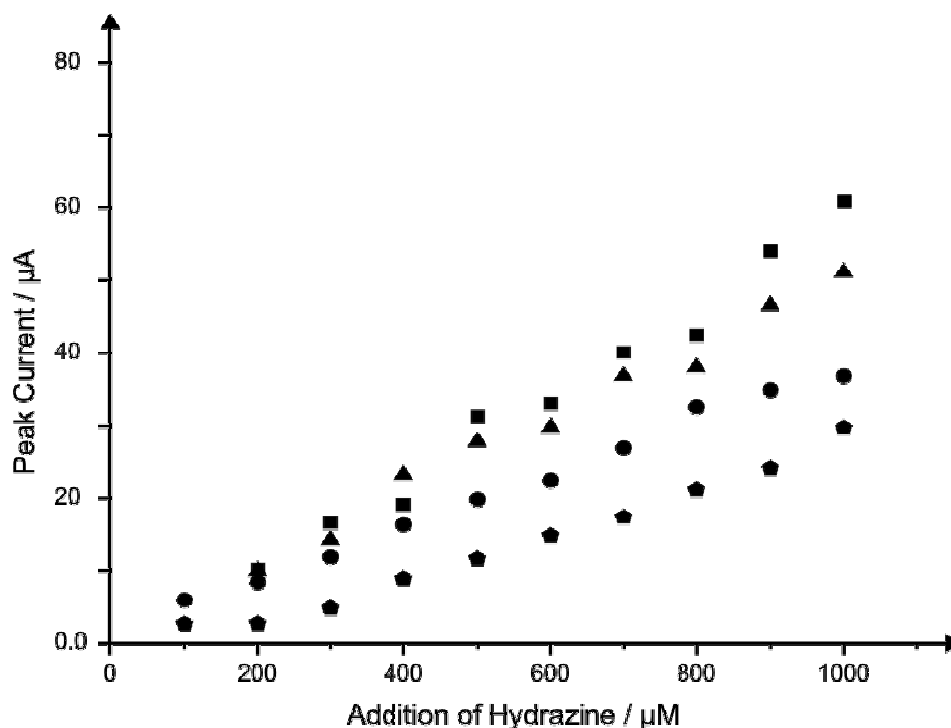


Figure 3.29 Typical calibration plots arising from additions of hydrazine (100 – 1000 μM) into a pH 7.4 phosphate buffer solution at the unmodified SPE (pentagons), SW-SPE (circles), DS-SW-SPE (triangles) and DS-MW-SPE (square).

The final model analyte selected for the investigation was capsaicin. Capsaicin belongs to the family of capsaicinoids, the main reason for the sharp flavour of hot peppers.²⁵⁸ The capsaicinoid family consists of around 11 components such as capsaicin and dihydrocapsaicin which are responsible for about 90% of the pungency flavour in hot peppers.²⁵⁹ Capsaicinoids also possess some biological properties that are thought to be beneficial for human health.²⁶⁰⁻²⁶² They have high antioxidant power,²⁶³ in addition to anti-tumoral,²⁶⁴ anti-mutagenic,^{265, 266} antibacterial^{267, 268} and anti-carcinogenic^{264, 269} properties to name but a few. Additionally they have also exhibited protective effects against cholesterol²⁷⁰ and obesity,²⁷¹ two of the most topical human health aspects today. Additionally they have been widely used as pain-inducing ingredients in the well-known “pepper spray” used by law enforcement officers. It has also been shown that an electrochemical chilli sensor is possible to be able to quantify the ‘heat’ of chilli peppers.^{272, 273}

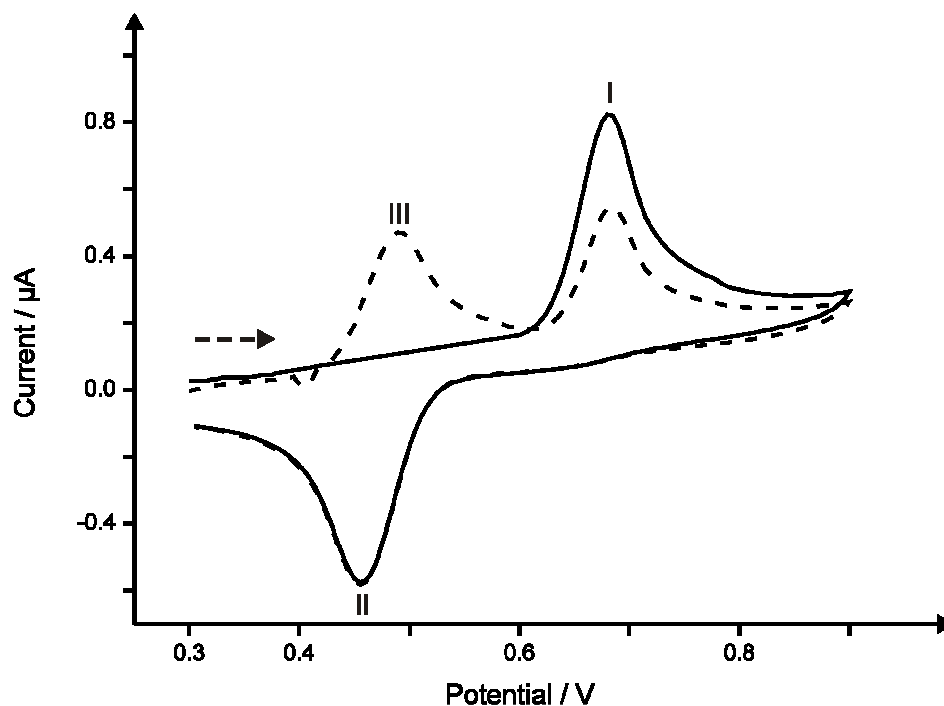
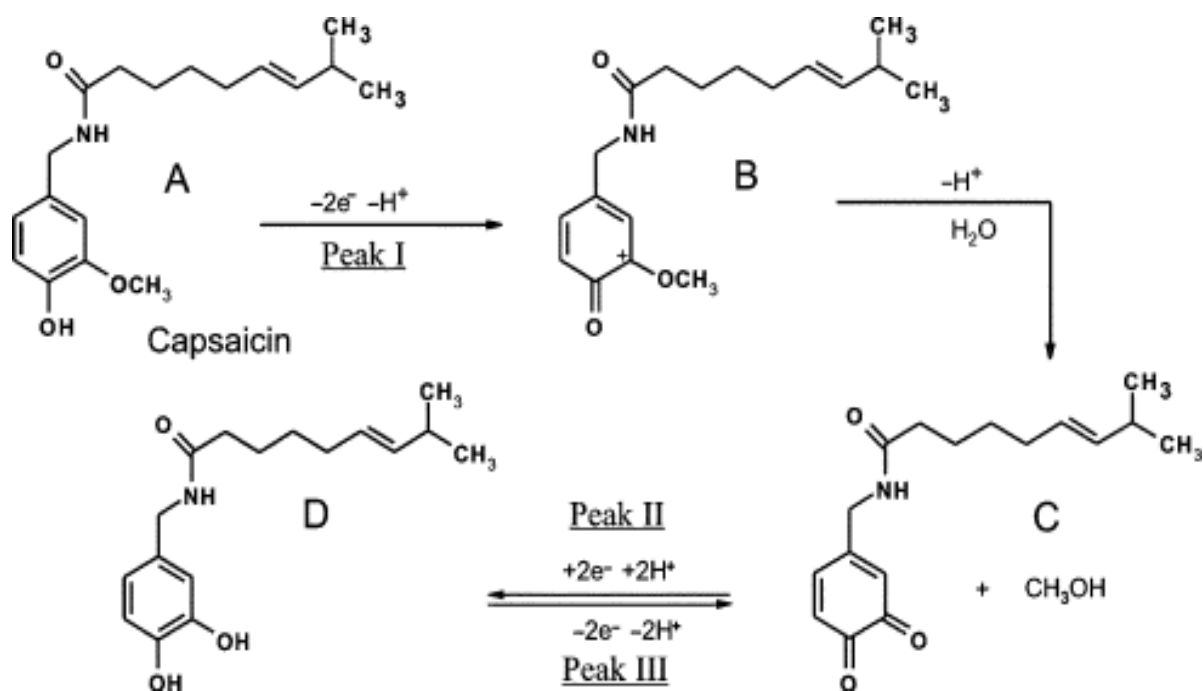


Figure 3.30 The first (solid line) and second (dashed line) scans using cyclic voltammetry at $5 \mu\text{M}$ capsaicin in a pH 1 buffer using the standard SPE. Scan rate: 100 mV s^{-1} . Dashed arrow signifies direction of scan.

The electroanalytical sensing of capsaicin was first studied using a concentration of $5 \mu\text{M}$ in a pH 1 buffer. A buffer of pH 1 was selected as Compton *et al* demonstrated that the peak height of greatest magnitude was observed at this pH value.²⁴⁷ As is clear in figure 3.30, two oxidation peaks at $+0.48 \text{ V}$ (*vs.* Ag/AgCl) and $+0.67 \text{ V}$ (*vs.* Ag/AgCl) with a single reduction peak at $+0.48 \text{ V}$ (*vs.* Ag/AgCl) over the potential range studied are apparent at the standard, unmodified SPE upon the first cycle. It is important to note that upon the first cycle, the oxidation peak at a potential of $+0.67 \text{ V}$ (*vs.* Ag/AgCl) is much greater in magnitude compared with that at $+0.48 \text{ V}$ (*vs.* Ag/AgCl). The subsequent second scan revealed a change in the ratio of peak current for the two oxidation peaks with the oxidation peak at $+0.48 \text{ V}$ (*vs.* Ag/AgCl) becoming more sharp, defined and greater in magnitude whilst in contrast the oxidation peak at $+0.67 \text{ V}$ (*vs.* Ag/AgCl) was seen to decrease in peak height.



Scheme 3.1 Proposed mechanism for the electrochemical oxidation/reduction of capsaicin.²⁴⁷

Compton *et al* suggest the mechanism for the electrochemical oxidation and reduction of capsaicin²⁴⁷ is as depicted in scheme 3.1 where upon the first scan, the electrochemical oxidation of capsaicin is coupled with an irreversible homogeneous chemical step. This results in the hydrolysis of the 2-methoxy group to form an o-benzoquinone unit²⁴⁷ in the structure of capsaicin. Finally, as suggested within scheme 3.1, the o-benzoquinone part of the capsaicin falls in a redox electrochemical process with catechol (C and D)²⁷⁴⁻²⁷⁶ which are observed as peaks II and III as shown in figure 3.30.²⁴⁷ Compton *et al* utilised these voltammetric responses using adsorption stripping voltammetry to facilitate the detection of capsaicin.²⁴⁷

Next explored was the effect of the accumulation time of the capsaicin upon the observed voltammetric responses, as the electrochemistry of capsaicin has been reported previously to proceed *via* an adsorptive stripping voltammetry mechanism.²⁴⁷ It is clear in figure 3.31 that the observed peak currents associated with the redox behaviour of capsaicin are larger after a 5 minute accumulation period than that of zero accumulation.

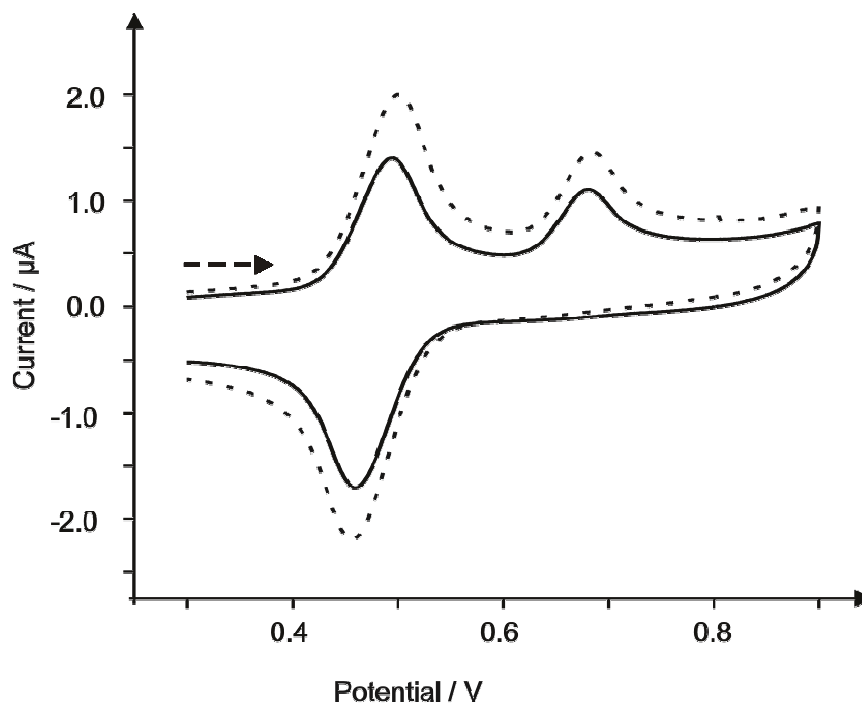


Figure 3.31 The effect of accumulation time upon the observed voltammetric profiles. Scan rate: 50 mV s^{-1} . Dashed arrow signifies direction of scan.

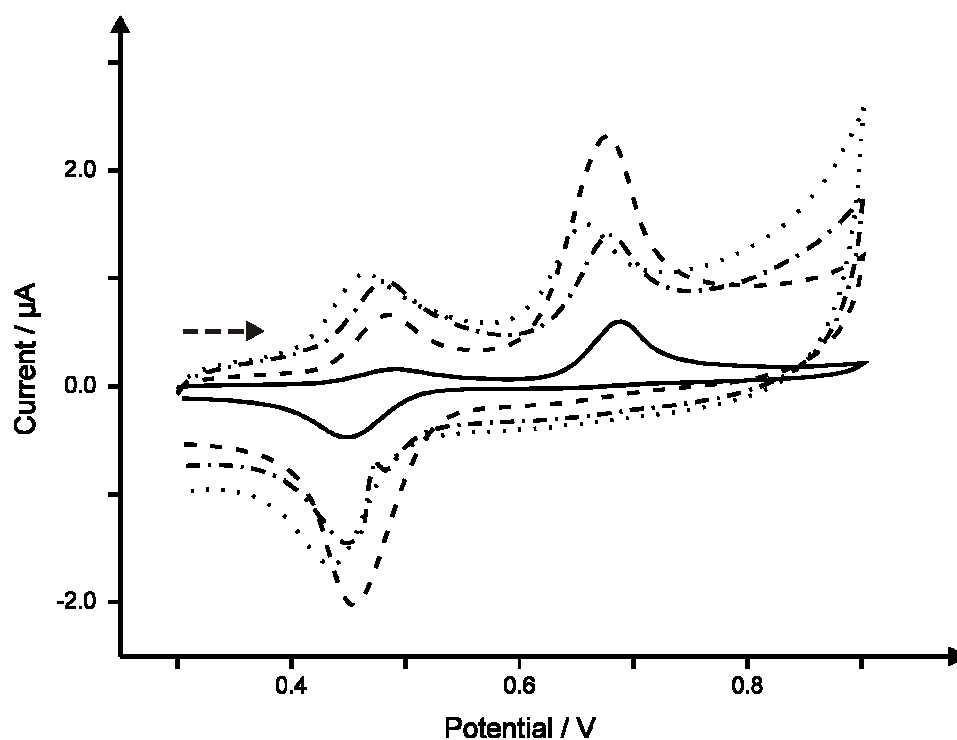


Figure 3.32 Typical cyclic voltammograms obtained in $35 \mu\text{M}$ capsaicin in a pH 1 buffer solution at an unmodified SPE (solid line), the SW-SPE (dashed line), DS-SW-SPE (dotted line) and the DS-MW-SPE (dot-dash line). Scan rate: 100 mV s^{-1} . Dashed arrow signifies direction of scan.

Figure 3.32 depicts an overlay of typical cyclic voltammograms for the first scan obtained in 35 μM capsaicin / pH 1 buffer obtained at a standard, unmodified carbon based SPE and the carbon nanotube-based sensors. Evidently, at each of the electrodes utilised there are two clear oxidation peaks along with the single reduction peak. Notably however, peaks I, II and III (see scheme 3.1) occur at a consistent potential when utilising the standard SPE, yet, a shift in peak potential is noted upon the introduction of carbon nanotubes with a shift to a more electronegative potential for each of the peaks when utilising the SW-SPE and DS-MW-SPE. A further reduction in the peak potential is noted upon measurement of capsaicin using the DS-SW-SPE. In addition to the reduced overpotential achievable at the carbon nanotube modified sensors over the standard SPE there is also a clear relationship between the resulting peak current and presence of the carbon nanotubes within the sensors. When studied at a fixed concentration of 5 μM capsaicin, the SW-SPE was found to offer the greatest improvement in the form of peak current and well defined shape for each of the oxidation and reduction peaks. Although the DS-MW-SPE and DS-SW-SPE offer an improved peak current in comparison with the standard SPE the resultant peaks from the oxidation of capsaicin are much smaller in observed current than that when utilising the SW-SPE. It was noted that only a slight improvement in peak current can be distinguished between the DS-SW-SPE and DS-MW-SPE with the former offering a slightly improved peak current of the two.

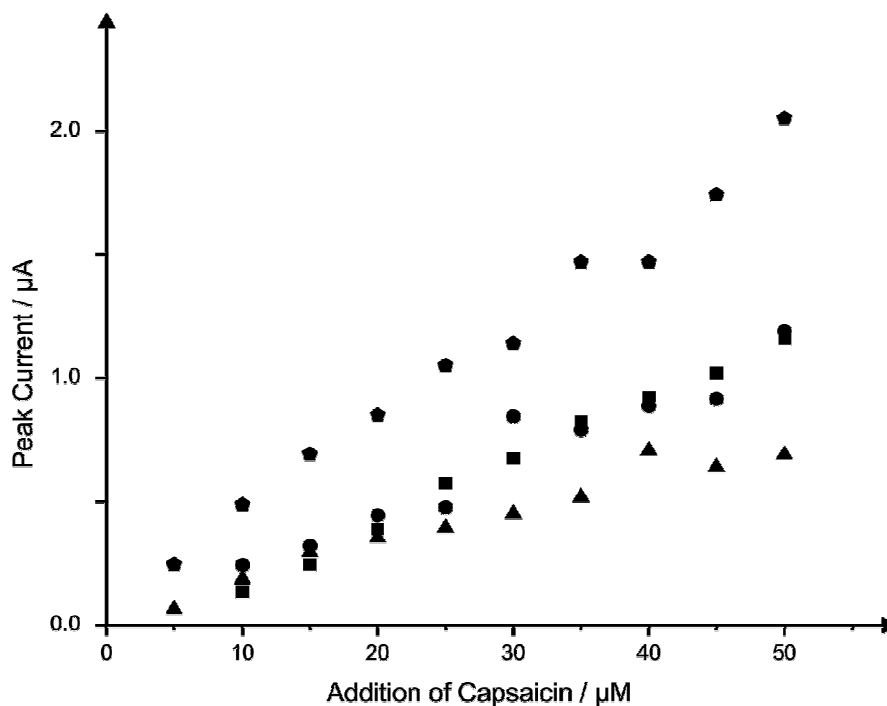


Figure 3.33 Typical calibration plots for the addition of capsaicin (5 – 50 μM) at a standard carbon screen printed sensor (triangles), SW-SPE (pentagons), DS-SW-SPE (circles) and DS-MW-SPE (squares) upon the first cyclic voltammetric scan. The peak height is recorded using the oxidation peak (Peak I; see figure 3.30). Scan rate: 100 mV s⁻¹.

Electroanalytical studies over a range of capsaicin concentrations utilising the three sensors was next explored. Additions of capsaicin over the range of 5 to 50 μM were made into a pH 1 buffer and tested at the standard SPE along with the SW-SPE and the DS-SW-SPE and DS-MW-SPE. Figure 3.33 shows typical calibration plots obtained utilising each of the sensors (note, once more error bars were omitted from these plots to avoid confusion of the complex figure). Evidently, the sensing of capsaicin is achievable at each of the sensors over the analytical range selected, though an improvement in the sensitivity of the analytical protocol was observed at the carbon nanotube-based sensors (standard SPE:

$$I_p / \mu A = 1.13 \times 10^{-2} \mu A / \mu M + 4.99 \times 10^{-2} \mu A; R^2 = 0.96; N = 10,$$

SW-SPE:

$$I_p / \mu A = 3.73 \times 10^{-2} \mu A / \mu M + 9.20 \times 10^{-2} \mu A; R^2 = 0.98; N = 10,$$

DS-SW-SPE:

$$I_p / \mu A = 2.25 \times 10^{-2} \mu A / \mu M + 3.01 \times 10^{-3} \mu A; R^2 = 0.94; N = 10,$$

DS-MW-SPE:

$I_p / \mu A = 2.61 \times 10^{-2} \mu A / \mu M - 1.19 \times 10^{-1} \mu A$; $R^2 = 0.98$; $N = 10$). Clearly the greatest peak current per given concentration is noted when utilising the SW-SPE, which exhibits an improved peak current in comparison with the other screen printed sensors over the entire range studied. The limits of detection (using 3σ in line with section 1.1.11) corresponding to each of the three sensors over the analytical range were calculated to be 4.8 μM , 1.9 μM , 2.88 μM and 4.39 μM for the standard SPE, SW-SPE, DS-SW-SPE and DS-MW-SPE respectively. Clearly the trend of electrochemical activity is SW-SPE > DS-SW-SPE > DS-MW-SPE > SPE indicating that the SW-SPE provides a more beneficial response. It is likely that the single-walled carbon nanotubes within the SW-SPE and DS-SW-SPE allow the adsorption of the capsaicin on the nanotube walls which is in agreement with Compton *et al* who reported that capsaicin adsorbs onto basal plane sites.²⁴⁷

3.3.3 CONCLUSIONS

A novel screen printed single-walled carbon nanotube sensor has been fabricated from a single-walled carbon nanotube ink printed upon a flexible plastic (polyester) substrate. The sensor is benchmarked against graphitic screen printed electrodes and commercially available single- and multi- walled carbon nanotube sensors towards analytically important targets. In particular, the use of the single-walled screen printed sensor fabricated in-house permits the low micromolar level sensing of capsaicin which could potentially be used as an electrochemical chilli sensor. These single-walled screen printed sensors allow researchers to be able to transfer laboratory-based experiments in to the 'field' through use of these reproducible and potentially mass produced sensors.

This novel work has since been further expanded by other research scientists in the Banks Group to explore the potential utilisation of the fabricated sensors for the determination of capsaicin in real chilli samples extracted from chillies and chilli sauces

utilising both cyclic voltammetry and electrochemical impedance spectroscopy.²⁷⁷ The work continued to explore different types of screen printed carbon nanotube electrodes, namely single- and multi- walled carbon nanotubes, finding that they are technique-specific: for the case of low capsaicin concentrations, single-walled carbon nanotube screen printed electrodes are found to be preferable; yet for the case of electrochemical impedance spectroscopy at high capsaicin concentrations, multi-walled carbon nanotube screen printed electrodes are preferable, based upon analytical responses.²⁷⁷

In this Chapter efforts are made to determine the true boundaries of screen printing technology using electrode design to facilitate improved electroanalytical performance through intuitive working electrode design which enables diffusion control. Previous Chapters have considered the applicability of standard co-planar screen printed electrodes of 3 mm in diameter (working electrode) and their potential applications into analytical protocols both unmodified (graphite) and modified using a range of materials.

As has been described in greater detail within Chapter 1 working electrode geometries differing to the traditional co-planar macro electrode has been of key interest within the field of electrochemistry, both fundamentally and in regards to the potential applications of such electrodes. Of those described within the literature, two electrode configurations have gained most interest: the micro electrode and recessed electrodes. Such electrodes are generally fabricated through the use of an inert material such as glass, which encases a metal wire of the desired material. Although such electrodes offer geometries in the micrometer range, typically 100 μm or less they are often expensive and time consuming to produce with vigorous electrode preparation (polishing) required before and between use. As such, herein described are different electrode geometries fabricated entirely through the use of screen printing technology with the sensors potentially offering comparative attributes to their traditional counterparts whilst also offering the previously documented benefits of sensors produced through screen printing.

4.1 RECESSED ELECTRODES: CAN SCREEN PRINTING TECHNOLOGY FACILITATE THE DEVELOPMENT OF NOVEL ELECTRODE GEOMETRIES?

This section is comprised of published work^[4] within which the development and utilisation, for analytical purposes, of a graphite-based disc-shaped recessed electrode fabricated entirely through screen printing techniques. Attempting to build further upon the findings of earlier Chapters and sections, in addition to the graphite-based sensor, platinum-based sensors are also fabricated allowing direct comparisons with not only existing literature, but also previous work described within this Thesis. Finally the effect of the recessed electrode geometry will also be investigated through the development of a novel pentagon-shaped recessed electrode; a design difficult to produce using traditional wire-based techniques.

4.1.1 INTRODUCTION

Electrochemists are forever exploring new approaches to improve mass transport of the target analyte towards the electrode surface which consequently influences the observed electrochemical response. One such approach to improve mass transport is to use microelectrodes which have unique features of high mass flux, low ohmic drop, steady-state currents and minimal stirring dependence characteristics which are highly important with regard to the development of practical electrochemical sensors.²⁷⁸

The advantages offered by an electrochemical sensor which incorporates a microelectrode and consequently steady-state behaviour are: greater analytical sensitivities, increased current densities, and improved signal-to-noise ratios⁶¹ which ultimately lead to enhancements in the electroanalytical performance towards the target analyte.^{62, 279} Various approaches have been reported for the fabrication of microelectrodes such as

⁴ J. P. Metters, F. Tan, R. O. Kadara and C. E. Banks, *Anal. Methods*, 2012, **4**, 3140.

photolithography and sealing wires within glass. Another approach is the screen printing of microelectrodes which have the advantage of reproducibility, simplicity and ability to produce *en mass* at a low production cost; recently, Kadara and co-workers have reported the fabrication of screen printed microelectrodes, producing microelectrodes with radii of 60 to 100 μm .⁷⁰

Related to microelectrodes are recessed electrodes, which reach steady-state responses faster than their co-planar counterparts due to the confinement of the diffusion layer by the recess.^{60, 103, 279} Thus it is easier and faster to achieve a sigmoidal response at a recessed microelectrode configuration over a coplanar microelectrode configuration which has the same disc size and geometry.²⁸⁰ Varying fabrication approaches have been reported for the fabrication of recessed electrodes. One approach towards screen printed microelectrode arrays has reported the coating of screen printed electrodes with polymeric films. These are then subjected to sonochemical ablation producing a random ensemble of microelectrodes, albeit with a large size distribution,²⁷⁹ which are also irregularly shaped and distorted which is likely to hamper the reproducibility between sensors from the same batch.^{64, 281} Another approach is the screen printing of a carbon layer onto which an inert material is placed, which is laser ablated to produce micron sized holes which expose the underlying screen printed carbon surface.⁶⁵ However, problems may be encountered between sealing the patterned material to the carbon layer leading to leakages of the solution media resulting in loss of microelectrode behaviour and giving irreproducible results within and between batches. Other approaches involve patterning inert material *in situ* but this can change the microstructure of the underlying carbon surface, ultimately affecting the electrochemical performance of the sensor. Note in these examples, since the dielectric (inert polymer) layer defines the working electrode geometry, shallow recessed electrodes will be realised. As noted above, this can provide beneficial enhancements in mass transport.

Consequently, in this section the fabrication of carbon based shallow recessed screen printed electrodes, one disc shaped with a working electrode of 250 μm radii, the other a pentagon with a working electrode width of 50 μm where in both configurations the screen printed dielectric (inert polymer) layer defines the working electrode geometry are described. The shallow recessed screen printed electrodes were first optically and electrochemically characterised, and consequently trialled towards the detection of two key analytes of interest, NADH and nitrite. It is demonstrated that this can be extended to other electrodes of various surface materials, such as in the case of platinum disc shaped shallow recessed screen printed electrodes which are explored towards the sensing of analytically useful analytes. The concept could easily be extended to other metallic surfaces such as gold, palladium, copper and so-on, and is only limited by the availability of commercially available inks.

4.1.2 EXPERIMENTAL

All chemicals used were of analytical grade and were used as received without any further purification and were obtained from Sigma-Aldrich. The specific chemicals utilised relevant to the analysis described within this Chapter included: sodium nitrite, β -nicotinamide adenine dinucleotide, hydrazine hydrate, manganese (II) chloride tetrahydrate, acetaminophen and potassium dichromate. All solutions were prepared with deionised water of resistivity not less than 18.2 Ω cm. All solutions (unless stated otherwise) were vigorously degassed with nitrogen to remove oxygen prior to analysis. Additionally all solutions contained 0.1 M KCl acting as an electrolyte, unless otherwise stated.

Voltammetric measurements were carried out using a Palmsens (Palm Instruments BV, The Netherlands) potentiostat. All measurements were conducted using a screen printed three electrode configuration consisting of a carbon-graphite geometric working electrode area of 250 μm radii; both the carbon disc-shaped and platinum disc-shaped shallow recessed

screen printed electrodes (denoted throughout as drSPE/PtdrSPE respectively) or 50 μm in width with respect to the pentagon-shaped shallow recessed screen printed electrode (denoted throughout as prSPE), carbon-graphite counter electrode and Ag/AgCl reference.

Screen printed recessed electrodes

Screen printed recessed electrodes were fabricated in-house with appropriate stencil designs using a microDEK 1760RS screen-printing machine (DEK, Weymouth, UK). The critical operating parameters of the screen printing machine consisted of print and flood speeds of 92 mm/s and 96 mm/s respectively, a print gap of 0.88 mm and printing pressure of 8.0 Kg. The screen meshes utilised for each of the layers comprising the sensors were sourced from MCI Screens Ltd¹¹² with the design parameters including a mesh number of 77/195 cm/inch, mesh material of: polyester, mesh opening of 77 μm and a mesh thread diameter nominal: 48 μm . The squeegees utilising for each of the printed layers were positioned at an angle of 60° comprising a straight edged, polyurethane 60 durometer blade.

A carbon–graphite ink formulation (Product Code: C2000802P2; Gwent Electronic Materials Ltd, UK) was first screen printed onto a polyester flexible film (Autostat, 250 micron thickness). This layer was cured in a fan oven at 60 degrees for 30 minutes. Next a silver/silver chloride reference electrode was included by screen printing Ag/AgCl paste (Product Code: C2040308D2; Gwent Electronic Materials Ltd, UK) onto the plastic substrate. Last a dielectric paste ink (Product Code: D2070423D5; Gwent Electronic Materials Ltd, UK) was printed to cover the connection and define the carbon–graphite working electrode, and the resultant recessed surface. After curing at 60 degrees for 30 minutes the screen printed electrode is ready to use. The platinum disc-shaped screen printed recessed electrodes were made in the same fashion using a platinum polymer paste comprising dendritic platinum (83 – 87 %) with particles sizes in the low micrometers range

(Product Code: C2050804D9; Gwent Electronic Materials Ltd, UK) in place of the previously utilised carbon–graphite ink formulation.

Screen printed microelectrode array

Screen printed microelectrode arrays were fabricated in the same manner as the screen printed recessed electrodes described above though utilising different screen designs and comprised a carbon-graphite working and counter electrodes (Product Code: C2000802P2; Gwent Electronic Materials Ltd, UK) and silver/silver chloride reference electrode (Product Code: C2040308D2; Gwent Electronic Materials Ltd, UK) with the connections defined once more through the utilisation of a non-conductive dielectric paste (Product Code: D2070423D5; Gwent Electronic Materials Ltd, UK). The gold screen printed microelectrode array was made in the same fashion using a gold polymer paste comprising dendritic gold (83 – 87 %) with particles sizes in the low micrometers range (Gwent Electronic Material Ltd, UK) in place of the previously utilised carbon-graphite ink formulation.

Screen printed microband electrodes

The 100 μm width carbon-graphite screen printed microband electrodes were fabricated as is described for the screen printed recessed electrodes comprising a carbon-graphite working and counter electrodes (Product Code: C2000802P2; Gwent Electronic Materials Ltd, UK) and silver/silver chloride reference electrode (Product Code: C2040308D2; Gwent Electronic Materials Ltd, UK) with the connections defined once more through the utilisation of a non-conductive dielectric paste (Product Code: D2070423D5; Gwent Electronic Materials Ltd, UK). In the case of the gold-based screen printed microband electrodes, the carbon-graphite ink was substituted with a gold polymer paste consisting of a

mixture of powder and dendritic gold with particles size in the range of low micrometres (82 % gold) (Product Code: C2041206P2; Gwent Electronic Materials Ltd, UK).

For the case of the 50 μm microband electrodes different printing parameters were selected for the application of the carbon-graphite/gold layer due to the intricate nature of the fine width of the microband. The critical operating parameters of the screen printing machine consisted of print and flood speeds of 80 mm/s and 96 mm/s respectively, a print gap of 0.88 mm and printing pressure of 8.0 Kg. The screen meshes utilised for this layer comprising the sensors was sourced from MCI Precision Screens Ltd¹¹² with the design parameters including the use of a newly devised V-mesh 330-023 (discussed in greater detail within section 4.4.2) with a mesh material of polyester, mesh opening of 54 μm and a mesh thread diameter nominal of 23 μm . The squeegees utilising for each of the printed layers were positioned at an angle of 60° comprising a straight edged, polyurethane 70 durometer blade.

Canal water was sampled at the edge of the canal bank (Rochdale Canal, Oxford Road, Manchester, UK) and collected in a polycarbonate bottle which was washed three times with canal water before being taken back to the laboratory. The sample was stored at room temperature and used within a day of sampling and was simply modified to either pH 7 using a phosphate buffer or acidified with H_2SO_4 to a concentration of 0.05 M before electroanalytical measurements were commenced depending on the analyte being studied.

Scanning electron microscope (SEM) images and surface element analysis were obtained with a JEOL JSM-5600LV model having an energy-dispersive X-ray microanalysis package.

4.1.3 RESULTS AND DISCUSSION

Disc-shaped shallow screen printed recessed electrodes

Disc-shaped recessed screen printed electrode (drSPE) were first fabricated as described in the Experimental section (5.1.2), by primarily printing a carbon layer with contacts and contact pad onto a plastic substrate (see figure 4.1A). Following curing in an oven, an insulating dielectric layer was screen printed over the initial carbon layer. The dielectric (inert polymer) defines the microelectrode size exposing the screen printed carbon surface below. The advantage of this technique over previous reports is that the dielectric is cured in the oven which allows efficient bonding of the insulating dielectric to the underlying carbon surface. Note that an additional carbon counter and a silver/ silver chloride reference electrodes are also incorporated onto this electrochemical sensing platform for ease of use (see figure 4.1A). Figure 4.1 shows the overall configuration of the drSPE forming the single-shot, disposable 3 electrode system, consisting of a carbon recessed working electrode ($250 \pm 6 \mu\text{m}$ radius), carbon counter electrode and silver/silver chloride reference electrode, which are all housed upon the same sensor. Figure 4.1B is an optical microscope image obtained at the drSPE which shows that a well-defined recessed electrode is present, though it is also clear that some migration of the non-conductive dielectric layer occurs during fabrication resulting in a non-uniform disc shape. Also presented in figure 4.1C is the SEM image obtained at the carbon based drSPE examining the working electrode area depicting a typical carbon-graphite structure as previously reported.¹⁰⁴ Since the dielectric defines the working electrode's geometry, the resulting electrode is naturally recessed with a depth of 4 microns, as reported similarly by Kadara *et al* for a screen printed recessed array.⁶⁸

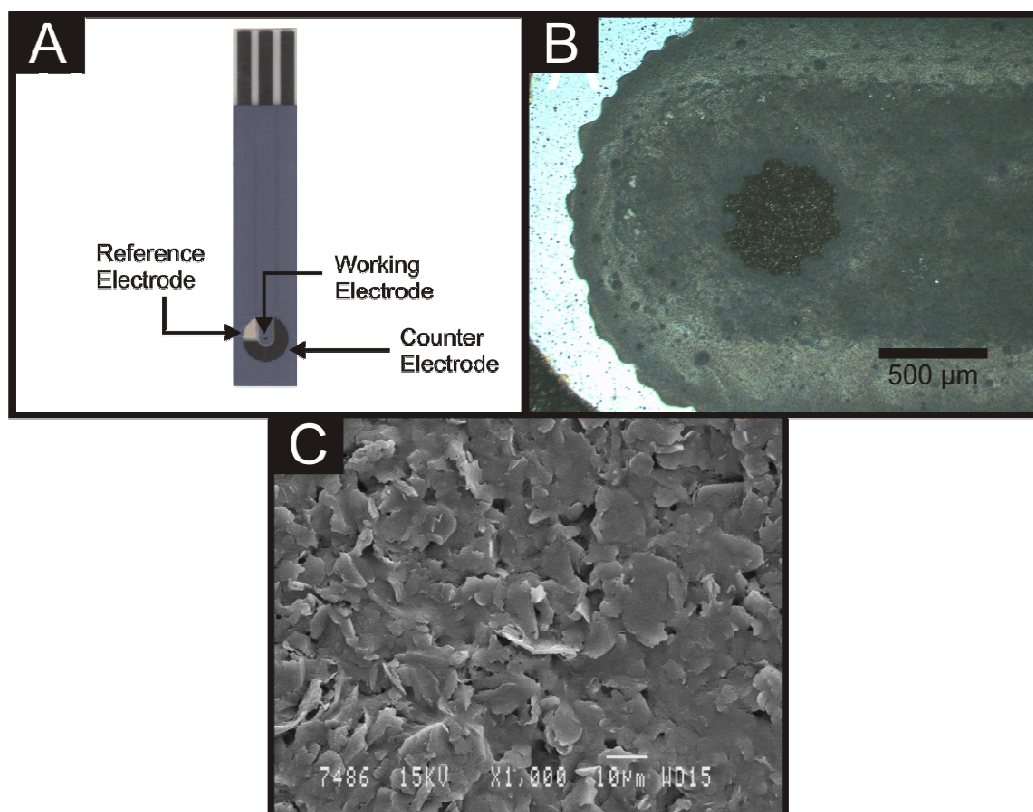


Figure 4.1.1 A single recessed screen printed electrode (drSPE; working area: 500 μm) (A), an image of the drSPE obtained using an optical microscope (x5 magnification) (B), SEM analysis of the drSPE working electrode at x 1000 magnification (D).

Electrochemical characterisation of the rSPE's was carried out using the common redox probe hexaammine-ruthenium (III) chloride. First, the effect of scan rate in 1 mM hexaammineruthenium (III) chloride was studied at the drSPE as shown in figure 4.2, where it is readily evident that at slow scan rates a steady-state type response is observed where upon faster scan rates, the voltammetric profile becomes peak shaped. Such responses are expected at a shallow recessed electrode where steady-state behaviour is reached faster than their non-recessed counterparts due to confinement of the diffusion layer by the recess.²⁸² In addition the effect of scan rate (*viz* figure 4.2) through observation of the voltammetric peak height, plotted as peak current (I_p) against square root of the applied scan rate over the range 5 – 200 mV s^{-1} was found to be linear

($I_p / \mu A = -0.0269 \mu A / (V s^{-1})^{1/2} + 1.0737 \mu A$; $R^2 = 0.98$; $N = 7$) confirming a diffusional process. The expected limiting current (I_L^{Recess}) at a shallow recessed electrode can be estimated from:^{283, 284}

$$I_L^{Recess} = 4nFD C \left(\frac{r^2}{4L + \pi r^2} \right) \quad (4.1)$$

where, n is the number of electrons involved in the redox reaction, F and D represent the Faraday constant and the diffusion coefficient ($9.1 \times 10^{-6} \text{ cm}^2 \text{ s}^{-1}$)²⁸⁵⁻²⁸⁷ respectively, r the radius of the microdisc (cm), C the bulk concentration (mol cm^{-3}) and L is the depth of the electrode recession (cm). The theoretically expected current observed at the drSPE can be estimated from equation (4.1) to correspond to $1.46 \mu A$ which agrees well with the experimentally observed value in 1 mM hexaammine-ruthenium (III) chloride in 0.1 M KCl of $7.69 \mu A$ (at 5 mV s^{-1}). Experimentally the limiting current for the recessed sensors was measured as the current at which the exponential increment in the voltammetric current began to plateau producing a peak-like formation. The slight deviation between the experimental and calculated value is likely due to the electrode geometry being departed from that of a true microelectrode.

Another useful approach is to explore the concept of fabricating recessed microelectrode arrays.²⁷⁹ During the fabrication process, the electrodes are produced upon a single sheet and are individually cut prior to use. One approach is to cut these in such a way that, say, three recessed electrodes are kept together to form a single sensor strip which comprises three recessed electrodes in an array. The potential application of an array comprising differing numbers of the drSPE ($N = 3$ and 5) was explored, initially through the characterisation of the arrays once again in 1 mM hexaammine-ruthenium (III) chloride to allow for comparison. Little improvement (peak current) was observed through the implementation of an array of increasing working electrode numbers in terms of current

density plots. In order for the array to function properly, that is, ensure diffusional interaction between working electrodes is negligible, a minimum geometric distance between working electrodes is required, defined as $d_{required}$,²⁸²

$$d_{required} = 10.86 + 6.218 \exp\left(-\frac{L + 0.0888}{0.222}\right) + 9.435 \exp\left(-\frac{L + 0.0888}{0.492}\right) \quad (4.2)$$

where $L = L_{recess} / r$ and where L is in the range $0 \leq L \leq 5$. Thus, the $d_{required}$ is found to correspond to 22.35, where $d_{required}$ is measured in units of r , resolving the $d_{required}$ to be 5.59 mm. In the experimental case of the recessed screen printed electrode, the centre-to-centre distance corresponds to 6 mm which is not significantly larger than $d_{required}$, the minimum distance between working electrodes, and hence an overlap of the diffusional zones of each of the shallow recessed working electrodes occurs which is in line with the experimental observations herein. Another approach would be to ‘miss-out’ every other working electrode, but the overall sensor size would then become excessive. Consequently, the decision was made to utilise the single drSPE only for further electroanalytical applications.

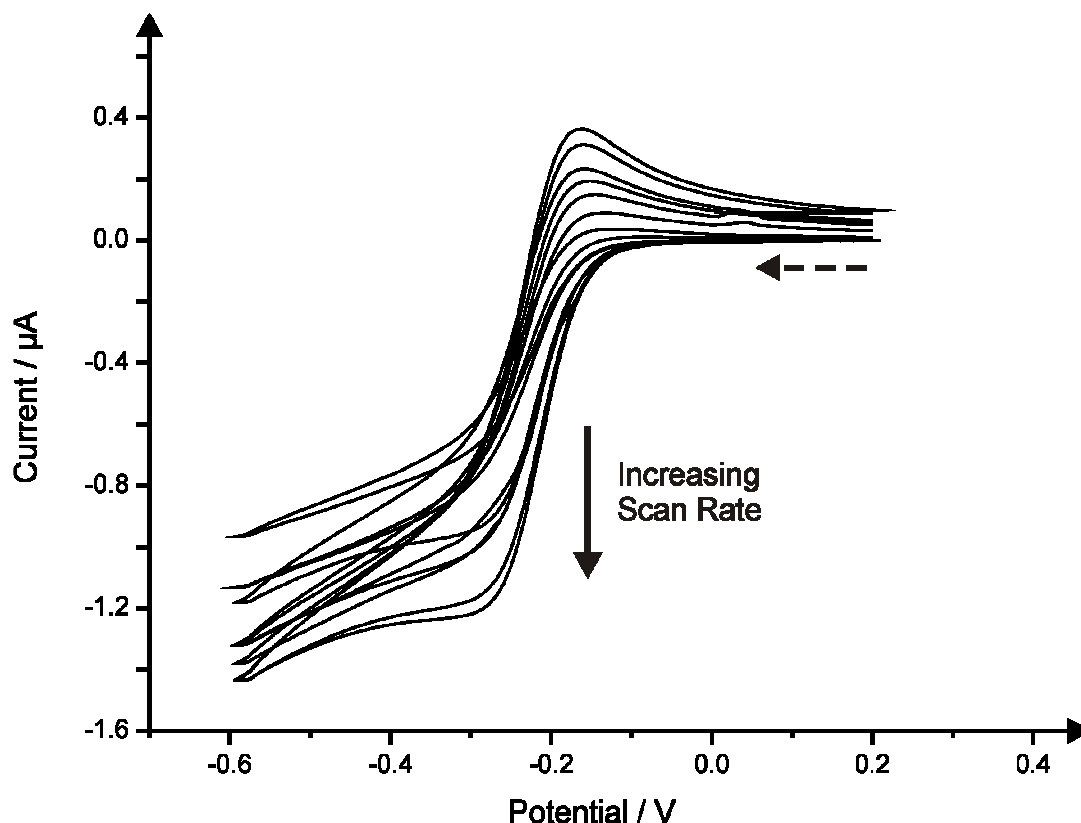


Figure 4.2 Typical cyclic voltammetric responses observed through scan rate studies using the drSPE in 1 mM hexammine-ruthenium (III) chloride/ 0.1 M KCl. Scan rates: 5 – 400 mV s^{-1} . Dashed arrow signifies direction of scan.

Explored next was the utilisation of the drSPE towards the sensing of the key analyte NADH; an analyte of great interest because it is used prolifically as the basis of over 300 biosensors.²⁸⁸⁻²⁹¹ For example, NADH-dependent dehydrogenases catalyse the oxidation of compounds such as ethanol and lactic acid.²⁹² The electroanalytical sensing of NADH *via* its oxidation (see scheme 4.1) was first explored with cyclic voltammetry using the drSPE. Figure 4.3 depicts typical cyclic voltammetric responses resulting from additions of NADH into a solution of pH 7 phosphate buffer over the range 10 to 90 μM . Clearly an oxidation wave is observed upon addition of NADH into the phosphate buffer at $\sim +0.45$ V (vs. Ag/AgCl). Note that a wave is observed at the drSPE rather than a well-defined peak which is commonly observed at co-planar electrodes due to the change in mass transport

characteristics occurring at the drSPE. Upon increasing concentration of NADH using the drSPE an increase in the peak height (nA) for the oxidation of NADH (+ 0.45 V (vs. Ag/AgCl)) can be observed over the entire analytical range whilst demonstrating linearity ($I / \mu A = 4.73 \times 10^{-4} \mu A / \mu M - 3.09 \times 10^{-3} \mu A; R^2 = 0.99; N = 9$) throughout (see figure 4.3B).

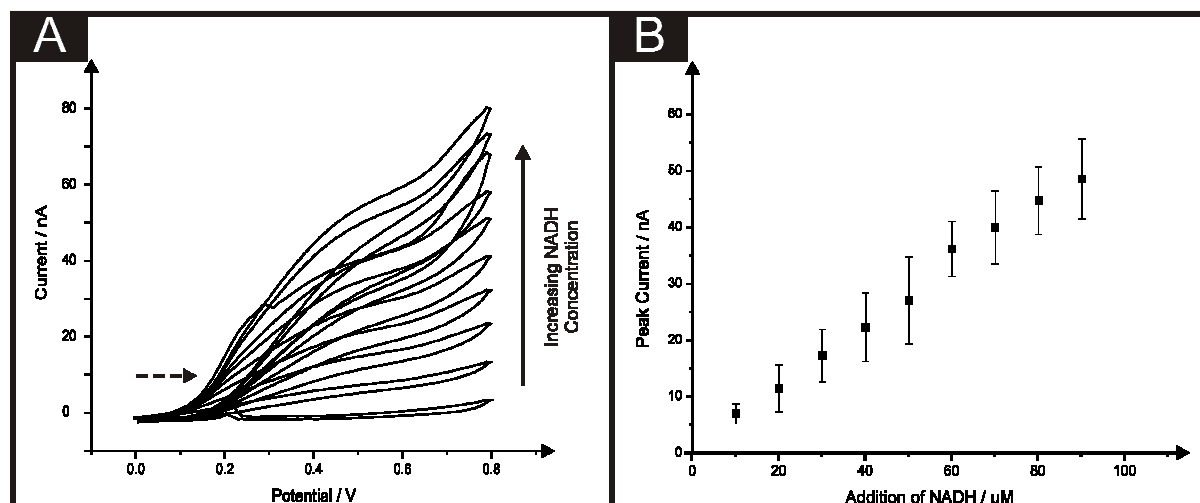
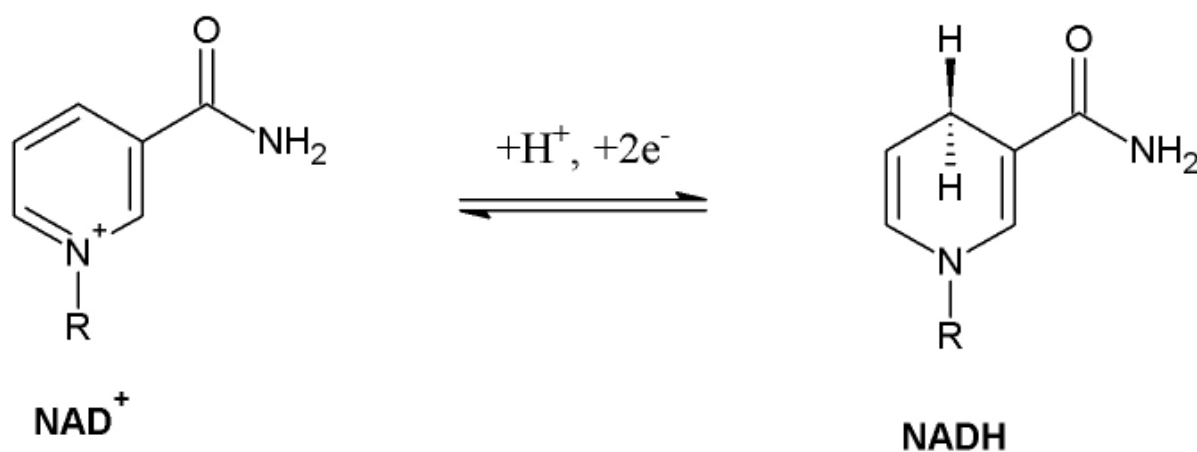


Figure 4.3 Typical cyclic voltammetric responses (A) and the corresponding calibration plot (B) resulting from additions over the range 10 to 90 μM of NADH into a phosphate buffer (pH 7) using the drSPE. Scan rate: 50 mV s^{-1} . Dashed arrow signifies direction of scan.

The response obtained for the detection of NADH was further compared and contrasted towards that of a more traditional graphite based screen printed co-planar macro electrode, with a working electrode area of 3 mm in diameter (previously reported in references ^{103, 104} and ²⁹³), over the previously studied analytical range (10 to 90 μM) using current density plots. As is shown in figure 4.4, a comparison of current density plots for the drSPE and traditional macro electrode demonstrates the much greater current per cm^2 realised at the drSPE opposed to that obtained at the more traditional co-planar macro electrode. Note, current density plots were constructed utilising the geometric area of the working electrodes allowing benchmarking of the sensors, however, if available, detailed surface analysis would allow for a more definitive working electrode area to be deduced (see Section 6.2

Suggestions For Future Work). Comparison of the slopes for the two contrasting calibration plots for the sensing of NADH provides an insight into the much improved sensitivity towards the detection of NADH offered through the utilisation of the drSPE, with typical slopes obtained for the drSPE and traditional macro electrode being 6.6 and $2.42 \times 10^{-4} \mu\text{A M}^{-1}$ respectively. Due to the changes in mass transport arising at the recessed sensor, an improvement by a factor of ~ 1.5 in the sensitivity is realised with such values demonstrating the drSPE's enhanced efficiency per area of electrode in comparison to that of the traditional macro electrode.



Scheme 4.1 Proposed mechanism for the electrochemical oxidation/reduction of β -nicotinamide adenine dinucleotide.

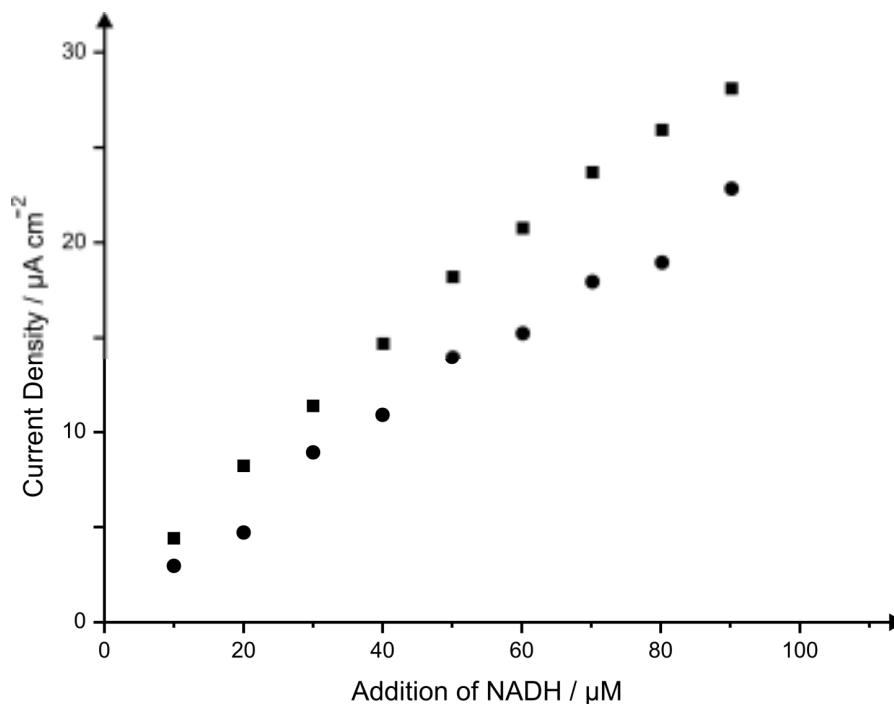


Figure 4.4 An overlay of typical current density calibration plots resulting from cyclic voltammetric measurement of additions of NADH into a phosphate buffer over the range of 10 to 90 μM using the drSPE (squares) versus a standard 3 mm diameter co-planar SPE (circles).

Returning to the drSPE, the limit of NADH detection (using 3σ in line with section 1.1.11) at the drSPE was determined to correspond to 5.2 μM . Such a detection limit highlights the analytical applicability of the drSPE, when compared to previous studies utilising differing electrode configurations, for example chemically reduced graphene oxide modified glassy carbon electrode has been used for the sensing of NADH with a reported limit of detection of 10 μM .²⁹⁴ A detailed listing of NADH detection at various electrode configurations has been recently compiled.²⁹⁵ Although many of the reported techniques do offer lower limits of NADH detection, it is worth noting that it is also a requirement that laborious pre-treatment and preparation of the electrodes is often required, a hurdle negated through the use of the drSPE.

Upon finding that the drSPE offered competitive limits of detection for the sensing of NADH, and furthermore, improved sensitivity over a traditional macro electrode, the

applicability of the drSPE towards analytical sensing of nitrite was undertaken. The excess uptake of nitrite can cause gastric cancer²⁹⁶ and it is therefore necessary to develop a reliable and sensitive sensor to detect nitrite in food, drinking water and environmental samples. Several techniques have been developed for nitrite determination, including spectrophotometry,²⁹⁷ chemiluminescence,²⁹⁸ chromatography²⁹⁹ and capillary electrophoresis.³⁰⁰ However, these methodologies usually have tedious detection procedures and therefore are time-consuming. Compared to these methods, the electrochemical methods can provide cheaper, faster and real-time analysis and thus have attracted more attention.³⁰¹

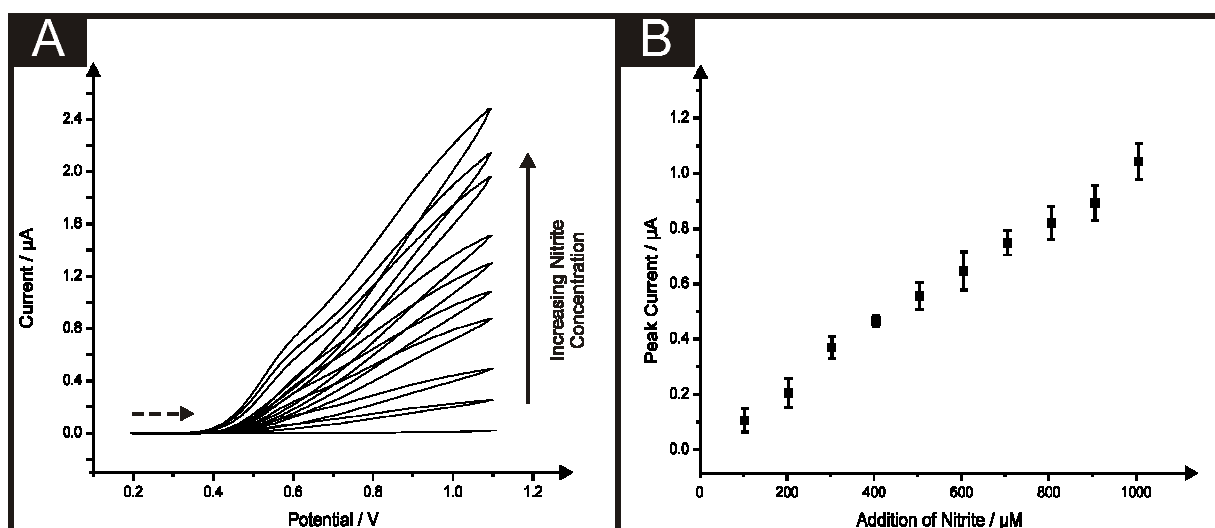


Figure 4.5 Typical cyclic voltammetric responses (A) and the corresponding calibration plot (B) resulting from additions of nitrite into a phosphate buffer (pH 7) using the drSPE; additions were made over the range 100 to 1000 μM . Scan rate: 50 mV s^{-1} . Dashed arrow signifies direction of scan.

As is clear from figure 4.5, cyclic voltammetric measurement of nitrite added to a pH 7 phosphate buffer at the drSPE results in an oxidation wave at $\sim +0.6$ V (vs. Ag/AgCl). Consequently the sensing of nitrite over the range 100 to 1000 μM in a pH 7 phosphate buffer was trailed at a drSPE; pH 7 was selected for analysis as it is the most likely pH value in which nitrite sample would be encountered.³⁰² Figure 4.5 shows typical cyclic voltammograms for the sensing of nitrite over the analytical range, with the corresponding

calibration plot ($I/\mu A = 1.2 \times 10^{-3} \mu A/\mu M - 1.46 \times 10^{-2}$; $R^2 = 0.99$; $N = 10$). As is evident excellent linearity is possible through the utilisation of the drSPE over the entire analytical range.

The sensing of nitrite at both the drSPE and a traditional macro screen printed sensor was compared and contrasted through the comparison of current density plots for both electrodes resulting from additions of nitrite over the range 100 to 1000 μM . As shown in figure 4.6, a comparison of current density plots for the drSPE and traditional macro electrode demonstrates the much greater current per cm^2 realised at the drSPE opposed to that obtained at the more traditional macro electrode. Once more, comparison of the slopes for the two contrasting calibration plots for the sensing of nitrite provides an insight into the vastly improved sensitivity towards the detection of nitrite offered through the utilisation of the drSPE with typical slopes obtained for the drSPE and traditional macro electrode being 0.5 and $3.49 \times 10^{-7} \mu A M^{-1}$ respectively. Such values demonstrate the drSPE's enhanced efficiency per area of electrode in comparison to that of the traditional co-planar macro electrode. The limit of detection (using 3σ in line with section 1.1.11) for nitrite using the drSPE within this phosphate buffer solution was determined to equate to 7.28 μM . Previously, composite copper electrodes modified with carbon powder and epoxy resin have been utilised for the sensing of nitrite, with a limit of detection claimed to be 600 nM.³⁰³ Other reports such as that by Chen *et al*³⁰⁴ utilising a nano diamond powder electrode state a nitrite limit of detection of 120 μM . Again it has been noted that, as with the sensing of NADH, lower limits of detection have been reported at other electrode configurations, for example 0.05 μM at a glassy carbon modified with $CuPtCl_6$ film.³⁰⁵

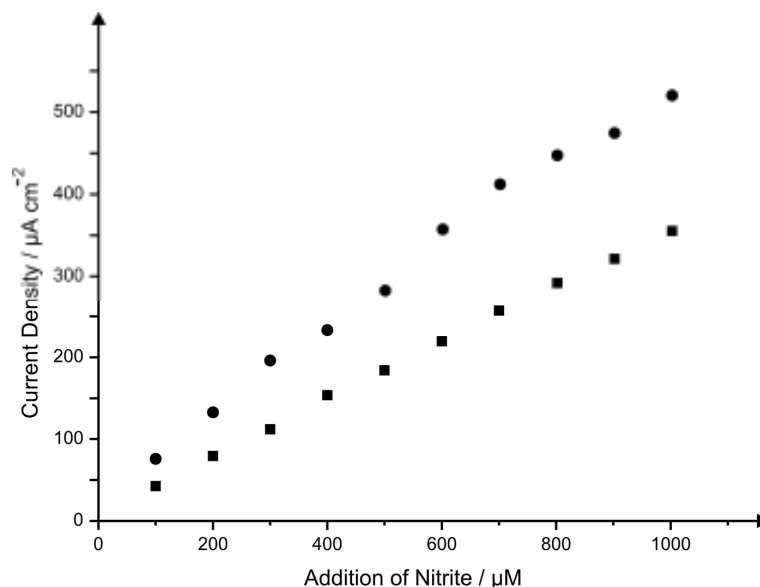


Figure 4.6 An overlay of typical current density calibration plots resulting from cyclic voltammetric measurement of additions of nitrite into a phosphate buffer over the range of 100 to 1000 μM using the drSPE (circles) versus a standard 3 mm diameter SPE (squares).

Next the feasibility of the analytical protocol towards the accurate determination of nitrite within a true environmental sample was determined. Additions of nitrite, over the range 100 to 1000 μM , were made into a canal water sample (collected and prepared as detailed within the Experimental section (5.1.2)) with cyclic voltammetric measurements made. This range was chosen since this is the range utilised within production of the ‘ideal’ calibration plots (see figure 4.6) and as such allowed useful insights into the effect upon sensor performance when utilising a different sample media. As is evident through the corresponding calibration plot for the sensing of nitrite in a canal water sample ($I/\mu\text{A} = 2.807 \times 10^{-1} \mu\text{A}/\mu\text{M} + 13.864 \mu\text{A}; R^2 = 0.99; N = 10$; see figure 4.7) which is compared with a typical calibration recorded in ‘ideal’ conditions, a reduction in the sensitivity of the sensor occurs, likely thought to be due to contaminants present within the sample; such as bio-organisms which may potentially foul the electrode surface. Although it has been ascertained that there is a reduction in the sensitivity of the sensor when applied to

the determination of nitrite in canal water samples, the detection of nitrite within the environmental sample was still possible over the entire range studied, with a limit of detection (using 3σ in line with section 1.1.11) for nitrite within the canal water sample corresponding to $43.6 \mu\text{M}$.

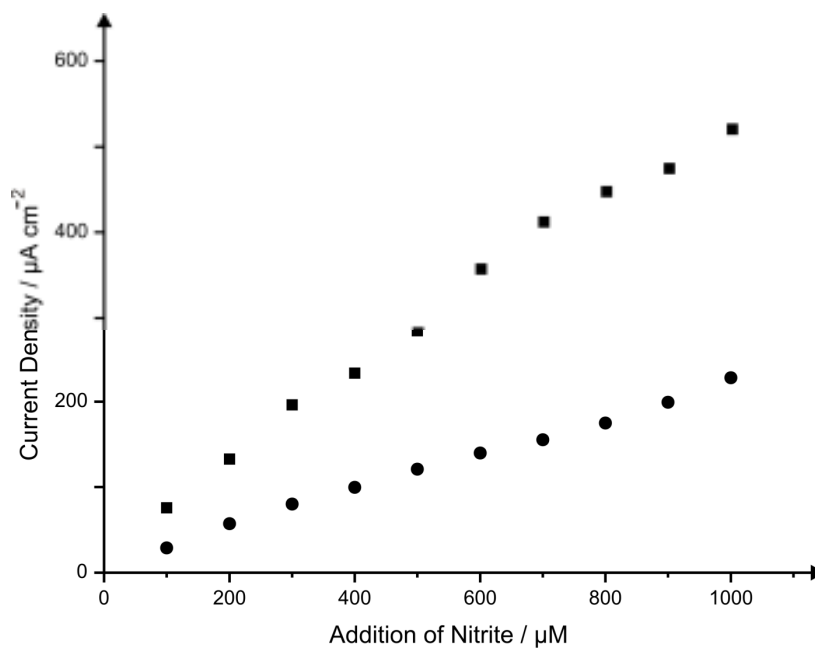


Figure 4.7 An overlay of typical current density calibration plots resulting from cyclic voltammetric measurement of additions of nitrite into a phosphate buffer (squares) and a canal water sample (circles) over the range of 100 to 1000 μM using the drSPE.

Platinum disc-shaped screen printed shallow recessed electrodes

To further explore the potential applications of the shallow recessed screen printed electrodes, further drSPE were fabricated utilising a platinum polymer paste as the working electrode (as described in the Experimental section (5.1.2)). The platinum drSPE (denoted throughout as Pt drSPE), of the same form as the carbon based drSPE, were utilised for the detection of two analytes of great interest; hydrazine and hydrogen peroxide. As has been described earlier within Chapter 3 these two key analytes have been investigated through utilisation of a platinum based macro screen printed electrode (PtSPE);³⁰⁶ thus consequential

studies at the PtdrSPE would allow definitive comparisons between the two electrodes to determine if the recessed electrode possessed beneficial characteristics.

The PtdrSPEs were first electrochemically characterised using the redox probe potassium hexachloroiridate (III). Firstly, scan rate studies were performed using the PtdrSPE in 1 mM potassium hexachloroiridate (III) in 0.1 M KCl (see figure 4.8), where observation of voltammetric peak height, plotted as peak current (I_p) against square root of the applied scan rate over the range 5 – 200 mV s^{-1} was found to be linear ($I_p / \mu\text{A} = 3.37 \times 10^{-2} \mu\text{A}/(\text{V s}^{-1})^{1/2} + 2.89 \times 10^{-1} \mu\text{A}; R^2 = 0.98; N = 8$) confirming a diffusional process. Again sigmoidal responses are observed at slow scan rates, with peak-shaped responses at faster scan rates as seen previously at the drSPE.

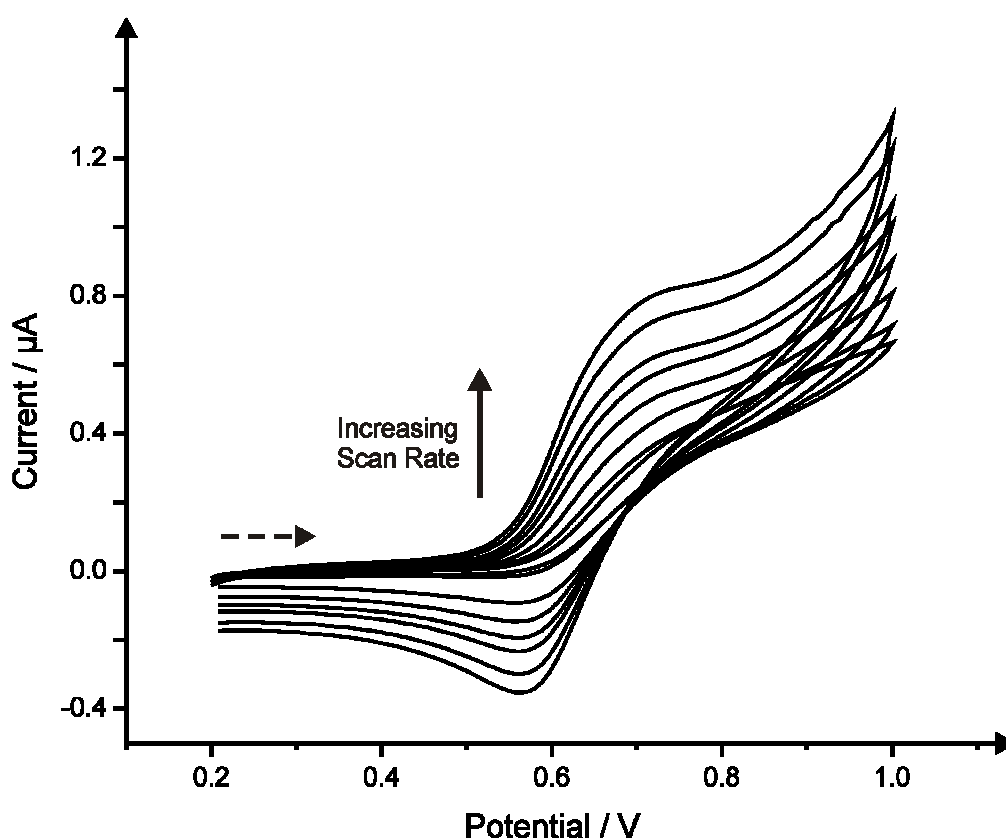


Figure 4.8 Typical cyclic voltammetric responses observed through scan rate studies using the PtdrSPE in 1 mM potassium hexachloroiridate (III) / 0.1 M KCl. Scan rates: 5 – 200 mV s^{-1} . Dashed arrow signifies direction of scan.

The model analyte, hydrazine, previously reported at a platinum based screen printed electrode³⁰⁶ was selected for the cyclic voltammetric studies using the PtdrSPE. The sensing of hydrazine was attempted over the analytically relevant concentration range of 50 to 500 μM . Figure 4.9A depicts the cyclic voltammetric response for additions of hydrazine to a pH 5 phosphate buffer solution. As is clear the oxidation of hydrazine is seen to occur at $\sim +0.4$ V (vs. Ag/AgCl), with the resulting wave increasing in peak height (I_p) at increasing hydrazine concentration over the entire analytical range. The corresponding calibration plot of peak current (I_p) versus concentration (μM) was found to be linear ($I/\mu\text{A} = 1.31 \times 10^{-2} \mu\text{A}/\mu\text{M} + 5.62 \times 10^{-1} \mu\text{A}$; $R^2 = 0.99$; $N = 10$) exhibiting a limit of detection (using 3σ in line with section 1.1.11) of 26.3 μM .

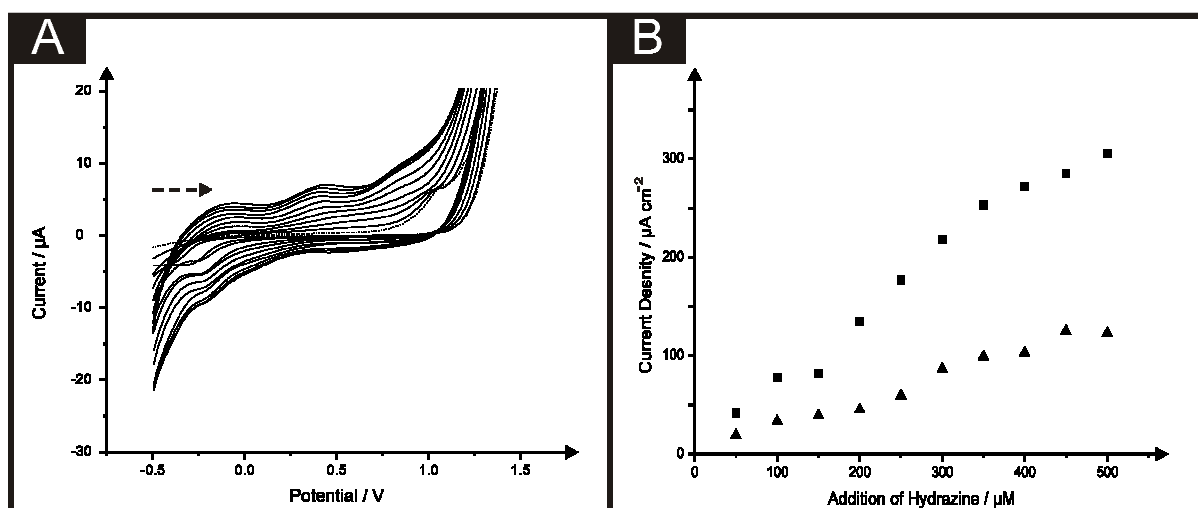


Figure 4.9 A) Typical cyclic voltammetric responses resulting from additions of hydrazine into a phosphate buffer (pH 7) (dotted line) at the PtdrSPE; additions made over the range 50 to 500 μM . Scan rate: 50 mV s^{-1} . Dashed arrow signifies direction of scan.

B) Typical current density calibration plots measured using cyclic voltammetry for the oxidation of hydrazine, arising from increasing concentrations at the PtdrSPE (squares) and PtSPE (triangles).

The PtdrSPE was then further utilised for the sensing of hydrazine in a pH 7 phosphate buffer solution using chronoamperometry through holding the potential at + 0.5 V (vs. Ag/AgCl) for 120 seconds, selected due to the observed oxidation potential of hydrazine

at the PtSPE through earlier cyclic voltammetric analysis. Once again, additions were made to the phosphate buffer solution over the range 50 to 500 μM of hydrazine at both the previously reported PtSPE and the PtdrSPE. Figure 4.9B depicts a comparison between the PtdrSPE and PtSPE for the sensing of hydrazine in a phosphate buffer solution. As is evident, greater sensitivity is seen at the PtdrSPE over the PtSPE when comparisons are made between the current densities obtained at increasing hydrazine concentration, demonstrating that some improvement is offered at the PtdrSPE over the previously reported PtSPE.³⁰⁶ Such observations further highlight, as has been found at the drSPE, that the recessed surface of the electrode offers an improved current density over a co-planar electrode of the same material, thus demonstrating that the findings are applicable to differing electrode materials. The determined limit of detection (using 3σ in line with section 1.1.11) at the PtdrSPE were calculated to be 25.1 μM ($I/\mu\text{A} = 6.54 \times 10^{-1} \mu\text{A}/\mu\text{M} + 9.79 \mu\text{A}$; $R^2 = 0.99$; $N = 10$). When the limit of detection realised at the PtdrSPE is compared with previous literature reports it can be seen that although lower limits of hydrazine detection are described at alternative electrode configurations such as at carbon paste electrode modified with copper porphyrin (1 μM),¹⁷⁷ iron(III) oxide graphite composite electrodes (1.18 μM)¹⁸⁹ and iron phthalocyanine film upon a gold macro electrode (11 μM),¹⁹⁰ the PtdrSPE offers the unique advantage of being screen printed, with the key attribute of the electrode being the simple configuration with the onboard additions of a reference and counter electrode, in addition to this, no prior treatment of the electrode, nor sample is required with the necessity for potential cycling alleviated as is required in other studies.^{193, 194}

The PtdrSPE was further utilised for the sensing of hydrogen peroxide, first cyclic voltammetric studies were carried out determining the reduction potential of hydrogen peroxide in a pH 7 phosphate buffer solution to be + 0.35 V (*vs.* Ag/AgCl) in agreement with previous reports.³⁰⁵ Consequently, chronoamperometric measurements (+ 0.35 V, 120 s) for

the addition of hydrogen peroxide into a pH 7 phosphate buffer solution were obtained over the range 100 to 1000 μM ($I/\mu\text{A} = 2.085 \times 10^{-2} \mu\text{A}/\mu\text{M} + 4.066 \times 10^{-4} \mu\text{A}$; $R^2 = 0.99$; $N = 10$). As with the sensing of hydrazine, the PtdrSPE was found to be much more sensitive for the sensing of hydrogen peroxide in terms of current density, as is depicted in figure 4.10. The determined limit of detection (using 3σ in line with section 1.1.11) at the PtdrSPE was calculated to be 44.3 μM . As was found for the sensing of hydrazine, the limits of detection calculated for hydrogen peroxide at the PtdrSPE are not as low as those reported at differing electrode configurations such as cobalt (II) hexacyanoferrate modified glassy carbon electrode,³⁰⁷ sol-gel modified glassy carbon³⁰⁸ and aluminium electrode modified with manganese hexacyanoferrate,¹⁹⁸ but has the potential benefit of being mass produced and single-shot without the requirement of a lengthy fabrication process.

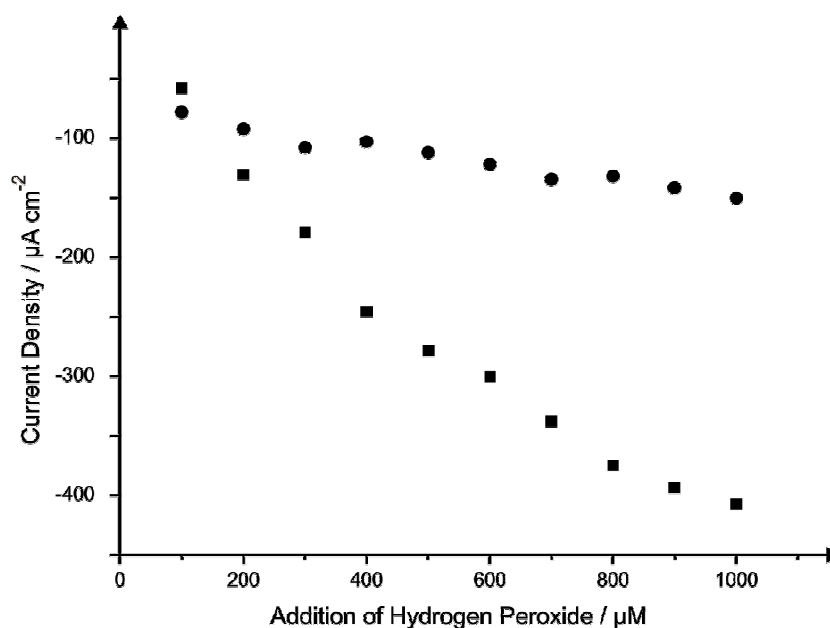


Figure 4.10 Typical current density calibration plots arising from chronoamperometric measurement (+ 0.35 V, 120 seconds) of hydrogen peroxide arising from increasing concentrations using the PtdrSPE (squares) and PtSPE (circles).

Pentagon-shaped screen printed shallow recessed electrodes

Microsquares have three main modes of diffusion – linear diffusion over the electrode, convergent edge diffusion at the long and the short edges, and point diffusion at the vertices of the electrode; this is depicted in figure 4.11.³⁰⁹ It is this point diffusion at the corners/vertices of the electrode that give rise to enhanced diffusion and hence the move by electrochemists to fabricate square electrodes and utilise the enhancement in mass transport which should ultimately improve the electrochemical response, and in particular electroanalytical performance where the transducer is employed. Indeed it has been shown *via* numerical simulation³¹⁰ that enhanced diffusion at microsquare corners occurs, where the concentration gradients generated are seen to be at their largest.³¹⁰ It is here that the current densities are therefore greatest and the diffusion layer is expected to increase most rapidly with time, faster than at the edge of a microdisc or long edge of a microsquare. Consequently square electrodes have recently been fabricated *via* lithography.^{61, 310}

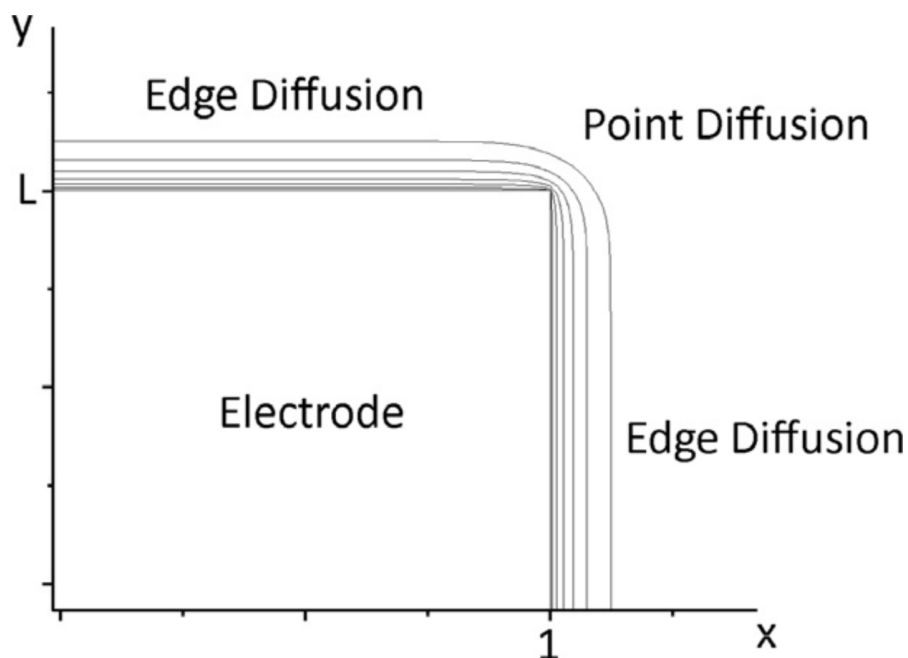


Figure 4.11 A representation of a two sides of the prSPE showing the modes of edge and point diffusion. Reproduced from Reference³⁰⁹.

An obvious step is then to utilise this point diffusion and make the step from a square, which has four points, to a geometry which has more points and consequently should exhibit even more enhancements in mass transport. This consequently inspired the fabrication of a pentagon shaped electrode; such an electrode has not yet been reported and will only likely be possible to be fabricated *via* lithography since the traditional technique of sealing a wire into glass would require a pentagon shaped wire. Here proof-of concept for the fabrication of pentagon-shaped electrodes (prSPE) fabricated entirely *via* screen printing is demonstrated. The prSPE were fabricated in the same manner as the drSPE (see Experimental section (5.1.2)) though the resulting electrode consists of a recessed pentagon-shaped working electrode ($45\ \mu\text{m} \times 45\ \mu\text{m} \times 45\ \mu\text{m} \times 35\ \mu\text{m} \times 25\ \mu\text{m}$). Presented in figure 4.12 are the SEMs obtained for the carbon based prSPE. As is evident, both the drSPE (figure 4.1) and prSPE (figure 4.12) display the physical properties of a recessed electrode, with the non-conductive layer printed on top of the underlying carbon producing the resultant recess; due to the fabrication approach where the screen define the thickness of the dielectric, the recess is consequently 4 microns resulting in a shallow recessed pentagon shaped screen printed electrode. Note that there is a slight deviation from a true well defined pentagon but approximates well (*viz* figure 4.12). It is important to realise that fabricating a pentagon working electrode in just carbon is not possible with the smallest geometry that can be fabricated being $\sim 100\ \mu\text{m}$,²⁹⁵ and as such, to allow smaller electrode geometries to be realised, utilising the dielectric to define the working electrode appears to be the only viable method.

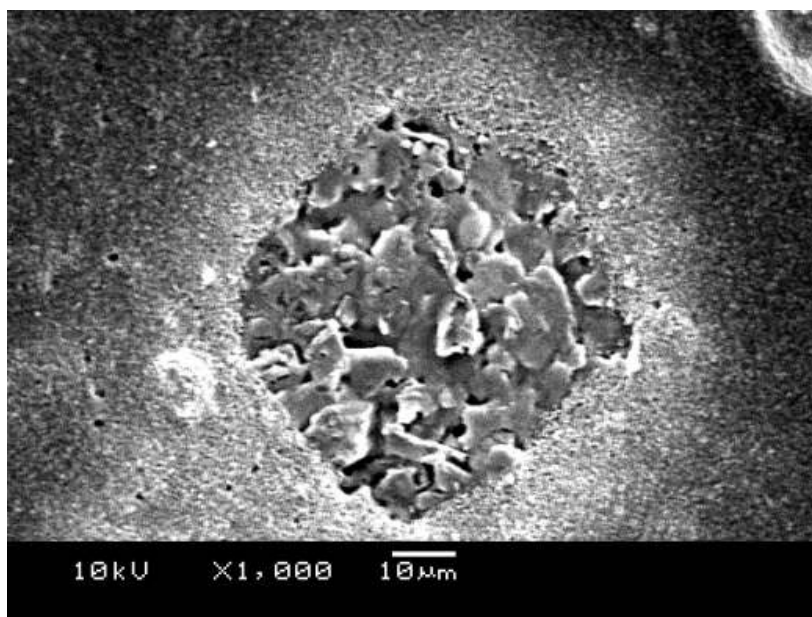


Figure 4.1.12 SEM of the prSPE working electrode (x 1,000 magnification).

The prSPE was characterised using the redox probe hexaammine-ruthenium (III) chloride where the effect of scan rate was explored, the result of which is depicted in figure 4.13A. It is readily evident that, as observed with the drSPE, at slow scan rates a steady-state type response is observed where upon faster scan rates, the voltammetric profile becomes peak shaped. In addition the observed effect of scan rate (figure 4.13A) demonstrates that the peak current in hexaammine-ruthenium (III) chloride is proportional to the square root of scan rate ($I_p / \mu A = -7.315 \times 10^{-3} \mu A / (V s^{-1})^{1/2} + 2.013 \times 10^{-1} \mu A; R^2 = 0.97; N = 9$) highlighting a diffusional process. Comparison of the responses obtained using the two recessed electrodes (drSPE and prSPE) in terms of current density ($\mu A cm^2$) are shown in figure 4.13B, clearly demonstrating the apparent superior nature of the prSPE which is due to the large number of points/vertices giving rise to enhanced mass transport.

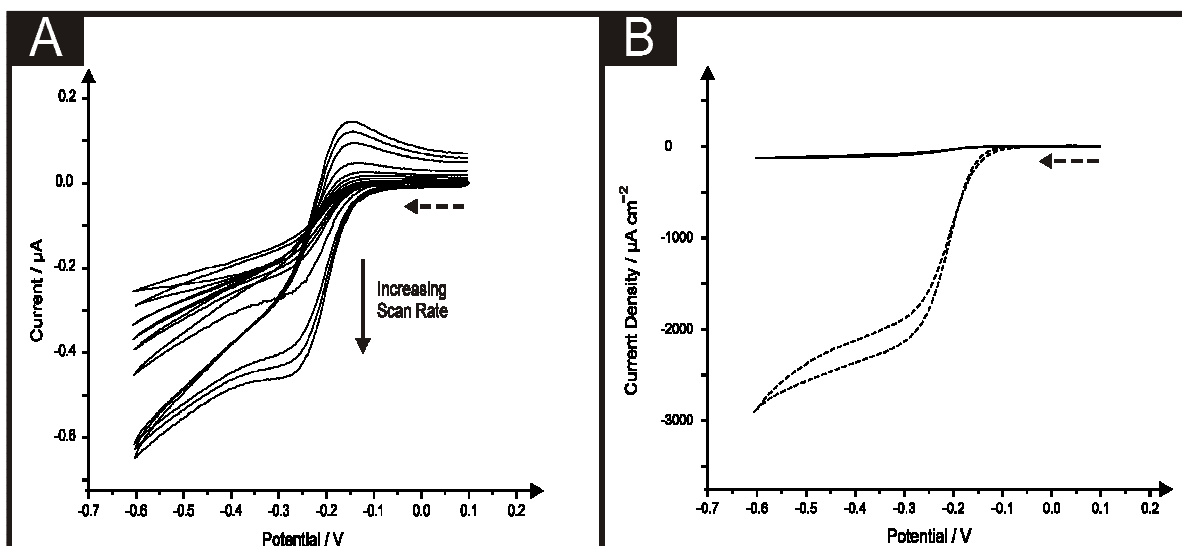


Figure 4.13 A) Typical cyclic voltammetric responses observed through scan rate studies using the prSPE in 1 mM hexaammine-ruthenium (III) chloride/ 0.1 M KCl. Scan rates: 5 – 400 mV s^{-1} . B) Comparison between the drSPE (solid line) and prSPE (dashed line) scan rates (of 5 and 10 mV s^{-1}) in 1 mM hexaammine-ruthenium (III) chloride / 0.1 M KCl. Dashed arrow signifies direction of scan.

The prSPE was finally assessed for the sensing of manganese (II) and contrasted with analysis at the drSPE. Manganese was chosen as a model analyte since it has been explored at other graphitic based electrodes. In terms of an analytical perspective, manganese is found in tea and is a rich source of dietary manganese.³¹¹ However, there is an analytical need to monitor this due to reports of the neurotoxic effects from chronic exposure to manganese.^{312, 313} Though, as described, the toxicity of manganese is rarely a grave problem, the facile monitoring, and detection of the analyte is still essential. As depicted in figure 4.14A, additions of manganese (II) were made into a solution of 0.1 M sodium acetate over the range 73 – 800 nM at the two recessed electrodes using square wave cathodic stripping voltammetry ($E_{dep} = + 0.9 \text{ V}$ (vs. SCE), 120 s). The sensing strategy is based upon the cathodic stripping voltammetry where the electrode potential is held sufficiently electro-positive for a set accumulation time to form insoluble manganese (IV) dioxide on the electrode surface³¹⁴ as described by:



The MnO_2 formed upon the electrode surface is then voltammetric stripped by sweeping the potential from positive to negative potential where a stripping peak is observed, giving rise to the electroanalytical signal as depicted in figure 4.14A. The resultant calibration plots of manganese concentration versus peak height (I_H) at the drSPE and prSPE ($I/\mu\text{A} = 9.988 \times 10^{-4} \mu\text{A}/\mu\text{M} + 1.764 \times 10^{-4} \mu\text{A}$; $R^2 = 0.99$; $N = 7$ and $I/\mu\text{A} = 1.01 \times 10^{-3} \mu\text{A}/\mu\text{M} + 1.518 \times 10^{-6} \mu\text{A}$; $R^2 = 0.99$; $N = 7$ respectively) are shown in figure 4.14B which demonstrate a superior response in terms of peak current is observed at the prSPE as opposed to the drSPE. Such findings are in agreement with the observations made during the electrochemical characterisation of the two recessed electrodes in hexaammine-ruthenium (III) chloride suggesting that the enhancement in point diffusion/mass transport provides benefits in electroanalysis. Linearity is evident at the prSPE from 73 to 504 nM with a slight plateau above these manganese (II) concentrations. Respective limits of detection of 63 nM and 36 nM for manganese (II) were determined at the drSPE and prSPE. Such low limits of detection offered by the prSPE highlight the excellent electroanalytical applicability of the recessed electrode and improve even over previous reports at an array of recessed electrodes, which boasted a limit of detection of 64 nM,²⁷⁹ which itself was superior over analytical reports such as spectrophotometric techniques³¹⁵ and flow-injection with flame atomic absorption spectrometry,³¹⁶ and electroanalytical protocols;³¹⁷⁻³²⁰ such a response indicates the greater current density observed at the prSPE due to the greater proportion of edges (point diffusion/mass transport), thus highlighting the beneficial utilisation of the prSPE.

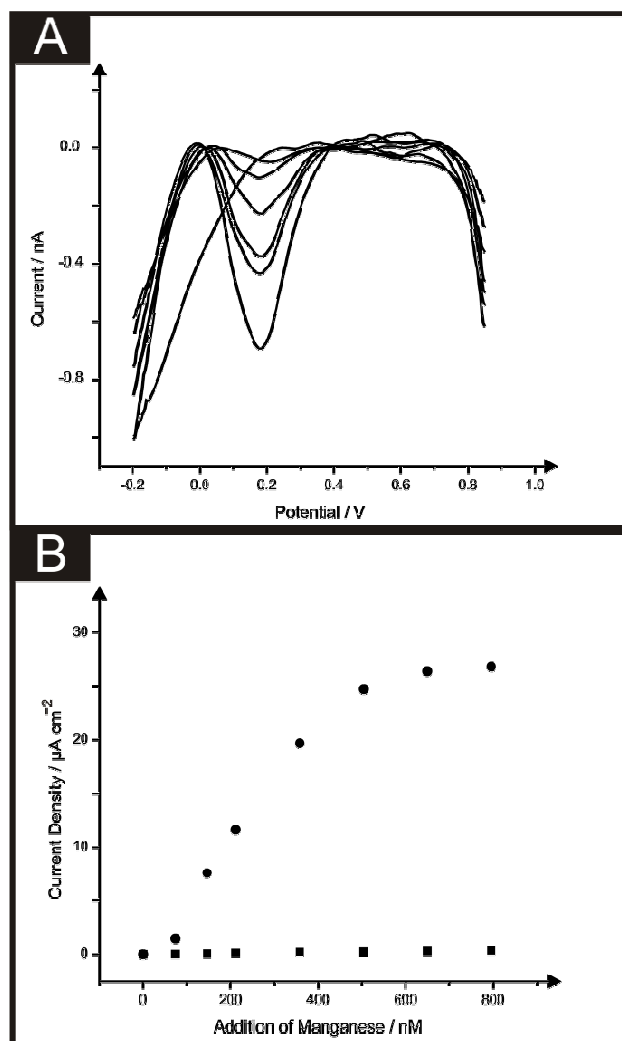


Figure 4.14 A) Typical square wave cathodic stripping voltammetry ($E_{dep} = +0.9 V$ (vs. SCE), 120 s) resulting from additions of manganese (II) into a 0.1 M sodium acetate solution.
 B) An overlay of typical calibration plots resulting from additions of manganese (II) into a 0.1 M sodium acetate solution over the range of 73 to 504 nM at the drSPE (squares) and prSPE (diamonds) ($N = 7$).

4.1.4 CONCLUSIONS

The successful fabrication of highly novel screen printed shallow recessed electrodes has been described. The ease of fabrication and facile modification for beneficial diffusional processes and improved analyte detection is highlighted through the development and implementation of two different types of shallow recessed electrodes; disc-like shallow recessed screen printed electrodes and pentagon shallow recessed screen printed electrodes.

Competitive limits of detection for the important analytes nitrite, NADH and manganese are shown to be possible.

Interestingly it can be noted that in addition to the clearly described benefits offered by the recessed electrode, the particular shape of the geometry also dominates the observed response and sensitivity offered by the electrode, where a pentagon-shaped shallow recessed electrode being determined to be the most beneficial design likely due to greater point diffusion/mass transport; further work is underway to explore this electrode geometry such as in a pentagon array which would yield even further benefits in mass transport and consequently offer greater electroanalytical performance. Furthermore due to the adaptability and facile modification of screen printed electrode design, the incorporation of electrocatalytic metals of interest within the inks used for fabrication is viable, as determined through the fabrication of a platinum-based recessed screen printed electrode which can be easily extended to other desired metals.

4.2 MASS TRANSPORT CONTROL: A SCREEN PRINTED MICROELECTRODE ARRAY

An alternative to the recessed electrode is a co-planar microelectrode. Such electrodes are favoured as has been described in detail due to their improved diffusion control and electrochemical behaviour. Critically however, with a reduction in the size of the working electrode the resultant current observed is also reduced. In order to combat this and thus allow for sensors which yield the benefits of microelectrodes without a great compromise in the observed electrochemical current, an array of microelectrodes is utilised which then multiplies the observed current by the number of electrodes comprising the array.

Within this section, which contains published work,^[5] a screen printed microelectrode array is described, which has been fabricated utilising screen printing technology. Two types of electrodes are discussed; graphite and gold-based screen printed microelectrode arrays, which are benchmarked against sensors within the literature and those detailed within this thesis in earlier Chapters using well-studied and understood analytes.

4.2.1 INTRODUCTION

Microelectrodes are utilised by electrochemists due to their reported benefits, which include; improved Faradaic-to-charging current ratios, steady-state (or quasi-steady state) responses for Faradaic processes, reduced ohmic (I_R) drop, and most importantly when used in sensing, improved signal-to-noise ratios allowing low detection levels to be reached compared to macroelectrodes.³²¹⁻³²⁵

The caveat with microelectrodes is that a very small Faradaic current is produced which can be hard or impossible to measure, especially due to their susceptibility to mains interference such that the Faradaic signal is engulfed beneath capacitively coupled mains

⁵ F. Tan, J. P. Metters and C. E. Banks, *Sens. Actuators, B*, 2013, **181**, 454.

interference.³²⁶ As pointed out by Fletcher and Horne,³²⁶ to overcome this – that is, to decrease the interference – one has to place all electrochemical apparatus inside earthed screens, and wire all circuits in a common ground plane, greatly complicating the experimental design and significantly limiting sensor implementation into the field.

The well-known solution to overcome these problems yet still use the benefits of microelectrodes is to assemble multiple microelectrodes wired in parallel, with ideally, each microelectrode independent of its neighbours; such an electrode will exhibit all the useful properties of a single microelectrode but generate a signal which is significantly greater.³²⁶⁻³²⁸
329, 330

Microelectrode arrays present an opportunity for the integration in ‘lab-on-a-chip’ devices which can be used in a plethora of applications, such as in-vitro and in-vivo biological biosensing.³³¹⁻³³⁶ Typically microelectrode arrays comprise noble metals and are constructed in a variety of approaches (see reference³³⁷ for a thorough overview) which involve sealing the chosen noble metal microwire within an inert substance, for example glass, so as to allow for realisation of micron sized electrode diameters whilst providing sufficient spacing between the microelectrodes comprising the array.³³⁸

Approaches such as photolithography are thus favoured for the design and production of microelectrode configurations since they offer the ability to fabricate microelectrode arrays with well-defined geometric and inter-electrode spacing³³⁹ such that diffusional interaction from neighbouring microelectrode comprising the array is minimal. Other approaches for the fabricated arrays have reported the use of screen printing technology.³⁴⁰⁻³⁴⁴ Such a method of fabrication is highly advantageous due to their single-shot use alleviating the requirement for preparatory steps such as electrode polishing and also their low-cost nature allowing for economical sensor production without comprising performance or reproducibility.³³⁷

In this section the fabrication and utilisation of a screen printed microelectrode array which comprises six microelectrodes of 50 μm radii, arranged in a circular configuration around a common counter and reference electrode and are separated from their nearest neighbour by an average distance of 2272 (± 0.3) μm is described. Due to their design, these screen printed microelectrode arrays are diffusional independent such that no diffusional interaction occurs between the individual microelectrodes comprising the array; such a configuration is seldom reported within the literature and additionally very few microelectrode arrays are produced *via* screen printing technology.

The microelectrodes comprising the screen printed microelectrode arrays are fabricated to have working electrodes comprised of either graphite or gold, though an array of any desired noble material could also be realised by using the desired corresponding metal ink (*i.e.* Pd, Pt, Cu etc). Clearly, screen printed electrodes have been fabricated previously utilising both carbon³⁴⁵ and gold³⁴⁶ inks, however such sensors are macro in size in comparison with the screen printed microelectrode array discussed herein. The microelectrode arrays are first characterised utilising the common electrochemical probe hexaammine-ruthenium (III) chloride and explored, in the case of the graphite microelectrode array towards the electroanalytical sensing of acetaminophen, nitrite and dopamine in the case of the gold microelectrode array, chromium (VI) and in all cases are found to yield analytically useful results. In the latter case, the sensing of chromium (VI) in an environmental sample is shown to be feasible suggesting these sensors have potential merit in the possible screening of water samples.

4.2.2 RESULTS AND DISCUSSION

Carbon Screen Printed Microelectrode Array (Carbon SPMA)

The carbon screen printed microelectrode arrays (carbon SPMA) fabricated consist of six separate working electrodes (radii 50 μm) surrounded by a common counter and reference electrode; images of the carbon SPMA are depicted in figure 4.15; a schematic representation of the sensors. Additionally shown in figure 4.16 are optical and scanning electron microscope images showing the configuration of the screen printed microelectrode array. All measurements were conducted using the screen-printed microelectrode array configuration which comprises 6 carbon-graphite geometric working electrodes with radii of 50 μm separated by an average of 2272 (\pm 0.3) μm arranged in a circular configuration around a common carbon-graphite counter and a Ag/AgCl reference electrode. Since the electrodes are in a circular pattern, the top two microelectrodes are the closest electrodes together which have a separation corresponding to 2249.4 microns; this is relevant in discussions later in terms of the sensors electrochemical response. As shown in figure 4.16C, closer inspection with SEM reveals that the microelectrodes are not typically circular as is found in other microelectrode fabrication routes and is rather, akin to a matchstick head but should still approximate to that of a microelectrode. Note that the microelectrode size is controlled by the screen mesh size and this design is on the limit of fabrication; any smaller attempted electrodes sizes are not feasibly produced and is effectively limited by a combination of the screen mesh and graphite/carbon particle size (with agglomeration a significant factor) used within the commercially utilised screen printing inks. Last, further inspection of the microelectrode (figure 4.16D) reveals the surface to consist of conductive carbon particles and is consistent with previous reports of graphite screen printed electrodes.^{347, 348}

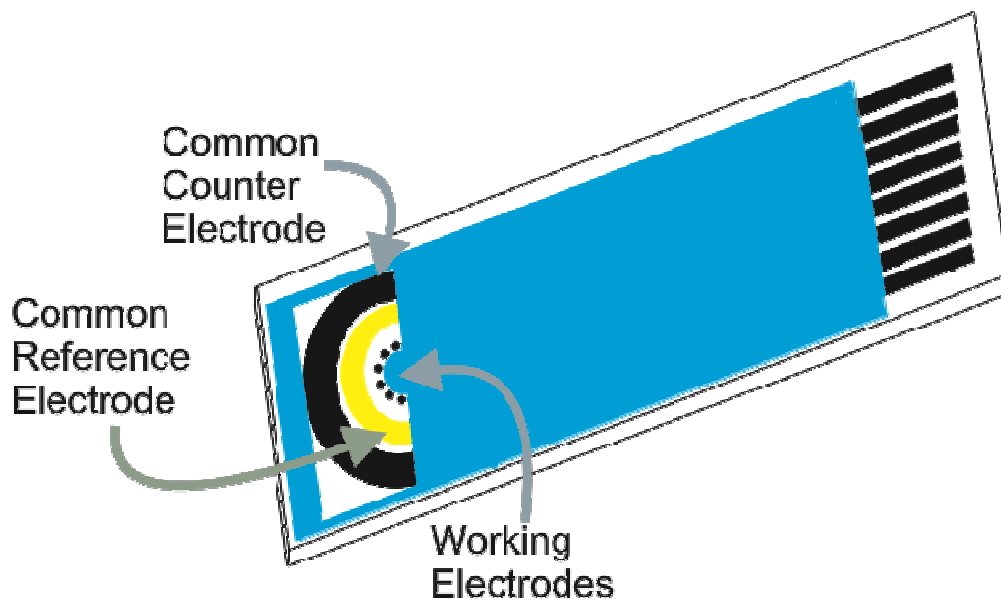


Figure 4.15 A schematic representation of the SPMA fabricated entirely through screen printing technology.

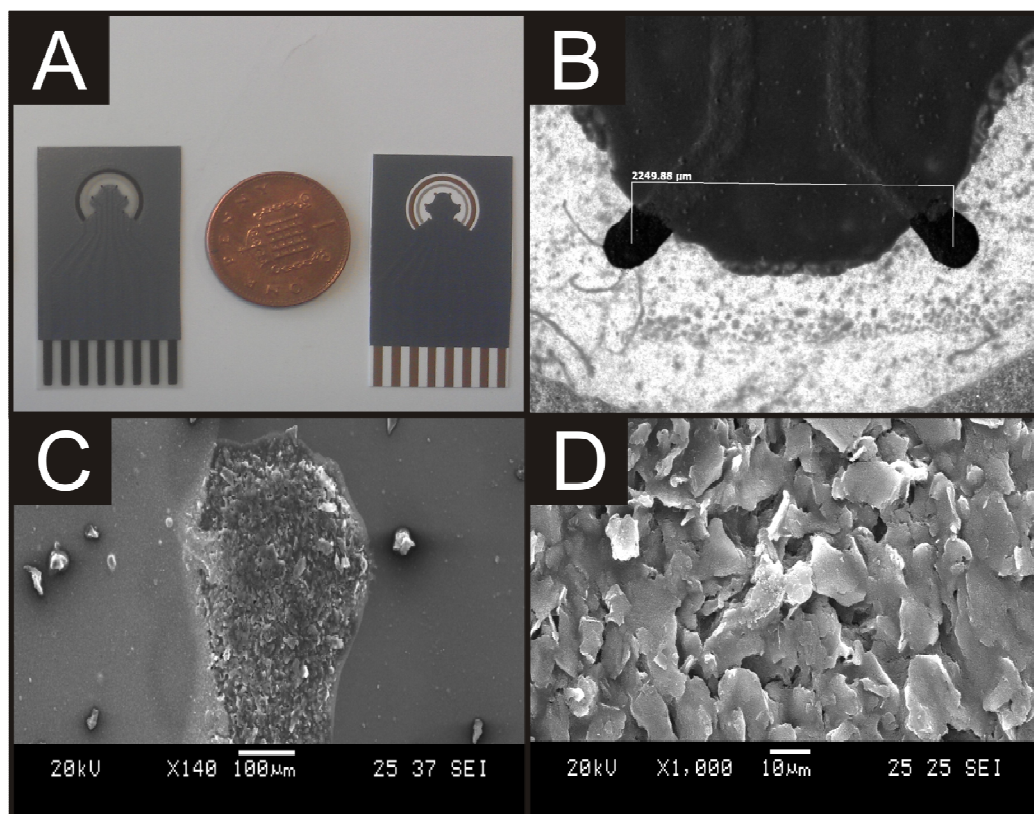


Figure 4.16 Photograph of the carbon (left image) and gold (right image) SPMA (A). An optical microscope image of the carbon SPME (B). Typical SEM images of the carbon SPMA at x140 (C) and x1000 magnification (D).

The carbon SPMA were next electrochemically characterised using the redox probe hexaammine-ruthenium (III) chloride in 0.1 M KCl. Figure 4.17 depicts the observed cyclic voltammetric signatures utilising the carbon SPMA using scan rates over the range 5 to 200 mV s^{-1} . It is evident through observation of figure 4.17 that at slow scan rates a steady-state type response is observed where upon faster scan rates, the voltammetric profile becomes peak shaped due to the increasing contribution from linear diffusion rather than solely convergent diffusion as expected at true microelectrodes.³⁴⁹ Figure 4.18 depicts the response of a single electrode from the carbon SPMA contrasted to all the electrodes on the carbon SPMA being utilised as an array, where an apparent improvement in voltammetric peak height of ~ 2.6 times occurs through utilisation of the SPMA over that of a single microelectrode is readily evident.

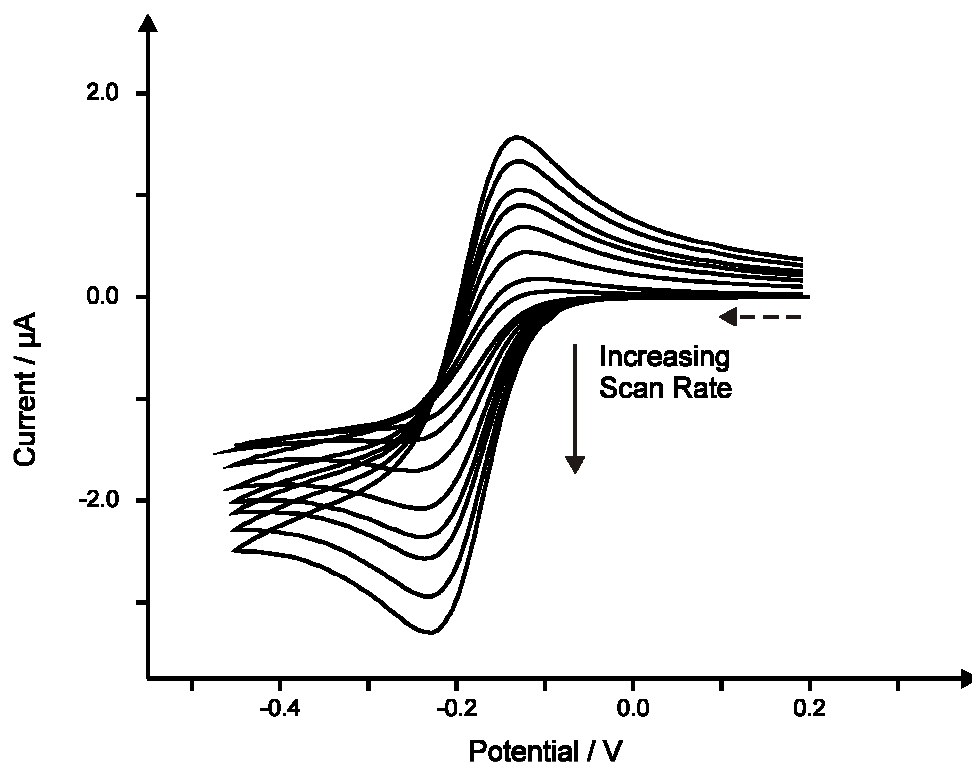


Figure 4.17 Cyclic voltammetric response arising from the carbon SPMA recorded in 1 mM hexaammine-ruthenium (III) chloride / 0.1 M KCl. Scan rates: 5 - 200 mV s^{-1} . Dashed arrow signifies direction of scan.

Assuming that the dominant form of mass transport is convergent in nature and that the electrochemical response of the carbon SPMA is microelectrode-like, the theoretical predicted current, I_p is given by:

$$I_p = nFrCDN \quad (4.4)$$

where n is the number of electrons, F the Faraday constant, C the concentration of the analyte, D the diffusion coefficient of the analyte and r the electrode radii. Note that N , the number of electrodes comprising the array, is present in equation (4.4) which for when a single microelectrode on the carbon SPMA is utilised, $N = 1$ while when the whole array is used, $N = 6$. Note that the current is amplified by the total number of electrodes comprising the array. Typically it is expected that equation (4.4) will be valid allowing researchers to determine the radius of the electrodes comprising the array. However this is unfortunately and incorrectly undertaken with little, or no regard to the interaction of diffusion layers of neighbouring electrodes.^{350, 351} Instead it is inferred that the diffusion layer is given by:

$$\delta \sim \sqrt{6Dt} \quad (4.5)$$

where D is the diffusion coefficient and t is the timescale of the experimental analysis, such that:

$$\delta = \sqrt{6D\left(\frac{\Delta E}{\nu}\right)} \quad (4.6)$$

When considering the SPMA shown in figure 4.16, for equation (4.4) to be valid, there should be no diffusion layer interaction between neighbouring microelectrodes such that the diffusion layer, δ , must be less than $f_{greater}$, as given by:

$$f_{greater} = \left(\frac{d_{centre}}{2}\right) - \left(\frac{d_{electrode}}{2}\right) \quad (4.7)$$

where d_{centre} is the centre-to-centre separation between the electrodes and $d_{electrode}$ is the diameter of the electrode. Using equation (4.5), where D is the diffusion coefficient ($9.1 \times 10^{-6} \text{ cm}^2 \text{ s}^{-1}$, ³⁵²), ν the voltammetric scan rate employed and ΔE the potential range over which electrolysis has occurred, the diffusion layer, δ , can be estimated over the range of experimentally utilised scan rates which spans between 67.4 and 465.4 μm for the fastest (200 mV s^{-1}) and slowest (5 mV s^{-1}) applied voltammetric scan rates respectively. Using equation (4.7) $f_{greater}$ was deduced for the carbon SPMA to equate to 1950 μm . Thus given that the diffusion layer will reach a maximum of 268.7 μm at the slowest applied voltammetric scan rate, the carbon SPMA has no diffusional interaction/ overlapping diffusion layers between the electrodes comprising the array; such an array is one of only a few published in the literature where no diffusional interaction is observed and indeed this is the first report of a disposable mass produced carbon SPMA with these characteristics.

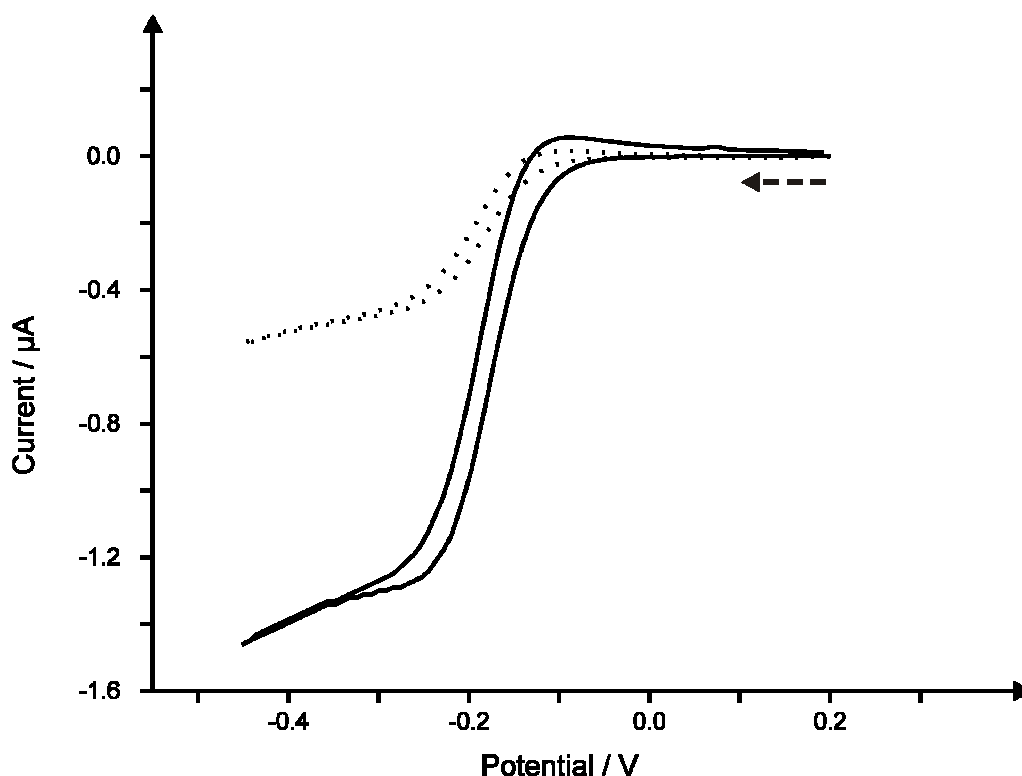


Figure 4.18 Typical cyclic voltammetric responses obtained using the carbon SPMA (solid line) and a single electrode from the carbon SPMA (dotted line) in 1 mM hexaammine-ruthenium (III) chloride / 0.1 M KCl. Scan rate: 5 mV s^{-1} . Dashed arrow signifies direction of scan.

Returning to the voltammetry presented in figure 4.18, the question arises as to why, if diffusional overlap doesn't occur in the experimental set-up, an increase from that of a single electrode ($N = 1$) to the array ($N = 6$), is not a factor of 6? The answer simply is that equation (4.4) is for the case of true microelectrodes where the dominant form of mass transport is convergent and the contribution from planar diffusion is minimal; in the case of the SPMA, there is a significant contribution from planar diffusion in addition to convergent diffusion (see figure 4.17) due to the limitations imposed by the fabrication procedure such that electrodes with radii of 50 microns are as small as reliably (limited by the particle size of the graphite/carbon within the ink formulation) can be produced and rather quasi-microelectrodes exist; comprising the SPMA. Furthermore, the above discussions are for a simple one step electron transfer process; deviation will clearly be observed for multi-step electron transfer processes, as is the case for the analytes explored below, such that a simple $\times 6$ improvement in using the SPMA over a single microelectrode will not be observed.

Following the electrochemical characterisation of the carbon SPMA, the task of assessing the sensor's electroanalytical robustness was explored, first through the sensing of acetaminophen. Acetaminophen, or as it is more commonly known paracetamol, is a widely used antipyretic and analgesic drug.³⁵³ In recent years it has become a more widely preferred alternative to aspirin, particularly for children and those sensitive to aspirin. At the recommended dosage, there are often no side effects, however, doses in excess of those recommended can result in liver and kidney damage.³⁵⁴ It is suspected that a metabolite of acetaminophen is the actual hepatotoxic agent.³⁵⁵⁻³⁵⁷ Clearly, with such wide use, the monitoring of acetaminophen levels within samples is of great interest.

Linear sweep voltammetric measurements were undertaken at increasing concentrations of acetaminophen into a pH 7 phosphate buffer solution; this buffer composition was selected as the optimal solution as it is close to that of biological samples in

which acetaminophen sensing is of key interest, but also in line with previous literature reports.³⁵⁸⁻³⁶¹ Figure 4.19A depicts typical linear sweep voltammetric measurements obtained using a carbon SPMA at a scan rate of 5 mV s^{-1} . Upon closer inspection the quasi-limiting current (I_L) is seen to increase with acetaminophen additions over the range of 10 to 100 μM . Figure 4.19B depicts the analysis of the limiting current plotted against acetaminophen concentration which is found to be linear in nature ($I_L / \mu\text{A} = 2.02 \times 10^{-3} \mu\text{A} / \mu\text{M} + 8.26 \times 10^{-3} \mu\text{A}; R^2 = 0.98; N = 10$). Additionally, figure 4.19A shows the calibration plot corresponding to additions of acetaminophen over the same concentration range using a single electrode from the carbon SPMA. Although a linear response ($I_L / \mu\text{A} = 6.41 \times 10^{-3} \mu\text{A} / \mu\text{M} - 8.26 \times 10^{-3} \mu\text{A}; R^2 = 0.98; N = 10$) is observed, a reduction in magnitude of the current is noted. The comparison of the gradients for the calibration plots (figure 4.19B) demonstrates a 3.2 x improvement when utilising the carbon SPMA over a single electrode from the SPMA; this deviation from the expected 6 x improvement is due to the array comprising quasi-microelectrodes (see earlier). Additionally analysis of the voltammetric data revealed the % Relative Standard Deviation to correspond to 1.92 % ($N = 3$) highlighting the intra-reproducibility of the carbon SPMA towards the sensing of acetaminophen.

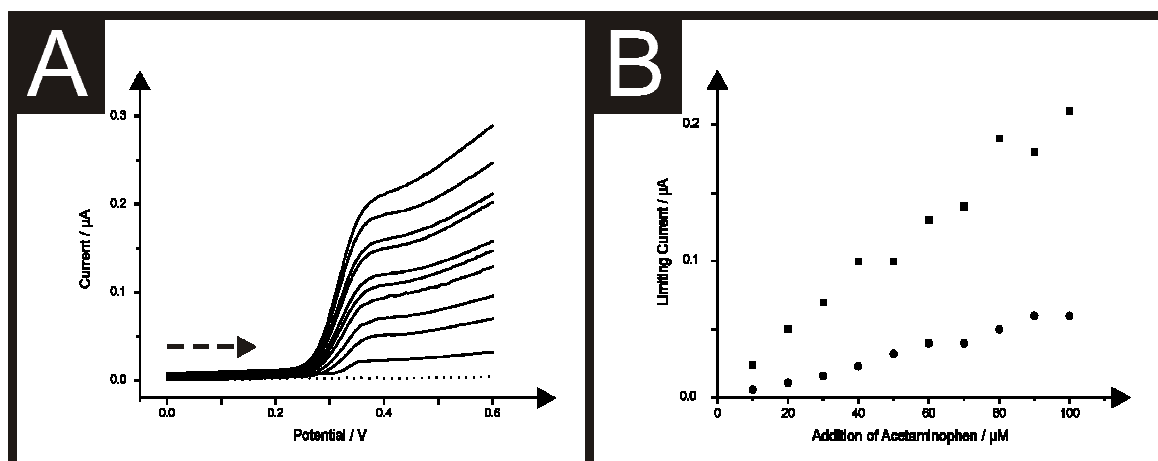


Figure 4.19 Linear sweep voltammograms recorded following the addition of acetaminophen into a pH 7 phosphate buffer solution (dotted line) over the concentration range 10 – 1000 μM using the carbon SPMA (A). Typical corresponding calibration plots using the carbon SPMA (squares) and a single electrode from the carbon SPMA (circles) (B). Scan rate: 5 mV s^{-1} . Dashed arrow signifies direction of scan.

The limit of detection (using 3σ in line with section 1.1.11) calculated for acetaminophen in pH 7 phosphate buffer solution using the carbon SPMA found to correspond to $4.3 \mu\text{M}$. Comparison of the determined limit of detection feasible at the carbon SPMA with existing literature finds the SPMA to offer comparable limitations with other electrochemical based sensors, though examples offering lower limits of detection are reported. For example, Wangfuengkanagul *et al*³⁵⁶ report the sensing of acetaminophen utilising a boron-doped diamond film electrode providing a limit of detection of $10 \mu\text{M}$.³⁵⁶ Further to this an improvement in the limit of detection is reported through the modification of glassy carbon electrodes with carbon-coated nickel magnetic nanoparticles allowing for the sensing of acetaminophen down to $2.3 \mu\text{M}$.³⁶² Similarly, glassy carbon electrodes coated with gold nanoparticles and an organophillic layered double hydroxide have offered a slight improvement with regard to the limit of detection towards acetaminophen of $0.13 \mu\text{M}$.³⁶³ The utilisation of carbon nanotubes has also been reported to be highly beneficial towards the sensing of acetaminophen offering ultra-low detection levels in the nM range.^{364, 365} A single-

walled carbon nanotube / graphene nanosheet hybrid film modified glassy carbon electrode has been demonstrated to allow for a limit of detection of 38 nM acetaminophen.³⁶⁴ Improving on this limit of detection Compton *et al*³⁶⁵ achieve the sensing of acetaminophen to 10 nM using a multi-walled carbon nanotube modified basal plane pyrolytic graphite electrode.³⁶⁵ Evidently electrode configurations exist within the literature which allow for improvement limits of detection for acetaminophen in comparison to that possible when using the carbon SPMA, it is however important to note that each of the reports discussed utilise electrodes which require preparatory steps prior to utilisation, in some cases resulting in extended time periods involved in their utilisation for analytical sampling and increasing the likelihood of poor reproducibility between electrode modifications. Critically, the carbon SPMA reported herein requires no such pre-treatment or preparation offering great improvements with regard to time and ease of use as is the case in other reported sensors.³⁶³⁻³⁶⁵

To further assess the useful analytical nature of the carbon SPMA, linear sweep voltammetric measurements were undertaken for the sensing of the well explored analyte dopamine which is one of the neurotransmitters playing a major role in addiction.³⁶⁶ As a chemical messenger, dopamine affects brain processes that control movement, emotional response, and ability to experience pleasure and pain. It has also been reported that dopamine has an important role in the pathogenesis or drug treatment of certain brain disease, *e.g.* Parkinson's disease, schizophrenia. Therefore, the rapid and accurate detection of dopamine is important not only for diagnostic but also for pathological research. It possesses very strong electrochemical activity and is one of the main objects of study in the electroanalytical chemistry of neurotransmitters.^{367, 368}

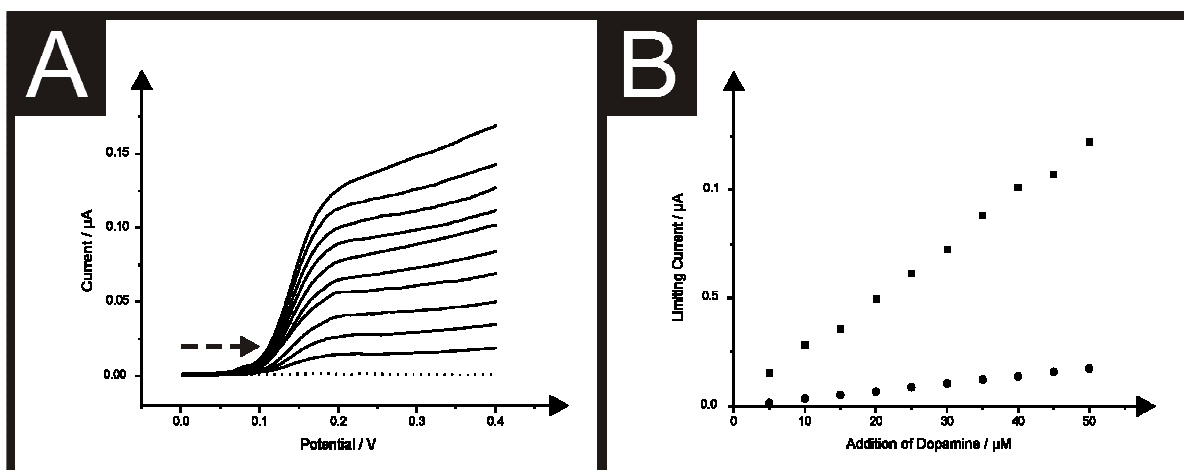


Figure 4.20 Linear sweep voltammograms recorded following the addition of dopamine hydrochloride into a pH 7 phosphate buffer solution (dotted line) over the concentration range 50 – 500 μM using the carbon SPMA (A). Typical corresponding calibration plots using the carbon SPMA (squares) and a single electrode from the carbon SPMA (circles) (B). Scan rate: 5 mV s^{-1} . Dashed arrow signifies direction of scan.

Figure 4.20A depicts the electrochemical oxidation of dopamine in a pH 7 phosphate using the carbon SPMA. As observed above, a quasi-steady-state response is observed for the oxidation of dopamine which correlates linearly ($I_L / \mu\text{A} = 2.38 \times 10^{-3} \mu\text{A} / \mu\text{M} + 2.62 \times 10^{-3} \mu\text{A}; R^2 = 0.99; N = 10$) with dopamine concentrations over the range 50 to 500 μM (see figure 4.20B). Comparison of the calibration plot arising from measurements over the analytical range utilising the carbon SPMA with that utilising a single electrode from the array (figure 4.20B) demonstrates the superior response over the entire range studied for the sensing of dopamine. Although a much improved response is facilitated with the carbon SPMA, a single electrode from the array does allow for a linear response ($I_L / \mu\text{A} = 3.51 \times 10^{-4} \mu\text{A} / \mu\text{M} - 1.01 \times 10^{-4} \mu\text{A}; R^2 = 0.99; N = 10$) over the range studied where an improvement using the array is evident. Analysis of the voltammetric data obtained for the sensing of dopamine using the carbon SPMA revealed the % Relative Standard Deviation to correspond to 1.64 % ($N = 3$) highlighting the reproducibility of the

screen printed sensor. Furthermore, a limit of detection (using 3σ in line with section 1.1.11) of $3.24\ \mu\text{M}$ was determined for the sensing of dopamine when using the carbon SPMA. The determination of dopamine is well reported within the literature and therefore comparisons between the carbon SPMA and existing electrode configurations can be made with ease. Examples of such reports include that by Thomas and co-workers³⁶⁹ who utilise a Poly(Rhodamine B) modified carbon paste electrode enabling the detection of dopamine at a concentration of $4\ \mu\text{M}$. Additionally, graphene modified electrodes have been shown to offer favourable limits of detection towards the sensing of dopamine. Screen printed graphene electrodes have been reported by Ping *et al* where chemically reduced graphene oxide was utilised to form an ink which could be screen printed. The fabricated sensor was determined to enable the detection of dopamine down to $0.12\ \mu\text{M}$.³⁷⁰ Similarly, a graphene has been used in a highly novel form; a three-dimensional graphene foam, which when utilised for the sensing of dopamine enables a limit of detection of $25\ \text{nM}$. Again it is clear that alternative electrode materials and configurations allow for improvements for the detection of dopamine in comparison to that possible at the carbon SPMA, however the simplistic nature and removal of the requirement of pre-treatment or electrode preparation necessary at some of the literature reports offers a true advantage, particularly when looking at large scale applications of the sensors at hand.

The final model analyte selected to ascertain a greater understanding of the analytical potential of the carbon SPMA was sodium nitrite. Nitrite is widely involved in environmental chemistry and public health, so the important roles played by nitrite in these areas were recognised long ago.^{371, 372} Although naturally-occurring concentrations of nitrites are usually of no significance to health, wastes from fertilizers and the intentional addition of nitrites for corrosion control are potential sources of nitrite contamination.³⁷³ Nitrite is reported to be a human health-hazard chemical the excess of which may cause poisoning and its derivatives

are also major components in low-level radioactive waste solution.^{374, 375} The excess uptake of nitrite could cause gastric cancer³⁷⁶ and it is therefore necessary to develop a reliable and sensitive sensor to detect nitrite in food, drinking water and environmental samples.

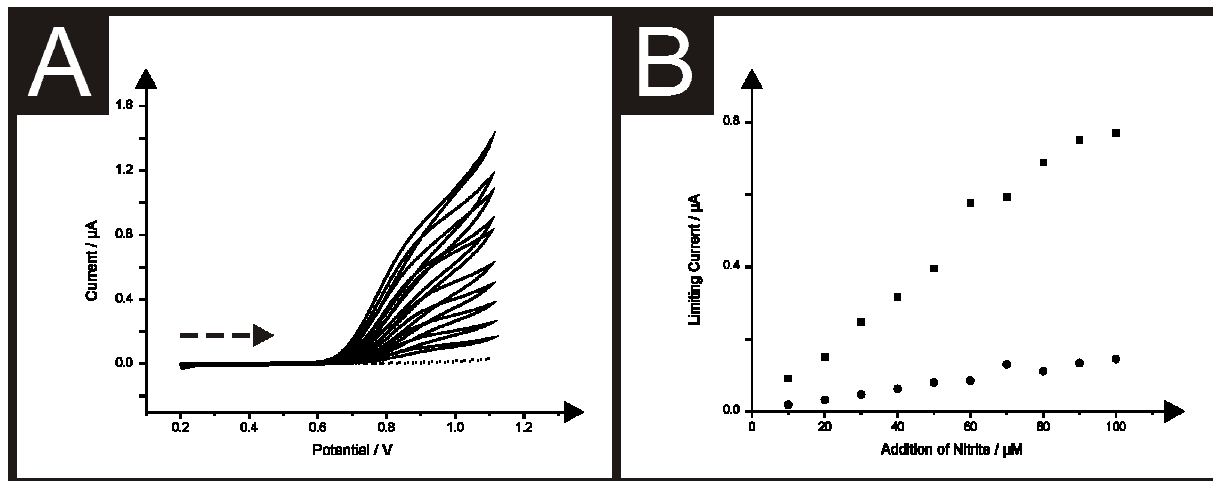


Figure 4.21 Cyclic voltammograms recorded following the addition of nitrite into a pH 7 phosphate buffer solution (dotted line) over the concentration range 10 – 100 μM using the carbon SPMA (A). Typical corresponding calibration plots using the carbon SPMA (squares) and a single electrode from the carbon SPMA (circles) (B). Scan rate: 5 mV s^{-1} . Dashed arrow signifies direction of scan.

Initially cyclic voltammetric studies for a solution of nitrite in a pH 7 phosphate buffer solution at a scan rate of 5 mV s^{-1} demonstrated the oxidation of nitrite was viable through utilisation of the carbon SPMA as shown in figure 4.21A. Voltammetric measurements were made at increasing concentrations (10 to 100 μM) of nitrite using a carbon SPMA as depicted in figure 4.21A, with the corresponding calibration plot for the carbon SPMA contrasted with the response obtained at a single electrode from the array shown in figure 4.21B. Clearly, both electrodes exhibit a linear response over the entire concentration range studied (SPMA: $I_L / \mu\text{A} = 8.22 \times 10^{-3} \mu\text{A} / \mu\text{M} + 5.92 \times 10^{-3} \mu\text{A}$; $R^2 = 0.98$; $N = 10$ and single electrode from the SPMA: $I_L / \mu\text{A} = 1.45 \times 10^{-3} \mu\text{A} / \mu\text{M} + 4.72 \times 10^{-3} \mu\text{A}$; $R^2 = 0.96$; $N = 10$) where a $\sim 5.7 \times$ improvement was evident through use of the carbon SPMA over that at a single

electrode. As with the previous analytes studied at the carbon SPMA a low % Relative Standard Deviation corresponding to 2.02 % ($N = 3$) was obtained. The limit of detection (using 3σ in line with section 1.1.11) using the carbon SPMA for nitrite in a pH 7 phosphate buffer was calculated to be 5.24 μM . This calculated limit of detection for the sensing of nitrite is found to be competitive when compared with existing reports within the literature (see table 4.1 for a non-exhaustive list of electrochemical reports). Chen *et al*³⁷⁷ have described the utilisation of a nano-diamond powder electrode reporting a nitrite limit of detection of 0.12 mM. An improvement upon these limits of detection has been reported through the utilisation of carbon based screen printed shallow recessed electrodes³⁴⁶ with a limit of detection of 7.28 μM for the sensing of nitrite and furthermore through the use of composite copper – carbon electrodes with a limit of detection of 0.6 μM found to be possible.³⁷⁸ Improving on these reports a glassy carbon modified with CuPtCl_6 film has been described to enable the detection of nitrite at concentrations as low as 0.05 μM .³⁷⁹ Again the use of a one-shot economical sensor has potential benefits over these literature reports. Only one other report exists within the literature for the sensing of nitrite using a screen printed microelectrode array as described by Kadara *et al*³⁸⁰ The work explored the application of unmodified screen printed shallow recessed graphite microelectrode arrays towards the sensing of nitrite in aqueous solutions. The screen printed array fabricated comprised 6 microdiscs each having radii of 116 (± 6) μm and are recessed by 4 microns and separated by 2500 μm from their nearest neighbour in a hexagonal arrangement. The screen printed arrays were determined to permit the low micromolar sensing of nitrite (12.7 μM) in aqueous solutions *via* cyclic voltammetry. Evidently such a limit of detection for the sensing of nitrite does not achieve the low level found to be possible through use of the carbon SPMA.³⁸⁰

Electrode	Linear Range (μM)	Limit of Detection (μM)	Reference
Composite copper electrode modified with carbon powder and epoxy resin	100 to 1250	600	378
Nanodiamond powder electrode	1000 to 20000	120	377
poly(3,4-ethylenedioxythiophene) modified carbon screen printed electrode	Δ	1.72	381
poly(3,4-ethylenedioxythiophene)/ multiwalled carbon nanotube modified carbon screen printed electrode	Δ	0.96	381
Composite lead oxide modified carbon powder and epoxy resin	100 to 700	0.9	382
Glassy carbon modified with poly-Nile Blue film	0.5 to 100	0.1	383
Glassy carbon electrode modified with alternated layers of iron (III) tetra-(N-methyl-4-pyridyl)-porphyrin (FeT4MPyP) and copper tetrasulfonated phthalocyanine	0.5 to 7.5	0.1	384
Graphite screen printed microband	10 to 700	0.05	348
Glassy carbon modified with CuPtCl_6 film	0.1 to 2000	0.05	379
Glassy carbon modified with an electrodeposited copper nanoparticles/carbon nanotubes/chitosan film	0.1 to 2500	0.024	385
Carbon SPMA	10 to 100	5.24	This work

Δ = Not stated

Table 4.1 A summary of electrochemical reports for the detection of nitrite.

Gold Screen Printed Microelectrode Array (Gold SPMA)

To further investigate the potential applications of the screen printed microelectrode array and demonstrate the ease of use and versatility of the screen printed design, gold SPMA's were fabricated utilising a gold polymer ink (see Experimental section (4.1.2)). These electrodes are exactly the same as the carbon SPMA described above with the only difference being that the carbon work electrode surface is modified with a gold polymeric ink. The gold SPMA's were characterised using the electrochemical redox probe hexaammine-ruthenium (III) chloride in 0.1 M KCl at scan rate over the range 5 – 200 mV s⁻¹. Clearly, as was also determined using the carbon SPMA, use of the gold SPMA at slow scan rates results in a steady-state type response being observed where upon faster scan rates, the voltammetric profile becomes peak shaped. The gold SPMA sensor was utilised for the sensing of chromium (VI),^{386, 387} a heavy metal of significant interest which has been demonstrated to be electrochemically viable utilising gold-based electrodes, though the SPMA offers the first example of a gold screen printed microelectrode array. Chromium (VI) poses a great environmental threat, being around 100 – 1000 times more toxic than chromium (III).³⁸⁸ This increased hazardous status is attributed to the high oxidation potential and as a result of this fact the WHO recommends chromium (VI) to be limited to 0.05 mg L⁻¹ (0.96 µM) within groundwater.³⁸⁹ This restrictions imposed due to the highly toxic nature of chromium have a direct effect on a vast array of industries which utilise or produce chromium species as waste and as such the monitoring of chromium is of upmost importance in many sectors of society.

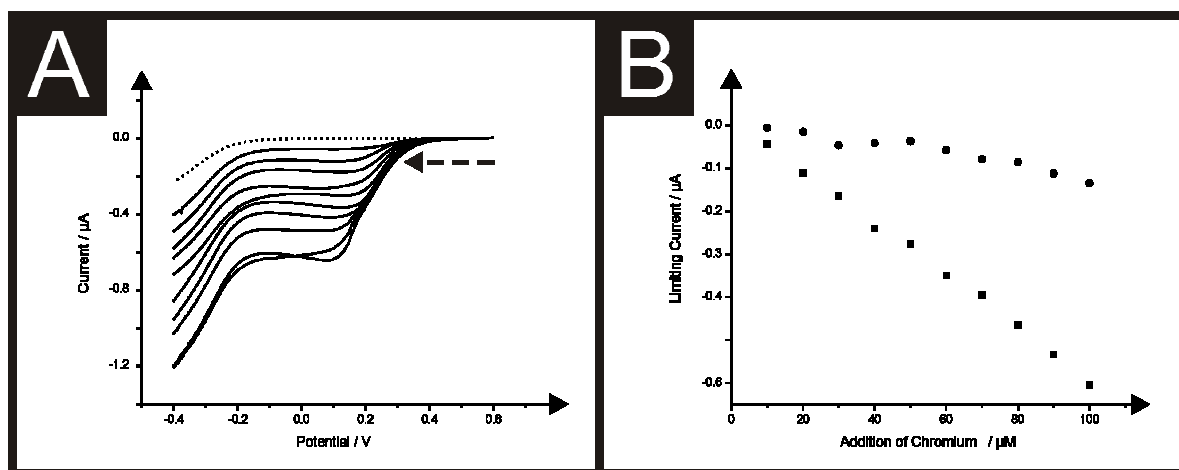


Figure 4.22 Linear sweep voltammograms recorded following the addition of chromium (VI) into a 0.05 M H₂SO₄ solution (dotted line) over the concentration range 10 – 100 μM using the gold SPMA (A). Typical corresponding calibration plots using the gold SPMA (squares) and a single electrode from the carbon SPMA (circles) (B). Scan rate: 5 mV s⁻¹. Dashed arrow signifies direction of scan.

First, linear sweep voltammetry was performed using the gold SPMA in 0.05 M H₂SO₄ at a scan rate of 5 mV s⁻¹, as depicted by figure 4.22A. Additions of chromium (VI) were made into the 0.05 M H₂SO₄ solution over the concentration range 10 to 100 μM, measured using linear sweep voltammetry as depicted in figure 4.22A. A linear response through the plot of voltammetric reduction peak height versus concentration (figure 4.22B) was found to be linear ($I_p / \mu A = 6.10 \times 10^{-3} \mu A / (V s^{-1})^{1/2} - 1.70 \times 10^{-2} \mu A; R^2 = 0.99; N = 10$) over the entire analytical range explored. The limit of detection utilising the gold SPMA for the sensing of chromium (VI) in 0.05 M H₂SO₄ was calculated (using 3σ in line with section 1.1.11) to correspond to 8.28 μM. The highly commendable % Relative Standard Deviations obtained at the carbon SPMA are maintained even when utilising the gold ink with a value of 2.81 % (N = 3) obtained for the sensing of chromium (VI) when using the gold SPMA further highlighting the intra-reproducibility and potentially broad applications of the SPMA. When comparing the obtained limits of detection for the monitoring of chromium (VI) through

utilisation of the gold SPMA to existing electrochemical reports present within the literature (table 3.1) it can be seen that the sensor is highly competitive and potentially analytically useful.

In order to assess the true viability of the gold SPMA for the sensitive detection of chromium (VI) in environmental samples, the sensing of chromium (VI) was explored in a canal water sample (sourced and pre-treated as reported in the Experimental section (4.1.2)). Linear sweep voltammetry was utilised as reported above in the ‘ideal’ 0.05 M H₂SO₄ solutions, for the measurement of low level additions of chromium (VI) over the concentration range 10 to 100 μM in the canal water sample. The gold SPMA was found to successfully facilitate the sensing of chromium (VI) over the entire analytical range, demonstrating a linear relationship ($I_L / \mu A = 6.30 \times 10^{-3} \mu A / \mu M - 1.95 \times 10^{-2} \mu A; R^2 = 0.97; N = 10$) between the quasi-limiting current and chromium (VI) concentrations even within the canal water sample as shown in figure 4.23 which potentially has other electroactive interferents present. Critically, when the calibration plots obtained under ‘ideal’ conditions are contrasted with those using canal water samples (figure 4.23), no deviation is notable in the sensitivity of the gold SPMA, emphasising the robust and reliable nature of the screen printed microelectrode array, even within such difficult media. Further to this, the limit of detection utilising the gold SPMA for the sensing of chromium (VI) in the acidified canal water sample was calculated (using 3σ in line with section 1.1.11) to be 9.46 μM, showing only a slight deviation from that calculated under ‘ideal’ conditions; such results indicate the gold SPMA sensors have potential for chromium (VI) sensing in environmental water samples.

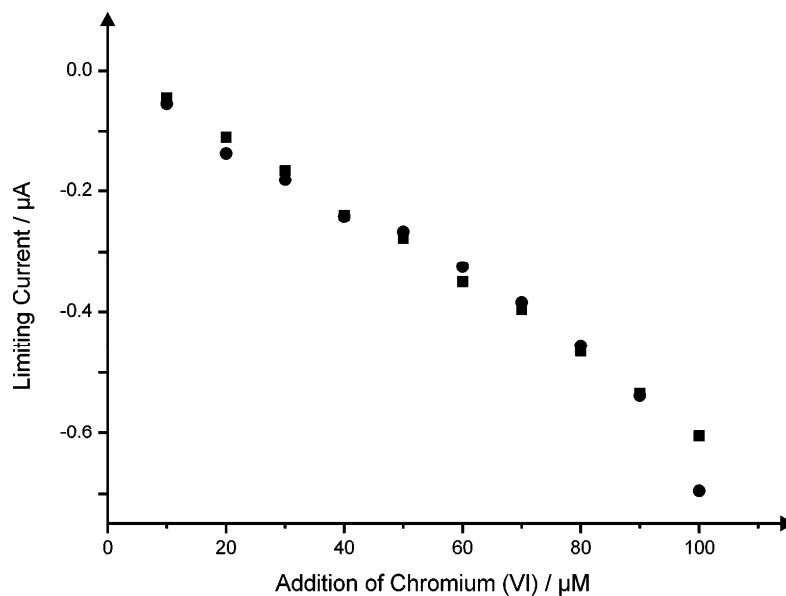


Figure 4.23 An overlay of typical corresponding calibration plots resulting from additions of chromium (VI) made into both an 'ideal' 0.05 M H_2SO_4 solution (squares) and a canal water sample (circles). Scan rate: 5 mV s^{-1} .

4.2.3 CONCLUSIONS

This section has demonstrated the successful fabrication of mass-produced disposable screen printed microelectrode arrays utilising both graphite and gold based inks demonstrating the versatility of the screen printing technique for the specific tailoring of sensors. The screen printed arrays were electrochemically characterised and contrasted with existing literature with the graphite screen printed microelectrode array benchmarked towards the detection of acetaminophen, dopamine and nitrite.

Similarly the gold based screen printed microelectrode array was benchmarked towards the sensing of the key analyte chromium (VI) with the analytical protocol further examined for the detection of chromium (VI) within canal water samples. Due to the availability of screen printable inks, other noble metal screen printed microelectrode arrays can be envisaged and given that these electrode can be mass-produced allowing single-shot

disposable sensors to be realised, researchers are able to translate laboratory derived electrochemical protocols into “the field”.

4.3 MICROBAND SCREEN PRINTED ELECTRODES

One alternative to recessed and multi microelectrode arrays which could allow for the yield of microelectrode benefits, but currents of a greater magnitude is a microband electrode. Such an electrode would comprise of a geometry which is in the micrometer range in one dimension, typically the electrode width, whilst being much greater in length. It is proposed that such an electrode may yield equal, if not greater benefits when compared to a microelectrode array whilst allowing for more simplistic fabrication *via* screen printing.

Within this section, containing published work,^[6] the possibility for the fabrication of such an electrode using screen printing is explored, with the sensor being applied towards the measurement of NADH and nitrite.

4.3.1 INTRODUCTION

The careful choice of working electrodes allow significant benefits in many areas of electrochemistry where the transition from macro- to micro- sized electrodes allows significant enhancements³⁹⁰ such as the ability to use reduced sample volumes, low background charging currents, improvements in the signal to noise ratio, application into resistive media such as samples which have low electrolyte concentrations and high current density arising from enhanced mass transport;¹⁰³ all of which ultimately leads to an increase in the sensitivity of the electroanalytical measurements.³⁹⁰ Such a beneficial response allows lower analyte concentration to be quantified with significant improvements in the electroanalytical sensitivity, ability to perform analyses on short time scales (μ -seconds)³⁹¹ and reduction in the limits of detection due to the enhanced mass transport of the target analyte towards the electrode surface due to the change in diffusion, which is typically linear at macro electrode, to that of convergent diffusion since the Faradaic current density

⁶ J. P. Metters, R. O. Kadara and C. E. Banks, *Sens. Actuators, B*, 201, **169**, 136.

increases with decreasing electrode dimensions while many contributors to the residual current are proportional to the area of working electrode.³⁹²

One of the most common electrode geometries is the micro-disc electrode which can involve sealing a microwire in an insulating material such as glass through to more scalable fabrication techniques such as lithography³⁹⁰ and screen printing.²⁴ It is well understood that convergent diffusion to micro-sized (and nano) electrodes provides the benefit of enhanced mass transport, this means that the current density (Amperes per unit area) at these individual electrodes is much greater than at a macro electrode under planar diffusion. However, there is a drawback, which is that the absolute current measured is much smaller, typically in the low microampere range which is problematic in electroanalytical applications, such as mains interference and instrumental difficulties when the quantification of dilute analyte concentrations are to be measured.³⁹³ To overcome this, arrays of microelectrodes which are wired in parallel are constructed which have fixed inter-electrode distances and if diffusional independence is observed on the experimental time scale then the current is simply the sum of currents exhibited at each electrode multiplied by the total number comprising the array.^{393, 394}

Another approach, but less utilised to overcome the observed low currents, is to fabricate the electrode as a microband and rather than a microdisc.^{390, 392} Band electrodes can be fabricated to be macroscopic in-length but microscopic in width allowing larger currents to be obtained compared to a microdisc due to the increased electrode area, whilst the width of the band is still maintained in the micrometre range to ensure convergent diffusion is still dominant, giving microelectrode characteristics identified above.^{390, 392}

In order to fabricate microband electrodes, thin metal films can be sandwiched between insulators, lithographic deposition of a thin metal strip on an insulating surface (line electrode)³⁹⁵ and also metal evaporation,³⁹⁶ sputtering^{392, 397} and chemical vapour

deposition³⁹⁸ can be utilised. Diamond ultra microband electrodes have been realised based on lithography and chemical vapour deposition.³⁹⁹ In order to scale up the fabrication process, microbands have been previously fabricated utilising screen printing where gold and platinum inks are printed onto a ceramic surface leaving a thin, typically ~ 10 micron thick layer.³⁹¹ Onto this, a Pyrex glass slide is glued resulting in the realisation of very thin platinum and gold microbands. An adaptation of this has been reported by Williams and co-workers³⁹¹ who reported upon microbands *via* screen printing a line of conductive ink (Au/Pt) typically 2- 8 mm in width and ~ 10 μm thick upon a ceramic surface. This is then screen printed with a polymer layer which is then cut perpendicular to the direction of the line.³⁹¹ Such an approach has been recently been adapted for electroanalytical applications.⁴⁰⁰⁻⁴⁰²

In this section the fabrication and implementation of graphite microband electrode produced exclusively by screen printing is described. The screen printed graphite microband electrodes are electrochemically characterised with their electroanalytical performance critically examined towards the electroanalytical sensing of NADH and nitrite.

in order to benchmark the microbands against literature reports where graphitic electrodes have been employed. The electroanalytical performance of the graphite microbands are found to be yield improvements over graphite screen printed macroelectrodes in terms of current density and graphite ultramicroelectrodes exhibit a greater current density than the graphite microband, greater reproducibility is observed using the graphite microbands due to the fabrication process; the reasons for this are discussed. The fabrication of the graphite microbands involves entirely screen printing and alleviates the need for sandwiching between insulators and dielectric polymer layers which is found to produce irreproducible analytical results suggesting the beneficial utilisation of the graphite microbands in a plethora of electrochemical applications.

4.3.2 RESULTS AND DISCUSSION

Characterisation of the Graphite Screen Printed Microband Electrodes

The graphite screen printed microband electrodes (denoted throughout as bSPE) were fabricated as detailed in the Experimental section (4.1.2). Inspection of the bSPE under optical microscopy, as depicted in figure 4.24, reveals the working electrode to be a solid graphite microband which is 10 mm in length and 100 μm in width. Energy-dispersive X-ray (EDAX) analysis was performed on the bSPE surface with typical values obtained using the semi-quantitative technique revealing the surface to consist of 7.80 % oxygen and 92.20 % carbon. Due to the emulsion screen used to define the microband electrodes, a carbon thickness of 5 μm is also produced. Also note, at the end of the band, as seen in figure 4.24, there is a slight deviation from a purely square end but should approximate diffusionally to that of a square end. Closer inspection as shown in figure 4.24D reveals the macroscopic surface to be similar to that reported previously.⁴⁰³

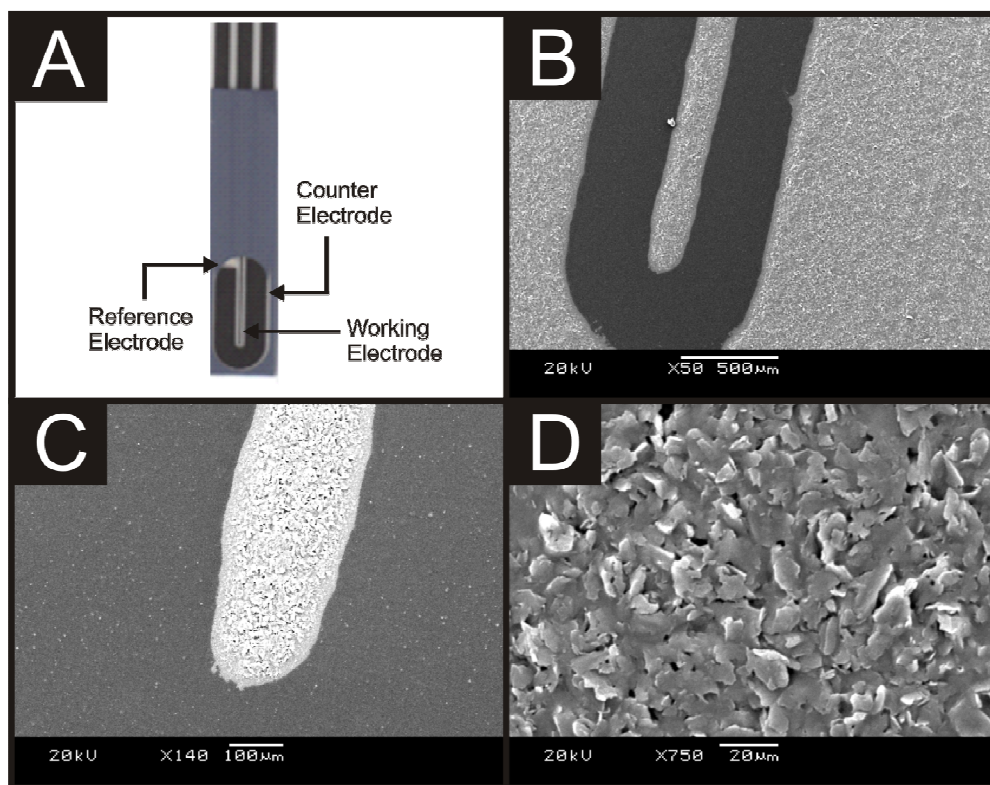


Figure 4.24 Optical and Scanning Electron Microscopy images of the bSPE. A: An optical microscopic image of the screen printed band electrode, B: SEM x50 magnification of the bSPE working area tip, C: SEM x140 magnification of the bSPE working area tip, D: SEM x750 magnification of the bSPE working area tip.

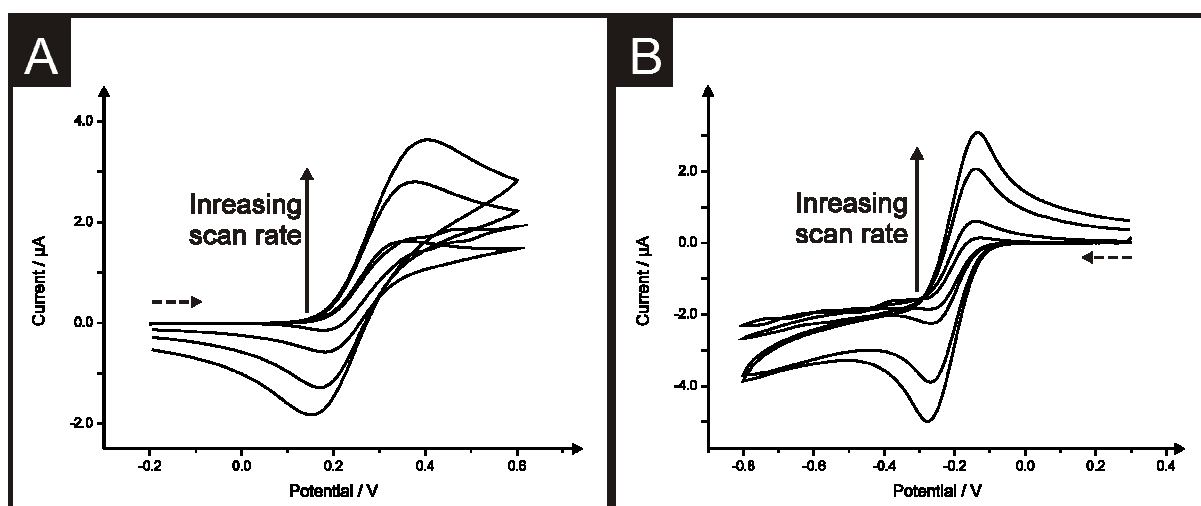


Figure 4.25 Typical cyclic voltammetric responses observed through scan rate studies using the bSPE at A: 1 mM potassium ferrocyanide in 0.1 M KCl and B: 1 mM hexaammine-ruthenium (III) chloride in 0.1 M KCl. Dashed arrow signifies direction of scan.

The bSPE were electrochemically characterised using the commonly utilised redox probes potassium ferrocyanide and hexaammine-ruthenium (III) chloride. Figure 4.25 depicts the electrochemical profiles of the bSPE using the redox couples over a range of voltammetric scan rates, where it is readily evident that at slow scan rates a steady-state type voltammetric profile is observed where upon faster scan rates, the voltammetric profile becomes peak shaped. This change of voltammetric profile is related to the diffusion layer thickness over the microscopic dimension of the band. The diffusion layer thickness, δ can be deduced through the use of equation (4.6) as described earlier. At slow scan rates, the diffusion layer is larger than the smallest dimension of the electrode (*viz* the microscopic band domain) such that the diffusional process is convergent in nature; such a response is typical of microelectrodes. At this point, the current can be described by the following:^{392, 396,}

404

$$I_L = 2\pi n F C D l \left[\frac{1}{\ln(4Dt\pi / w^2)} \right] \quad (4.8)$$

where, n is the electron number involved within the electrochemical process, F the Faraday constant, D the diffusion coefficient ($9.1 \times 10^{-6} \text{ cm}^2 \text{ s}^{-1}$)^{285, 286}, C the concentration of the analyte, l the band length, w is the width of the band and $t = RT / Fv$. Upon increasing the scan rate the diffusion layer becomes less or comparable to the size of the microscopic domain and consequently a peak-shaped response is evident. In this region the voltammetric current is given by the Randles-Ševčík equation, and for a simple reversible electron transfer process is given by;

$$I_p = 2.69 \times 10^5 n^{3/2} v^{1/2} D^{1/2} [A] w l \quad (4.9)$$

where n , is the number electrons involved in the electrochemical process, v the voltammetric scan rate, D the diffusion coefficient of the analyte, $[A]$ is the bulk concentration of the analyte, w is the band width and l is the band length.

At slow scan rates of 5 mV s^{-1} the theoretically expected current using the bSPE with the redox probe 1 mM hexaammine-ruthenium (III) chloride is determined, *via* equation (4.8) to correspond to $1.89 \times 10^{-6} \text{ A}$ which compares with $2.8 \times 10^{-6} \text{ A}$ observed experimentally; the slight deviation is likely due to a small contribution of linear diffusion³⁹⁷ which can be observed on the voltammetry in figure 4.25 which has some slight hysteresis. Using equation (4.9), the theoretically expected current using the bSPE with the redox probe 1 mM hexaammine-ruthenium (III) chloride is determined to be $9.02 \times 10^{-6} \text{ A}$ at 50 mV s^{-1} which compares to $1.72 \times 10^{-6} \text{ A}$ observed experimentally. Again, such a deviation is due to convergent diffusion still contributing.³⁹⁷ Thus in employing the correct scan rate the voltammetric response can be more akin to a microelectrode (slower scan rates) or act like that of a macro electrode (faster scan rates) which is of course related to the magnitude of the diffusion layer, as governed by equation (4.7) and also the diffusion coefficient of the electroactive species under investigation.

The inter-reproducibility of the fabricated batches ($N = 3$) of bSPEs was explored through comparison of cyclic voltammetric responses using 1 mM hexaammine-ruthenium (III) chloride / 0.1 M KCl. Analysis of the voltammetric data revealed the % Relative Standard Deviation to correspond to 0.92 % ($N = 3$) highlighting the reproducibility of the bSPE through the batches of fabricated electrodes.

Electroanalytical Applications of the Screen Printed Microband Electrodes

Next attention is turned to exploring the analytical applicability of the bSPE towards the electrochemical sensing of target analytes of interest. The bSPEs were trialled towards the detection of NADH and consequently contrasted with their macro counterparts namely, graphite screen printed macro electrodes as utilised in recent papers.^{104, 403, 405-407} The electrochemical oxidation of dihydronicotinamide adeninedinucleotide reduced form

(NADH) to the corresponding oxidized form (NAD⁺) receives considerable attention owing to its very important role as a cofactor in many naturally occurring enzymatic reactions, and mainly because of the potential application in over 300 NAD⁺/NADH-dependent dehydrogenase-based biosensors.^{241, 408-411}

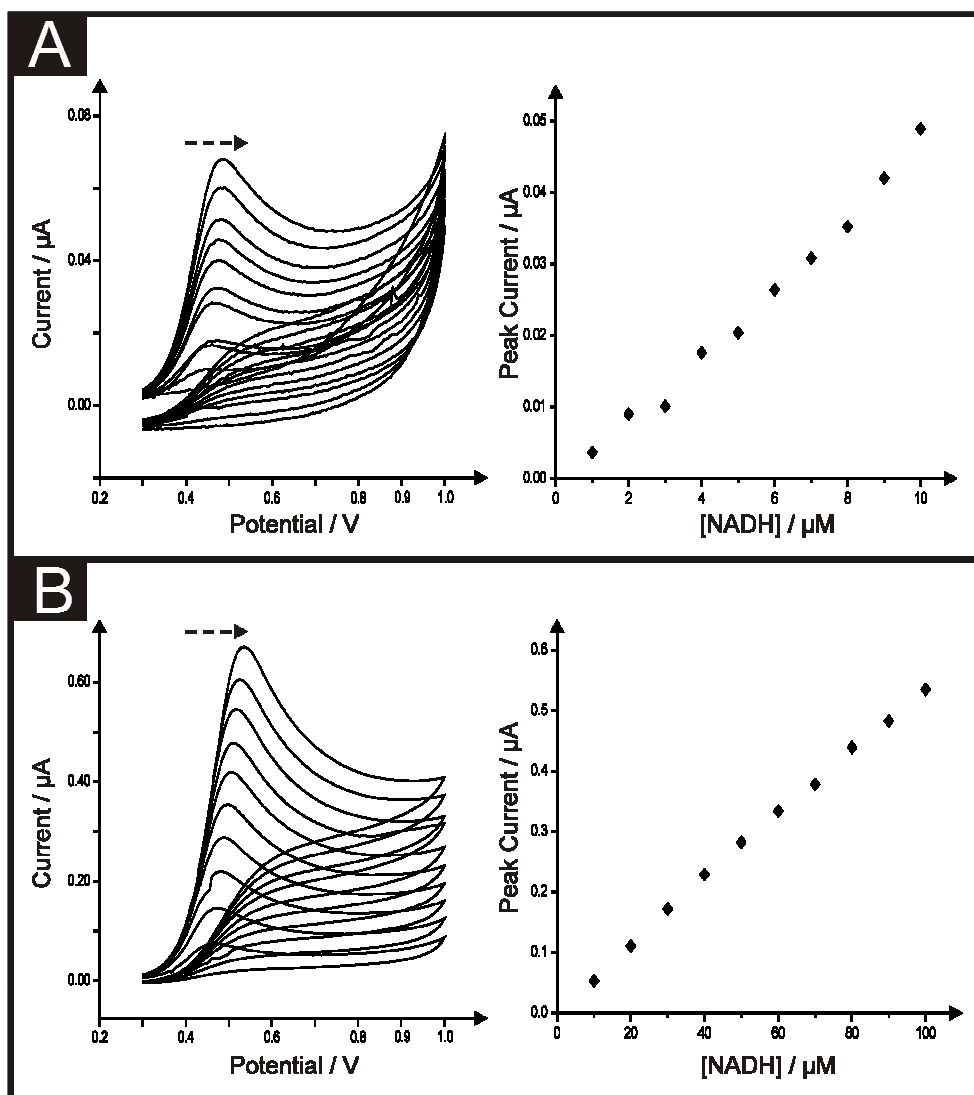


Figure 4.26 Typical cyclic voltammetric responses and their corresponding calibration plots resulting from additions of NADH into a pH 7 phosphate buffer using the bSPE; additions over the range A: 1 to 10 μM and B: 10 to 100 μM. Scan rate: 50 mV s⁻¹. Dashed arrow signifies direction of scan.

The response of cyclic voltammetry for the electrochemical oxidation of NADH was explored at the bSPE in a phosphate buffer (pH 7) with increasing concentrations of NADH.

It is important to develop sensors for use in pH 7 which is reflected in the choice of pH in the literature,⁴¹² whilst also being of physiological relevance. As shown in figure 4.26 the oxidation of NADH is evident at a potential of $\sim + 0.48$ V (vs. Ag/AgCl) in agreement with previous studies using graphitic electrodes⁴¹³ indicating a high proportion of edge plane like-sites/defects upon the electrodes surface.^{394, 414} The observed voltammetric peak height is observed (figure 4.26) to increase in magnitude upon additions of NADH over the range 1 to 100 μM ($I_p / \mu\text{A} = 4.91 \times 10^{-3} \mu\text{A} / \mu\text{M} + 2.57 \times 10^{-3} \mu\text{A}$; $R^2 = 0.99$; $N = 10$ and $I_p / \mu\text{A} = 5.32 \times 10^{-3} \mu\text{A} / \mu\text{M} + 9.02 \times 10^{-3} \mu\text{A}$; $R^2 = 0.99$; $N = 10$ for figure 4.26 A and B respectively). The corresponding calibration plots of peak height (μA) versus NADH concentration are depicted in figure 4.26 which are observed to exhibit linearity over the entire analytical range observed using the bSPE. The measurement was repeated using other bSPEs from the batch and a limit of detection for the sensing of NADH was calculated (using 3σ in line with section 1.1.11) to correspond to $0.48 \mu\text{M}$ ($N = 3$). Table 4.2 depicts the analysis of current literature reporting the electroanalytical sensing of NADH enabling us to benchmark the performance of the bSPEs. Such a limit of detection is favourable when compared with previous reports for the sensing of NADH, for example as reported by Marty *et al*⁴¹⁵ where carbon based screen printed sensors modified using Medola Blue reporting a limit of detection of $2.5 \mu\text{M}$. Ultra-low NADH detection limits ($0.16 \mu\text{M}$) have also been reported by Zen and co-workers⁴⁰¹ using mediator-less screen printed carbon electrodes, though the exceptionally low detection limits are attributed to the surface reorientation which is said to generate more edge plane arising from a pre-anodization procedure where the screen printed sensor used was electrochemically oxidised by applying a potential at $+ 2.0$ V (vs. Ag/AgCl).⁴⁰¹ A more laborious method reported for the detection of NADH involves the modification of a traditional gold macro electrode with a thin thiol film as described by

Behera and Raj⁴¹⁶, where both thiocytasine and mercaptopyrimidine were utilised to form the thiol films obtaining detection limits of 0.5 μM and 2.5 μM respectively.

Electrode Configuration	Linear Range (μM)	Limit of Detection (μM)	Reference
Chemically reduced graphene oxide modified glassy carbon electrode	40 – 800	10	294
Meldola's blue in $\text{SiO}_2/\text{TiO}_2$ graphite composite electrode	18 – 7290	8	417
Carbon nanotube/chitosan modified glassy carbon electrode	5 – 300	3	418
Graphite screen printed electrode electropolymerised with meldola's blue	Ω	2.5	415
Bifunctional poly(thionine) modified electrode	20 – 1000	1.74	419
Highly ordered mesoporous carbon modified glassy carbon electrode	5 – 900	1.61	420
Polycrystalline gold electrode modified with a thiocytosine film	0.5 - 57	0.5	416
bSPE	1 - 100	0.48	This Work
Carbon nanotube modified edge plane pyrolytic graphite electrode	8.2 – 108	0.3	413
Glassy carbon modified with	2 – 4.69	0.23	421

graphite nanosheets			
Electrochemically preanodised carbon screen printed electrode	Up to 100	0.16	401
Carbon nanofibre film modified glassy carbon electrode	0.2 – 686	0.11	422
Glassy carbon with deposition of silver nanoparticles incorporated poly(3,4-ethylene dioxythiophene-sodium dodecyl sulfate) (PEDOT _{SDS})	10 – 560	0.1	423
Meldola's blue functionalised carbon nanotubes	Upto 500	0.05	424

Ω = Value not provided

Table 4.2 A summary of electrochemical reports for the detection of NADH.

When comparing the bSPE with existing graphite based screen printed macro electrodes, where the working electrode area is 3 mm in diameter, current density plots as a function of NADH concentration, as shown in figure 4.27 demonstrate a greater sensitivity towards NADH is achieved using the bSPE; a gradient of 0.255 $\mu\text{A M}^{-1}$ and 0.548 $\mu\text{A M}^{-1}$ is evident on the macro and bSPE electrodes respectively where the improvement observed in the latter over the former here demonstrates the bSPE's superior efficiency per area of electrode in comparison to that of the standard macro electrode due to the microdomain exhibiting convergent diffusion over that obtained at the macro electrode.

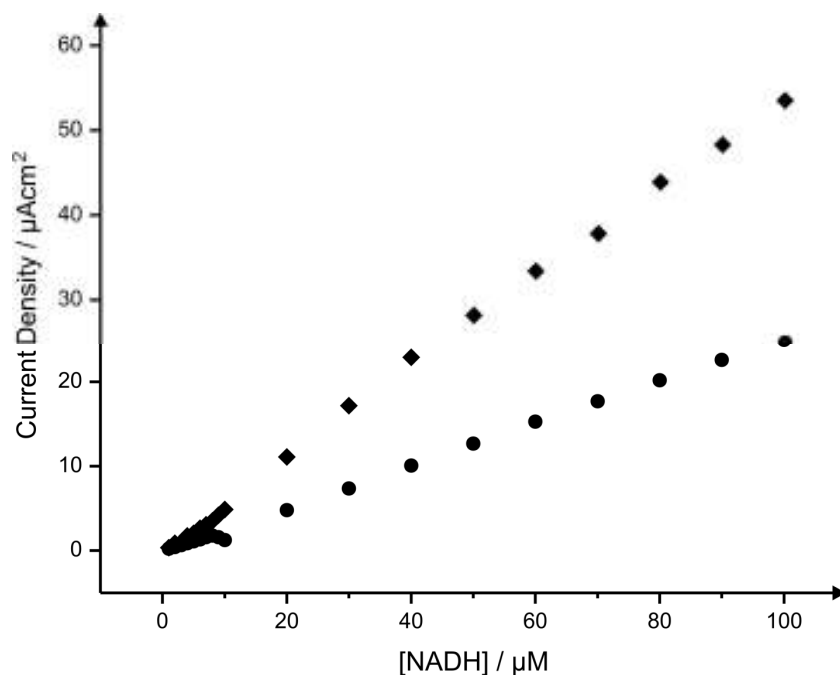


Figure 4.27 An overlay of typical current density calibration plots resulting from additions of NADH into a pH 7 phosphate buffer over the range of 1 to 100 μM using the bSPE (diamonds) versus a standard 3 mm diameter SPE (circles).

Previous work by Zen and co-workers⁴⁰⁰ has reported on the extension of the work by Williams and co-workers³⁹¹ upon the fabrication of ultramicroband electrodes (μbSPE) which are fabricated *via* a screen printing process which required the printing of the working, counter, and reference electrodes on top of one another, each separated by an insulating layer. The ultramicroband electrode is finally unveiled through the slicing off of the end of the screen printed surface. The study demonstrates the great potential versatility possessed through the use of screen printing fabrication methods as the dimensions of the band electrode can be tailored through both the screen printed film thickness and width. In addition to this, the ultramicroband electrodes demonstrated promising limits of detection towards the sensing of nitrite (0.38 μM) with linearity being observed up to concentrations of 3 μM .⁴⁰⁰ Similarly more recently, Honeychurch *et al*⁴⁰² have reported on the use of disposable sensors fabricated through screen printing techniques for the measurement of lead in acetate leachates

from ceramic glazed plates. The microband electrode was created through the modification of a 3×3 mm based screen printed sensor as previously reported⁴²⁵⁻⁴²⁸, where the end of the working electrode was cut-off perpendicular to the screen printed carbon track exposing a 2 mm wide section of the carbon connection strip, sandwiched between the insulating layer and PVC substrate, hence forming the microband electrode ($2 \text{ mm} \times 20 \mu\text{m}$).⁴⁰²

Though both Zen⁴⁰⁰ and Honeychurch⁴⁰² propose exciting analyte detection limits through miniaturised electrodes in the form of screen printed ultramicroband electrodes, reservations must be upheld regarding the final fabrication processes which involve the mechanical cutting of the screen printed surface to unveil the ultramicroband. It is undoubtedly possible that through the forces involved in the mechanical process of cutting through the screen printed surface so closely to the final working electrode surface, that the insulating layer encasing the working surface may lift slightly unveiling a third dimension to the proposed “two-dimensional” working surface which would then include the parameter depth in addition to the proposed length and width. Such an occurrence would clearly result in an alteration in the observed response due to the increased working electrode area available to the solution, whilst also affecting the potential reproducibility of the band electrode.

Figure 4.28 shows a schematic representation of potential problems occurring when utilising the fabricated ultramicroband produced by cutting (other layers ignored). The fundamental problem associated with this method of fabrication is that the cutting pulls the dielectric away from the graphite microband, such that at slow scan rates, convergent diffusion dominates as soon as the volume of solution contained within the expanded/raised area between the dielectric and graphite is electrochemically exhausted. At faster scan rates, linear diffusion dominates and is the summation of horizontal and vertical mass transport. Such a response has been obtained for thin metals trapped within glass which are not sealed properly.³⁹⁵ Such changes in the mass transport regime, which are not controllable and

dependent upon cutting, could clearly contribute to the observed (variable) electrochemical response.

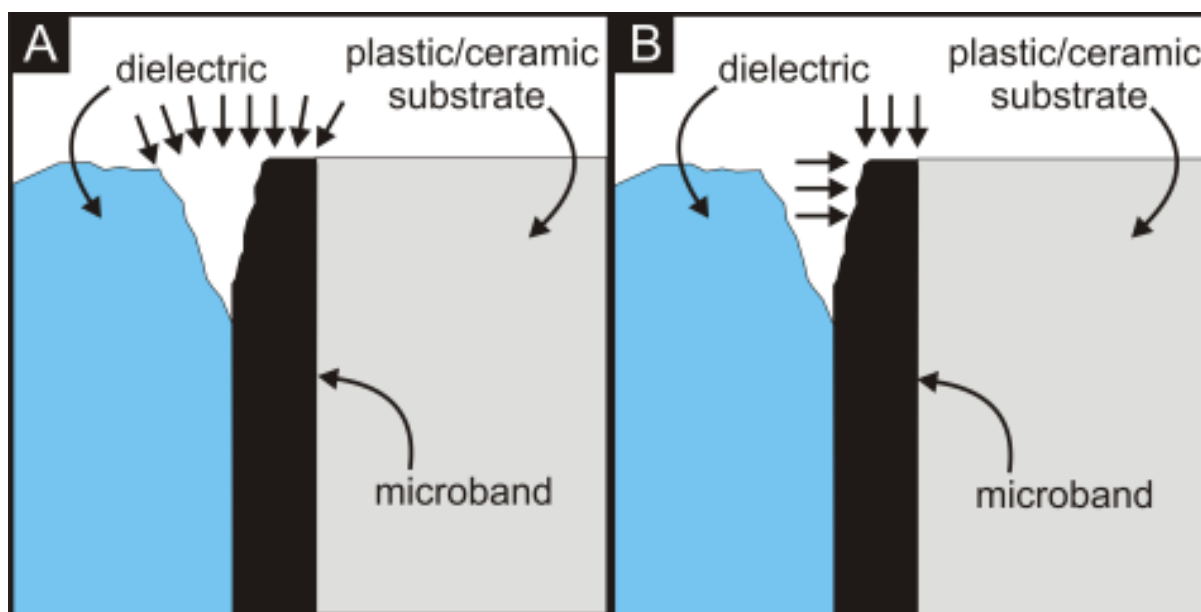


Figure 4.28 A schematic representation of convergent diffusion (A) and linear diffusion (B) at μ SPEs which arise from cutting with scissors.

In order to assess the reproducibility of band electrodes created in a similar fashion to the work of Zen⁴⁰⁰ and Honeychurch⁴⁰², the μ SPE (see figure 4.24) were cut at the very base of the carbon working electrode where the insulating layer ceases, thus forming a microband electrode with the width of the microband now defining its length and the height of the printed graphite layer now defining its width; instantly a ultramicroband electrode is fabricated. As shown in figure 4.29 additions of NADH over the analytical range of 1 to 40 μ M, were made to a phosphate buffer solution (pH 7) using three separately fabricated μ SPE. It is instantly apparent that the suggested drawbacks with such methodologies relating to the reproducibility of the μ SPE are well-founded, where it is likely that the cutting lifts up the dielectric, resulting in changes to the mass transport in addition to the geometric area as depicted in figure 4.28. Such an approach has benefits in the improvements in mass transport in going from a microband (figure 4.24) to an ultramicroband but is a play-

off with the lack of reproducibility. Additionally in the work of Zen *et al* and Honeychurch *et al*, the dielectric layer might be better bonded to the underlying graphite layer such that less departure of the graphite layer from the dielectric is realised (see figure 4.28). After determining that the bSPE offered improved sensitivity (current density) to macro carbon SPEs and the potential drawbacks to the use of μ bSPEs, the bSPE were explored for the sensing of nitrite.

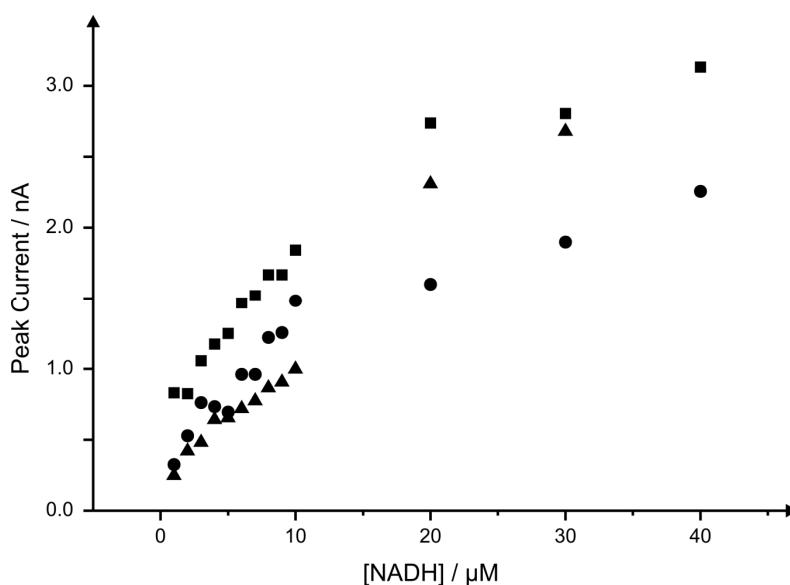


Figure 4.29 Calibration plots resulting from additions of NADH in a pH 7 phosphate buffer, over the range 1 to 40 μ M at three separate μ bSPE.

First, in order to find the pH dependence of the electrochemical oxidation of nitrite using the bSPE, cyclic voltammograms were recorded at a scan rate of 50 mV s^{-1} in 1 mM nitrite solutions of various pHs from 1 to 12. The obtained cyclic voltammograms show an oxidation peak shifting between $\sim + 0.6 \text{ V}$ and $+ 1.0 \text{ V}$ (*vs.* Ag/AgCl) dependent upon pH. The voltammograms were then analysed through a plot of peak potential, E_P , at each pH, as depicted in figure 4.30. The oxidation of nitrite is found to be essentially independent of pH for solutions of pHs higher than 4 (the pKa for nitrous acid, HNO_2 , is between 3.2 and 3.4⁴²⁹⁻⁴³¹). Such observations are in excellent agreement with previous literature using graphite

electrodes.⁴³²⁻⁴³⁵ The mechanism for nitrite oxidation at solid electrodes has been previously thoroughly investigated on graphitic electrode,^{432, 434, 436} with the following proposed:



where k^0 is the standard electrochemical rate constant and k is the association rate constant for nitrous acid (HNO_2). The chemical step (equation (4.10)) accounts for the reduction in current at pH values below the pKa of HNO_2 .⁴³² It is highly likely that this mechanism is in operation on the bSPE.

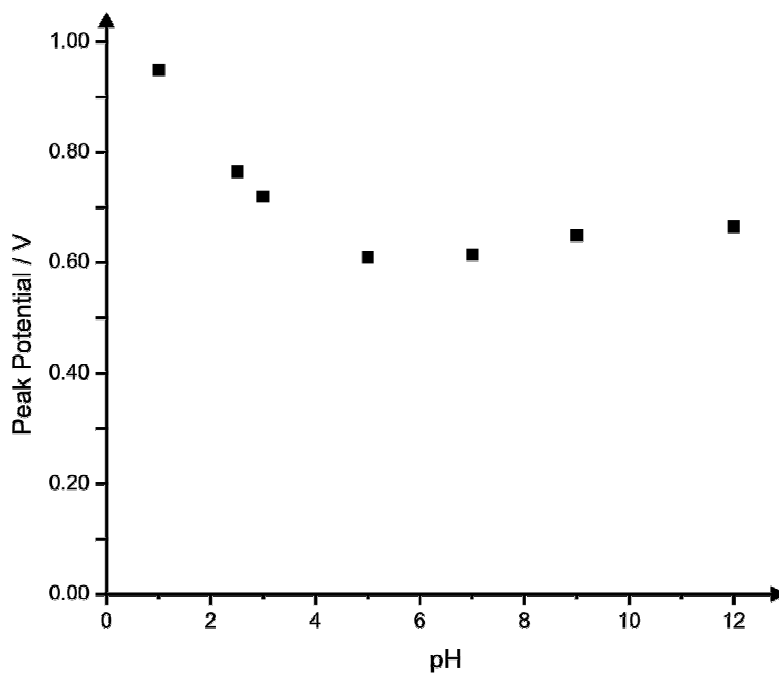


Figure 4.30 Peak potential dependence on solution pH for oxidation of 100 μ M nitrite on a bSPE over the pH range 1 to 12 using the bSPEs.

The response of nitrite was explored using the bSPE through cyclic voltammetry which exhibited a peak potential of $\sim +0.6$ V (vs. Ag/AgCl) in a phosphate buffer (pH 5), over the concentration range 10 to 700 μ M. As is shown in figure 4.31, calibration plots

corresponding to additions of nitrite monitored through cyclic voltammetric studies show linearity over the entire analytical range studied ($I_p / \mu A = 7.27 \times 10^{-3} \mu A / \mu M + 1.79 \times 10^{-1} \mu A$; $R^2 = 0.99$; $N = 16$). The limit of detection (using 3σ in line with section 1.1.11) was determined to be $0.05 \mu M$ ($N = 3$). Such a low limit of detection and extensive linear range obtained when using the bSPE compare well with previous literature reporting on the sensing of nitrite; table 4.1 depicts an analysis of the literature reports. Crossley and co-workers³⁰³ reported nitrite sensing with $0.6 \mu M$ stated as the limit of detection at a copper oxide-graphite composite electrode. Similarly within reference³⁰³, other previous literature reports for the sensing of nitrite are tabulated, with only a glassy carbon electrode with a thin film of mixed-valent $CuPtCl_6$ deposited upon the surface as reported by Pei *et al*³⁰⁵ seen to demonstrate an improved limit of detection in comparison with the bSPE at the ultra-low nitrite concentration of $0.05 \mu M$; such improvements may likely be attributed to the microscopic domain (exhibiting convergent diffusion) of the microband.

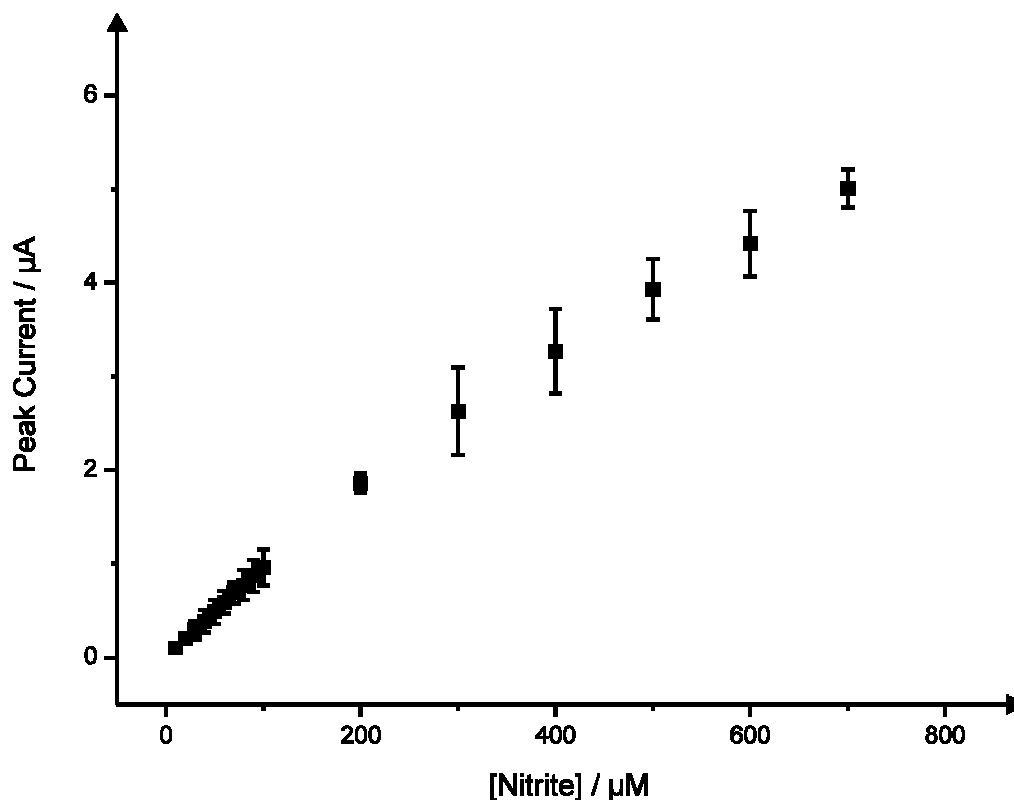


Figure 4.31 A typical calibration plot corresponding to the addition of nitrite over the range of 10 to 700 μM at the bSPE using cyclic voltammetry. Scan rate: 50 mV s^{-1} .

4.3.3 CONCLUSIONS

This section has explored the development, characterisation and application of novel, disposable, single-shot screen printed microband electrodes with their analytical performance towards the sensing of NADH and nitrite being compared and contrasted with existing studies. Improvements over graphite macroelectrodes and other electroanalytical approaches for the target analytes are evident due to the microdomain feature of the microband electrode exhibiting improvements in mass transport. Comparisons have been made with ultramicroband electrodes and while our screen printed microband electrodes do not compare in terms of mass transport due to the formers unique geometry, the lack of reproducibility of the former is evident, suggesting that the microband electrodes are a superior approach which can be readily fabricated on a larger volume scale. It is envisaged that such microband

electrodes could also be tailored such that the graphite surface can be modified, for example, with enzymes for use in biosensors utilising the improvements in mass transport from the microband geometry as well as being modified with gold and platinum inks.

4.4 SCREEN PRINTED MICROBAND ELECTRODES: REDUCING THE MICROSCOPIC SIZE

Owing to new developments in screen printing technology, specifically the screens utilised for electrode fabrication, the ability to build upon the foundations laid by the 100 μm microband through the fabrication of a 50 μm microband was realised.

The study within this section has been published^[7] where the electrochemical characterisation of this new microband electrode is described, which through the utilisation of newly available screen printing materials, allows for the fulfilment of the development and fabrication of an improved microband electrode; the first of its kind. Furthermore comparison between the two microband dimensions fabricated is provided determining the validity for the utilisation of such a sensor.

4.4.1 INTRODUCTION

The beneficial attributes of microelectrodes is an area which is well documented with an abundance of reports to be found within the literature.^{393, 402, 437-445} Microelectrodes offer many advantages compared with macro-sized electrodes, such as a lower ohmic drop, improved faradic/capacitive currents ratio (lower interfacial capacitance), faster mass-transport rates and steady-state currents without reverting to forced convection.⁴³⁷⁻⁴⁴⁰ However the manufacture of microelectrodes generally requires a number of relatively involved manufacturing steps, and does not readily lend itself to commercialisation.

A variant on the traditional co-planar disc-shaped microelectrode which continues to gather further interest is the microband electrode.^{397, 400-402, 442, 443, 446} Band electrodes can be fabricated to be macroscopic in-length but microscopic in width.⁴⁴⁶ Such an electrode configuration is reported to offer the additional advantage of allowing larger currents to be

⁷ J. P. Metters, R. O. Kadara and C. E. Banks, *Analyst*, 2013, **138**, 2516.

obtained compared to a microdisc due to the increased electrode area, whilst the width of the band is still maintained in the micrometre range to ensure convergent diffusion is still dominant, giving rise to the microelectrode characteristics identified above.^{390, 392, 446}

Screen printing enables extensive control over the tailoring and fabrication of electrochemical sensors which require intricate designs and offers the ability to scale up the fabrication process. Microbands fabricated partially through screen printed have been reported where gold and platinum inks are printed onto a ceramic surface leaving a thin, typically $\sim 10\ \mu\text{m}$ thick layer.³⁹¹ Onto this, a Pyrex glass slide is glued resulting in the realisation of very thin platinum and gold microbands. An adaptation of this has been reported by Williams and co-workers³⁹¹ who reported upon microbands *via* screen printing a line of conductive ink (Au/Pt) typically 2–8 mm in width and $\sim 10\ \mu\text{m}$ thick upon a ceramic surface. This is then screen printed with a polymer layer which is then cut perpendicular to the direction of the line.³⁹¹ Such an approach has been recently been adapted for electroanalytical applications by Hart and Zen independently^{400-402, 447} where ultramicrobands produced as described above were trialled towards the sensing of lead in acetate leachates⁴⁰² and determination of reduced glutathione.⁴⁴⁷ However, the reproducibility of the electrodes fabricated in this manner is questionable.⁴⁴⁶ Additionally as has been described within the previous section the production of a screen printed microband electrode of 100 μm in diameter which was demonstrated to offer noteworthy analytical performances when benchmarked towards the sensing of selected analytes.⁴⁴⁶

In this section, due to recent developments in screen printing technology, is presented the fabrication, electrochemical characterisation and potential analytical application of an entirely screen printed co-planar microband, printed in both graphite and gold, of 50 μm in width which is shown to be viable for the first time.

Graphite screen printed microband electrodes

The graphite screen printed microband electrodes (denoted throughout as graphite-50bSPE) were fabricated as detailed in the Experimental section (4.1.2) with a working electrode dimension of 50 μm in width and 20 mm in length (see figure 4.32). The previous section described the fabrication of a screen printed graphite microband with a width of 100 μm ⁴⁴⁶ having determined through empirical evaluation that 100 microns is the smallest feature that can be reproducibly fabricated using the current commercially available inks and screens; with a geometry smaller than 100 microns producing a largely variable sized width throughout the screen printed batch.⁴⁴⁶ The ability to fabricate a screen printed microband electrode with a width of less than 100 microns was facilitated through the recent development of a V-mesh; an alternative to the more traditionally utilised stainless steel and polyester meshes for the production of screens.¹¹² The V-mesh is produced by using filaments of Vecry, a hybrid fibre with both unique construction and characteristics. Vecry is a sheathed filament surrounding a liquid crystal based polymer core, and can be woven into a high “Open Area” construction having very fine filaments.¹¹² The main advantages of the V-mesh include very high tensile strength – greater than stainless steels, critically this higher tension enables screen peel to occur with less snap-off, enhancing paste release without reducing gasketing and the risk to both edge definition and “overfilling” of the print volume.¹¹² Further attributes such as very low elongation with a high elastic recovery, low sensitivity to changes in temperature and humidity, outstanding abrasion resistance and to the fibrillation typical in other “super fibres” and excellent response to the UV wavelengths used in pattern exposure are also offered through the utilisation of a V-mesh within the screen printing process.¹¹² It is important to note that although successful printing of both graphite-50bSPE was possible, only a limited number of graphite-based sensors could be produced

before blocking effects began to occur within the screen. These blocking effects are attributed to the uneven particle size and distribution within the graphite ink in combination with the small width of the electrode design; a further discussion on this is presented towards the end of this communication.

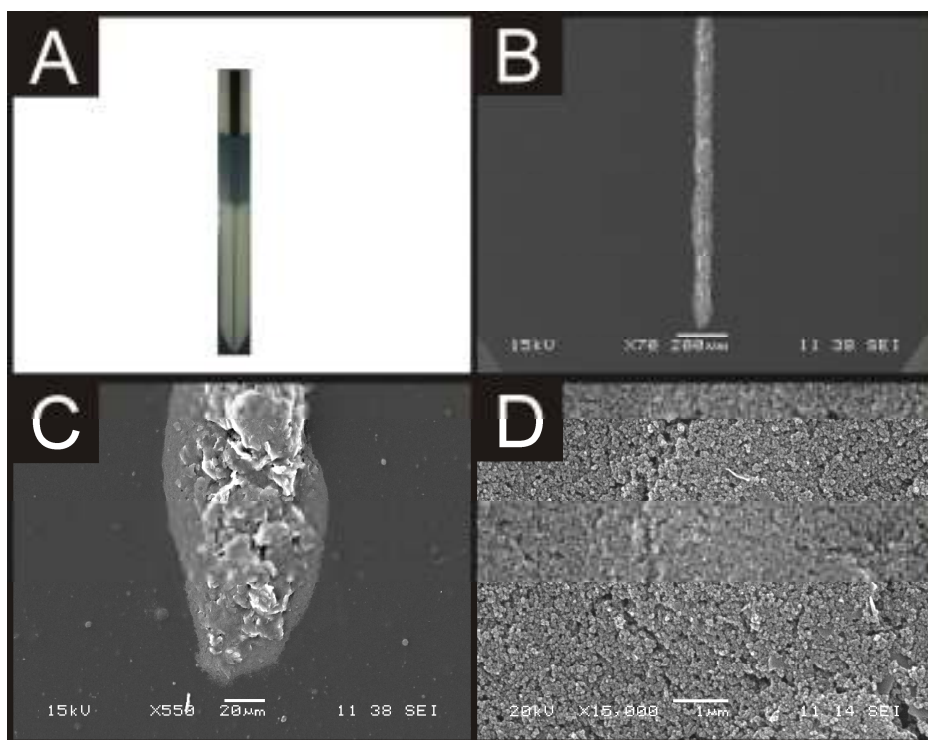


Figure 4.32 Optical and Scanning Electron Microscopy images of the 50 μm graphite-50bSPE. A: An optical microscopic image of the screen printed band electrode, B, C, D: SEM magnification of the bSPE working area.

As is depicted in figure 4.32 a well formed graphite band was possible through utilisation of screen printing, with the resultant band exhibiting a typical screen printed carbon-graphite structure as has been well reported within the literature.^{70, 104, 293, 405} It is however noted that under high magnification it is clear that a slight deviation from a perfectly straight microband occurs. Further to this it was apparent that during the screen printing process of the graphite layer for the production of the 50 μm microband, only a small number of prints (~ 5 sheets) was possible prior to the V-mesh becoming blocked with the larger

sized particles present within the graphite ink which requires cleaning before further use. Of the electrodes fabricated, less than 5 % were determined to fail quality control testing using the redox probe hexaammine-ruthenium (III) chloride. Although such a value is not excessive, such an occurrence provides a potentially significant potential problem when considering large scale fabrication of such sensors but allows small numbers to be readily produced.

First the electrochemical characterisation of the graphite-50bSPE was undertaken using 1 mM hexaammine-ruthenium (III) chloride / 0.1 M KCl through scan rate studies over the range 5 – 200 mV s⁻¹ which revealed a linear response ($I_p / \mu A = -2.02 \times 10^{-1} \mu A / (V s^{-1})^{1/2} - 1.93 \mu A; R^2 = 0.99; N = 8$) realised through the plot of voltammetric peak current (μA) versus the square root of scan rate. It is readily evident that at slow scan rates a steady-state type voltammetric profile is observed where upon faster scan rates, the voltammetric profile becomes more peak-shaped. This change of voltammetric profile is related to the diffusion layer thickness over the microscopic dimension of the band since as the scan rate is increased linear diffusion predominates resulting in peak shaped voltammetry.⁴⁴⁶

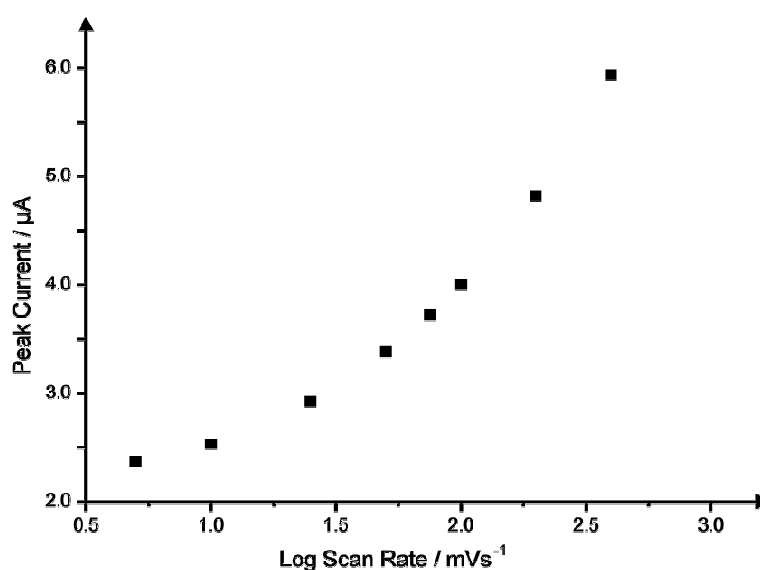


Figure 4.33 Dependence of the peak current on the voltammetric scan rate obtained in 1 mM hexaammine-ruthenium (III) chloride / 0.1 M KCl using the graphite-50bSPE.

At band electrodes of micrometre dimensions, and under conditions of non-linear diffusion, Wehmeyer and co-workers have shown that the faradaic current can be predicted by the equation for the current at a hemicylinder of equivalent area:³⁹²

$$i = 2\pi nFDCl[1/(\ln 4\Theta)] \quad (4.13)$$

where n is the number of electron involved in the reaction, F the Faraday constant, D the diffusion coefficient of hexaammine-ruthenium (III) chloride, C the concentration of the redox probe, l (cm) is the length of the microband, and $\Theta = Dt/(w/\pi)^2$ where w (cm) is the width of the band and $t = RT/Fv$. Under experimental conditions with $w = 50 \mu\text{m}$ and $l = 0.2 \text{ cm}$, the theoretical current was calculated at a scan rate of 5 mV s^{-1} to be $0.01 \mu\text{A}$. Interestingly however, the experimental current at the given scan rate was determined to be $2.35 \mu\text{A}$. Figure 4.33 depicts the response of current plotted against \log_{10} of scan rate. For a true band electrode, the current should be identical over the scan rates studied,³⁹² however as can be observed, around 25 mV s^{-1} the deviation from ideality occurs which is indicative of the change of diffusion regimes from that of convergent/radial to that of linear/planar; this is consistent with the qualitative change in the shape of the observed voltammetric signatures. The deviation observed between that in the current predicted *via* equation (4.13) and that observed experimentally is since the fabricated microelectrode is not a true microelectrode and the contribution from linear/planar diffusion is still significant.³⁹⁷

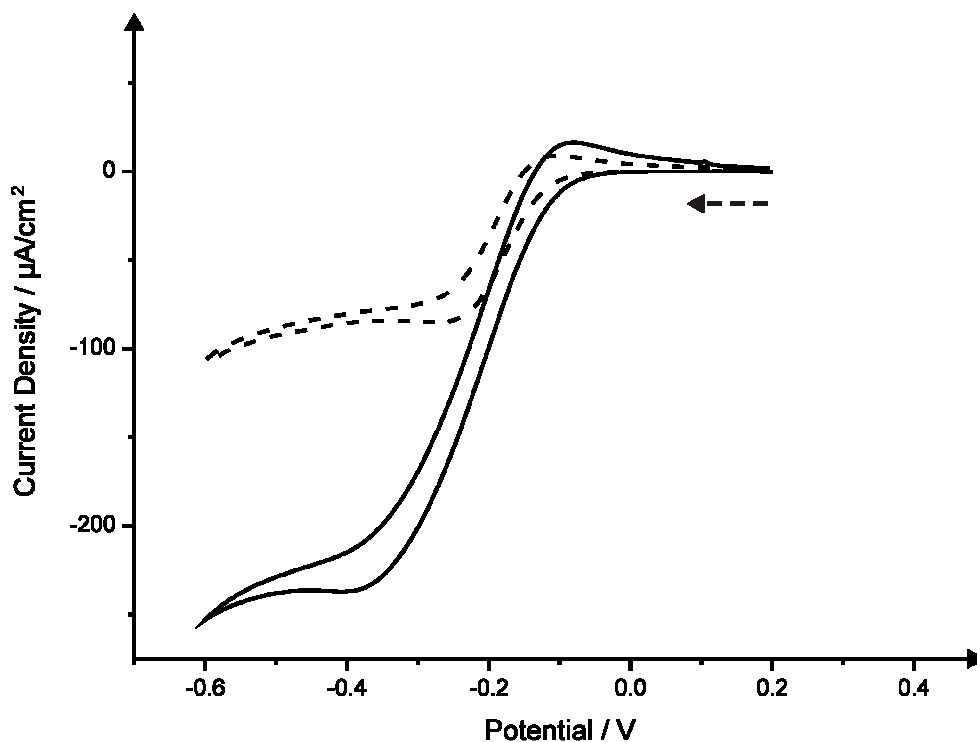


Figure 4.34 Cyclic voltammetric traces obtained in 1 mM hexaammine-ruthenium (III) chloride / 0.1 M KCl) using the graphite-50bSPE (solid line) and graphite-100bSPE (dashed line). Scan rate: 5 mV s^{-1} . Dashed arrow signifies direction of scan.

Next comparison was sought between the observed voltammetric responses obtained utilising the 50 μm graphite-50bSPE and a 100 μm graphite-bSPE of the same length. Figure 4.34 shows an overlay of the cyclic voltammetric responses at each of the sensors upon the implementation of a scan rate of 5 mV s^{-1} . It is important to note that each of the microbands, although varying in width, comprise the same working electrode length of 20 mm, yet interestingly a greater current density is readily observed at the 50 μm graphite-50bSPE over that of 100 μm where the enhanced diffusive mass transport arises at the former resulting in very large current densities to be observed.

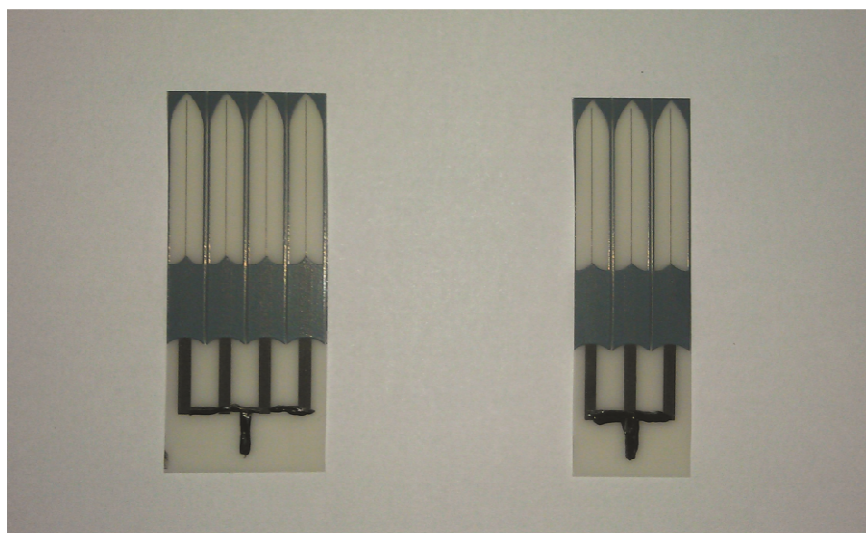


Figure 4.35 Image of the graphite-50bSPE arrays, left $N = 4$ and right $N = 3$.

Additionally a band array can be readily constructed through the simultaneous electrical connection of multiple $50\ \mu\text{m}$ graphite-50bSPE (see figure 4.35) where an improvement in the observed voltammetric peak current is readily observed. Figure 4.36 depicts cyclic voltammetric responses obtained in $1\ \text{mM}$ hexaammine-ruthenium (III) chloride / $0.1\ \text{M}$ KCl using a single $50\ \mu\text{m}$ graphite-50bSPE and additionally using an array comprising three and four of the $50\ \mu\text{m}$ graphite-50bSPEs. As would be expected, since the microband are positioned far from each other; they do not have any diffusional interaction at the chosen experimental scan rate. This is determined as it is inferred that the diffusion layer (in 3D) is given by equation (4.6) (detailed earlier). Considering the graphite-50bSPE arrays shown in figure 4.35, there should be no diffusion layer interaction between neighbouring microelectrodes such that the diffusion layer, δ , must be less than f_{greater} ; equation (4.7). When a single array comprising three graphite-50bSPE is utilised, $N = 3$ while when four graphite-50bSPE is used, $N = 4$, the diffusion layer, δ , can be estimated over the range of experimentally utilised scan rates which spans between 112.7 and $567.5\ \mu\text{m}$ for the fastest ($200\ \text{mV s}^{-1}$) and slowest ($5\ \text{mV s}^{-1}$) applied voltammetric scan rates respectively for the three

electrode graphite-50bSPE array and between 120.2 and 622.6 μm for the four electrode graphite-50bSPE array. Using equation (4.7) f_{greater} was deduced for the graphite-50bSPE to equate to 2475 μm . Thus given that the diffusion layer will reach a maximum of 509.1 μm at the slowest applied voltammetric scan rate ($N = 4$), the graphite-50bSPE has no diffusional interaction/overlapping diffusion layers between the electrodes comprising the array.

An increase in the number of graphite-50bSPE results in a uniform increment in the observed peak current with an array comprising three of the microbands resulting in a current almost three times greater than that observed at the single microband (3.11 x increase), with an array comprising four of the microband electrodes producing a voltammetric current increase of around four times over that observed at the single microband electrode (4.22 x increase). Clearly, if one needs to amplify the response, the microbands electrically wired together can produce enhancements; future work will consider their electroanalytical application.

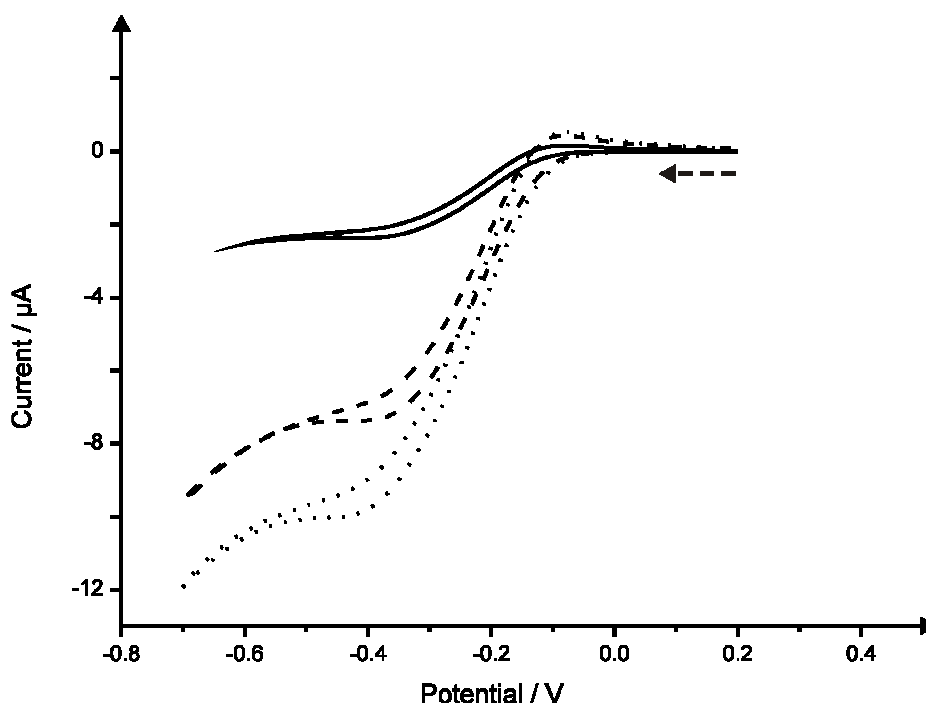


Figure 4.36 Typical cyclic voltammetric traces obtained in 1 mM hexaammine-ruthenium (III) chloride / 0.1 M KCl) using the graphite-50bSPE (solid line) and at arrays of graphite-50bSPE; $N = 3$ (dashed line) and $N = 4$ (dotted line). Scan rate: 5 mV s^{-1} . Dashed arrow signifies direction of scan.

Following the electrochemical characterisation of the graphite-50bSPE the microband was utilised for the sensing of NADH which was, as has been discussed earlier within this Chapter, a key analyte of interest within the literature and also allowed for comparison between the behaviour of the graphite-50bSPE and previously described bSPE (section 4.3). The sensing of NADH was explored with additions of increasing concentrations over the range of 1 to 10 μM into a 0.1 M phosphate buffer of pH 7.4. A buffer of \sim pH 7 was selected due to the plethora of reports present within the literature detailing such experimental conditions⁴⁴⁸ but also as a neutral pH reflects that of which such a biological sample is likely to reside.

Figure 4.37A shows the cyclic voltammetric responses obtained over the analytical range studied. When utilising the graphite-50bSPE the electrochemical oxidation of NADH is found to occur at $\sim + 0.5$ V (*vs.* SCE). Evidently upon an increase in the NADH concentration an improvement in the magnitude of the voltammetric peak current is observed with a linear response ($I / \mu\text{A} = 3.6 \times 10^{-3} \mu\text{A} / \mu\text{M} + 4.3 \times 10^{-4} \mu\text{A}; R^2 = 0.99; N = 10$) through the plot of voltammetric peak current (μA) versus NADH concentration (see figure 4.37B).

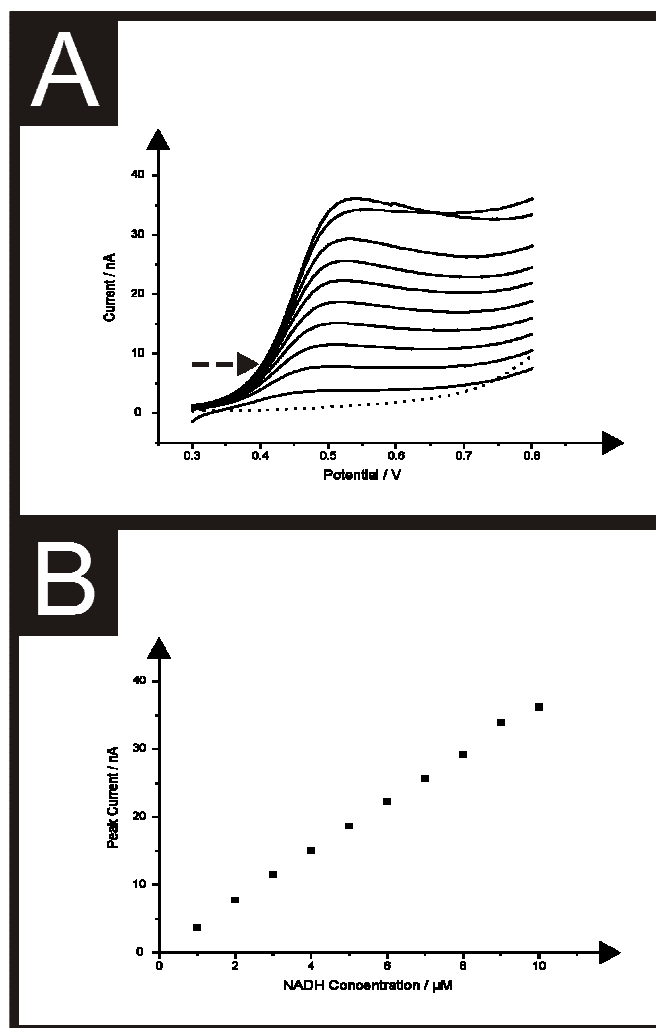


Figure 4.37 A) Typical cyclic voltammograms arising from additions of NADH in to a pH 7.4 buffer using the graphite-50bSPE. Scan rate: 5 mV s^{-1} . Dashed arrow signifies direction of scan. B) A corresponding calibration plot from A) over the range studied (1 – 10 μM) NADH.

Consequently, a limit of detection (using 3σ in line with section 1.1.11) of $0.24 \mu\text{M}$ was determined for the sensing of NADH using the $50 \mu\text{m}$ graphite-50bSPE. This obtained limit of detection is seen to improve upon that obtained when utilising the $100 \mu\text{m}$ width graphite screen printed microband where a limit of detection (using 3σ in line with section 1.1.11) of $0.48 \mu\text{M}$ for the sensing of NADH.⁴⁴⁶ Similarly, improvements over other bare carbon macro electrode configurations is evident^{413, 414} due to improvements in mass transport through the use of the microband.

Gold screen printed microband electrodes

To further understand and explore the potential applications of the microband electrodes gold screen printed microband sensors (denoted throughout as gold-50bSPE) of the same dimensions were also successfully fabricated as detailed in the Experimental section (4.1.2). In contrast with the graphite-50bSPE, no such blocking effects were observed when utilising the gold ink during the screen printing process, likely due to the ink consisting of smaller sized particles. As with the graphite-50bSPE, the gold-50bSPE was first characterised using SEM analysis, shown in figure 4.38, evidently the resultant microband is uniform with the gold particle size being in the very low micron range. Such observations deviate from that observed in figure 4.32C where much larger graphite particle sizes are readily apparent which provides a clear indication as to why blocking of the V-mesh occurs during fabrication of the graphite-50bSPE.

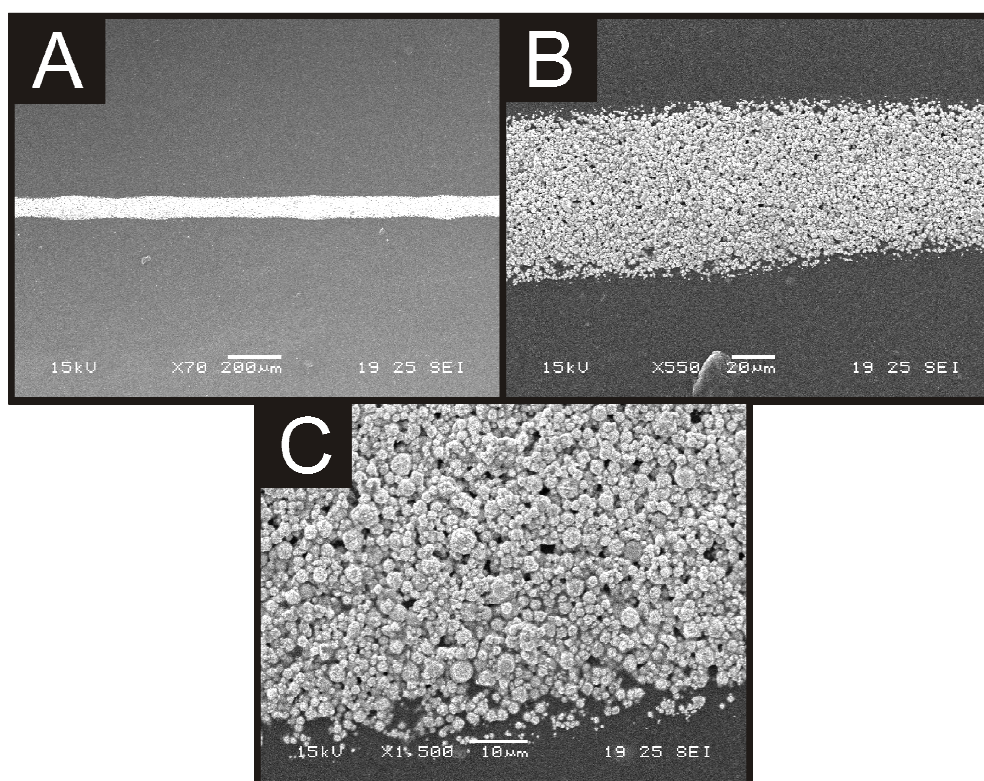


Figure 4.38 SEM images of the 50 μm gold-50bSPE working area.

Electrochemical characterisation of the gold-50bSPE was also undertaken utilising the well-documented redox probe hexaammine-ruthenium (III) chloride. Figure 4.39 depicts typical cyclic voltammetric scan rate studies over the range 5 – 200 mV s^{-1} obtained utilising a gold-50bSPE which revealed a linear response ($I / \mu\text{A} = -2.57 \mu\text{A} / (\text{V s}^{-1})^{1/2} - 2.84 \times 10^{-1} \mu\text{A}; R^2 = 0.94; N = 8$) realised through the plot of voltammetric peak current (μA) versus the square root of scan rate. Again, the resultant cyclic voltammograms are found to indicate a steady-state type voltammetric profile at slow scan rates with a transition to a peak-shaped profile as the scan rate is increased (see above).

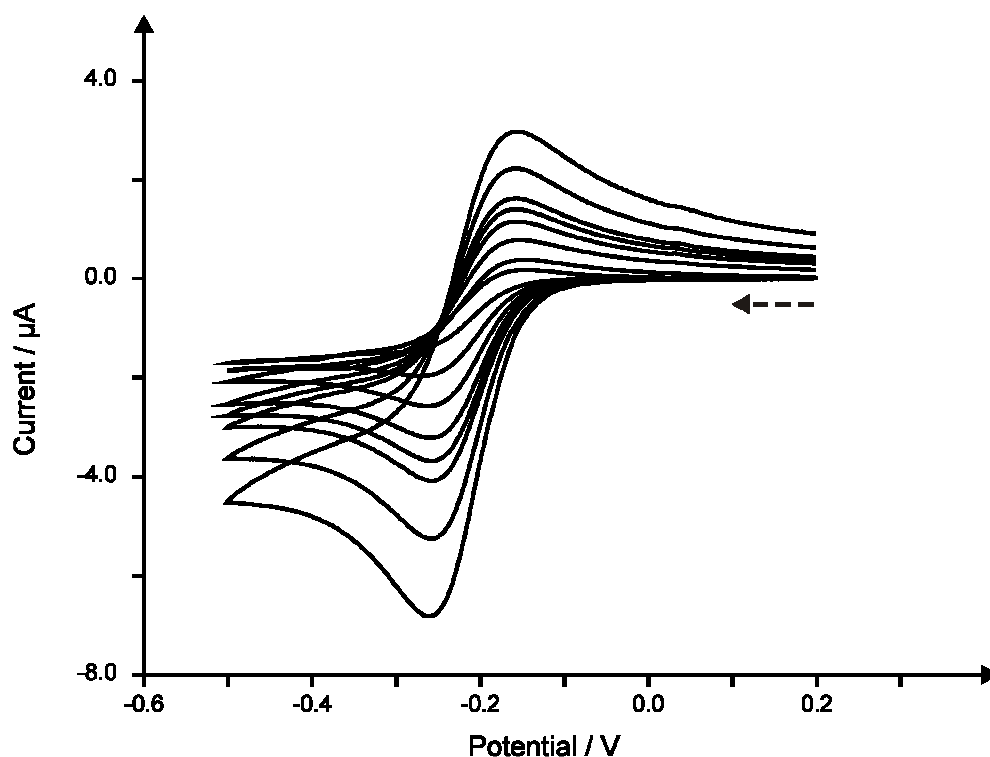


Figure 4.39 Typical cyclic voltammetric responses observed through scan rate studies (5 – 200 mV s^{-1}) using the gold-50bSPE at 1 mM hexaammine-ruthenium (III) chloride in 0.1 M KCl. Dashed arrow signifies direction of scan.

Upon determining that the electrochemical characteristics of the gold-50bSPE mirrored that of the graphite-50bSPE in terms of diffusional behaviour, attempts were made to benchmark the gold microband towards other electrochemical methodologies reported

within the literature through the sensing of chromium (VI). Chromium (VI) poses a great environmental threat with its hazardous status being attributed to the high oxidation potential.⁴⁴⁹ As has been discussed in greater detail in earlier Chapters, due to the serious risk to health posed by chromium (VI) its existence with regards to concentration is limited by the WHO to 0.05 mg L^{-1} ($\sim 0.17 \text{ }\mu\text{M}$) within groundwater.⁴⁴⁹

Figure 4.40A depicts typical linear sweep voltammograms for the electrochemical reduction of chromium (VI) using the gold-50bSPE in $0.05 \text{ M H}_2\text{SO}_4$ over a concentration range of 10 to $150 \text{ }\mu\text{M}$. As is easily distinguishable, with increased chromium (VI) concentration an increased reduction peak current (μA) is observed at the gold-50bSPE. Further analysis of such data demonstrates a strong, reliable correlation between the concentration of chromium (VI) and the determined reduction peak height ($I / \mu\text{A} = 8.3 \times 10^{-3} \mu\text{A} / \mu\text{M} + 3.9 \times 10^{-2} \mu\text{A}; R^2 = 0.99; N = 10$) (figure 4.40B). Consequently a limit of detection for chromium (VI) was calculated (using 3σ in line with section 1.1.11) to correspond to $2.65 \text{ }\mu\text{M}$. In comparison with existing electrochemical methodologies for the sensing of chromium (VI) reported within the literature the gold-50bSPE is found to offer a competitive limit of detection.^{108, 109, 450}

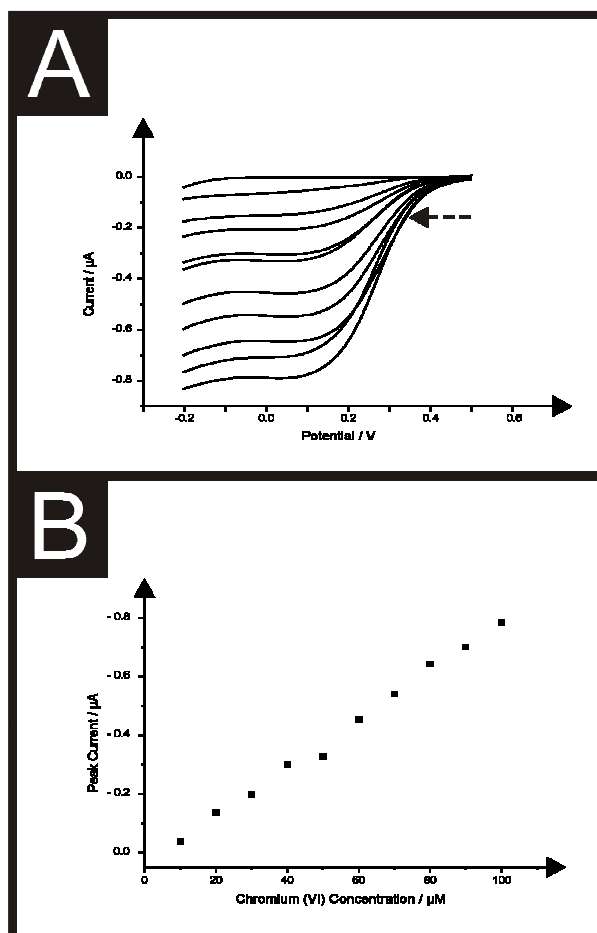


Figure 4.40 A) Typical cyclic voltammograms arising from additions of chromium (VI) in to 0.05 M H_2SO_4 using the gold-50bSPE. Scan rate: 5 mV s^{-1} . Dashed arrow signifies direction of scan. B) A corresponding calibration plot from A) over the range studied (1 – 10 μM) chromium (VI).

As has been seen above, recent developments in screen technology has allowed a smaller band microelectrode to be fabricated which has obvious useful electroanalytical applications. The question arises, how can even smaller microband electrodes be fabricated? The first limiting factor is the graphite/carbon particle size within the ink as it is impossible to print narrow lines with using screen printing inks containing large particles. Indeed, in the commercially obtained ink utilised within this work, which is used due to its good printability over large batch sizes and useful electrochemical properties, it is observed that quite quickly the screen becomes blocked and no-more printing can be performed; while this allows enough useful electrodes to be performed it greatly reduces the size of the batch. Thus, a new

ink carbon/graphite would need to be fabricated which is printable over a large batch containing reduced particle sizes yet, most importantly, still retaining its useful electrochemical properties. In terms of the gold, the particle size of the ink is smaller and as such doesn't have the same problems; however, given the cost of gold versus graphite, the latter is demanded more by researchers/end-users. Secondly the screen itself is a limiting factor. The generally accepted rule of thumb in selecting the most suitable mesh type is that the maximum paste particle size should be less than a third of the mesh opening. Also the minimum line width should be at least three times greater than the thread diameter. In the utilised V-mesh screen this corresponds to 23 μm meaning that thread diameter below 15 μm is needed in order to be able to comfortably print smaller than 50 μm lines. Hence, these two are the limiting factors in improving resolution which go hand-in-hand.

4.4.3 CONCLUSIONS

This section has successfully demonstrated the first example of a 50 μm microband printed entirely *via* screen printing which has clear useful benefits in electroanalytical applications. The following section group continues to try and push the boundaries of screen printing and to produce even smaller microbands which give rise to true microelectrode behaviour (near elimination of contributions from planar diffusion rather than solely radial/convergent diffusion) and further enhancements in the electroanalytical sensing performances. To further improve the resolution from the level presented in this communication, focus will be on the availability/bespoke development of pastes with the desired printing behaviours (generally screen printing paste are prepared for easy printing rather than for printing fine lines with good definition) and the screen used to define the microband. In the former, the carbon graphite paste characteristics including the viscosity, particle size and thixotropic behaviour needs to be enhanced for optimal printing behaviour.

In the latter, the screen, mesh size, thread thickness, calendaring and the angle of the screen fabric in the frame all need to be carefully optimised/tailored. Additionally having different coating properties on the screen fabric wires could aid the reduction of paste adhesion and enhance the detachment of paste from the screen. Other improvements could also come from having meshes with super high dimensional accuracy.

4.4.3 SCREEN PRINTED MICROBAND ELECTRODES: REDUCING THE MICROSCOPIC SIZE - LIMITATIONS

As has been explored in depth within sections 5.3 and 5.4 the development of the microband electrode has given rise to interesting voltammetry whilst offering improvements over traditionally employed sensors for the monitoring of key analytes. When considering the voltammetry achieved when utilising the two microband sensors of 100 and 50 μm in width it was noted, as has been discussed, that although both offered more desirable electrochemical behaviour and consequently analytical performance for the selected analytes, each still failed to exhibit true microelectrode behaviour with a pseudo-microelectrode response being typical. Clearly, through consideration of the work detailed within section 4.4, the reduction of the microscopic size (width) of the microband electrode yielded improvements in sensor performance with the observed behaviour transitioning further towards that of a typical microelectrode than was observed at the 100 μm microband electrode (section 4.3). Combined with the continual evolution of screen printing technologies; particularly the screen meshes and inks available the development of a microband electrode of 10 μm in width was sought.

The fabrication of microband electrodes of 10 μm was attempted utilising the newly developed V-mesh and gold ink (utilised for the fabrication of the gold modified co-planar electrodes (Chapter 3) and the 50 μm microbands described earlier within this Chapter. The screen printing parameters utilised for the fabrication of the newly designed 10 μm width

microband were the same as those detailed within the Experimental section (4.1.2) for the 50 μm microband with the appropriate stencil design being employed. The gold ink was favoured due to its small particle size ($\sim 2.5 \mu\text{m}$ diameter) in comparison with that of the typical graphite flakes comprising the carbon-graphite ink ($\sim 20 \mu\text{m}$ diameter) which is a critical parameter when attempting to print such small geometries due to the potential hindrance arising from screen/mesh blocking (see Chapter 2).

During the fabrication of these 10 μm microband electrodes the instantaneous blocking of the screen or mesh occurred during the first print, even though the gold ink was selected. These problems can be accounted for due to two critical parameters. First the generally accepted rules of thumb in selecting the most appropriate ink for printing that the minimum line width (electrode geometry) should (ideally) be at 3 times greater than the thread diameter. Current screen printed mesh technologies do not allow for a thread diameter lower than 23 μm utilised within the V-mesh and as such in theory a greatly reduced mesh thread width would be necessary for the fabrication of such designs. Secondly it is a feasible assumption that in combination with the problems posed by the mesh thread, the particle size of the inks utilised could result in the mesh spacing becoming blocked. In some circumstances this problem may be alleviated through the introduction of diluent (solvent) used to thin the ink and aid in the reduction of particle coagulation, however when considering the fabrication of such intricate geometries such actions would most certainly result in too great a reduction in ink viscosity which would ultimately sacrifice the reproducibility of the electrode geometry throughout the batch fabricated. With one of the critical aims of screen printed sensor fabrication considered within this thesis being the reproducibility of the electrodes, such actions were not practical. At present these two parameters; mesh thread diameter and commercially available ink particle size limit the further development of screen printed sensors with regards to the fabrication of truly

microscopic domains. This work is currently on-going and is identified in the future work section.

CHAPTER 5 SUBSTRATE SELECTION: AN OFTEN OVERLOOKED PARAMETER?

The conventional substrate material of choice for the fabrication of screen printed electrodes is polyester owing to its flexible, yet durable nature. When compared to more traditional electrochemical configurations the ease of mass production and allowance for the fabrication of screen printed sensors which are light, small and easily manipulated is of vast importance when considering application for ‘in the field’ sensing.

As the requirement for sensors utilised in an ever expanding range of functions increases it would be naive to overlook the importance of the ‘starting blocks’ that is, the starting substrate material. This key parameter which is often overlooked and neglected has the potential to further increase the potential applications of such electrochemical sensors. As such, this Chapter considers the role of the electrode substrate; attempting to determine the possible viability of alternative materials whilst interrogating existing ones.

5.1 TRADITIONAL POLYESTER-BASED SUBSTRATES VERSUS PAPER-BASED ALTERNATIVES: A NEW OUTLOOK ON SUBSTRATES FOR USE IN ELECTROANALYSIS

This section, containing published work,^[8] aims to determine if the use of different substrate materials, particularly paper-based materials, for the fabrication of screen printed electrodes for use in electroanalysis is feasible. It is hoped that the ability to utilising different substrate materials could potentially pave the way for the development of truly ultra-flexible sensors which would undoubtedly widen the potential applications of such electrochemical devices, for example to be attached to the human body!

5.1.1 INTRODUCTION

Society is in a constant state of growth and development and it is inevitable that demands for sensing devices related to clinical and industrial applications will increase. In order to achieve this, inexpensive and disposable, yet highly accurate and rapid devices are greatly sought. Additionally the portability of such devices is of fundamental importance, especially when the sensing in hard to reach locations, is required. One of the fundamental developments which continues to successfully allow for the miniaturisation and low cost electrochemical systems is screen printing and associated fabrication techniques which allows simplification of electrochemical systems allowing the transition from the laboratory to the field to be realised.^{103, 451-454} These inherent advantages of screen printing allowed the commercialisation of glucose sensors such that diabetics may routinely monitor their blood glucose levels on the spot within their own homes.

The ease of electrode modification and design through the use of screen printing makes it an exciting and ever evolving technique.¹⁰³ Those skilled in the ‘art’ are able to fabricate sensors specific to particular requirements utilising the easily modified systems to

⁸ J. P. Metters, S. M. Houssein, D. K. Kampouris and C. E. Banks, *Anal. Methods*, 2013, **5**, 103.

affect parameters such as improvements in mass transport to impart low detection limits and greater sensitivities and the fabrication of multiple-sensors upon a single strip allows for a range of analytes to be screened within a single sample while still being economical in nature.

One such demographic for which low cost, rapid sensors such as screen printed sensors offer great promise is the developing countries. Typical diagnostic technologies that are successful in the economically developed world often are difficult to use in developing countries due to high costs, with those in developing countries struggling to afford even modestly expensive tests. Furthermore, basic infrastructures such as; reliable power, refrigeration, and trained personnel are often not available in such areas, compounding the case for the requirement of cheap, low cost sensors that can provide in-the-field diagnosis without the necessity for specialised personnel and high cost equipment.⁴⁵⁵⁻⁴⁵⁹ Such sentiments are outlined by the World Health Organisation using the acronym ‘ASSURED’: Affordable, Sensitive, Specific, User-friendly, Rapid and Robust, Equipment-free and Deliverable to end-users.⁴⁶⁰ The potential for the coupling of screen printing technologies and real-world applications for the detection of disease and illness is perfectly captured through fascinating work by Rusling *et al*⁴⁶¹ who utilise multi-electrode screen printed sensors within an immunoassay system with the study holding great promise for accurate, sensitive multiplexed detection of diagnostic cancer biomarkers.

A further advantage of screen printed technology is the feasibility of printing upon many different substrate materials. Typically screen printed electrode are produced upon ceramics due to the high firing temperatures that are required with some inks but generally plastic substrates are more favoured due to its flexibility (depending on its thickness). Wang and co-workers⁴⁶² recently reported of the elegant use of screen printing technologies within clothing, “biosensors in briefs”. The group developed durable biosensors that can be printed directly onto clothing, namely underwear, which could potentially enable continuous

biomedical monitoring outside hospitals. The tight contact of the clothing and direct exposure to the skin is shown to allow the detection of hydrogen peroxide and the enzyme co-factor NADH; both of which are associated with numerous biomedical processes to be readily monitored.^{103, 462, 463}

Inspired by this exciting work, herein is explored, the first study into the utilisation of different paper materials for the fabrication of electrochemical sensors. It is noted that other work has focussed on paper-based microfluidics⁴⁶⁴⁻⁴⁶⁸ and flow-injection analysis,⁴⁶⁹ where capillary wicking facilitates the microfluidic flow and recently, a potentiometric sensor has been reported,⁴⁷⁰ but to date, paper-based electroanalytical sensors produced *via* screen printing have not yet been reported which allow for highly bendable electroanalytical sensors based upon renewable substrate materials which are ultra-low cost. Consequently, these exciting paper-based electrochemical sensing platforms are physically and electrochemically characterised and explored towards the sensing of key model analytes in this section.

5.1.2 EXPERIMENTAL

All chemicals used were of analytical grade and were used as received without any further purification and were obtained from Sigma-Aldrich. The specific chemicals utilised relevant to the analysis described within this Chapter included: sodium nitrite and β -nicotinamide adenine dinucleotide. All solutions were prepared with deionised water of resistivity not less than 18.2 M Ω cm. All solutions (unless stated otherwise) were vigorously degassed with nitrogen to remove oxygen prior to analysis. Additionally all solutions contained 0.1 M KCl acting as an electrolyte, unless otherwise stated.

Voltammetric measurements were carried out using a μ -Autolab III (ECO-Chemie, The Netherlands) potentiostat. All measurements were conducted using a screen-printed electrode configuration consisting of a disc-shaped working electrode with a geometric

working electrode area of 3 mm diameter. Additionally a saturated calomel electrode (SCE) and platinum wire were externally utilised as the reference and counter electrodes respectively for all measurements.

Screen-printed graphite electrodes were fabricated in-house with appropriate stencil designs using a microDEK1760RS screen-printing machine (DEK, Weymouth, UK). A carbon– graphite ink formulation (Product Code: C2000802P2) (Gwent Electronic Materials Ltd, UK) previously utilised was first screen printed onto pre-selected substrates. For the fabrication of the standard SPE, a polyester flexible film (Autostat, 250 μm thickness) was utilised as the substrate. For the fabrication of the paper based electrodes the substrates utilised included: A4 text and graphic paper 160 g/m^2 , A4 lined refill pad paper 80 g/m^2 and Filter Paper QL 100 for the IP-SPE, RP-SPE, and FP-SPE respectively. This layer was cured in a fan oven at 60 degrees for 30 minutes. This layer produced the working electrodes, contacts and counter electrode. Last a dielectric paste ink (Product Code: D2070423D5) (Gwent Electronic Materials Ltd, UK) was printed to cover the connections and define the 3 mm diameter graphite working electrode. After curing at 60 degrees for 30 minutes the fabricated screen printed electrodes are ready to use. Throughout all electrochemical measurements, external SCE reference electrode and platinum counter electrode was utilised.

Exploration of the effects of mechanical stress

In this section of the study (section 5.2) the paper-based screen-printed electrodes were fabricated in the same manner described above with both a carbon and insulating dielectric layer being printed upon the paper substrate (A4 text and graphic paper 160 g/m^2). Additionally the paper-based electrodes were then treated using two different methods to further define the working electrode area; one using a clear nail varnish (denoted throughout as pv-SPE) and the other using sellotape (denoted throughout as ps-SPE). In all experiments

utilising both the polymer- and paper-based screen printed electrodes, a platinum and SCE were used as the counter and reference respectively for comparative purposes.

Canal water was sampled at the edge of the canal bank (Rochdale Canal, Oxford Road, Manchester, UK) and collected in a polycarbonate bottle which was washed three times with canal water before being taken back to the laboratory. The sample was stored at room temperature and used within a day of sampling and was simply utilised in place of deionised water for the preparation of specific buffers before electroanalytical measurements were commenced.

Scanning electron microscope (SEM) images and surface element analysis were obtained with a JEOLJSM-5600LV model having an energy-dispersive X-ray microanalysis package.

5.1.3 RESULTS AND DISCUSSION

Substrate Selection

Paper-based screen printed sensors were fabricated as described within the Experimental section. With a plethora of paper-based materials available, the decision was made to first test the viability of screen printing using various paper substrates. Of the paper-based substrates available, the four most practical and readily available were selected for printing upon. Those selected included inkjet, ruled pad paper and filter paper, denoted as IP-SPE, RP-SPE and FP-SPE throughout. Successful screen printing of the inks was possible at each of the substrates all allowing for highly reproducible and well defined electrode geometries. No substrate contraction was noted at any of the substrates as is highlighted through the successful screen printing of the subsequent non-conductive dielectric ink layer. Slight curling of the substrates was noted after curing which was remedied through the

standard storage procedure of vacuum packing the electrodes to avoid contamination/fouling prior to use.

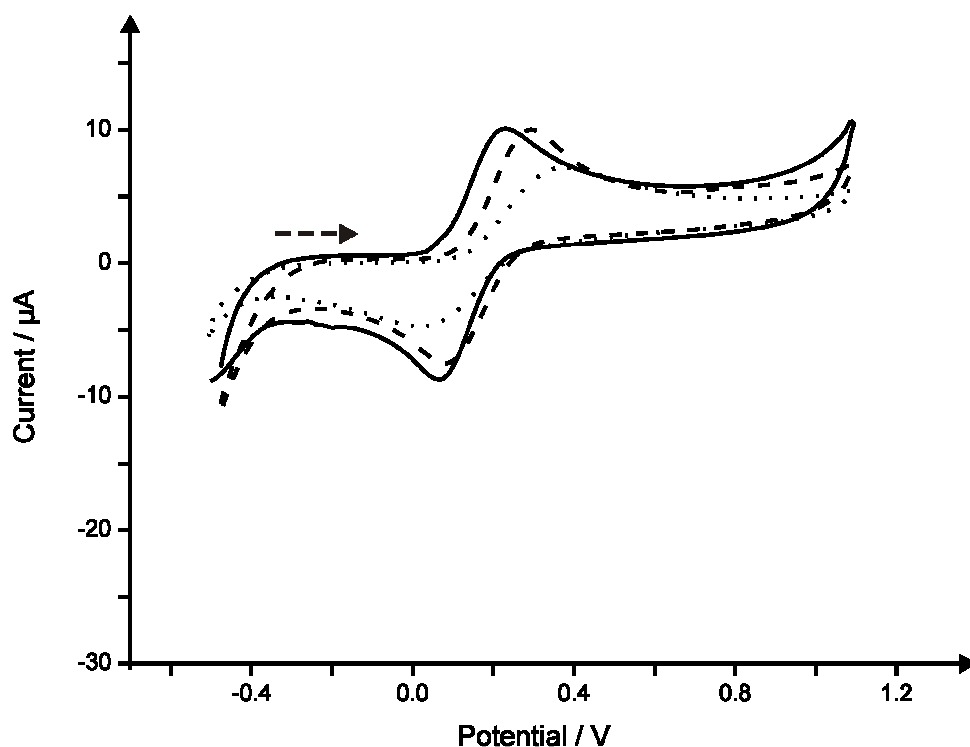


Figure 5.1 Typical cyclic voltammograms comparing the response in 1 mM ferrocyanide (II) in 0.1 M KCl using a standard SPE (solid line), IP-SPE (dashed line) and RP-SPE (dotted line). Scan rate: 50 $mV s^{-1}$. Dashed arrow signifies direction of scan.

Next, to further examine the feasibility of the paper-based substrates for use as electroanalytical sensors, cyclic voltammetric measurements were conducted in 1 mM ferrocyanide (II) / 0.1 M KCl using each of the screen printed sensors, which are depicted in figure 5.1. Additionally comparisons were made using a previously characterised¹³⁴ graphite based screen printed electrode printed upon a polyester substrate (see Experimental section (5.1.2)). Note, cyclic voltammetry using the FP-SPE is not depicted in figure 5.1, as upon introduction to the solution, the highly absorbent paper-based substrate rapidly became saturated with water, with the crucial connections made between the sensor and the potentiostat being compromised due to rapid capillary wicking of the paper. A substrate with

such high porosity and therefore rapid absorption of the solution thus deems the electrode unsuitable for use in this intended application area; note that such a material is reported to be useful where capillary wicking is required such as in the detection of glucose in urine where a flow of solution is continuously required.⁴⁶⁹

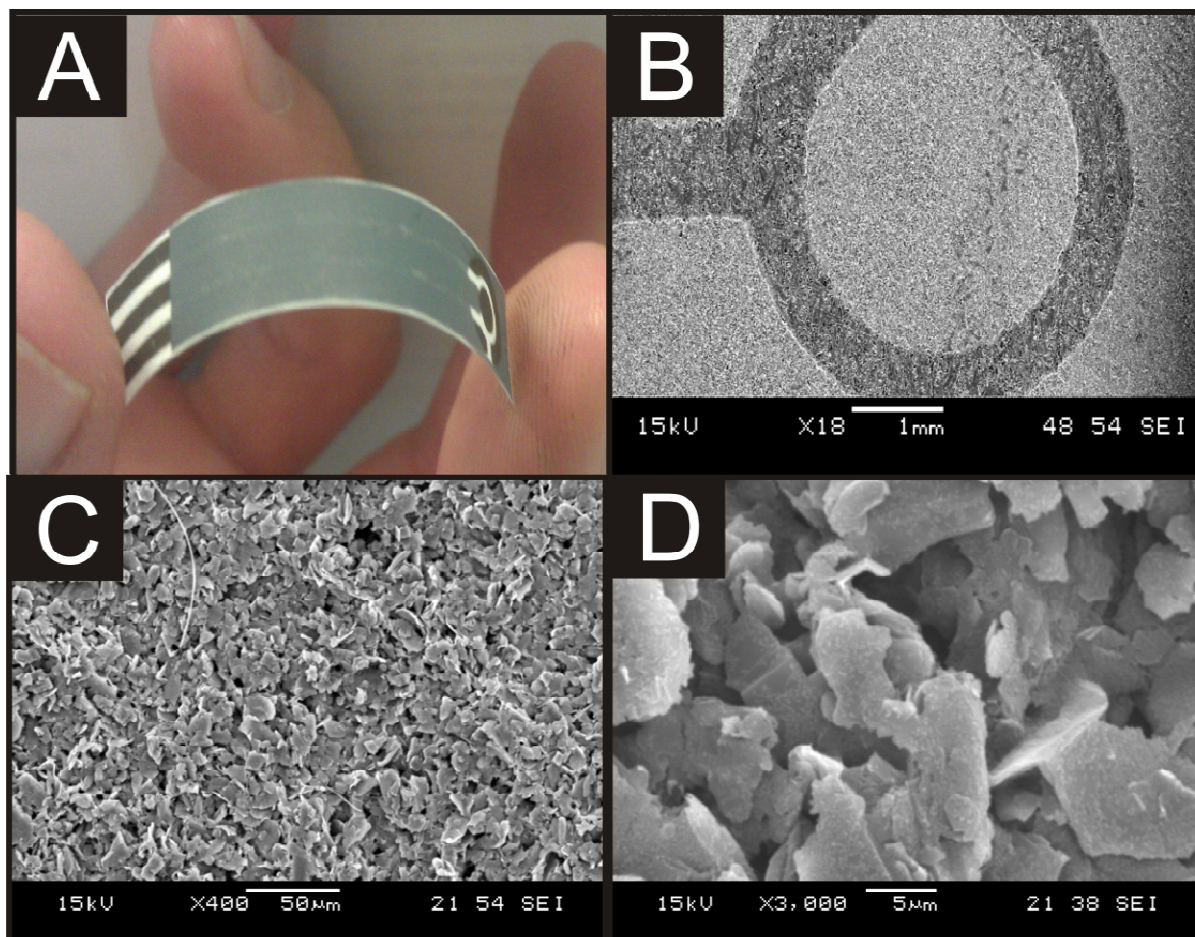


Figure 5.2 An image demonstrating the ultra flexible and robust nature of the IP-SPE (A) and typical SEM images of the sensor at increasing magnifications; x 18 (B), x 400 (C) and x 3000 (D).

Characterisation of the screen printed sensors was sought using SEM analysis of the graphite based surface of the working electrode of each. Inspection *via* SEM analysis reveals a typical graphitic surface at the IP-SPE (see figure 5.2B-D), not dissimilar to that found at the standard SPE which has been fabricated upon polyester substrates.¹³⁴ As is clear in figure 5.2B, a well-defined working electrode geometry is achieved when printing upon the paper-

based substrate. Figure 5.3 also depicts typical SEM images of the RP-SPE and FP-SPE, initial inspection at a low magnification of x 35 which appear to indicate that although the substrate utilised is clearly much more porous and fibrous in appearance, successful screen printing of the graphite ink is achievable. Critically however, at an increased magnification of x 1000 it is evident that a badly formed working electrode surface had in fact been produced (viz figure 5.3D) far removed from the ideal geometry offered by the standard SPE and also the IP-SPE and RP-SPE. Such a deviation from the ideal geometry observed at the FP-SPE is attributed to the fibrous surface.

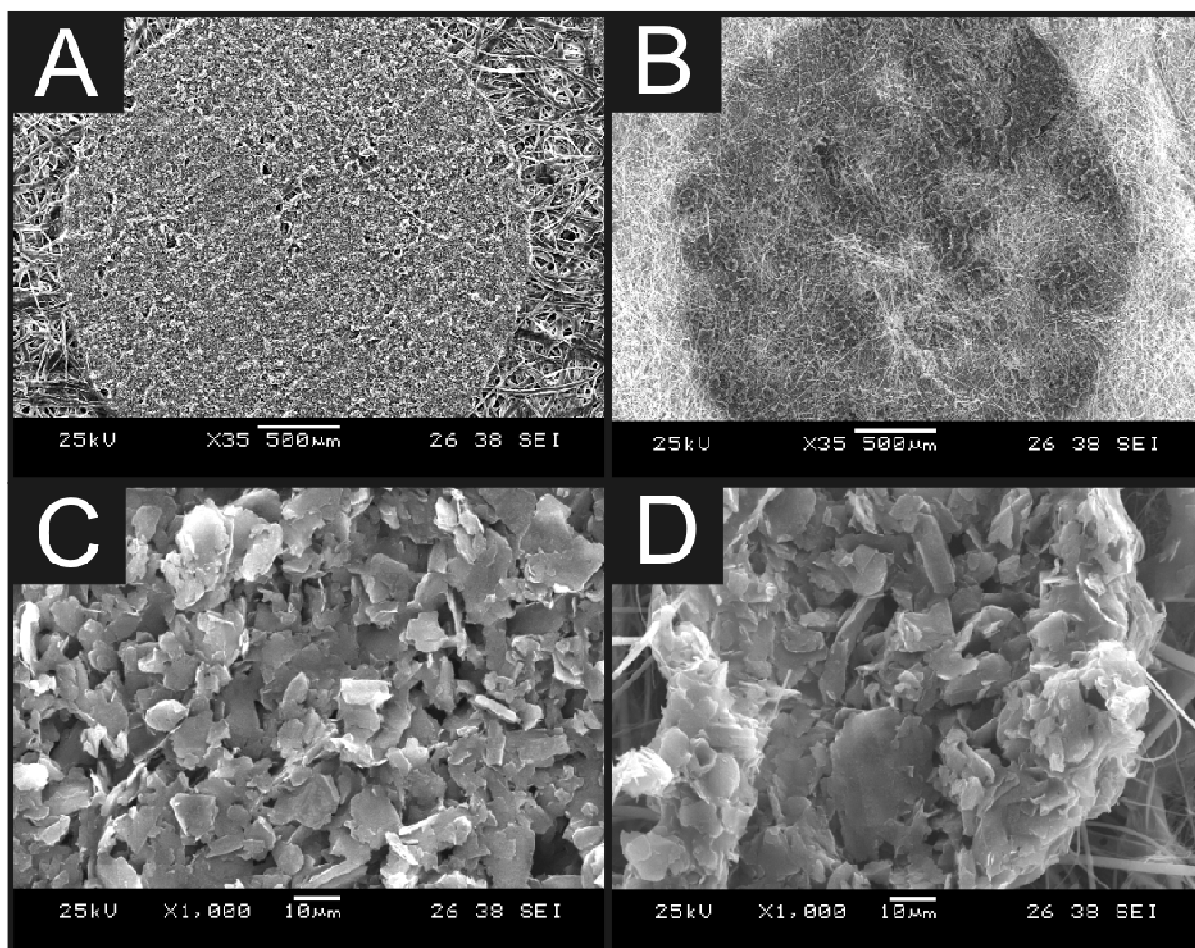


Figure 5.3 Typical SEM images of the paper-based electrodes screen printed upon different paper substrates; A) RP-SPE and B) FP-SPE at a magnification of x 35, whilst C) and D) show the RP-SPE and FP-SPE at an increased magnification of x 1000.

In comparing the IP-SPE and RP-SPE it is clear that IP-SPE exhibits voltammetric signatures which are most similar to that of the ideal and well characterised response of the standard SPE. As has been highlighted by Wang and co-workers,⁴⁶² when fabricating screen printed sensors, additional parameters such as flexibility and durability are important factors for consideration. In the case of the paper-based sensors, using paper as a substrate offered excellent durability and flexibility allowing complete folding of the sensor without any detrimental effect upon the physical appearance of the sensor, and more importantly, its electroanalytical performance; see figure 5.2A which shows a complete paper-based sensor which is extremely light and flexible due to the paper as the electrode substrate.

In addition to the observed electrochemical responses (*viz* figure 5.1) and due to the nature of paper-based materials, that is, capillary wicking, out of the three fabricated sensors, IP-SPE was selected for further use within the study due to its excellent electrochemical performance as demonstrated in figure 5.1 with the electrode being able to remain in solution for over 1 hour without electrical connection being compromised (see above). To further reduce capillary wicking and to examine the electrochemical performance of the sensors, the working electrode was isolated using sellotape on both the back and front of the sensor; note that while this reduced capillary wicking, it will not completely eliminate it (see later, *viz* figure 5.5) but allow for reproducible sensors to be obtained.

Characterisation of the Paper-based Sensor

Electrochemical characterisation was first carried out utilising well-established outer-sphere and inner-sphere redox probes, namely potassium ferrocyanide (II), hexaammine-ruthenium (III) chloride, potassium hexachloroiridate and N,N,N',N'-tetramethyl p-phenylenediamine (TMPD) the responses of which are shown in figure 5.4. Observation of voltammetric peak height, plotted as peak current (I_P) against square root of the applied scan

rate ($v^{1/2}$) over the range 5 – 200 mV s^{-1} was found to be linear at each of the electrochemical probes utilised; potassium ferrocyanide (II) ($I_p / \mu\text{A} = 192.6 \mu\text{A} / (\text{V s}^{-1})^{1/2} + 16.10 \mu\text{A}; R^2 = 0.99; N = 7$), hexaammine-ruthenium (III) chloride ($I_p / \mu\text{A} = +41.70 \mu\text{A} / (\text{V s}^{-1})^{1/2} + 2.133 \mu\text{A}; R^2 = 0.99; N = 7$), potassium hexachloroiridate ($I_p / \mu\text{A} = 80.90 \mu\text{A} / (\text{V s}^{-1})^{1/2} - 0.27 \mu\text{A}; R^2 = 0.99$) and TMPD ($I_p / \mu\text{A} = 108.8 \mu\text{A} / (\text{V s}^{-1})^{1/2} + 13.96 \mu\text{A}; R^2 = 0.96; N = 7$ at ~ 0.25 V and $I_p / \mu\text{A} = 125.0 \mu\text{A} / (\text{V s}^{-1})^{1/2} + 16.96 \mu\text{A}; R^2 = 0.99; N = 7$ at ~ 0.75 V) suggesting a diffusional process occurring at the electrode surface when using each electrochemical probe.

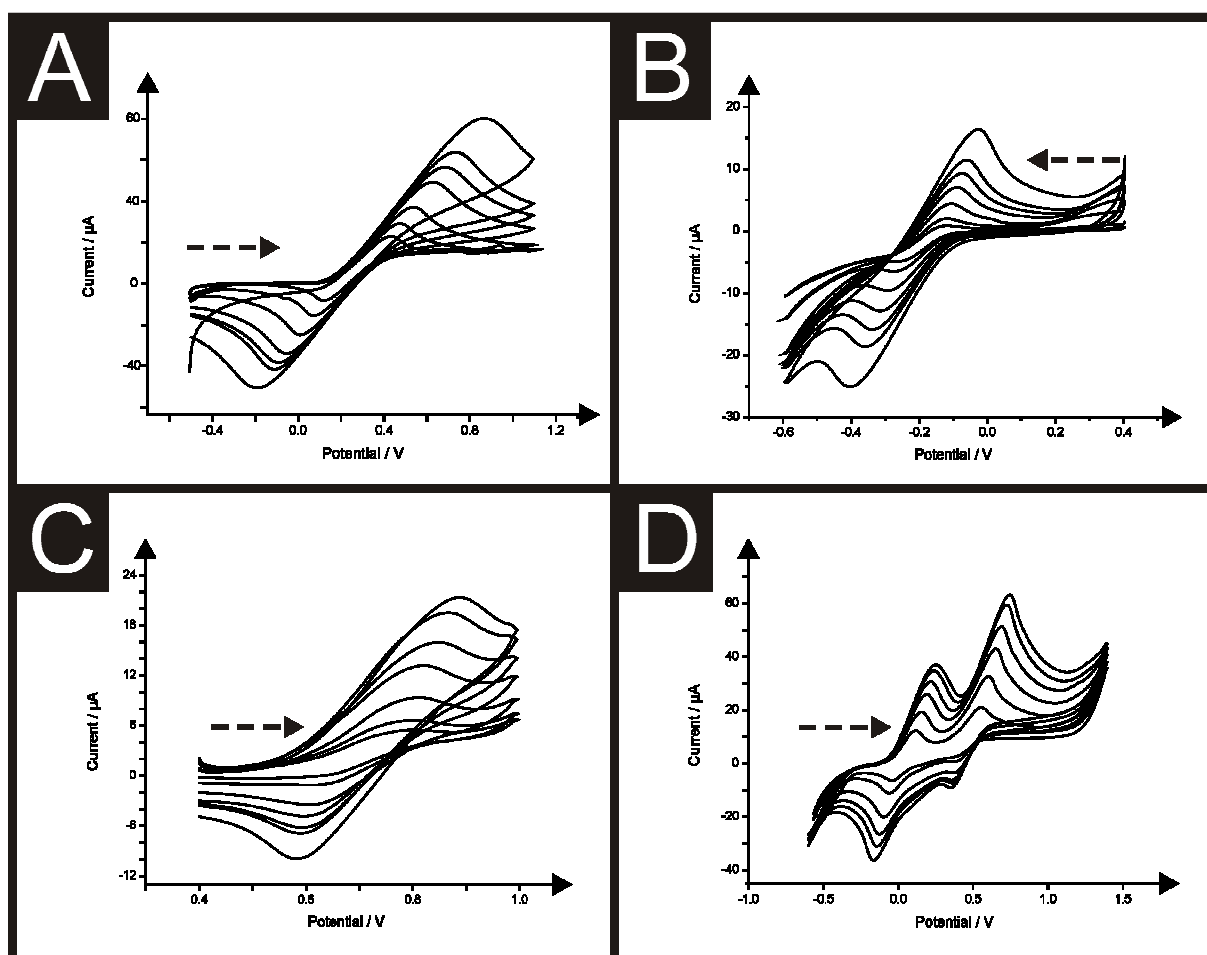


Figure 5.4 Typical cyclic voltammograms resulting from increasing scan rates (mV s^{-1}) at the IP-SPE in 1 mM potassium ferrocyanide (II) and 0.1 M KCl (A), 1 mM hexaammine-ruthenium (III) chloride in 0.1 M KCl (B), 1 mM potassium hexachloroiridate in 0.1 M KCl (C) and 1 mM TMPD in 0.1 M KCl (D). Scan rate range in all cases: 5 – 200 mV s^{-1} . Dashed arrow signifies direction of scan.

The heterogeneous electron transfer rate constant, k^0 , was estimated at the IP-SPE and standard SPE when studied using the outer-sphere electron transfer probe hexaammine-ruthenium (III) chloride. Visual inspection of the cyclic voltammograms depicted in figure 5.4 suggest a quasi-reversible response. The Nicholson method⁷ is routinely used to estimate the observed standard heterogeneous electron transfer rate for quasi-reversible systems as is discussed in greater detail in Chapter 1. Through utilisation of equations (1.27) and (1.28) the standard heterogeneous rate transfer constant, k^0 can be readily determined. Using this approach, the heterogeneous electron transfer rate constant, k^0 of $1.9 \times 10^{-3} \text{ cm s}^{-1}$ was determined at the standard SPE comparing well with a value of $7.26 \times 10^{-4} \text{ cm s}^{-1}$ deduced at the IP-SPE both deduced over the scan rate range studied (5 - 200 mV s^{-1}); it is likely the difference in adhesion of the graphitic ink used to fabricate the screen printed sensors on the paper with that of the polyester substrate is the cause of the deviation in the rate constants.

Additionally, the working electrode area of the electrodes was experimentally determined using the Randles-Sevcik equation for an electrochemically quasi-reversible case:¹³⁴

$$A = \frac{I_p}{2.65 \times 10^5 n^{3/2} D^{1/2} \nu^{1/2} C} \quad (5.1)$$

where, A , is the electrode area, I_p , is the experimentally determined peak current, n , is the number of electrons per molecule involved in the electrochemical process, D is the diffusion coefficient, ν is the voltammetric scan rate and C is the analyte concentration. The electrochemically deduced area of the sensor was determined from cyclic voltammetric response using 1 mM hexaammine-ruthenium (III) chloride / 0.1 M KCl with five scans being carried out using a single IP-SPE with a time period of 5 minutes between each. The experimental working area was determined to range from 0.069 to 0.108 (± 0.05) cm^2 . Upon the first voltammetric scan, an experimental working area of 0.069 cm^2 was realised which is

close to its expected physical geometric area (0.075 cm^2). After a period of 5 minutes immersed in the solution, the experimental working area was estimated to be 0.108 cm^2 with little change being noted in the calculated experimental working electrode area after further extended periods in solution. This is clearly observed through the relative cyclic voltammograms which, as shown in figure 5.5, clearly depict an increase in the observed peak current upon the second scan after a time period of 5 minutes in solution, with little change being observed with greater time in solution (figure 5.5; inset) suggesting the electrode area has reached the maximum. Such changes in the observed peak current are attributed to the absorption of the solution by the paper-based substrate.

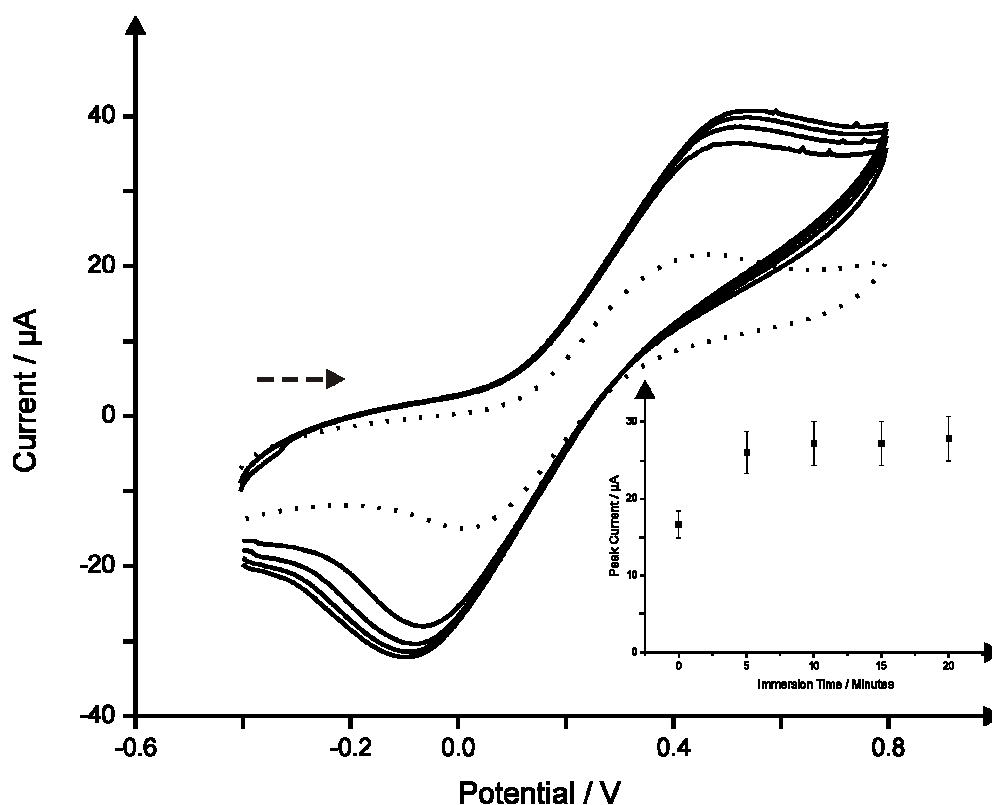


Figure 5.5 The effect of immersion time in solution upon the observed cyclic voltammetric response using a single IP-SPE in 1 mM potassium ferrocyanide / 0.1 M KCl with scans carried out at 5 minute intervals. The first scan at 0 minutes is depicted using a dotted line. Scan rate: 50 mV s^{-1} . Dashed arrow signifies direction of scan. Inset: Corresponding plot of peak height versus immersion time.

Electroanalytical Performance of the Paper-based Sensor

Following characterisation of the novel paper-based sensor the task of assessing the sensor's electroanalytical robustness was undertaken, first through determination of the biologically important molecule; NADH. The electrochemical oxidation of NADH (dihyronicotinamideadenine dinucleotide reduced form) to the corresponding oxidised form (NAD^+) receives considerable attention owing to its role in a plethora of enzymatic reactions and potential application in many NAD^+/NADH -dependent dehydrogenase based biosensors,^{409, 411, 446, 471-473} as has been discussed in greater detail earlier.

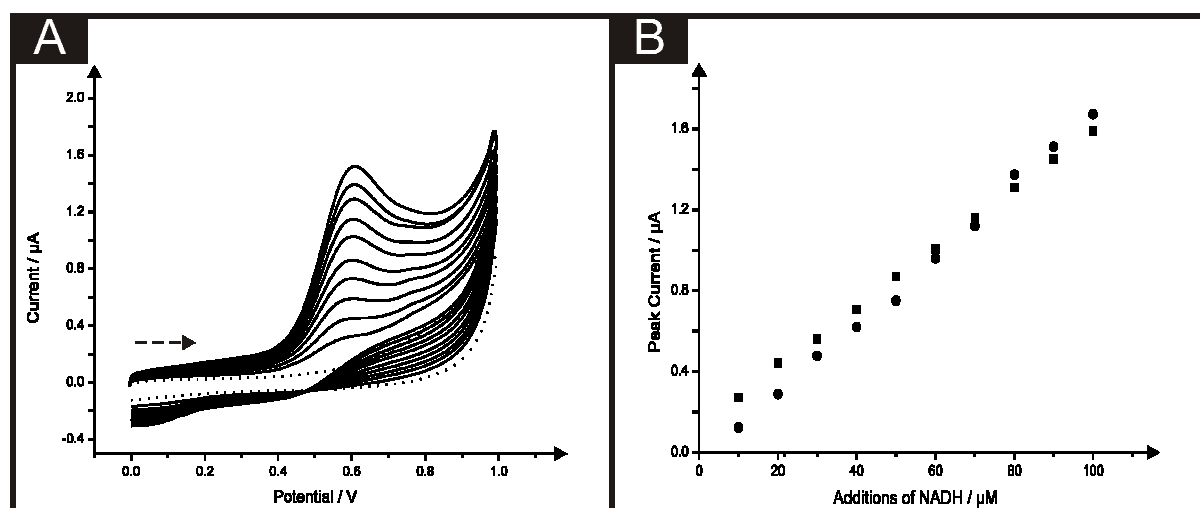


Figure 5.6 A) Typical cyclic voltammograms arising from additions of NADH in to a pH 7 buffer using the IP-SPE. Scan rate: 100 mV s^{-1} . Dashed arrow signifies direction of scan. B) Corresponding calibration plots over the range studied ($10 - 100 \mu\text{M}$) NADH using the IP-SPE (squares) and standard SPE (circles).

Cyclic voltammetric measurements were undertaken at increasing concentrations of NADH in a pH 7 phosphate buffer using the IP-SPE. Note, a buffer of pH 7 was selected as this pH is typical of biological samples, which would be of interest when monitoring NADH. As is shown in figure 5.6, a peak due to the oxidation of NADH is observed at $\sim +0.6 \text{ V}$ (vs. SCE), with the peak current found to increase upon additions of NADH (see figure 5.6B). A linear response over the entire analytical range ($10 - 100 \mu\text{M}$) was observed at the IP-SPE

($I_p / \mu A = 1.5 \times 10^{-2} \mu A / \mu M + 1.0 \times 10^{-1} \mu A$; $R^2 = 0.99$; $N = 10$). For a comparison, cyclic voltammetric measurements were also carried out over the same concentration range using the standard SPE printing upon a traditional polyester substrate ($I_p / \mu A = 1.7 \times 10^{-2} + 6.2 \times 10^{-1} \mu A$; $R^2 = 0.99$; $N = 10$); note, error bars were not included in figure 5.6B to avoid confusion owing to the closely overlaying calibration plots. Impressively, the IP-SPE was found to perform in accordance with the response observed at a standard SPE as shown in figure 5.6B, demonstrating the excellent performance of the IP-SPE yielding the equivalent electroanalytical performance of the standard SPE whilst offering the added attribute of being ultra-flexible, light weight and low cost. The limit of detection (using 3σ in line with section 1.1.11) for NADH using the IP-SPE was deduced to correspond to $1.8 \mu M$. Such low levels of detection are comparable, not only to that obtained at the standard graphite based screen printed electrode, but also to other screen printed electrode configurations reported within the literature. A limit of detection of $2.5 \mu M$ was reported by Hart *et al*⁴⁷⁴, using a graphite based screen printed sensor which was coupled with meldola blue reagent during fabrication, which is reported to be electrocatalytic towards the NADH detection. Further studies using meldola blue as an electrocatalytic species within screen printed electrodes for the sensing of NADH by Marty and co-workers report a limit of detection of $2 \mu M$ at the optimised electrode configuration.⁴⁷⁵ It is important to note that the incorporation of the mediator meldola blue reagent does have the added attribute of facilitating the electrochemical oxidation of NADH at lower, more facile potentials.^{474, 475} Clearly the limit of detection obtained using the IP-SPE is highly competitive, not only with the standard graphite screen printed electrode used herein, but also with existing literature.

Following confirmation that the IP-SPE offered comparable sensitivity to the standard SPE for the detection of NADH, the performance of the electrode was tested towards the

monitoring of nitrite; a human health hazard (in excess) and the derivatives of which are also major components in low-level radioactive waste solution.^{476, 477}

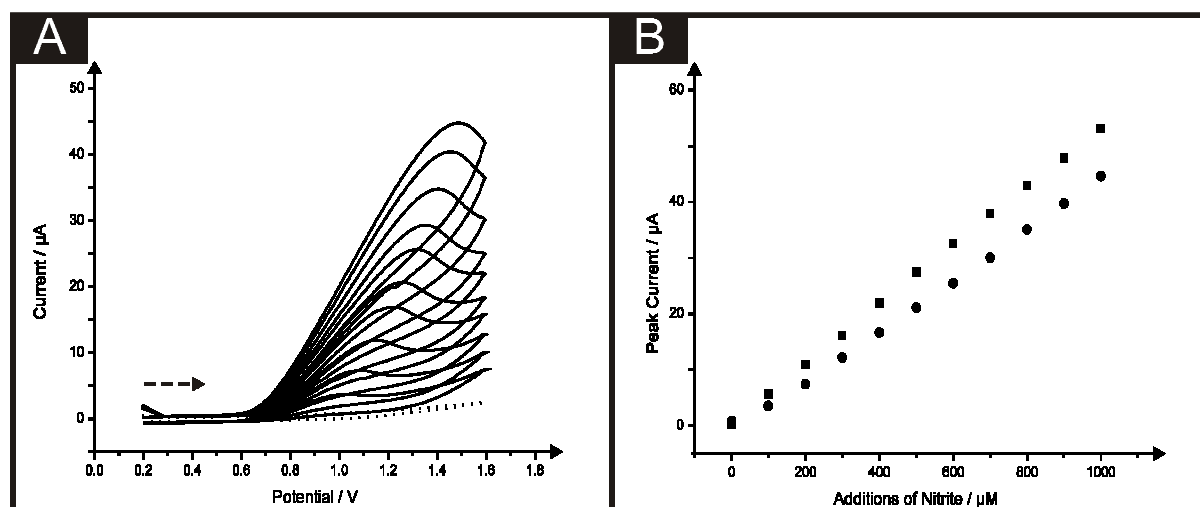


Figure 5.7 A) Typical cyclic voltammograms arising from additions of nitrite in to a pH 7 buffer using the IP-SPE. Scan rate: 100 mV s^{-1} . Dashed arrow signifies direction of scan. B) Corresponding calibration plots over the range studied ($100 - 1000 \mu\text{M}$) nitrite using the IP-SPE (circles) and standard SPE (squares).

In the same manner as the IP-SPE was compared and contrasted with a standard SPE for the sensing of NADH, cyclic voltammetric measurements for the sensing of nitrite were carried out. A peak arising from the oxidation of nitrite in a pH 7 phosphate buffer solution was evident at $\sim +1.0 \text{ V}$ (vs. SCE) using the IP-SPE as seen in figure 5.7A; such a potential value is in agreement with the literature using carbon-based electrodes.⁴⁷⁸ The oxidation peak was found to increase upon the addition of nitrite over the concentration range $100 - 1000 \mu\text{M}$ with a linear response observed throughout. Figure 5.7B shows the linear range studied using the IP-SPE with an additional plot demonstrating the response obtained over the same set concentrations of nitrite using a standard SPE. It is clear that the response obtained using the IP-SPE is comparable to that when using a standard SPE with both sensors demonstrating no deviation from linearity over the entire range studied (IP-SPE: $I_p / \mu A = 4.4 \times 10^{-2} \mu A / \mu M - 8.0 \times 10^{-1} \mu A$; $R^2 = 0.99$; $N = 10$, standard SPE:

$I_p / \mu A = 5.3 \times 10^{-2} \mu A / \mu M - 5.3 \times 10^{-1} \mu A; R^2 = 0.99; N = 10$), though a slightly improved response in terms of peak current is seen using the standard SPE. Once more error bars were not included in figure 5.7B to allow for deconvolution of the plots allowing for greater comparison between the closely related overlaying calibration plots. The limit of detection (using 3σ in line with section 1.1.11) for nitrite using the IP-SPE was deduced to be $15.1 \mu M$. Such a limit of detection demonstrates the great potential of the novel paper-based sensor with the fatal dose of nitrite ingestion reported as being between $8.7 \mu M$ and $28.3 \mu M$.⁴⁷⁹⁻⁴⁸¹ Clearly, although the paper-based sensor does not enable the monitoring of nitrite at the ultra-low concentrations of $\sim 8.7 \mu M$, the limit of detection does allow for concentrations within the fatal range. It is however critical to note that the requirement of such relatively high oxidation potentials could give rise to interference by compounds such as ascorbic and uric acid.

To gain further insights into the behaviour of the IP-SPE, particularly when used for analytical purposes, further information relating to the effect of the solution upon the electrode surface was sought. To do so, comparisons were made between the cyclic voltammetric measurement of increasing nitrite concentrations over the same range ($100 - 1000 \mu M$) using a single IP-SPE throughout and also a new IP-SPE for each addition of nitrite. Calibration plots corresponding to the peak currents observed through each method are shown in figure 5.8. It is apparent that a slightly greater peak current is observed when using the single IP-SPE over that of a new IP-SPE for each addition throughout the analysis, though this deviation is not sufficient enough to affect the sensitivity of the IP-SPE. Such responses indicate the excellent reproducibility of the paper-based sensors.

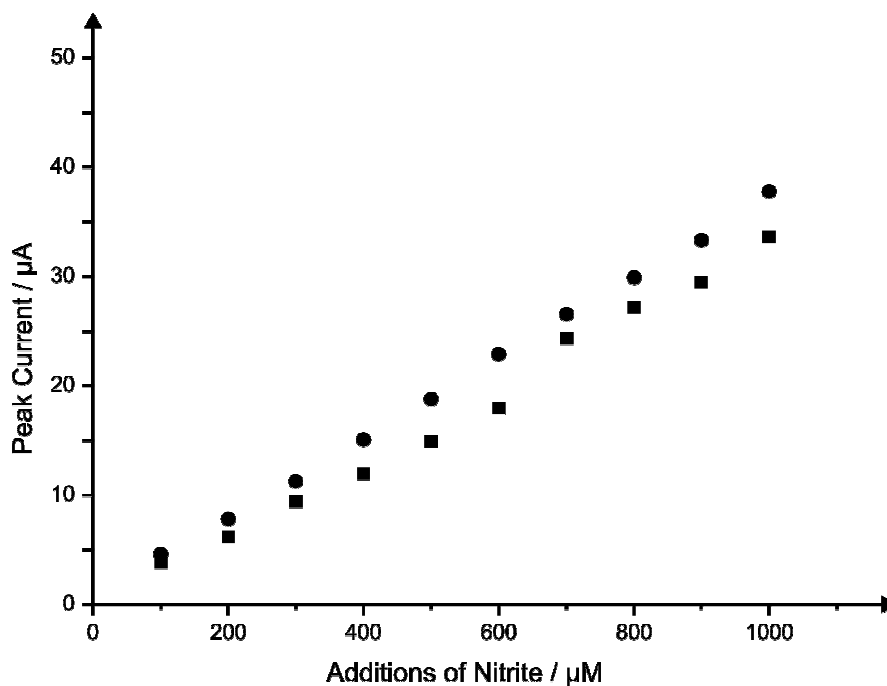


Figure 5.8 Typical calibration plots resulting from the addition of nitrite into a pH 7 buffer using a single IP-SPE for the entire concentration range (circles) and a new IP-SPE (squares) for each concentration. Scan rate: 100 mV s^{-1} .

Exploring the applicability of the paper-based sensor towards ‘real-world’ samples

Finally, after concluding that the IP-SPE allowed for comparable analytical performance with that found using a standard SPE, attempts were made to determine whether the performance of the paper-based sensor was hampered in any way when utilised for the sensing of the model analyte within a sample that would typically be presented. Once more the model analyte nitrite was chosen for determination. The media selected was canal water (collected and pre-treated as described within the Experimental section (5.1.2), with the requirement for the monitoring of nitrite typically being within water sources.⁴⁴⁶

Additions of nitrite over the same set range of concentrations (100 – 1000 μM) were made to a modified canal water sample using the IP-SPE. The peak currents recorded upon each addition of nitrite into the canal water sample are overlaid with a typical calibration plot constructed through measurement under ‘ideal’ buffer conditions using an IP-SPE; figure 5.9

depicts typical calibration plots obtained within the two media resulting from cyclic voltammetric measurements. Clearly, no detrimental effect upon the sensitivity and performance of the electrode is found towards the detection of nitrite within a canal water sample with the resultant calibration plot providing an almost perfect overlay when compared with that arising from additions in to an ‘ideal’ buffer solution. Such findings highlight the robust nature of the sensor with the novel substrate utilised allowing for excellent sensitivity even in difficult sample media.

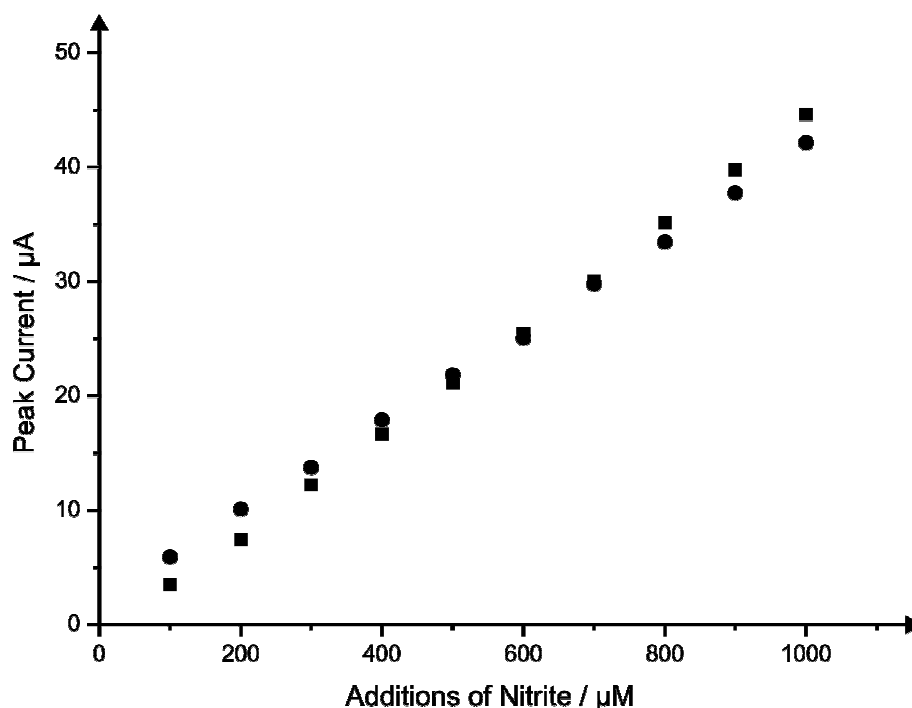


Figure 5.9 Typical calibration plots corresponding to additions of nitrite into a pH 7 buffer solution (squares) and canal water solution (circles) using the IP-SPE. Scan rate: 100 mV s^{-1} .

5.1.4 CONCLUSIONS

This section has considered the potential utilisation of differing substrate materials for the production of screen printed sensors intended for use within electroanalytical applications. The characterisation and application of novel, disposable, single-shot paper-based screen printed sensors with their analytical performance towards the sensing of NADH and nitrite being compared and contrasted with well characterised commercially available

screen printed sensors printed upon a traditional polyester substrate has been described. The potential for paper-based substrates for use within screen printing was explored providing insights into the essential parameters requiring consideration when using such material, in particular, the porosity of the substrate material.

The paper-based sensors were found to be robust in nature, whilst providing highly reproducible responses when utilised for the model analytes selected. Critically, when contrasted with the commercial available standard screen printed electrode, the paper-based sensors were found to exhibit almost identical electrochemical characteristics to their commercial counter-parts for the sensing of the model analytes NADH and nitrite. Furthermore the paper-based sensors were found to successfully maintain excellent levels of sensitivity even within samples of canal water.

5.2 TRADITIONAL POLYESTER-BASED SUBSTRATES VERSUS PAPER-BASED ALTERNATIVES: FLEXIBILITY VERSUS STABILITY

In order to further investigate the role played by the substrate material, particularly in circumstances when the sensor may be placed under duress, a study into the effects of mechanical forces placed upon the fabricated sensors was carried out.

In this section the effects of such forces in relation to time and frequency of the force applied is examined utilising both the polyester-based and paper-based sensors with the aim of truly exploring the potential of such sensors for real-world applications in situations where such movement or forces may arise.

5.2.1 INTRODUCTION

Screen printed electrochemical derived sensors have revolutionised the field due to their capability to bridge the gap between laboratory experiments with in-field implementation.^{103, 452, 482-484} This is of course witnessed by the billion dollar (per annum) glucose sensing market which has been revolutionary since it now allows individuals to be able to measure their blood glucose levels at home, without recourse to a hospital / clinic, where a result is instantly realised.^{485, 486} The basis of such technology is largely based upon screen printing which permits the mass production of highly reproducible electrode configurations and due to its scales of economy, inexpensive sensing and disposable electrochemical sensing platforms can be realised.^{103, 486} Typically through careful choices of inks and screens, unique sensing platforms can be produced such as screen printed arrays,⁴⁸⁷⁻⁴⁹⁰ recessed electrodes⁴⁹¹ and microbands.^{492, 493} Such electrode designs offer improvements in sensitivity, signal-to-noise ratios and reduced sample volumes, producing potential replacements for conventional (solid and re-usable) electrode substrates. Further to this the ease of the mass production of screen printed sensors enables their use as one-shot sensors,

allowing possible contamination to be avoided, and alleviate the need for electrode pre-treatment as is the case for solid electrodes prior to their use.^{103, 306, 450, 490, 494}

Screen printed sensors, such as those discussed earlier, can be fabricated upon either flexible polymeric or ceramic substrates and usually the former is the predominant choice due to its ease of use and implementation into devices; such as in the case of applying into flow cells.⁴⁹⁵ Other unique surfaces where sensors have been printed have included fabrics and neoprene.^{496, 497} In the former, so called "biosensors in briefs" have been fabricated and used to measure analytes such as hydrogen peroxide and nicotinamide adenine dinucleotide.⁴⁹⁶ In the latter, Wang *et al*⁴⁹⁷ developed wearable electrochemical sensors on underwater garments comprised of the synthetic rubber neoprene. The neoprene-based sensor was evaluated towards the voltammetric detection of trace heavy metal contaminants and nitro-aromatic explosives in seawater samples, with further applications involving the first example of enzyme (tyrosinase) immobilization on a wearable substrate towards the amperometric biosensing of phenolic contaminants in seawater also being described.^{497, 498} Other work has explored the mechanical contortion and stress on polymeric sensors comprised of Mylar, polyethylene naphthalate and Kapton which was found to be able to withstand such mechanical stress and still electrochemically function.⁴⁹⁹

The work carried out in section 5.1 raised vital questions about the importance of substrate material, an often overlooked parameter, and as such it was deemed worthwhile and important to further investigate the potentially robust nature of these newly devised sensors alongside the more conventional polymeric-based sensors. Particular interest was paid to the influence of mechanical contortion upon the electrochemical activity and performance of paper-based screen printed sensors, with their efficacy being contrasted with that of polymeric-based screen printed sensors having undergone the same mechanical contortion. Such a situation can be envisaged in the case of wearable sensors where extreme bending and

mechanical contortion can be encountered and as such is of both fundamental and of applied interest. For example, such an application is the incorporation of sensors into wearable items such as underwear and sports clothing.^{496-498, 500} In this section it is found that the traditional polymeric-based screen printed sensors electrochemical behaviour is largely influenced by mechanical stress where, in contrast, the paper-based substrates offer much more robust sensing platforms when considering the effects of mechanical stress in relation to both the effect of contortion time and frequency upon electrochemical performance.

5.2.2 RESULTS AND DISCUSSION

Figure 5.10 depicts optical images of the three screen printed sensors fabricated (as described within the Experimental Section) which are utilised in this study. The polymer-based screen printed sensor (denoted throughout as standard-SPE) and both the paper-based screen printed electrodes are modified using sellotape (denoted throughout as ps-SPE) and a clear nail varnish (denoted throughout as pv-SPE). The sellotape and clear nail varnish are required in order to cover / insulate the carbon screen-printed connections and thus define the screen printed working electrode ensuring only the desired electrode area is able to interact with the solution since it has been found that although paper-based sensors can yield highly competitive results when applied into analytical protocols, they are susceptible, as would be expected, to wetting and solution absorption which over time can lead to the connections of the sensors being compromised.⁵⁰¹ Also shown in figure 5.10B and C are the two contortion angles to which the sensors were placed under mechanical stress during the study; 45 and 90 degrees respectively.

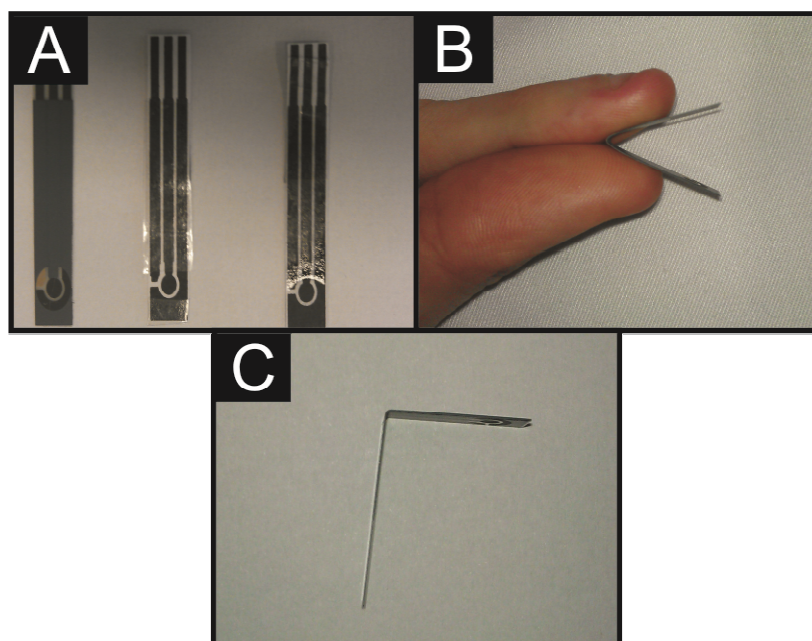


Figure 5.10 Photographs of: (A) The standard polymer-based screen printed electrode (standard-SPE) (left), the sellotape coated paper-based screen printed sensor (ps-SPE) (middle) and the clear nail varnish coated paper-based screen printed sensor (pv-SPE) (right). The contortion angles of 45 and 90 degrees utilised throughout this investigation are shown in (B) and (C) respectively.

Resistivity was used as a measure to explore the effect of mechanical stress placed upon the sensors at the two angles specified and as such the resistivity between two fixed points on each sensor relative to the contortion time utilised. The resistivity of such sensors is of course important in electrochemistry since the lower this is, the less impedance there is to the flow of current with little or no loss of energy. A high resistivity generally results in slow electron transfer and a poor sensor response. Note that contortion time is defined as the period of time during which the sensor has the mechanical stress exerted upon it. Figure 5.11 depicts the effect of contortion time upon resistivity (ohms cm) observed at each of the three screen printed sensors. As is evident in figure 5.11A, when exerting mechanical stress upon the standard-SPE, a change in resistivity is observed from an average value of 1.1 ohms cm prior to mechanical stress, to 3.7 ohm cm after the application of the contortion angle of 90 degrees for 60 minutes. Additionally, upon the exertion of a greater mechanical stress, 45

degrees (see figure 5.10), a large change in resistivity is noted of ~ 32.4 ohms cm following a contortion time of 60 minutes. Clearly the introduction of mechanical stress, particularly that of 45 degree contortion angle, has a notable effect upon the resistivity of the sensor printed upon a polymer-based substrate. In contrast, lesser effects upon the observed resistivity are noted at the much more flexible paper-based substrates (*viz* figure 5.11B and C). The ps-SPE were determined to exhibit a resistivity increase from an average of 1.4 ohms cm prior to manipulation to that of 1.9 ohms cm after a period of 60 minutes at an angle of 90. Little change in the resistivity was also observed when utilising the ps-SPE after being contorted to an angle of 45 degrees with a maximum resistivity of 1.9 ohms cm found after 10 minutes of contortion. Similar results are also evident upon utilisation of the pv-SPE with the resistivity prior to contortion found to be 2.7 ohms cm which was seen to increase up to a period of 60 minutes of mechanical stress to a value of 6.3 ohms cm at 45 degree contortion, though little change was observed over the entire contortion time period at an angle of 90 degrees. Such findings would suggest that although the ‘traditional’ commonly utilised polymer-based substrate offers the lowest resistivity prior to mechanical stress when compared to the paper-based substrates, upon the implementation of such mechanical contortion, it is in fact the two paper-based sensors which exhibit substantially lesser detrimental effects in terms of resistivity over the angles and contortion times utilised. It is likely that the observed effects upon resistivity may be attributed to changes in surface structure due to the mechanical stresses exerted upon the carbon material.

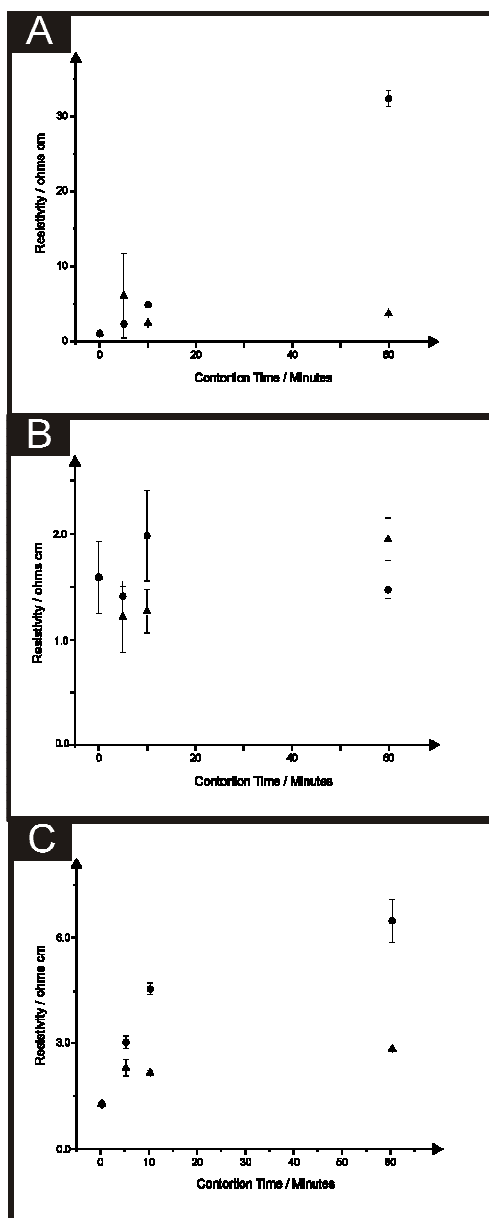


Figure 5.11 The effect of contortion time on the resistivity observed at various electrodes when contorted at angles of 45 (circles) and 90 (triangles) degrees. (A): standard-SPE; (B) ps-SPE; (C) pv-SPE. The data points (circles and triangles) represent the average response ($N = 3$) with the error bars representing the standard deviation.

Next, the electrochemical activity as a function of applied mechanical stress / contortion utilising the redox probe potassium ferrocyanide (II) was explored. First attention was turned to the effect upon the cyclic voltammetric responses observed at the standard-SPE which are shown in figures 6.12A and B following mechanical stress at angles of 45 and 90

degrees respectively for fixed contortion times of 5, 10 and 60 minutes. Figure 5.12C depicts a plot of peak-to-peak separation (ΔE_p) versus contortion time at the two angles (45 and 90 degrees). Note the peak-to-peak separation indicates the degree of reversibility of the heterogeneous electron transfer where the smaller the value, the faster the electron transfer rate. Figure 5.12C indicates the detrimental effect upon the electrochemical reversibility of the electrode material occurring as a result of mechanical stress / contortion and contortion time where the electrochemical performance deteriorates.

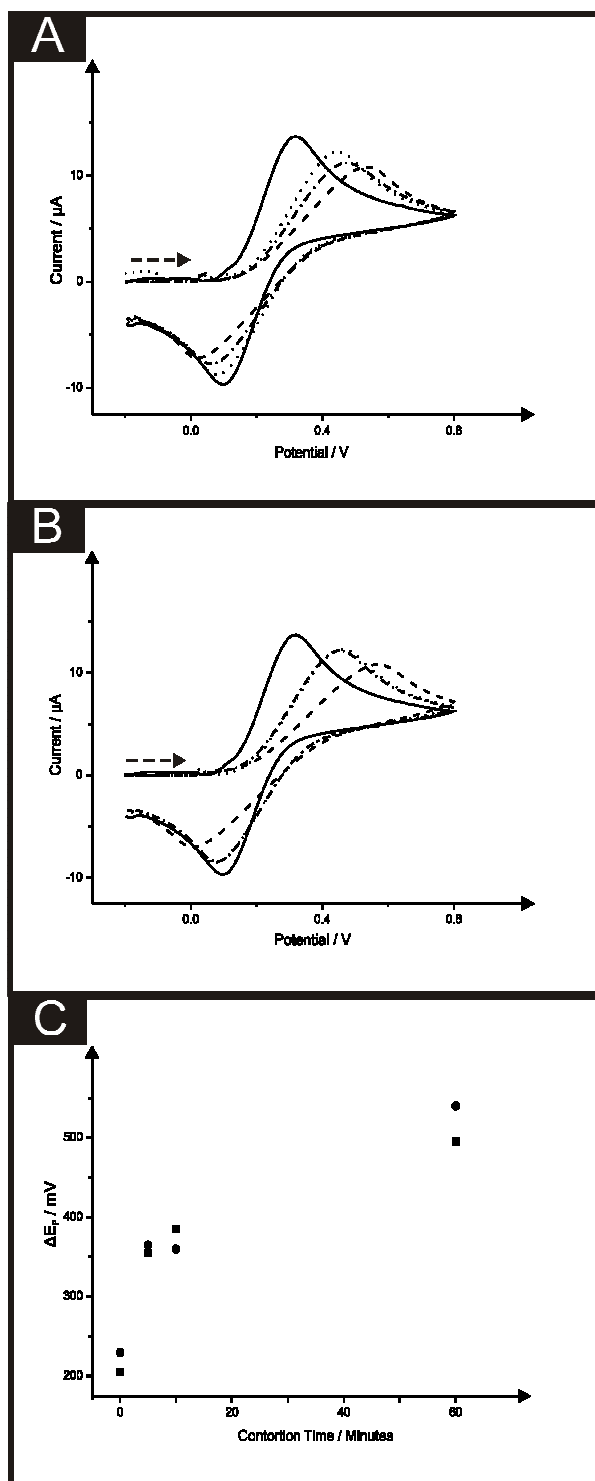


Figure 5.12 Cyclic voltammetric responses obtained at standard-SPE contorted at angles of (A): 45 and (B): 90 degrees, recorded in 1 mM ferrocyanide (II) / 1 M KCl. Contortion times of 60 (dashed line), 10 (dash-dotted line), 5 (dotted line) and 0 minutes (solid line) were utilised for each of the SPEs. Scan rate: 100 mV s^{-1} . Dashed arrow signifies direction of scan. Also shown is the effect of contortion time for the two angles upon voltammetric peak-to-peak separation (ΔE_p): 45 degrees (squares) and 90 degrees (circles).

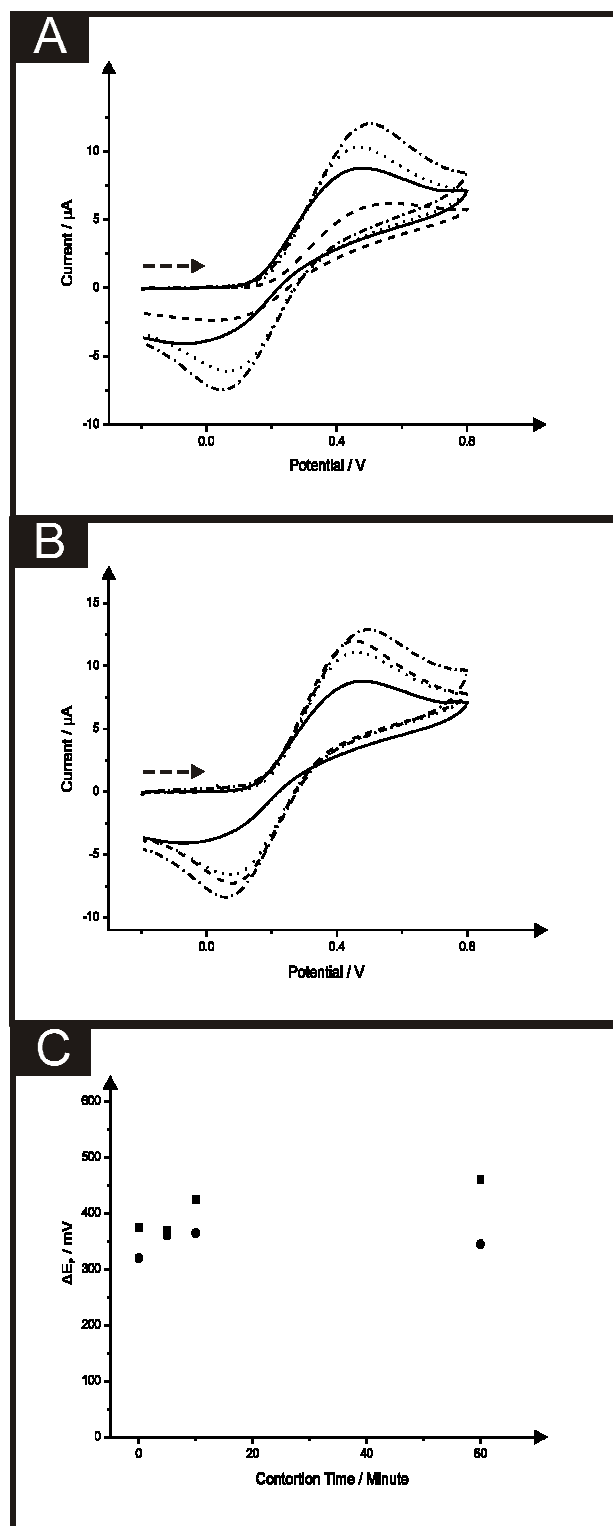


Figure 5.13 Cyclic voltammetric responses for ps-SPE contorted at angles of (A): 45 and (B): 90 degrees, recorded in 1 mM ferrocyanide (II) / 1 M KCl. Contortion times of 60 (dashed line), 10 (dash-dotted line), 5 (dotted line) and 0 minutes (solid line) were utilised for each of the SPEs. Scan rate: 100 mV s^{-1} . Dashed arrow signifies direction of scan. Also shown is the effect of contortion time for the two angles upon peak-to-peak separation (ΔE_p): 45 degrees (squares) and 90 degrees (circles).

Next the paper-based sensors were explored with the effect of contortion angle and time upon electrochemical performance being studied utilising the redox probe potassium ferrocyanide (II). Figures 5.13A and B show the cyclic voltammetric responses obtained utilising a ps-SPE. As has been previously reported⁵⁰¹ the electrochemical resistivity (and resultant ΔE_p) is greater at the ps-SPE compared to that at the standard-SPE prior to mechanical stress which is related to the resistivity of the printed layer (see earlier). Upon the introduction of mechanical stress at the fixed angles for the given contortion times there is a less of a change from the un-treated ΔE_p (320 mV) with a maximum peak-to-peak separation of 365 and 470 mV being observed at angles of 90 and 45 degrees respectively (figure 5.13C). Although as seen in figure 5.13C, the ΔE_p shifts to a greater value when contorted at 45 degrees rather than 90 degrees, the amount of time the electrodes are subjected to this stress has little bearing on the overall peak positions. Similarly the cyclic voltammograms obtained when utilising the pv-SPEs, as shown in figures 5.13A and B, show the same electrochemical behaviour as is noted at the ps-SPE; the overall peak potential does become slightly larger for the electrodes contorted at 45 degrees, however for 90 degrees there is little movement as you can observe in figure 5.13C. The differences owing to mechanical stress upon the ΔE_p of the paper- and polymer-based substrates as is highlighted within figures 5.12 to 5.15 might potentially be linked to the earlier determined effect of mechanical stress upon the resistivity recorded at each of the sensors. Evidently, comparisons may be drawn between the two sets of data, suggesting that the polymer-based substrate utilised for the standard-SPE are much more susceptible to mechanical stress. It is important to note that although these paper-based sensors offer greatest resilience in relation to mechanical stress over the pre-set periods, the initial voltammetry (prior to mechanical stress) exhibited by the sensors in terms of ΔE_p is larger than at the polymer-based sensor when utilising the redox probe potassium ferrocyanide (II); the polymer-based screen printed sensor exhibit a ΔE_p value of ~ 205 mV

which is in excellent agreement with previous literature⁵⁰² while the paper-based sensors exhibit greater voltammetric peak-to-peak separations of 425 and 355 mV for the pv- and pc-SPE, respectively.

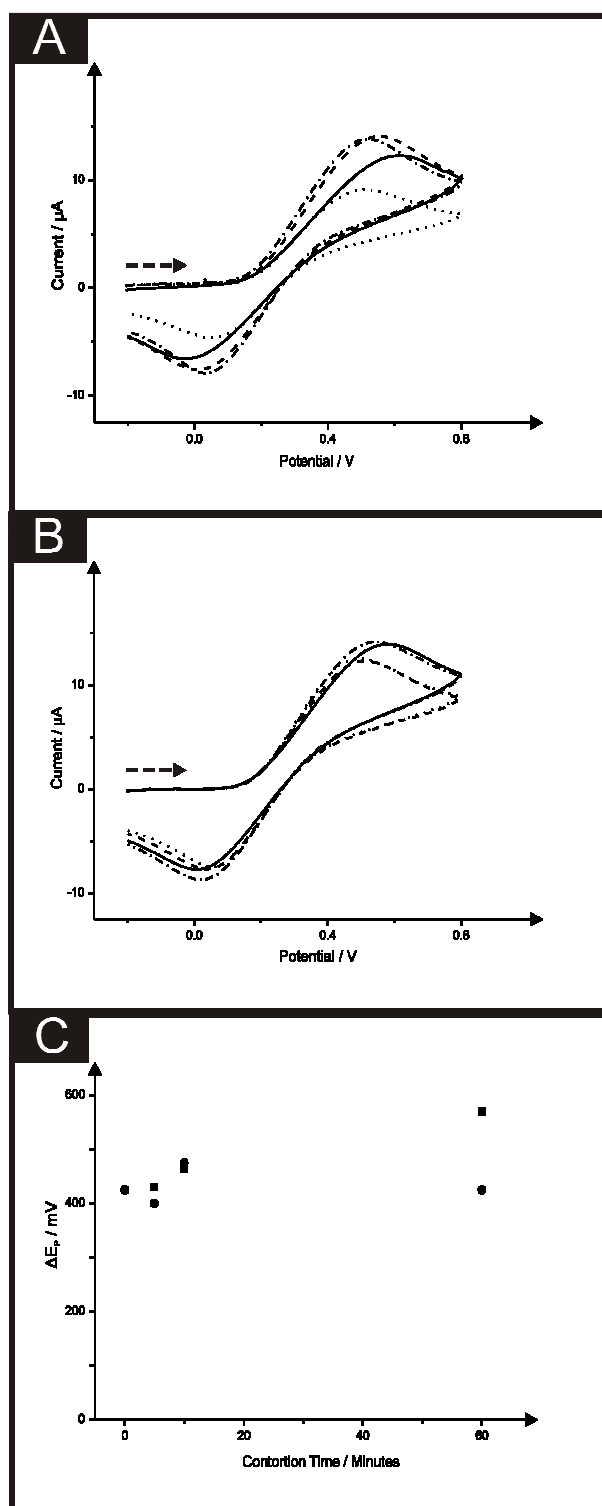


Figure 5.14 Cyclic voltammetric responses for pv-SPE contorted at angles of (A): 45 and (B): 90 degrees, recorded in 1 mM ferrocyanide (II) / 1 M KCl. Contortion times of 60 (dashed line), 10 (dash-dotted line), 5 (dotted line) and 0 minutes (solid line) were utilised for each of the SPEs. Scan rate: 100 mV s^{-1} . Dashed arrow signifies direction of scan. Also shown is the effect of contortion time for the two angles upon peak-to-peak separation (ΔE_p); 45 degrees (squares) and 90 degrees (circles).

To allow for comparisons and further understanding the studies relating to the effect of contortion time and angles upon the electrochemical performance and characteristics of the three electrodes, the outer-sphere electrochemical probe hexaammine-ruthenium (III) chloride was also utilised. As is highlighted in figures 5.15A-C, when comparing the overall resulting peak-to-peak separation at the three sensors following contortion time at the two angles, less change is noted compared with that seen when utilising the electrochemical probe potassium ferrocyanide (II). From the sensors explored in this study it is clear through assessment of this data that the standard-SPE (screen printed upon the plastic substrate) demonstrates the greatest susceptibility to contortion with a positive correlation between contortion time and peak-to-peak separation (figure 5.15A) being observed. The same trends, that is a positive correlation between the resultant peak-to-peak separation and contortion time are noted for both the ps- and pv-SPE's (figures 5.15B and C respectively) though these paper-based sensors offered greater resilience in relation to contortion time and degree over that of the standard-SPE since at longest contortion time and angle (45 degree), there is no significant deviation from the initial electrodes response before being contorted.

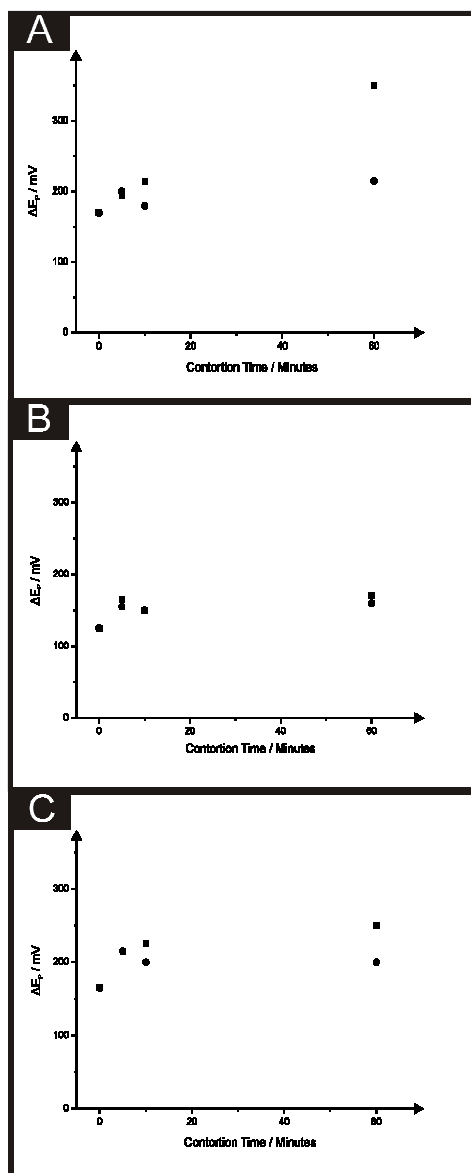


Figure 5.15 The effect of contortion time for the two angles upon peak-to-peak separation (ΔE_p): 45 degrees (squares) and 90 degrees (circles), in a solution of 1 mM hexamine-ruthenium (III) chloride / 0.1 M KCl when utilising the standard-SPE (A), ps-SPE (B) and pv-SPE (C). Scan rate: 100 mV s^{-1} .

Next, the effect of mechanical stress upon the screen printed electrochemical sensors were evaluated using the electrochemical oxidation of NADH (dihyronicotinamide adenine dinucleotide reduced form) to the corresponding oxidized form (NAD^+). The effect of mechanical stress upon the standard-SPE towards the sensing of $100 \mu\text{M}$ NADH in a pH 7 phosphate buffer solution using cyclic voltammetry following mechanical stress at angles of

45 and 90 degrees at fixed contortion times of 5, 10 and 60 minutes was first studied. As observed in figure 5.16A at a contortion angle of 90 degrees over the studied time period there is no significant change in the voltammetric peak current until 60 minutes where a slight reduction in the voltammetric peak height with an additional shift in the oxidative peak potential to a slightly more electropositive potentials occurs. However, following a more severe contortion at an angle of 45 degrees, the electrochemical response at the standard-SPE is more severe following a time of 60 minutes at which point the voltammetric peak is completely lost; clearly this is a limitation if these standard-SPE are used as the basis of biosensors in environments where mechanical contortion might be encountered.

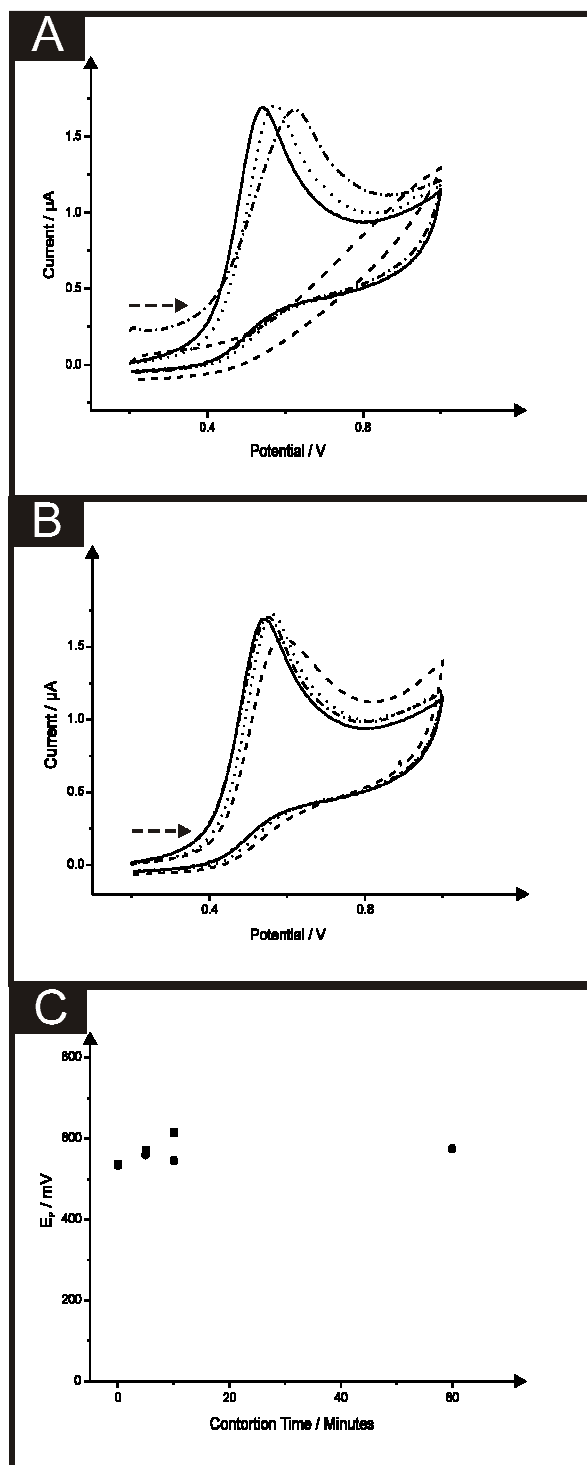


Figure 5.16 Cyclic voltammetric responses for standard-SPE contorted at angles of (A): 45 and (B): 90 degrees, recorded in 100 μM NADH in pH 7 phosphate buffer. Contortion times of 60 (dashed line), 10 (dash-dotted line), 5 (dotted line) and 0 minutes (solid line) were utilised for each of the SPEs. Scan rate: 100 mV s^{-1} . Dashed arrow signifies direction of scan. Also shown is the effect of contortion time for the two angles upon the voltammetric peak potential (E_p): 45 degrees (squares) and 90 degrees (circles).

In comparison, the initial electrochemical oxidation peak potential occurs at higher potentials at the ps- and pv- SPE over that of the standard-SPE which reflects the difference in the resistivity observed earlier; this potentially could be detrimental when these are applied into real sensing applications, but the full exact is yet to be fully explored. As observed in figures 5.17 and 5.18, the effect of mechanical contortion in terms of applied angles and times reveals there is a reduction in the peak magnitude at both ps- and pv- SPE with no shift in peak potential to higher overpotential which the largest effect on the electrochemical activity occurring from a time of 60 minutes being contorted at an angle of 45 degrees.

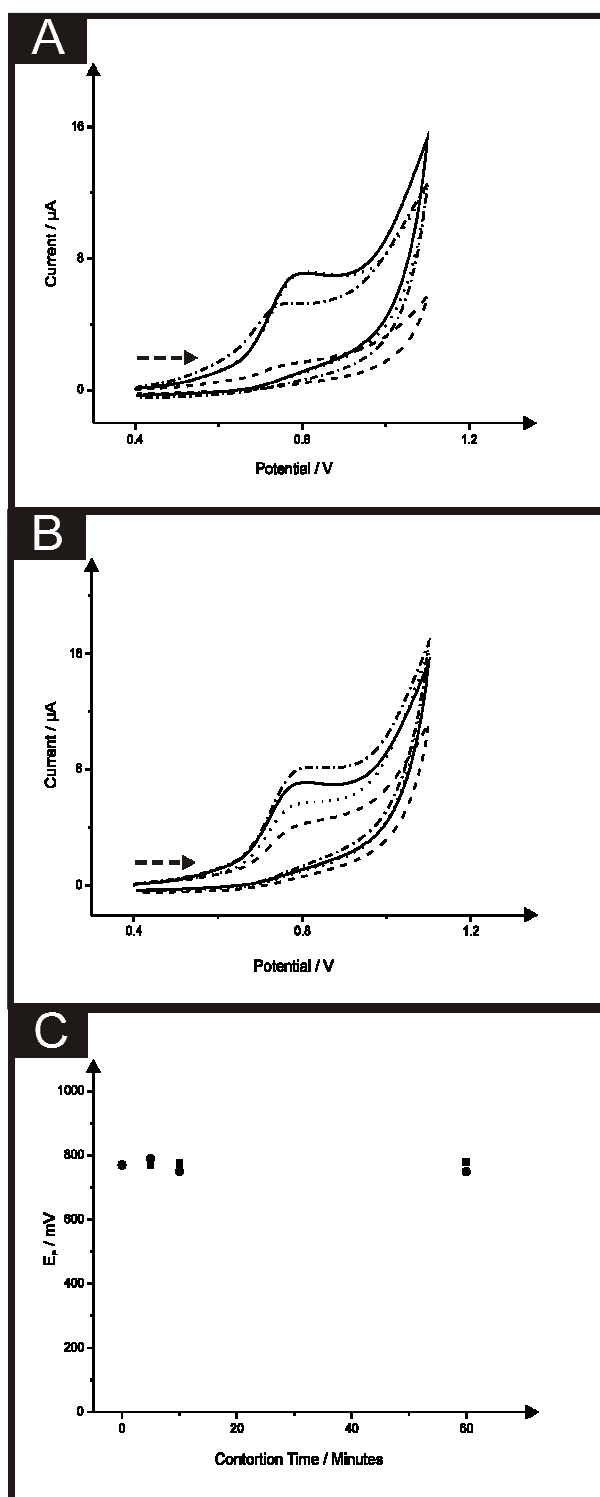


Figure 5.17 Cyclic voltammetric responses for ps-SPE contorted at angles of (A): 45 and (B): 90 degrees, recorded in 100 μM NADH in pH 7 phosphate buffer. Contortion times of 60 (dashed line), 10 (dash-dotted line), 5 (dotted line) and 0 minutes (solid line) were utilised for each of the SPEs. Scan rate: 100 mV s^{-1} . Dashed arrow signifies direction of scan. Also shown is the effect of contortion time for the two angles upon the voltammetric peak potential (E_p): 45 degrees (squares) and 90 degrees (circles).

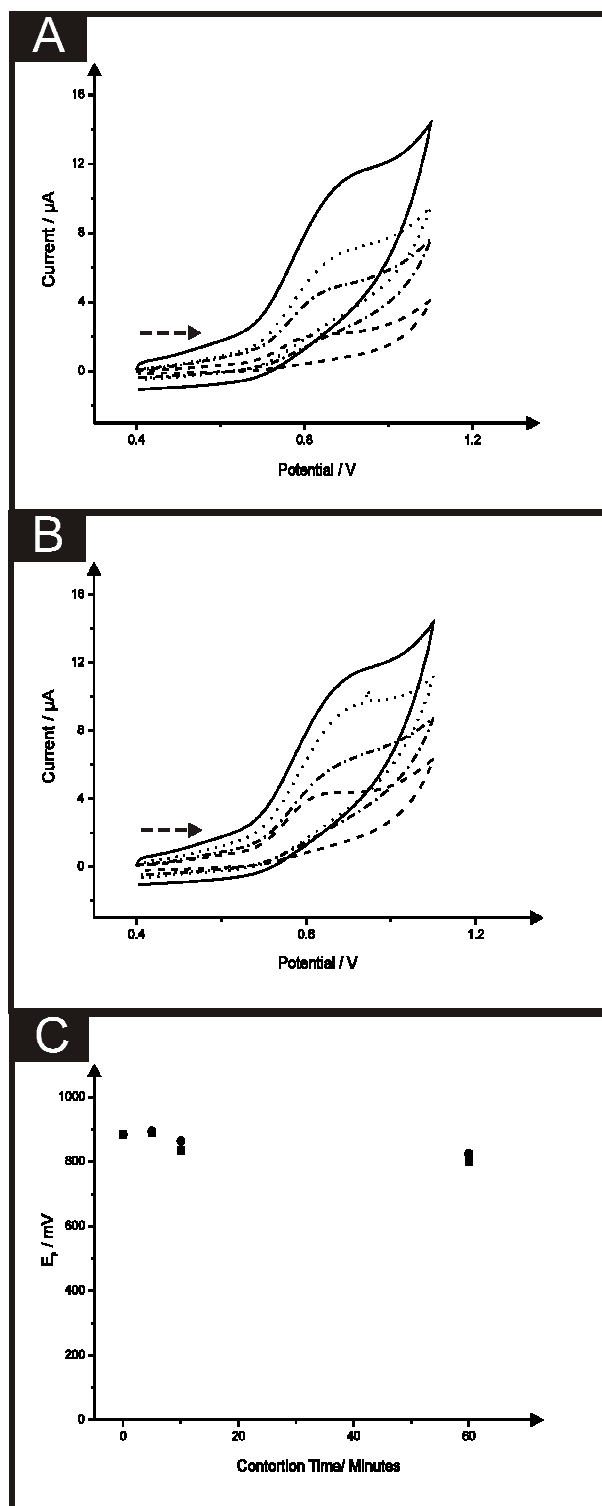


Figure 5.18 Cyclic voltammetric responses for pv-SPE contorted at angles of (A): 45 and (B): 90 degrees, recorded in 100 μM NADH in pH 7 phosphate buffer. Contortion times of 60 (dashed line), 10 (dash-dotted line), 5 (dotted line) and 0 minutes (solid line) were utilised for each of the SPEs. Scan rate: 100 mV s^{-1} . Dashed arrow signifies direction of scan. Also shown is the effect of contortion time for the two angles upon the voltammetric peak potential (E_p): 45 degrees (squares) and 90 degrees (circles).

In comparison of the all the screen printed electrodes as evaluated with the NADH/NAD⁺ probe (figures 6.16-18), while mechanical contortion has an effect on the electrochemical performance/activity, which will translate into sensing, the observed response, that is, reduction in voltammetric peak height and potential shift occurs to a lesser extent at the ps- and pv- SPEs than at the standard-SPEs; this is clearly reflected in the material used where the underlying paper based SPEs are inherently more flexible than those on polymeric based substrates. A payoff for this more flexible nature is that the electrochemical performance (in terms of the peak height/shape and potential) is worse than at the standard-SPEs which is likely due to adhesion of the carbon screen printed inks to the respective substrates. In order to gain further insights into the effect of mechanical stress / contortion, surface analysis was attempted. Figure 5.19 shows that damage can be observed to the conductive track which is where the impact of the mechanical contortion occurs. It was noted however that this is far from quantitative and hard to prove unambiguously. This coupled with the electrochemical observations as evaluated using electrochemical probes, it is likely that origin of the effects upon electrochemical performance/activity is due to the conductive path/track being altered/broken during the mechanical force/stress.

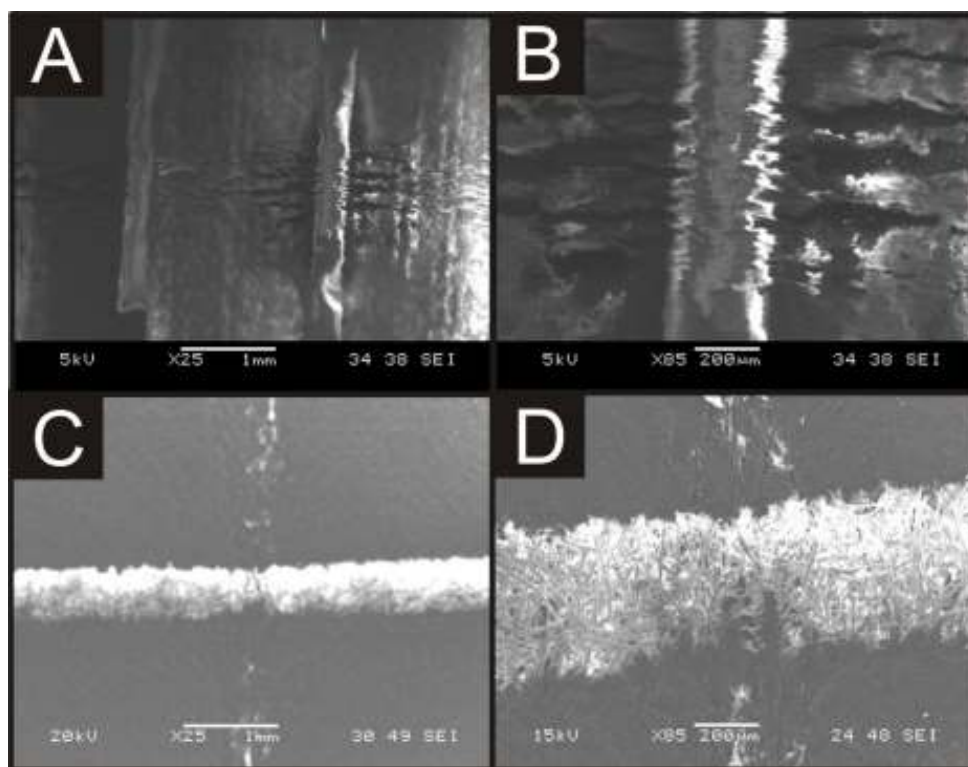


Figure 5.19 SEM images of the conductive track of a carbon screen printed electrodes on polyester substrates (A and B) and a paper based substrate (C and D, prior to coating with nail varnish or sellotape), following 60 minutes contorted at an angle of 45 degrees at magnifications of x 25 and x

85.

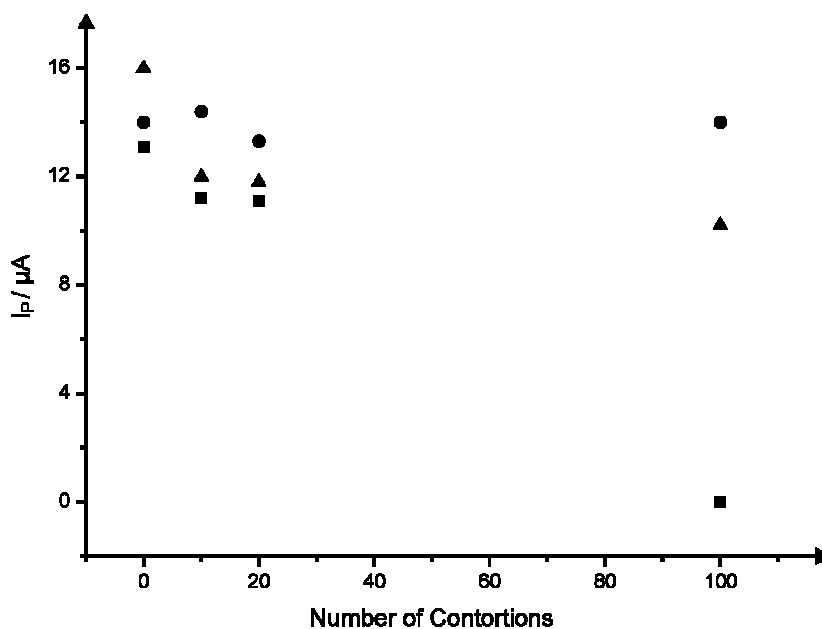


Figure 5.20 The effect of numerous and consecutive contortions to an angle of 45 degrees on voltammetric peak current (I_p), in a solution of 1 mM potassium ferrocyanide (II) / 0.1 M KCl when utilising the standard-SPE (squares), ps-SPE (circles) and pv-SPE (triangles). Scan rate: 100 $mV s^{-1}$.

Last, attention was focused upon the effect of repeated mechanical stress upon the three SPE sensors; in the above work the time and angle is controlled and the continual bending is also of importance. For continuity, the same electrochemical probes, potassium ferrocyanide (II) and NADH were utilised. The sensors underwent mechanical stress at an angle of 45 degrees, the most aggressive contortion angle, though in this instance rather than time, the effect of the number of contortion/bends was explored over a range of 0 to 100 contortions. In the case of the redox probe potassium ferrocyanide (II), figure 5.20 reveals that the ps-SPE demonstrates minimal effects in terms of electrochemical performance as a result of mechanical stress with the voltammetric peak current, and additionally both the peak-to-peak separation, remaining largely unchanged up to 100 contortions at an angle of 45 degrees. In contrast, the pv-SPE, was found to exhibit a decrease in the observed voltammetric peak current over the number of contortions studied and an increase in the peak-to-peak separation upon 100 contortions. The standard-SPE was determined to perform the worse with complete loss of electrochemical response. When utilised for the monitoring of 100 μM NADH in a pH 7 phosphate buffer solution the sensors utilised demonstrated behaviour close to that observed in potassium ferrocyanide (II) with the paper-based sensors providing more robust performance overall. Figure 5.21 depicts plots of voltammetric peak currents derived from cyclic voltammetric analysis in the solution of NADH after the set numbers of contortion applied to the sensors. As was the case for potassium ferrocyanide (II), the ps-SPE is shown to offer the most stable electrochemical performance in relation to repeated mechanical stress. Evidently when utilising the ps-SPE where after 20 contortions there is an increase in the voltammetric peak current and additionally a shift in the peak potential to less facile, more electropositive potentials. Further to this after 100 contortions the voltammetric signal is found to diminish greatly. The other paper-based sensor, the pv-SPE, exhibited a decrease in the recorded voltammetric peak current but notably, no change

in the oxidative peak potential, however, unlike the ps-SPE, the pv-SPE was found to fail after 100 contortions with no signal or voltammetric peak being recorded. Once more it was confirmed that of the sensors utilised, the standard-SPE, printed upon the polymer substrate was most susceptible to the effects of mechanical stress with notable effects on the voltammetric peak current after 20 contortions and a shift in the voltammetric potential, to that of a more electropositive region, for the oxidation of NADH occurring after 10 contortions. Further to this, as was noted for the ps-SPE, no signal was observed after 100 contortions suggesting that the connections of the electrode had been compromised.

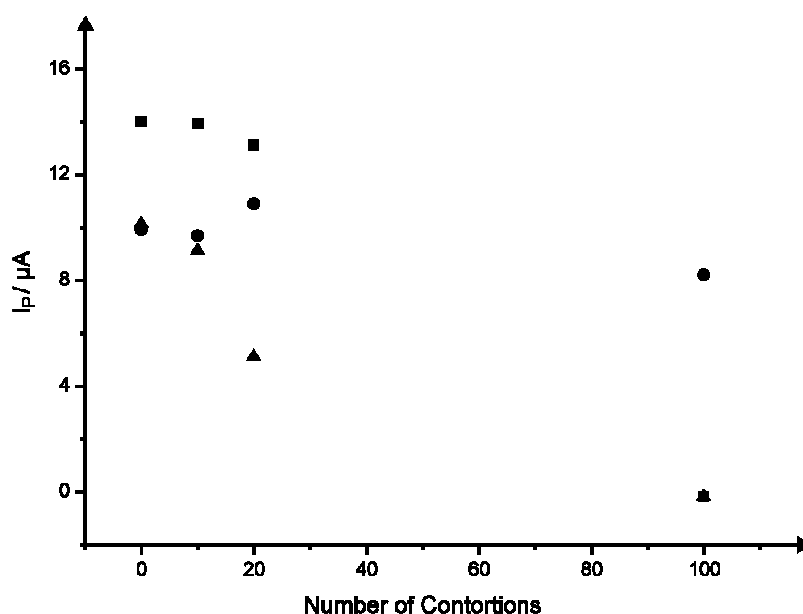


Figure 5.21 The effect of numerous and consecutive contortions to an angle of 45 degrees on voltammetric peak current (I_p), in a solution of $100 \mu M$ NADH in a pH 7 phosphate buffer solution when utilising the standard-SPE (squares), ps-SPE (circles) and pv-SPE (triangles). Scan rate: $100 mV s^{-1}$.

In summary, this section has determined that that the polymer-based substrate utilised for the fabrication of the standard-SPE is hindered by its lack of flexibility, which effects the observed electrochemical performance, unlike that of paper based sensors used within this study which are seen to be much more robust in nature.

5.2.3 CONCLUSIONS

It has been shown that screen printed electrodes based upon a polyester substrate are not as flexible and durable as initially thought. Throughout the literature there has been an over running theme that screen-printed electrodes had no limitations and were seen as very flexible as they are easy to manipulate but this study proves that excessive mechanical contortion and stress can have very detrimental effects upon the electrochemical response/activity. However, this study has also shown the ultra-flexibility of paper based screen printed which can undergo mechanical contortion/stress and are potentially useful for use in such environments where this would be encountered, such as in wearable sensors. However, the downside is that the initial electrochemical response at the paper-based sensors is worse in comparison to the polymeric based sensors, in terms of peak characteristics (height, potential, shape) which is likely due to the way the ink is adhered to the surface and is reflected in the differing resistivity's. The incorporation of these paper-based screen-printed sensors into analytical applications where mechanical contortion/stress will be encountered is currently being undertaken and will be reported separately.

6.1 OVERALL CONCLUSIONS

This thesis has reported two main significant contributions to the field of electrochemistry and particularly electroanalysis utilising screen printed electrodes. The first, major contribution disseminated in Chapter 3 arises from the development of “modified” electrodes which include the first true electroanalytical examples of noble metal and carbon nanotube modified single-walled screen printed electrodes. Again, benchmarking against the current literature reveals these to be novel and give rise to useful electroanalytical benefits in addition to the improved facile nature and practicality of the sensors over existing electrochemical techniques which require electrode modification.

Second, the importance and potential intuitive utilisation of working electrode geometry is also considered. Through utilisation of the changes in mass transport arising from altering the physical design of screen printed sensors, next generation screen printed sensors have been realised with the production of recessed, micro array and microband electrodes (see Chapter 4). Importantly, in all cases, whilst acting typically akin to pseudo-microelectrodes each electrode geometry offers exciting new insights within the area of the development of electrode geometries. An example of this is the microelectrode array which, unlike many microelectrodes or simple macro electrode arrays offers a sensor which actively considers and avoids the often overlooked issue of electrode spacing, ensuring sufficient spacing between neighbouring electrodes and as such avoiding diffusion layer interaction. Such configurations have never been reported before in the literature. Additionally the development of thinner (critical width; see Chapter 4) screen printed microband electrodes is reported for the first; such work is highly novel and continues to push the boundaries of

screen printed derived electrochemical sensors. Consequently, the aims and objectives of the thesis have been met.

6.2 SUGGESTIONS FOR FUTURE WORK

As this thesis has shown, next generation screen printed electrodes have been reported. The limitations for the fabrication of even smaller electrodes arise from the screen meshes available and the composition of the inks utilised (see Chapters 2 and 4 for further details). As new screens are constantly being developed (see Chapter 4, where a new V-screen mesh allowing 50 μm band electrodes to be realised is discussed) future work should consider the production of new printing inks such as graphene-based inks which would be expected to easily pass through small mesh sizes and should allow smaller screen printed geometries to be realised.

Additionally very little work focuses upon the polymeric constituents (binder) of the screen printed electrode inks, an area which could give potential rise to improvements through the exploration of different polymers/co-polymers for use within screen printing. Furthermore the graphite/carbon black itself is a key consideration, not only in terms of providing useful electron transfer but the functionality (along with the binder and constituents) which can change the hydrophobicity/hydrophilicity which will likely change the interaction of the target analyte. Other physical parameters also need to be monitored and controlled. For example, towards the end of this thesis, work has been directed to obtaining profile maps of the fabricated screen printed sensors and as shown in Appendix I.1, surface profile analysis has been performed. Such an approach is useful as it characterises the whole surface and profiles the variation in print thickness: a key parameter when considering screen printed sensors, particularly when considering reproducibility. Preliminary data has revealed that changing the printing angle is a major component which can dramatically change the profile of the print, something never highlighted in the literature.

The parameters identified above (inks and screens) limit the size of electrodes than can be reproducibly fabricated. As such typically, in the case of arrays, due to the size

pseudo-microelectrodes and arrays are achieved and thus significant improvements could still be realised through the development of ‘true’ microelectrodes. Another approach to overcome this is to screen print the carbon layer and a dielectric layer upon this and then produce microelectrodes through laser ablation of the dielectric layer exposing the underlying carbon layer. Such an approach was reported in the 1980’s⁵⁰³, but was not expanded further; the exact reasons not being clear. In the final stages of this thesis this novel approach has been re-explored. Appendix II shows a microelectrode array ($N = 400$) where three configurations are evident. The microelectrodes fabricated are 20 μm in diameter and are separated from their nearest neighbour by 50, 100 and 150 μm (figures AII.1 A, B and C respectively).

Closer inspection of the fabricated microelectrode arrays reveal that they appear to be recessed due to the fabrication approach. The electrochemical performance of the electrodes was explored towards the redox probe hexaammine-ruthenium (III) chloride where figures AII.2 A, B and C show the corresponding voltammetry and figure AII.3 overlays the response for each at a scan rate of 5 mV s^{-1} . It is clear that a macro electrode type peak-shaped response is evident at the microelectrode array with electrode separations of 50 μm , with increasing electrode separation (100 and 150 μm) the voltammetry turns towards that typical of a microelectrode array response.

The current expected at a 20 μm microelectrode comprising an array of N microelectrodes is given by:

$$I = 4nFrDCN \quad (6.1)$$

where n is the number of electrons transferred, r the electrode radius, D the diffusion coefficient of the redox probe, C the analyte concentration and N the number of electrode comprising the array. For each of the different sensors (50, 100 and 150 μm separation) the

theoretical current was deduced and compared to the experimental current obtained as is shown in table 6.1; clearly there is some disparity.

Electrode Separation (μm)	Theoretical Current (at 5 mV s^{-1}) (A)	Experimental Current (at 5 mV s^{-1}) (A)
50	3.51×10^{-7}	6.95×10^{-7}
100	3.51×10^{-7}	8.32×10^{-7}
150	3.51×10^{-7}	4.58×10^{-7}

Table 6.1 A comparison of the theoretical and experimental currents arising from utilisation of the laser ablated arrays of different electrode separations (50, 100 and 150 μm).

At each scan rate the experimental diffusion layer thickness (δ) can be determined to see if the diffusion clouds of the electrodes comprising the array overlap. In order to assess this the following equation is employed:

$$\delta = \sqrt{6D(\Delta E / \nu)} \quad (6.2)$$

where D is the diffusion coefficient ($9.1 \times 10^{-6} \text{ cm}^2 \text{ s}^{-1}$,⁵⁰⁴), ν the voltammetric scan rate employed and ΔE the potential range over which electrolysis has occurred. The diffusion layer is calculated to be 3097.6, 13585.8, 979.5, 738.3 and 653.2 μm at scan rates of 5, 25, 50, 75 and 100 mV s^{-1} respectively at the 150 μm separation laser ablated microelectrode array. The separation which is required between electrodes is given by:

$$d_{\text{required}} = \left(\frac{A}{2}\right) - \left(\frac{B}{2}\right) \quad (6.3)$$

where A is the distance between neighbouring microelectrodes and B is the diameter of the microelectrode. Thus, for the 150 μm array:

$$\left(\frac{150}{2}\right) - \left(\frac{20}{2}\right) = 65\mu m \quad (6.4)$$

Hence in all applied scan rates, diffusional overlap occurs even at this, the largest separation of the three electrodes fabricated. The % Relative Standard Deviation towards the redox probe hexaammine-ruthenium (III) chloride when utilising the 150 μm separation laser ablated array is found to correspond to 3.17 %, suggesting that although electrode diffusion cloud overlap does occur, the screen printed microelectrode arrays to allow for highly reproducible responses.

Future work should involve the increase of the electrode separation of the laser ablated microelectrodes comprising the array to give rise to significant improvements in the electrochemical behaviour and current response observed at the laser ablated microelectrode arrays. Additionally, the underlying material, currently graphite, could be readily changed to a metallic oxide surface greatly expanding the range of electroanalytical sensors.

Further work can be summarised as follows:

- 1) Development of next generation screen printed inks (both graphite and noble metal based) and their detailed characterisation.
- 2) Metallic pentagon (and related shapes with more “edge”) electrodes utilising the benefits of both the mass transport improvements and metal oxide inks (see Chapters 4 and 5).
- 3) The development of a 20 μm (and smaller) screen printed microband electrodes through the careful utilisation of novel inks of reduced particle sizes and printing parameters and screens.
- 4) Laser ablated true microelectrodes and their arrays as identified above.

- 5) The extension of paper based electrochemical sensors (as presented in Chapter 5) into novel scenarios, especially those where extensive mechanical stress/strain will be encountered.

6.4 APPENDICES

6.4.1 APPENDIX I



3-Dimensional Interactive Display

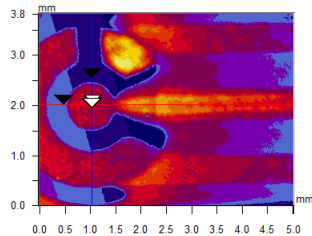
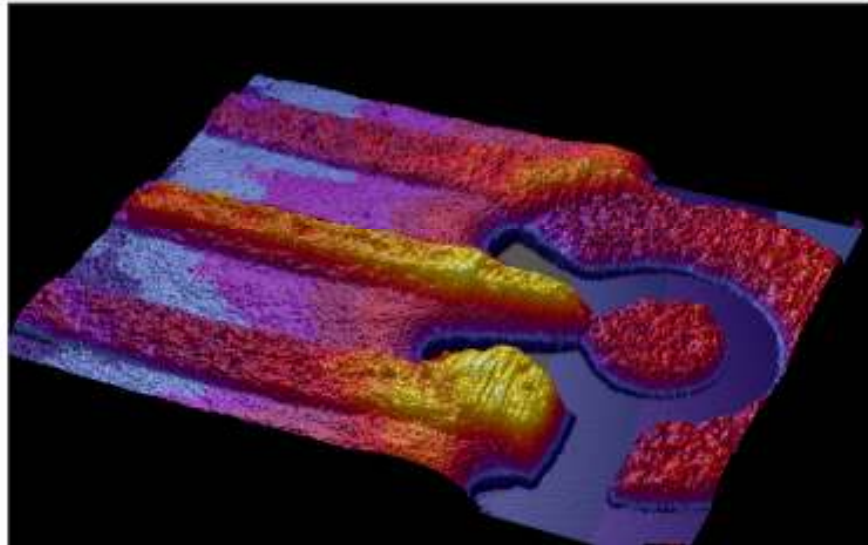
Date: 06/13/2013
Time: 13:06:42

Surface Stats:

Ra: 7.58 μm
Rq: 9.46 μm
Rt: 48.36 μm

Measurement Info:

Magnification: 1.25
Measurement Mode: VSI
Sampling: 6.83 μm
Array Size: 736 X 480



X	1.03	-	-	mm
Y	2.02	-	-	mm
Ht	7.26	-	-	μm
Dist		-	-	mm
Angle		-	-	$^{\circ}$

Title:

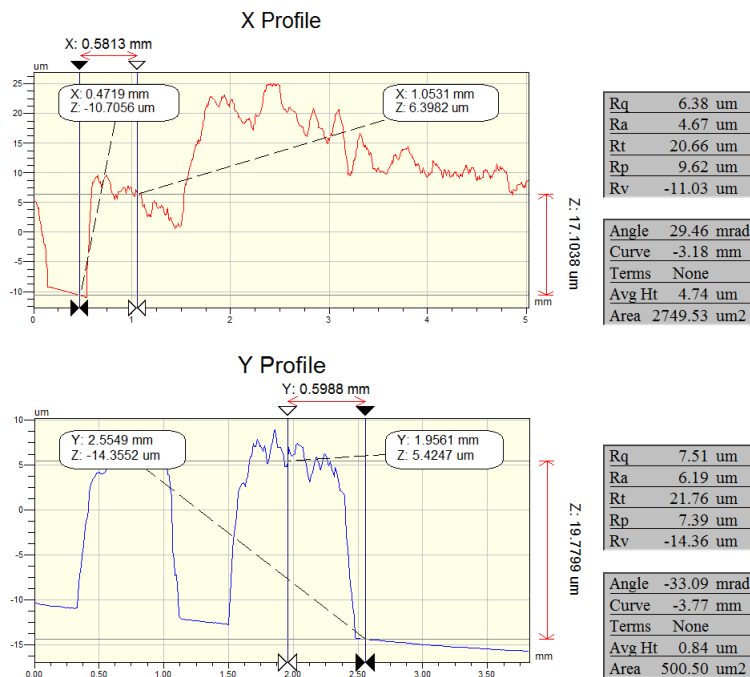


Figure AI.1 3-dimensional analysis of a standard screen printed sensor (top image) and profile analysis (bottom image). Analysis performed by: Dr Walter Perrie, School of Engineering, University of Liverpool.

6.4.2 APPENDIX II

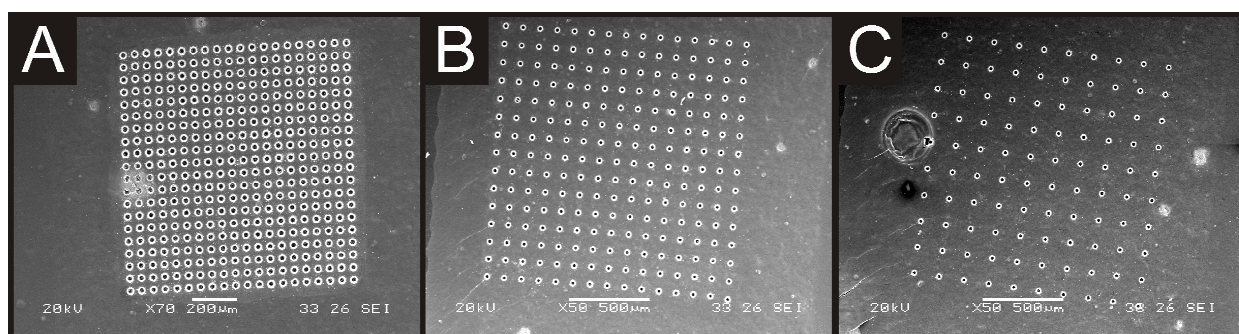


Figure AII.1 Typical SEM images depicting the laser ablated graphite microelectrode arrays with different electrode separations of: A) 50 μm , B) 100 μm and C) 150 μm .

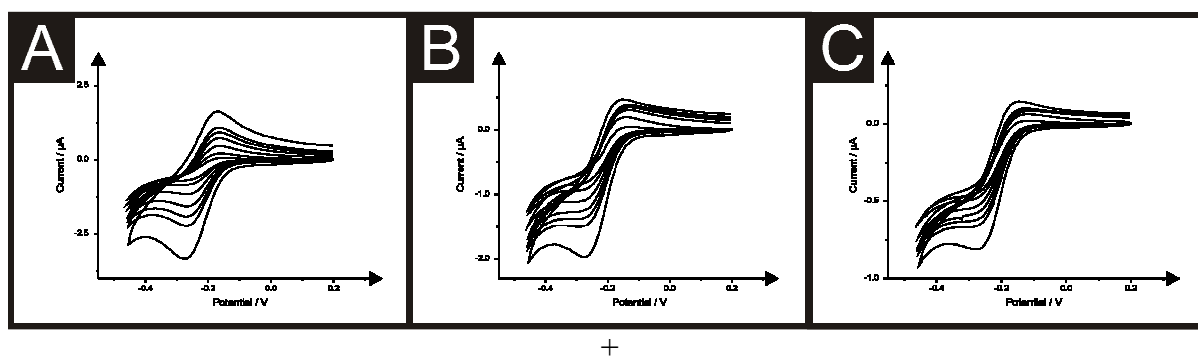


Figure AII.2 Typical cyclic voltammetric responses observed through scan rate studies ($5 - 200 \text{ mV s}^{-1}$) at the laser ablated graphite microelectrode arrays with different electrode separations of: A) 50 μm , B) 100 μm and C) 150 μm in 1 mM hexaammine-ruthenium (III) chloride in 0.1 M KCl.

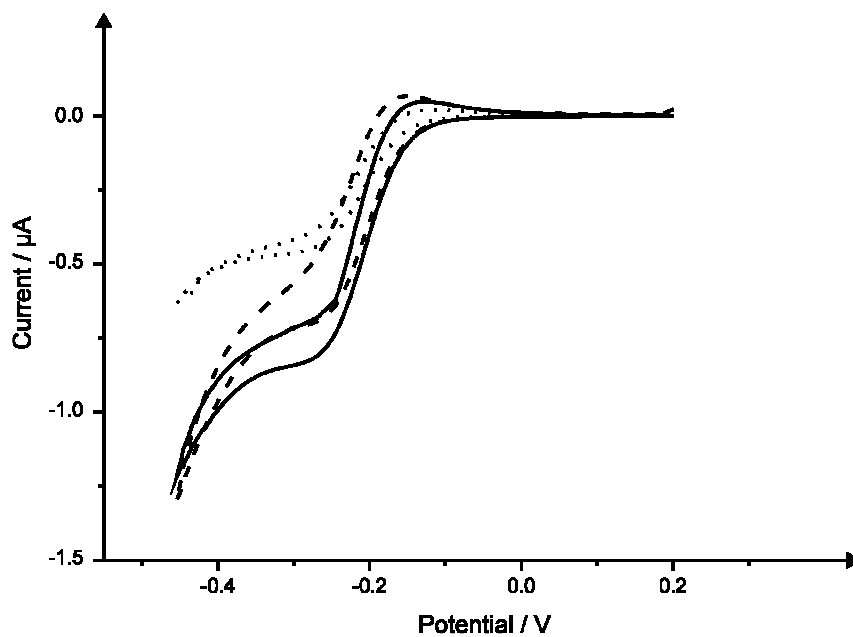


Figure AII.3 A comparison of typical cyclic voltammograms obtained at the laser ablated graphite microelectrode arrays with different electrode separations of: 50 μm (dashed line), 100 μm (solid line) and 150 μm (dotted line) in 1 mM hexaammine-ruthenium (III) chloride in 0.1 M KCl. Scan rate: 5 mV s^{-1} .

REFERENCES

1. A. J. Bard and L. R. Faulkner, *Electrochemical Methods*, 2001, 2nd Ed., Wiley, New York.
2. A. C. Fisher, *Electrode Dynamics*, 2009, Oxford University Press, New York.
3. J. Wang, *Analytical Electrochemistry*, 2000, 2nd Ed., Wiley-VCH, New York.
4. F. Scholz, *Electroanalytical Methods*, 2010, Springer-Verlag Berlin Heidelberg.
5. R. G. Compton and C. E. Banks, *Understanding Voltammetry*, 2007, 1st Ed., World Scientific Ltd.
6. P. Zanello, *Inorganic Electrochemistry: Theory, Practise and Application*, 2003, The Royal Society of Chemistry.
7. R. S. Nicholson, *Anal. Chem.*, 1965, **37**, 1351.
8. I. Lavagnini, R. Antiochia and F. Magno, *Electroanalysis*, 2004, **16**, 505.
9. H. O. Pierson, *Handbook of Carbon, Graphite, Diamond and Fullerenes Properties: Processing and Applications*, 1995, Noyes Publications, New Jersey.
10. M. S. Mauter and M. Elimelech, *Envir. Sci. and Tech.*, 2008, **42**, 5843.
11. N. S. Novoselov, A. K. Geim, S. V. Morozov, D. Jiang, Y. Zhang, S. V. Dubonos, I. V. Grigorieva and A. A. Firsov, *Science*, 2004, **306**, 666.
12. A. K. Geim and K. S. Novoselov, *Nat. Mater.*, 2007, **6**, 183.
13. D. A. C. Brownson, L. J. Munro, D. K. Kampouris and C. E. Banks, *RSC Advances*, 2011, **1**, 978.
14. F. Kreupl, "Carbon Nanotubes in Microelectronic Applications" in; *Carbon Nanotube Devices: Properties, Modeling, Integration and Applications*, 2008, Wiley-VCH.
15. G. M. Jenkins and K. Kawamura, *Nature*, 1971, **231**, 175.

16. A. MacDougal, 2008, *Screen Printing Today: The Basics*, ST Media Group International Inc (2nd Ed.).
17. S. Abbott, *How To Be A Great Screen Printer*, 2008, Macdermid Autotype Limited, Wantage.
18. J. Wang, B. Tian, V. B. Nascimento and L. Angnes, *Electrochim. Acta*, 1998, **43**, 3459.
19. P. Fanjul-Bolado, D. Hernandez-Santos, P. J. Lamas-Ardisana, A. Martin-Pernia and A. Costa-Garcia, *Electrochim. Acta.*, 2008, **53**, 3635.
20. R. O. Kadara, N. Jenkinson and C. E. Banks, *Sens. Actuators*, 2009, **142**, 342.
21. R. Baron, B. Sljukić, C. Salter, A. Crossley and R. G. Compton, *Electroanalysis*, 2007, **19**, 1062.
22. C. E. Banks and R. G. Compton, *Electroanalysis*, 2003, **15**, 329.
23. C. E. Banks and R. G. Compton, *Analyst*, 2004, **129**, 678.
24. N. A. Choudhry, D. K. Kampouris, R. O. Kadara and C. E. Banks, *Electrochem. Commun.*, 2009, **12**, 6.
25. T. J. Davies, M. E. Hyde and R. G. Compton, *Angew. Chem.*, 2005, **117**, 5251.
26. N. A. Choudhry, R. O. Kadara and C. E. Banks, *Phys. Chem. Chem. Phys.*, 2010, **12**, 2285.
27. N. A. Choudhry, R. O. Kadara, N. Jenkinson and C. E. Banks, *Electrochem. Commun.*, 2010, **12**, 406.
28. K. C. Honeychurch, J. P. Hart and D. C. Cowell, *Electroanalysis*, 2000, **12**, 171.
29. K. Z. Brainina, N. F. Zakharchuk, D. P. Synkova and I. G. Yudelevich, *Electroanal. Chem.*, 1972, **35**, 165.
30. N. A. Choudhry and C. E. Banks, *Anal. Methods*, DOI: 10.1039/C0AY00527D, 2011.
31. M. H. Chiu, H. H. Yang, C. H. Liu and J. M. Zen, *J. Chromatogr.*, 2009, **877**, 991.

32. K. S. Prasad, G. Muthuraman and J. M. Zen, *Electrochem. Commun.*, 2008, **10**, 559.
33. T. H. Yang, C. L. Hung, J. H. Ke and J. M. Zen, *Electrochem. Commun.*, 2008, **10**, 1094.
34. N. Y. Stozhko, N. A. Malakhova, M. V. Fyodorov and K. Z. Brainina, *J. Solid State Electrochem.*, 2008, **12**, 1219.
35. J. Wang, N. Naser, L. Angnes, H. Wu and L. Chen, *Anal. Chem.*, 1992, **64**, 1285.
36. J. H. Yoon, G. Muthuraman, J. E. Yang, Y. B. Shim and M. S. Won, *Electroanalysis*, 2007, **19**, 1160.
37. R. Ojani, J. B. Raouf and S. Fathi, *J. Solid State Electrochem.*, 2009, **13**, 927.
38. J. Wu, J. Suls and W. Sansen, *Electrochem. Commun.*, 2000, **2**, 90.
39. P. Kotzian, P. Brazdilova, K. Kalcher and K. Vytras, *Anal. Lett.*, 2005, **38**, 1099.
40. N. A. Choudhry, D. K. Kampouris, R. O. Kadara, N. Jenkinson and C. E. Banks, *Anal. Methods*, 2009, **1**, 183.
41. P. M. Hallam, D. K. Kampouris, R. O. Kadara, N. Jenkinson and C. E. Banks, *Anal. Methods*, 2010, **2**, 1152.
42. N. W. Beyene, P. Kotzian, K. Schachl, H. Alemuc, E. Turkušić, A. Čopra, H. Moderegger, I. Švancara, K. Vytřas and K. Kalcher, *Talanta*, 2004, **64**, 1151.
43. R. O. Kadara and I. E. Tothill, *Anal. Chim. Acta.*, 2008, **623**, 76.
44. C. Kokkinos and A. Economou, *Curr. Anal. Chem.*, 2008, **4**, 183.
45. J. Wang, *Electroanalysis*, 2005, **17**, 1341.
46. A. Economou, *Trends Anal. Chem.*, 2005, **24**, 334.
47. M. Khairy, R. O. Kadara, D. K. Kampouris and C. E. Banks, *Electroanalysis*, 2010, **22**, 1455.
48. J. Kruusma, C. E. Banks and R. G. Compton, *Anal. Bioanal. Chem.*, 2004, **379**, 700.

49. C. E. Banks, J. Kruusma, M. E. Hyde, A. Salimi and R. G. Compton, *Anal. Bioanal. Chem.*, 2004, **379**, 227.
50. W. Zhang, H. Tang, P. Geng, Q. H. Wang and L. T. Jin, *Electrochem. Commun.*, 2007, **9**, 833.
51. B. Nigovic, B. Simunic and S. Hocevar, *Electrochim. Acta*, 2009, **54**, 5678.
52. A. Charalambous and A. Economou, *Electrochim. Acta*, 2005, **547**, 53.
53. M. L. Yang, Z. J. Zhan, Z. B. Hu and J. H. Li, *Talanta*, 2006, **69**, 1162.
54. O. Zaouak, L. Authier, C. Cugnet, A. Castetbon and M. Potin-Gautier, *Electroanalysis*, 2009, **21**, 689.
55. S. B. Hocevar, I. Svancara, K. Vytras and B. Ogorevc, *Electrochim. Acta*, 2005, **51**, 706.
56. G. J. Lee, H. M. Lee, Y. R. Uhm, M. K. Lee and C. K. Rhee, *Electrochem. Commun.*, 2008, **10**, 1920.
57. R. Kadara and I. E. Tothill, *Anal. Chim. Acta.*, 2008, **623**, 76.
58. R. G. Compton and C. E. Banks, *Understanding Voltammetry*, World Scientific, Singapore, 2007.
59. D. K. Kampouris and C. E. Banks, *Environmentalist*, 2010, **104**, 14.
60. J. Guo and E. Linder, *Anal. Chem.*, 2009, **81**, 130.
61. A. Berduque, Y. H. Lanyon, V. Beni, G. Herzog, Y. E. Watson, K. Rodgers, F. Stam, J. Alderman and D. W. M. Arrigan, *Talanta*, 2007, **71**, 1022.
62. P. N. Bartlett and S. L. Taylor, *Electroanal. Chem.*, 1998, **453**, 49.
63. D. D. Gornall, S. D. Collyer and S. P. J. Higson, *Electroanalysis*, 2010, **22**, 384.
64. A. C. Barton, S. D. Collyer, F. Davies, D. D. Gornall, K. A. Law, E. C. D. Lawrence, D. W. Mills, S. Myler, J. A. Pritchard, M. Thompson and S. P. J. Higson, *Biosens. Bioelectron.*, 2004, **20**, 328.

65. S. Wilke, M. D. Osborne and H. H. Girault, *Electroanal. Chem.*, 1997, **436**, 53.
66. C. Cugnet, O. Zaouak, A. Rene, C. Pecheyran, M. Potin-Gautier and L. Authier, *Sens. Actuators*, 2009, **143**, 158.
67. E. Dock, A. Christenson, S. Sapelnikova, J. Krejci, J. Emneus and T. Ruzgas, *Anal. Chim. Acta.*, 2005, **531**, 165.
68. S. J. Hood, R. O. Kadara, D. K. Kampouris and C. E. Banks, *Analyst*, 2010, **135**, 76.
69. M. Khairy, R. O. Kadara, C. E. Banks, *Anal. Methods*, 2010, **2**, 851.
70. R. O. Kadara, N. Jenkinson and C. E. Banks, *Electrochem. Commun.*, 2009, **11**, 1377.
71. J. C. Ball, D. L. Scott, J. K. Lump, S. Daunert, J. Wang and L. G. Bachas, *Anal. Chem.*, 2000, **72**, 497.
72. T. Schüler, T. Asmus, W. Fritzsche and R. Möller, *Biosens. Bioelectron.*, 2009, **24**, 2077.
73. J. L. Chang and J. M. Zen, *Electrochem. Commun.*, 2006, **8**, 571.
74. T. H. Yang, C. Y. Liao, J. L. Chang, C. H. Lien and J. M. Zen, *Electroanalysis*, 2009, **21**, 2390.
75. C. Y. Liao, C. C. Chang, C. Ay and J. M. Zen, *Electroanalysis*, 2007, **19**, 65.
76. D. H. Craston, C. P. Jones, D. E. Williams and N. E. Murr, *Talanta*, 1991, **38**, 17.
77. J. L. Chang and J. M. Zen, *Electrochem. Commun.*, 2007, **9**, 2744.
78. J. L. Chang and J. M. Zen, *Electroanalysis*, 2006, **18**, 941.
79. C. H. Chou, J. L. Chang and J. M. Zen, *Electroanalysis*, 2009, **21**, 206.
80. C. H. Chou, J. L. Chang and J. M. Zen, *Sens. Actuators*, 2010, **147**, 669.
81. F. J. Rawson, W. M. Purcell, J. Xu, R. M. Pemberton, P. R. Fielden, N. Biddle and J. P. Hart, *Talanta*, 2009, **77**, 1149.
82. R. M. Pemberton, F. J. Rawson, J. Xu, R. Pittson, G. A. Drago, J. Griffiths, S. K. Jackson and J. P. Hart, *Microchim. Acta.*, 2010, **170**, 321.

83. R. M. Pemberton, J. Xu, R. Pittson, N. Biddle, G. A. Drago, S. K. Jackson and J. P. Hart, *Anal. Biochem.*, 2009, **385**, 334.
84. N. G. Karousos, R. Carrington, S. J. Wilkins, C. Livingstone and J. Davies, *Electrochem. Commun.*, 2005, **7**, 500.
85. C. M. Welch, M. E. Hyde, O. Nekrassova and R. G. Compton, *Phys. Chem. Chem. Phys.*, 2004, **6**, 3153.
86. J. B. Vincent, *J. Trace Elem. Exp. Med.*, 2003, **16**, 227.
87. R. M. Cespon-Romero, M. C. Yebra-Biurrun and M. P. Bermejo-Barrera, *Anal. Chim. Acta*, 1996, **327**, 37.
88. World Health Organisation, 1993, Guidance for Drinking Water Quality, Second Ed., Vol. 1. Recommendations, Geneva.
89. D. Golub and Y. Oren, *J. Appl. Electrochem.*, 1989, **19**, 311.
90. R. J. Kieber, J. D. Willey and S. D. Zvalaren, *Environ. Sci. Technol.*, 2002, **36**, 5321.
91. J. H. Larochell and D. C. Johnson, *Anal. Chem.*, 1978, **50**, 240.
92. A. M. Bond and G. H. Wallace, *Anal. Chem.*, 1982, **54**, 1706.
93. J. d. Joung and A. U. T. Brinkman, *Anal. Chem.*, 1978, **98**, 243.
94. W. Salvin, *Atom. Spectr.*, 1983, **2**, 163.
95. A. J. Pik, J. M. Eckert and K. L. Williams, *Anal. Chim. Acta*, 1981, **124**, 351.
96. R. E. Cranston and J. W. Murray, *Anal. Chem.*, 1978, **99**, 275.
97. I. Turyan and D. Mandler, *Anal. Chem.*, 1997, **69**, 894.
98. J. Kalembkiewicz and E. Soso, *WaidomosciChameczne*, 2002, **56**, 855.
99. Q. Li, K. J. Morris, P. K. Dasgupta, I. M. Raimundo and H. Temkin, *Anal. Chim. Acta*, 2003, **749**, 151.
100. M. Korolczuk and M. Grabareczyk, *Talanta*, 1999, **49**, 703.
101. N. A. Carrington, L. Yong and Z.-L. Xue, *Anal. Chim. Acta*, 2006, **572**, 17.

102. C. M. A. Brett, O. M. S. Fillipe and C. S. Neves, *Anal. Lett.*, 2003, **36**, 955.
103. J. P. Metters, R. O. Kadara and C. E. Banks, *Analyst*, 2011, **136**, 1067.
104. P. M. Hallam, D. K. Kampouris, R. O. Kadara and C. E. Banks, *Analyst*, 2010, **135**, 1947.
105. O. Dominguez-Renedo, L. Ruiz-Espelt, N. Garcia-Astorgano and M. J. Arcos-Martinez, *Talanta*, 2008, **76**, 854.
106. L. Lin, N. S. Lawrence, S. Thingngamdee, J. Wang and Y. Lin, *Talanta*, 2005, **65**, 144.
107. M. F. Beramini, D. P. d. Santos and M. V. B. Zanoni, *Sens. Actuators, B*, 2007, **123**, 902.
108. C. M. Welch, O. Nekrassova and R. G. Compton, *Talanta*, 2005, **65**, 74.
109. M.-C. Tsai and P.-Y. Chen, *Talanta*, 2008, **76**, 533.
110. G. Liu, Y.-Y. Lin, H. Wu and Y. Lin, *Environ. Sci. Technol.*, 2007, **41**, 8129.
111. J. A. Cox and P. J. Kulesza, *Anal. Chim. Acta*, 1993, **154**, 71.
112. MCI Precision Screens Ltd., <http://www.mciprecisionscreens.com/>.
113. Southwest Nanotechnologies, http://www.swentnano.com/tech/docs/SWeNT_MSDS_V2Vi_100x.pdf, Accessed July 2012.
114. Dropsens, http://www.dropsens.com/en/pdfs_productos/110cnf+c1110cnf.pdf, Accessed June 2012.
115. F. Machalet, K. Edinger, J. Melnhailis, M. Diegel, K. Steenbeck and E. Steinbeiss, *Appl. Phys., A*, 2000, **71**, 331.
116. C. E. Banks, A. O. Simm, R. Bowler, K. Dawes and R. G. Compton, *Anal. Chem.*, 2005, **77**, 1928.

117. T. J. Davies, C. E. Banks and R. G. Compton, *J. Solid State Electrochem.*, 2005, **9**, 797.
118. R. S. Nicholson and I. Shain, *Anal. Chem.*, 1964, **36**, 706.
119. R. S. Nicholson and I. Shain, *Anal. Chem.*, 1965, **37**, 179.
120. H. Matsuda and Y. Ayabe, *Z. Elektrochem*, 1955, **59**, 494.
121. R. N. Adams, 1968, *Electrochemistry at Solid Electrodes*, Marcel Dekker, Inc.: New York.
122. R. O. Kadara, N. Jenkinson and C. E. Banks, *Sens. Actuators, B*, 2009, **138**, 556.
123. P. Zanello and G. Rapsi, *Anal. Chem.*, 1977, **88**, 237.
124. I. Danilov and A. B. Velichenko, *Electrochim. Acta*, 1993, **38**, 437.
125. R. I. Stefan, S. G. Bairu and J. F. van Staden, *Anal. Chem.*, 2003, **376**, 844.
126. S. T. Crosmun and T. R. Mueller, *Anal. Chim. Acta*, 1975, **75**, 199.
127. M. H. Fekri, H. Khanmodammadi and M. Darvishpour, *Int. J. Electrochem.*, 2011, **6**, 1679.
128. A. Abbaspour and A. Izadyar, *Talanta*, 2006, **71**, 887.
129. World Health Organisation, 1996, *Guidelines for Drinking-Water Quality*, Geneva.
130. E. R. Lowe, C. E. Banks and R. G. Compton, *Anal. Bioanal. Chem.*, 2005, **382**, 1169.
131. C. M. Welch and R. G. Compton, *Anal. Bioanal. Chem.*, 2006, **384**, 601.
132. I. Narin and M. Soylak, *Anal. Chim. Acta*, 2003, **493**, 205.
133. J. P. Hart, A. Crew, E. Crouch, K. C. Honeychurch and R. M. Pemberton, *Anal. Lett.*, 2004, **37**, 789.
134. R. O. Kadara, N. Jenkinson and C. E. Banks, *Sens. Actuators B*, 2009, **138**, 556.
135. S. A. Wring, J. P. Hart, L. Bracey and B. J. Birch, *Anal. Chim. Acta*, 1990, **231**, 203.
136. I. L. d. Mattos, L. Gorton and T. Ruzgas, *Biosens. Bioelectron.*, 2003, **18**, 193.
137. M. P. O'Halloran, M. Pravda and G. G. Guilbault, *Talanta*, 2001, **55**, 605.

138. B. R. Sljukic, R. O. Kadara and C. E. Banks, *Anal. Methods*, 2011, **3**, 105.
139. M. Khairy, R. O. Kadara, D. K. Kampouris and C. E. Banks, *Electroanalysis*, 2010, **22**, 1455.
140. R. O. Kadara, N. Jenkinson and C. E. Banks, *Electroanalysis*, 2009, **21**, 2410.
141. R. O. Kadara and I. E. Tothill, *Anal. Bioanal. Chem.*, 2004, **378**, 770.
142. R. O. Kadara and I. E. Tothill, *Talanta*, 2005, **66**, 1089.
143. R. O. Kadara and I. E. Tothill, *Anal. Chim. Acta*, 2008, **623**, 76.
144. Y. Lin, F. Lu and J. Wang, *Electroanalysis*, 2004, **16**, 145.
145. P. J. L. Ardisana, P. Queipo, P. F. Bolado and A. C. Garcia, *Anal. Chim. Acta*, 2008, **615**, 30.
146. O. Dominguez-Renedo, L. Ruiz-Espelt, N. Garcia-Astorgano and M. J. Acros-Martinez, *Talanta*, 2008, **76**, 854.
147. F. Kiralay, S. Campuzano, D. A. Haake and J. Wang, *Talanta*, 2011, **85**, 1330.
148. O. A. Loaiza, S. Campuzano, M. Pedrero, P. Garcia and J. M. Pingarron, *Analyst*, 2009, **134**, 34.
149. R. Garcia-Gonzalez, M. T. Fernandez-Abedul, A. Pernia and A. Costa-Garcia, *Electrochim. Acta*, 2008, **53**, 3242.
150. M. F. Bergamini, A. L. Santos, N. R. Stradiotto and M. C. B. Zanoni, *J. Pharm. Biomed. Anal.*, 2005, **39**, 54.
151. J. Maly, J. Masojidek, A. Masci, M. Ilie, E. Cianci, V. Foglietti, W. Vastarella and R. Pilloton, *Biosens. Bioelectron.*, 2005, **21**, 923.
152. S. Susmel, G. G. Guilbault and C. K. O'Sullivan, *Biosens. Bioelectron.*, 2003, **18**, 881.
153. S. Laschi, I. Palchetti and M. Mascini, *Sens. Actuators B*, 2006, **114**, 460.
154. E. Bernalte, C. M. Sanchez and C. P. Gil, *Anal. Chim. Acta*, 2011, **689**, 60.

155. P. M. Ndangili, A. M. Jijana, P. G. L. Baker and E. I. Iwuoha, *J. Electroanal. Chem.*, 2011, **653**, 67.
156. S. Campuzano, B. E.-F. d. Avila, J. Yuste, M. Pedrero, J. L. Garcia, P. Garcia, E. Garcia and J. M. Pingarron, *Biosens. Bioelectron.*, 2010, **26**, 1225.
157. S. Zanarini, E. Rampazzo, L. D. Ciana, M. Marcaccio, E. Marzocchi, M. Montalti, F. paolucci and L. Prodi, *J. Am. Chem. Soc.*, 2009, **131**, 2260.
158. V. Bhalla, X. Zhao and V. Zazubovich, *J. Electroanal. Chem.*, 2011, **657**, 84.
159. T. Garcia, M. Revenga-Parra, B. Sobrinod, A. Carrecedo, C. Alonso, E. Lorenzo and F. Pariente, *Biosens. Bioelectron.*, 2011, **27**, 40.
160. O. A. Loaiza, S. Campuzano, M. Pedrero, P. Garcia and J. M. Pingarron, *Electroanalysis*, 2008, **20**, 1397.
161. V. Escamilla-Gomez, S. Campuzano, M. Pedrero and J. M. Pingarron, *Biosens. Bioelectron.*, 2009, **24**, 3365.
162. M. Gamella, S. Campuzano, C. Parrado, A. J. Reviejo and J. M. Pingarron, *Talanta*, 2009, **78**, 1303.
163. O. A. Loaiza, S. Campuzano, M. Pedrero, M. I. Pividori, P. Garcia and J. M. Pingarron, *Anal. Chem.*, 2008, **80**, 8239.
164. V. Escamilla-Gomez, S. Campuzano, M. Pedrero and J. M. Pingarron, *Talanta*, 2008, **77**, 876.
165. J. B. Vincent, *J. Trace Elem. Med. Biol.*, 2003, **16**, 227.
166. L. Lin, N. S. Lawrence, S. Thongngamdee, J. Wang and Y. Lin, *Talanta*, 2005, **65**, 144.
167. L. d. T.-d. Roman, M. A. Alonso-Lomillo, O. Dominguez-Renedo, C. Merino-Sanchez, M. P. Merino-Amayuelas and M. J. Arcos-Martinez, *Talanta*, 2011, **86**, 324.
168. P. Dutronc, B. Carbonne, F. Menil and C. Lucat, *Sens. Actuators B*, 1992, **6**, 279.

169. S. D. Zelnick, D. R. Mattie and P. C. Stepaniak, *Aviat. Space Environ. Med.*, 2003, **74**, 1285.
170. J.-W. Mo, B. Ogoreve, X. Zhang and B. Pihlar, *Electroanalysis*, 2000, **12**, 48.
171. S. Garrod, M. E. Bollard, A. W. Nicholls, S. C. Connor, J. Connelly, J. K. Nicholson and E. Holmes, *Chem. Res. Toxicol.*, 2005, **18**, 115.
172. J. Wang and Z. Lu, *Electroanalysis*, 1989, **1**, 517.
173. M. Ebadi, *Can. J. Chem.*, 2003, **81**, 161.
174. R. Gilbert and R. Rioux, *Anal. Chem.*, 1984, **56**, 106.
175. A. Safavi and A. A. Ensafi, *Anal. Chim. Acta*, 1995, **300**, 307.
176. S. M. Golabi and H. R. Zare, *Electroanalysis*, 1999, **11**, 1293.
177. S. V. Guerra, L. T. Kubota, C. L. Xavier and S. Nakagaki, *Anal. Sci.*, 1999, **15**, 1231.
178. J. W. White, M. H. Subers and A. I. Schepartz, *Biochim. Biophys. Acta*, 1963, **73**, 57.
179. N. Kiba, T. Tokizawa, S. Kato, M. Tachibana, K. Tanai, H. Koizumi, E. Edo and E. Yonezawa, *Anal. Sci.*, 2003, **19**, 823.
180. E. C. Hurdis and H. Romeyn, *Anal. Chem.*, 1954, **26**, 320.
181. X.-M. Miao, R. Yuan, Y.-Q. Chai, Y.-T. Shi and Y.-Y. Yuan, *J. Electroanal. Chem.*, 2008, **612**, 157.
182. C. M. Welch, C. E. Banks, A. O. Simm and R. G. Compton, *Anal. Bioanal. Chem.*, 2005, **382**, 12.
183. C. Batchelor-McAuley, Y. Du, G. G. Wildgoose and R. G. Compton, *Sens. Actuators B*, 2008, **135**, 230.
184. J. J. Watkins and H. S. White, *Langmuir*, 2004, **20**, 5474.
185. H. Matsuda and Y. Ayabe, *Z. Elektrochem.*, 1955, **59**, 494.
186. F. C. Anson and J. J. Lingane, *J. Am. Chem. Soc.*, 1957, **79**, 4901.

187. M. L. Smiljanic, I. L. Srejjic, V. M. Marinovic, Z. L. Rakocevic and S. B. Strbac, *Hemijaska Industrija*, 2011, 97.
188. European Pharmacopeia Scientific Notes, *Acceptance criteria for levels of hydrazine in substances for pharmaceutical use and analytical methods for its determination*, 2008.
189. B. Sljukic, C. E. Banks, A. Crossley and R. G. Compton, *Electroanalysis*, 2006, **18**, 1757.
190. K. I. Ozoemena and T. Nyokong, *Talanta*, 2005, **67**, 162.
191. J. Wang, M. Chicharro, G. Rivas, X. Cai, N. Dontha, P. A. M. Farias and H. Shiraishi, *Anal. Chem.*, 1996, **68**, 2251.
192. C. Batchelor-McAuley, C. E. Banks, A. O. Simm, T. G. J. Jones and R. G. Compton, *Analyst*, 2006, **131**, 106.
193. L. Aldous and R. G. Compton, *Phys. Chem. Chem. Phys.*, 2011, **13**, 5279.
194. L. Aldous and R. G. Compton, *ChemPhysChem*, 2011, **12**, 1280.
195. C. Malitesta, F. Palmisano, L. Torsi and P. G. Zambonin, *Anal. Chem.*, 1990, **62**, 2735.
196. Y. Li, R. Lenigk, X. Wu, B. Gruendig, S. Dong and R. Renneberg, *Electroanalysis*, 1998, **10**, 671.
197. M. S. Lin, B. I. Jan, *Electroanalysis*, 1997, **9**, 340.
198. A. Eftekhari, *Talanta*, 2001, **55**, 395.
199. J. P. Metters and C. E. Banks, *Vacuum*, 2012, **86**, 507.
200. W. B. Choi, D. S. Chung, J. H. Kang, H. Y. Kim, Y. W. Jin and I. T. Han, *Appl. Phys. Lett.*, 1999, **75**, 3129.
201. W. B. Choi, D. S. Chung, J. H. Kang, H. Y. Kim, Y. W. Jin and I. T. Han, *Appl. Phys. Lett.*, 2001, **78**, 1547.

202. C. Liu, Y. Y. Fan, M. Liu, H. T. Cong, H. M. Cheng and M. S. Dresselhaus, *Science*, 1999, **286**, 1127.
203. F. Darkrim, *J. Phys. Chem. B*, 2000, **104**, 6773.
204. Y. F. Yin, T. Mays and B. McEnaney, *Langmuir*, 2000, **16**, 10521.
205. S. S. Wong, J. D. Harper, P. T. Lansbury and C. M. Lieber, *J. Am. Chem. Soc.*, 1998, **120**, 603.
206. A. T. Woolley, C. L. Cheung, J. H. Hafner and C. M. Lieber, *Chem. Biol.*, 2000, **17**, 193.
207. M. Bockrath, D. H. Cobden, P. L. McEuen, N. G. Chopra, A. Zettl, A. Thess and R. E. Smalley, *Science*, 1997, **275**, 1922.
208. Z. Yao, C. Postma, L. Balents and C. Dekker, *Nature*, 1999, **402**, 273.
209. M. S. Fuhrer, J. Nygard, L. Shih, M. Forero, Y. G. Yoon, M. S. C. Mazzoni, H. J. Choi, J. Ihm, S. G. Louie, A. Zettl and P. L. McEuen, *Science*, 2000, **288**, 494.
210. C. Zhou, J. Kong, E. Yenilmez and H. Dai, *Science*, 2000, **290**, 1552.
211. S. A. Curran, P. M. Ajayan, W. J. Blau, D. L. Carroll, J. N. Coleman and A. B. Dalton, *Adv. Mater.*, 1998, **10**, 1091.
212. L. S. Schadler, S. C. Giannaris and P. M. Ajayan, *Appl. Phys. Lett.*, 1998, **73**, 3842.
213. S. Gullapalli and M. S. Wong, *Chemical Engineering Progress*, 2011, **107**, 28.
214. M.-F. Yu, O. Lourie, M. J. Dyer, K. Moloni, T. F. Kelly and R. S. Rouff, *Science*, 2000, **287**, 637.
215. J. M. Nugent, K. S. V. Santhanam, A. Rubio and P. M. Ajayan, *Nano Lett.*, 2001, **1**, 87.
216. <http://nano.com/index.html>, Accessed March 2012.
217. H. Luo, Z. Shi, N. Li, Z. Gu and Q. Zhuang, *Anal. Chem.*, 2001, **73**, 915.
218. J. Wang, M. Li, Z. Shi, N. Li and Z. Gu, *Anal. Chem.*, 2002, **74**, 1993.

219. K. Wu, J. Fei and S. Hu, *Anal. Biochem.*, 2003, **318**, 100.
220. M. Musameh, A. M. J. Wang and Y. Lin, *Electrochem. Commun.*, 2002, **4**, 743.
221. F.-H. Wu, G.-C. Zhao and X.-W. Wei, *Electrochem. Commun.*, 2002, **4**, 690.
222. M. Guo, J. Chen, J. Li, B. Tao and S. Yao, *Anal. Chim. Acta*, 2005, **532**, 71.
223. X. B. Ji, R. O. Kadara, J. Krussma, Q. Y. Chen and C. E. Banks, *Electroanalysis*, 2010, **22**, 7.
224. C. E. Banks, R. R. Moore, T. J. Davies and R. G. Compton, *Chem. Commun.*, 2004, **16**, 1804.
225. C. E. Banks, A. Crossley, C. Salter, S. J. Wilkins and R. G. Compton, *Angew. Chem.*, 2006, **45**, 2533.
226. B. Sljukic, C. E. Banks and R. G. Compton, *Nano Lett.*, 2006, **6**, 1556.
227. X. Dai, G. G. Wildgoose and R. G. Compton, *Analyst*, 2006, **131**, 901.
228. E. J. E. Stuart and M. Pumera, *J. Phys. Chem. C*, 2010, **114**, 21296.
229. C. Batchelor-McAuley, G. G. Wildgoose, R. G. Compton, L. Shao and M. L. H. Green, *Sens. Actuators B*, 2008, **132**, 356.
230. L. Siegert, D. K. Kampouris, J. Kruusma, V. Sammelselg and C. E. Banks, *Electroanalysis*, 2009, **21**, 48.
231. J. Kruusma, N. Mould, K. Jurkschat, A. Crossley and C. E. Banks, *Electrochem. Commun.*, 2007, **9**, 2330.
232. C. P. Jones, K. Jurkschat, A. Crossley and C. E. Banks, *J. Iranian Chem. Soc.*, 2008, **5**, 279.
233. K. Jurkschat, X. B. Ji, A. Crossley, R. G. Compton and C. E. Banks, *Analyst*, 2007, **132**, 21.
234. C. P. Jones, K. Jurkschat, A. Crossley, R. G. Compton, B. L. Riehl and C. E. Banks, *Langmuir*, 2007, **23**, 9501.

235. L. Highton, R. O. Kadara, N. Jenkinson, B. L. Riehl and C. E. Banks, *Electroanalysis*, 2009, **21**, 2387.
236. M. Merisalu, J. Kruusma and C. E. Banks, *Electrochem. Commun.*, 2010, **12**, 144.
237. A. Ambrosi and M. Pumera, *Chem. Eur. J.*, 2010, **16**, 10946.
238. C. E. Banks, T. J. Davies, G. G. Wildgoose and R. G. Compton, *Chem. Commun.*, 2005, 829.
239. I. Streeter, G. G. Wildgoose, L. D. Shao and R. G. Compton, *Sens. Actuators B*, 2008, **133**, 462.
240. J. Wang and M. Musameh, *Analyst*, 2004, **129**, 1.
241. J. Wang, *Electroanalysis*, 2005, **17**, 7.
242. M. Li, Y.-T. Li, D.-W. Li and Y.-T. Long, *Anal. Chim. Acta*, 2012, **734**, 31.
243. C. Boero, S. Carrar, G. D. Vecchio, L. Calza and G. D. Micheli, *Sens. Actuators B*, 2011, **157**, 216.
244. F. Berti, C. Eisenkolbl, D. Minocci, P. Nieri, A. M. Rossi, M. Mascini and G. Marrazza, *J. Electroanal. Chem.*, 2011, **656**, 55.
245. M. D. Fusco, C. Tortolini, D. Deriu and F. Mazzei, *Talanta*, 2010, **81**, 235.
246. M. Moreno, A. S. Arribas, E. Bermejo, M. Chicharro, A. Zapardiel, M. C. Rodriguez, Y. Jalit and G. A. Rivas, *Talanta*, 2010, **80**, 2149.
247. R. T. Kachoosangi, G. G. Wildgoose and R. G. Compton, *Analyst*, 2008, **133**, 888.
248. M. J. Sims, Q. Li, R. T. Kachoosangi, G. G. Wildgoose and R. G. Compton, *Electrochim. Acta*, 2009, **54**, 5030.
249. H. Karadeniez, A. Erdem and A. Caliskan, *Electroanalysis*, 2008, **20**, 1932.
250. Y. Li, L. Zhang, M. Li, Z. Pan and D. Li, *Chem. Cent. J.*, 2012, **6**, 103.
251. S. Mu, X. Wang, Y.-T. Li, Y. Wang, D.-W. Li and Y.-T. Long, *Analyst*, 2012, **137**, 3220.

252. M. Kumar and Y. Ando, *J. Nanosci. Nanotechnol.*, 2010, **10**, 3739.
253. S. B. Sinnott, R. Andrews, D. Qian, A. M. Rao, Z. Mao, E. C. Dickey and F. Derbyshire, *Chem. Phys. Lett.*, 1999, **315**, 25.
254. Y. Homma, Y. Kobayashi and T. Ogino, *J. Phys. Chem. B*, 2003, **107**, 12161.
255. M. Giovanni and M. Pumera, *Electrochem. Commun.*, 2011, **13**, 203.
256. K. S. Prasad, G. Muthuraman and J.-M. Zen, *Electrochem. Commun.*, 2008, **10**, 559.
257. M. Pumera and H. Iwai, *Chem. Asian. J.*, 2009, **4**, 554.
258. G. F. Barbero, A. Liazid, M. Palma and C. G. Barroso, *Food Chem.*, 2008, **107**, 1276.
259. A. Laskaridou-Monnerville, *J. Chromatogr. A*, 1999, **838**, 293.
260. J. George, G. Tharion, J. Richard, A. S. Macaden, R. Thomas and S. Bhattacharji, *TheScientificWorld*, 2007, **7**, 1683.
261. W. Robbins, *Clin. J. Pain*, 2000, **16**, S86.
262. S. Chanda, G. Erexson, D. Frost, S. Babbar, J. A. Burlew and K. Bley, *Int. J. Toxicol.*, 2007, **26**, 12.
263. D. E. Henderson, A. M. Slickman and S. K. Henderson, *J. Agric. Food Chem.*, 1999, **47**, 2563.
264. A. M. Sanchez, M. G. Sanchez, S. Malagarie-Cazenave, N. Olea and I. Diaz-Laviada, *Apoptosis*, 2006, **11**, 89.
265. B. Toth, P. Gannett, E. Rogan and J. Williamson, *In Vivo*, 1992, **6**, 487.
266. Y. J. Surh, R. C. J. Lee, K. K. Park, S. T. Mayne, A. Liem and J. A. Miller, *Carcinogenesis*, 1995, **16**, 2467.
267. M. N. Satyanarayana, *Crit. Rev. Food Sci. Nutr.*, 2006, **46**, 275.
268. R. H. Chichewicz, *J. Ethnopharmacol.*, 1996, **52**, 61.
269. H. T. Huynh and R. W. Teel, *Anticancer Res.*, 2005, **25**, 117.
270. R. K. Kempaiah, H. Manjuntha and K. Srinivasan, *Mol. Cel.. Biochem.*, 2005, **275**, 7.

271. M. S. Westerterp-Plantenga, A. Smeets and M. P. Lejeune, *Int. J. Obes.*, 2005, **29**, 682.
272. L. K. Pershing, C. A. Rielly, J. L. Corlett and D. J. Crouch, *J. Appl. Toxicol.*, 2006, **26**, 88.
273. V. Cavett, E. M. Waninger, J. J. Kritak and B. A. Eckenrode, *J. Forensic Sci.*, 2004, **49**, 469.
274. A. Nilsson, U. Palmquist, T. Pettersson and A. Ronlan, *J. Chem. Soc., Perkin Trans.*, 1978, **1**, 696.
275. D. Nematollahi, M. Alimoradi and S. W. Husain, *Electroanalysis*, 2004, **16**, 1359.
276. D. Nematollahi, H. Goodarzi and E. Tammari, *J. Chem. Soc., Perkin Trans.*, 2002, **2**, 696.
277. E. P. Randviir, J. P. Metters, J. Stainton and C. E. Banks, *Analyst*, 2013, **138**, 2970.
278. H. Ping Wu, *Anal. Chem.*, 1993, **65**, 1643.
279. R. O. Kadara, N. Jenkinson and C. E. Banks, *Sens. Actuators B*, 2009, **142**, 342.
280. J. Guo and E. Linder, *J. Electroanal. Chem.*, 2009, **629**, 180.
281. D. D. Gornall, S. D. Collyer and S. P. Higson, *Electroanalysis*, 2010, **22**, 384.
282. J. Guo and E. Linder, *Anal. Chem.*, 2009, **77**, 2147.
283. R. Ferrigno, P. F. Brevet and H. H. Girault, *Electrochim. Acta*, 1997, **42**, 1895.
284. F. A. Aguiar, A. J. Gallant, M. C. Rosamond, A. Rhodes, D. Wood and R. Katakay, *Electrochem. Commun.*, 2007, **9**, 879.
285. C. E. Banks, R. G. Compton, A. C. Fisher and I. E. Henley, *Phys. Chem. Chem. Phys.*, 2004, **6**, 3147.
286. Y. Wang, J. G. Limon-Petersen and R. G. Compton, *J. Electroanal. Chem.*, 2011, **652**, 13.

287. D. A. C. Brownson, L. J. Munro, D. K. Kampouris and C. E. Banks, *RSC Adv.*, 2011, **1**, 978.
288. A. Radoi and D. Compagnone, *Bioelectrochem.*, 2009, **76**, 126.
289. F. Pariente, E. Lorenzo, F. Tobalina and H. D. Abruna, *Anal. Chem.*, 1995, **67**, 3936.
290. F. Pariente, F. Tobalina, G. Moreno, L. Hernandez, E. Lorenzo and H. D. Abruna, *Anal. Chem.*, 1997, **69**, 4065.
291. T. Huang, A. Warsinke, T. Kuwana and F. W. Scheller, *Anal. Chem.*, 1998, **70**, 991.
292. T. N. Rao, I. Yagi, T. Miwa, D. A. Tryka and A. Fujishima, *Anal. Chem.*, 1999, **71**, 2506.
293. N. A. Choudhry, D. K. Kampouris, R. O. Kadara and C. E. Banks, *Electrochem. Commun.*, 2010, **12**, 6.
294. M. Zhou, Y. Zhai and S. Dong, *Anal. Chem.*, 2009, **81**, 5603.
295. J. P. Metters, R. O. Kadara and C. E. Banks, *Sens. Actuators, B*, 2012, **169**, 136.
296. W. Lijinskt and S. S. Epstein, *Nature*, 1970, **225**, 21.
297. M. Bru, M. I. Burguete, F. Galindo, S. V. Luis, M. J. Marin and L. Vigarà, *Tetrahedron Lett.*, 2006, **47**, 1787.
298. P. Mikuska and Z. Vecera, *Anal. Chim. Acta*, 2003, **495**, 225.
299. I. M. Ferreira and S. Silva, *Talanta*, 2008, **15**, 1598.
300. E. Szoko, T. Tabi, A. S. Halasz, M. Palfi and K. Magyar, *J. Chromatogr. A*, 2004, **1051**, 177.
301. C.-Y. Lin, V. S. Vasantha and K.-C. Ho, *Sens. Actuators B*, 2009, **140**, 51.
302. M. J. Moorcroft, J. Davis and R. G. Compton, *Talanta*, 2001, **54**, 785.
303. B. Sljukic, C. E. Banks, A. Crossley and R. G. Compton, *Electroanalysis*, 2007, **19**, 79.

304. L. H. Chen, J. B. Zang, Y. H. Wang and L. Y. Bian, *Electrochim. Acta*, 2008, **53**, 3442.
305. J. Pei and X.-Y. Li, *Talanta*, 2000, **51**, 1107.
306. J. P. Metters, F. Tan, R. O. Kadara and C. E. Banks, *Anal. Methods*, 2012, **4**, 1272.
307. M. S. Lin and B. I. Jan, *Electroanalysis*, 1997, **9**, 340.
308. B. Wang and S. Dong, *Talanta*, 2000, **51**, 565.
309. I. J. Cutress and R. G. Compton, *J. Electroanal. Chem.*, 2010, **645**, 159.
310. H. L. Woodvine, J. G. Terry, A. J. Walton and A. R. Mount, *Analyst*, 2010, **135**, 1058.
311. J. J. Powell, T. J. Burden and R. P. H. Thompson, *Analyst*, 1998, **123**, 1721.
312. H. Frumkin and G. Solomon, *Am. J. Ind. Med.*, 1997, **31**, 107.
313. A. Iregren, *Neurotoxicology*, 1994, **15**, 671.
314. A. J. Saterlay, J. S. Foord and R. G. Compton, *Analyst*, 1999, **124**, 1791.
315. S. Somnam, K. Grudpan and J. Jakmunee, *Spectrosc. Lett.*, 2008, **41**, 221.
316. M. Knap, K. Killian and K. Pyrzynska, *Talanta*, 2007, **71**, 406.
317. M. Rievaj, P. Tomick, Z. Janosikova, D. Bustin and R. G. Compton, *Chem. Anal. (Warsaw)*, 2008, **53**, 153.
318. B. Rezaei, M. Ghiaci and M. E. Sedaghat, *Sens. Actuators B*, 2008, **131**, 439.
319. O. M. S. Filipe and C. M. A. Brett, *Talanta*, 2003, **61**, 643.
320. C. E. Banks, J. Kruusma, R. R. Moore, P. Tomick, J. Peters, J. Davis, S. Komorsky-Lovric and R. G. Compton, *Talanta*, 2005, **65**, 423.
321. J. Whitson, D. Kubota, K. Shimono, Y. Jia and M. Taketani, *Adv. Net. Electrophys.*, 2006, 38.
322. M. Fejtl, A. Stett, W. Nisch, K.-H. Boven and A. Moller, *On Micro-Electrode Array Revival: Its Deveopment, Sophistication Of Recording and Simulation*, 2006, In:

- Baudry M, Taketani M, (Eds.), *Advances in Network Electrophysiology Using Multi-Electrode Arrays*. Springer Press, New York, p. 24.
323. S. G. Weber, *Anal. Chem.*, 1989, **61**, 295.
324. K. Stulik, C. Amatore, K. Holub, V. Marecek and W. Kutner, *Pure Appl. Chem.*, 2000, **72**, 1483.
325. D. E. Tallman, *J. Solid State Electrochem.*, 2011, **15**, 1703.
326. S. Fletcher and M. D. Horne, *Electrochem. Commun.*, 1999, **1**, 502.
327. N. A. M. Said, K. Twomey, V. I. Ogurtsov, D. W. M. Arrigan and G. Herzog, *J. Phys.: Conf. Ser.*, 2011, **307**.
328. R. G. Compton, G. G. Wildgoose, N. V. Reese, I. Streeter and R. Baron, *Chem. Phys. Lett.*, 2008, **459**, 1.
329. D. W. M. Arrigan, *Analyst*, 2004, **129**, 1157.
330. T. J. Davies and R. G. Compton, *J. Electroanal. Chem.*, 2005, **585**, 63.
331. K. M. Wassum, V. M. Tolosa, J. Wang, E. Walker, H. G. Monbouquette and N. T. Maidment, *Sensors*, 2008, **8**, 5023.
332. P. Thiebaud, C. Beuret, M. Koudelka-Hep, M. Bove, S. Martinoia, M. Grattarola, H. Jahnsen, R. Rebaudo, J. Zimmer and Y. Dupont, *Biosens. Bioelectron.*, 1999, **14**, 61.
333. G. Jobst, I. Moser, P. Svasek, M. Varahram, Z. Tranjanoski, P. Wach, P. Kotanko, F. Skrabal and G. Urban, *Sens. Actuators B*, 1997, **43**, 121.
334. A. Guiseppi-Elie, S. Brahim, G. Slaughter and K. R. Ward, *Sensors*, 2005, **5**, 345.
335. G. S. Wilson and R. Gifford, *Biosens. Bioelectron.*, 2005, **20**, 2388.
336. J. Piehler, *Curr. Opin. Struct. Biol.*, 2005, **15**, 4.
337. J. P. Metters, R. O. Kadara and C. E. Banks, *Analyst*, 2011, **136**, 1067.
338. R. G. Compton and C. E. Banks, 2010, *Understanding Voltammetry*, 2nd Ed., Imperial College, London.

339. A. E. Cohen and R. R. Kunz, *Sens. Actuators B*, 2000, **62**, 23.
340. J. Wang, J. Lu, B. Tian and C. Yarnitzky, *J. Electroanal. Chem.*, 1993, **361**, 77.
341. K. C. Honeychurch and J. P. Hart, *TrAC, Trends Anal. Chem.*, 2003, **22**, 456.
342. S. Piermarini, L. Micheli, N. H. S. Ammida, G. Palleschi and D. Moscone, *Biosens. Bioelectron.*, 2007, **22**, 1434.
343. B. P. Corgier, C. A. Marquette and L. J. Blum, *Anal. Chim. Acta*, 2005, **538**, 1.
344. B. V. Chikkaveeraiah, V. Mani, V. Patel, J. S. Gutkind and J. F. Rusling, *Biosens. Bioelectron.*, 2011, **26**, 4477.
345. P. M. Hallam, D. K. Kampouris, R. O. Kadara and C. E. Banks, *Analyst*, 2010, **135**, 1947.
346. J. P. Metters, F. Tan, R. O. Kadara and C. E. Banks, *Anal. Methods*, 2012, **4**, 3140.
347. R. O. Kadara, N. Jenkinson and C. E. Banks, *Sens. Actuators B*, 2009, **138**, 556.
348. J. P. Metters, R. O. Kadara and C. E. Banks, *Sens. Actuators B*, 2012, **169**, 136.
349. C. G. Zoski, *Electroanalysis*, 2002, **14**, 1041.
350. T. J. Davies, S. Ward-Jones, C. E. Banks, J. d. Campo, R. Mas, F. X. Munoz and R. G. Compton, *J. Electroanal. Chem.*, 2005, **585**, 51.
351. A. O. Simm, C. E. Banks, S. Ward-Jones, T. J. Davies, N. S. Lawrence, T. G. J. Jones, L. Jiang and R. G. Compton, *Analyst*, 2005, **130**, 1303.
352. F. Marken, J. C. Eklund and R. G. Compton, *J. Electroanal. Chem.*, 1995, **395**, 335.
353. D. A. C. Brownson, J. P. Metters, D. K. Kampouris and C. E. Banks, *Electroanalysis*, 2011, **23**, 894.
354. N. Hanawa, M. Shinohara, B. Saberi, W. A. Gaarde, D. Han and N. Kaplowitz, *J. Biol. Chem.*, 2008, **283**, 13565.
355. D. L. Laskin, C. R. Gardner, V. F. Price and D. J. Jollow, *Hepatology*, 1995, **21**, 1045.

356. N. Wangfuengkanagul and O. Chailapakul, *J. Pharm. Biomed. Anal.*, 2002, **28**, 841.
357. M. Black, *Annual Rev. Med.*, 1984, **35**, 577.
358. A. Babaei, M. Afrasiabi and M. Babsadeh, *Electroanalysis*, 2010, **22**, 1743.
359. Q. Wan, X. Wang, F. Yu, X. Wang and N. Yang, *J. Appl. Electrochem.*, 2009, **39**, 1145.
360. F. Ghorbani-Bidkorbeh, S. Shahrokhian, A. Mohammadi and R. Dinarvand, *Electrochim. Acta*, 2010, **55**, 2752.
361. S. A. Kumar, C.-F. Tang and S.-M. Chen, *Talanta*, 2008, **76**, 997.
362. S.-F. Wang, F. Xie and R.-F. Hu, *Sens. Actuators B*, 2007, **123**, 495.
363. H. Yin, K. Shang, X. Meng and S. Ai, *Microchim. Acta*, 2011, **175**, 39.
364. X. Chen, J. Zhu, Q. Xi and W. Yang, *Sens. Actuators B*, 2012, **161**, 648.
365. R. T. Kachoosangi, G. G. Wildgoose and R. G. Compton, *Anal. Chim. Acta*, 2008, **618**, 54.
366. J. N. Stuart, A. B. Hummon and J. V. Sweedler, *Anal. Chem.*, 2004, **76**, 120.
367. Y. Sun, B. Ye, W. Zhang and X. Zhou, *Anal. Chim. Acta*, 1998, **363**, 75.
368. T.-F. Kang, G.-L. Shen and R.-Q. Yu, *Analytica Chimica Acta*, 1997, **354**, 343.
369. T. Thomas, R. J. MAscarenhas and B. E. K. Swamy, *J. Mol. Liq.*, 2012, **174**, 70.
370. J. Ping, J. Wu, Y. Wang and Y. Ying, *Biosens. Bioelectron.*, 2012, **34**, 70.
371. T. R. Camp, 1963, *Water and its Impurities*. Reinhold Publishing, New York.
372. D. E. Metzler, 1977, *Biochemistry: The Chemical Reactions of Living Cells*. Academic, New York.
373. N. Spataru, T. N. Rao, D. A. Tryk and A. Fujishima, *J. Electrochem. Soc.*, 2001, **148**, E112.
374. *Drinking Water Standards 1962, 1988*, US Department of Health, Education and Welfare, Public Health Service, Washington DC.

375. J. M. Concon, 1988, *Food Toxicology: Principles and Concepts*, Part A, Marcel Dekker, New York.
376. W. Lijinsky and S. S. Epstein, *Nature*, 1970, **225**, 21.
377. L. H. Chen, J. B. Zang, Y. H. Wang and L. Y. Bian, *Electrochim. Acta*, 2008, **53**, 3442.
378. B. Sljukic, C. E. Banks, A. Crossley and R. G. Compton, *Electroanalysis*, 2007, **19**, 79.
379. J. Pei and X.-Y. Li, *Talanta*, 2000, **51**, 1107.
380. M. Khairy, R. O. Kadara and C. E. Banks, *Anal. Methods*, 2010, **2**, 851.
381. C.-Y. Lin, V. S. Vasantha and K.-C. Ho, *Sens. Actuators B*, 2009, **140**, 51.
382. B. Sljukic, C. E. Banks, A. Crossley and R. G. Compton, *Anal. Chim. Acta*, 2007, **587**, 240.
383. X. Chen, F. Wang and Z. Chen, *Anal. Chim. Acta*, 2008, **623**, 213.
384. W. J. R. Santos, P. R. Lima, A. A. Tanaka, S. M. C. N. Tanaka and L. T. Kubota, *Food Chem.*, 2009, **113**, 1206.
385. S. Yang, X. Liu, X. Zeng, B. Xia, J. Gu, S. Luo, N. Mai and W. Wei, *Sens. Actuators B*, 2010, **145**, 762.
386. J. P. Metters, R. O. Kadara and C. E. Banks, *Analyst*, 2012, **137**, 896.
387. C. M. Welch, O. Nekrassova and R. G. Compton, *Talanta*, 2005, **65**, 74.
388. R. M. Cespon-Romero, M. C. Yebra-Biurrun and M. P. Bermejo-Barrera, *Anal. Chim. Acta*, 1996, **327**, 37.
389. World Health Organisation, 1993, *Guidance for Drinking Water Quality*, Second Edition, Vol 1. Recommendations, Geneva.
390. R. G. Compton, G. G. Wildgoose, N. V. Reese, I. Streeter and R. Baron, *Chem. Phys. Lett.*, 2008, **459**, 1.

391. D. H. Craston, C. P. Jones and D. E. Williams, *Talanta*, 1991, **38**, 17.
392. K. R. Wehmeyer, M. R. Deakin and R. M. Wightman, *Anal. Chem.*, 1985, **57**, 1913.
393. S. Fletcher and M. D. Horne, *Electrochem. Commun.*, 1999, **1**, 502.
394. C. G. Zoski, *Handbook of Electrochemistry*, 2007, Elsevier.
395. Z. Porat, J. C. Crooker, Y. Zhang, Y. L. Mest and R. W. Murray, *Anal. Chem.*, 1997, **69**, 5073.
396. B. J. Seddon, M. J. Eddowes, A. Firth, A. E. Owen and H. H. J. Girault, *Electrochim. Acta*, 1991, **36**, 763.
397. A. M. Bond, T. L. E. Henderson and W. Thormann, *J. Phys. Chem.*, 1986, **90**, 2911.
398. B. L. Drogoff, M. A. E. Khakani, P. R. M. Silva, M. Chaker and A. K. Vijh, *Electroanalysis*, 2001, **13**, 1491.
399. K. L. Soh, W. P. Kang, J. L. Davidson, Y. M. Wong, D. E. Cliffel and G. M. Swain, *Diamond Relat. Mater.*, 2008, **17**, 240.
400. J.-L. Chang and J.-M. Zen, *Electrochem. Commun.*, 2006, **8**, 571.
401. K. S. Prasad, J.-C. Chen, C. Ay and J.-M. Zen, *Sens. Actuators B*, 2007, **123**, 715.
402. K. C. Honeychurch, S. Al-Berezanchi and J. P. Hart, *Talanta*, 2011, **84**, 717.
403. R. O. Kadara, N. Jenkinson and C. E. Banks, *Sens. Actuators B*, 2009, **2009**, 556.
404. J. Wang, 2006, *Analytical Electrochemistry*, Wiley & Sons, New Jersey.
405. N. A. Choudhry and C. E. Banks, *Anal. Methods*, 2011, **3**, 74.
406. M. Gomez-Mingot, J. Iniesta, V. Montiel, R. O. Kadara and C. E. Banks, *Analyst*, 2011, **136**, 2146.
407. M. Gomez-Mingot, J. Iniesta, V. Montiel, R. O. Kadara and C. E. Banks, *Sens. Actuators B*, 2011, **155**, 831.
408. L. Gorton, *Encyclopedia of Electrochemistry*, Wiley-VCH, Weinheim, 2002, 67.
409. H. K. Chenault and G. M. Whitesides, *Appl. Biochem. Biotechnol.*, 1987, **14**, 147.

410. W. M. Clark, *Oxidation-Reduction Potentials of Organic Systems*, R. E. Krieger Publishing, Huntington, New York, 1972.
411. F. L. Rodkey, *J. Biol. Chem.*, 1955, **213**, 777.
412. P. N. Bartlett, P. R. Birkin and E. N. K. Wallace, *J. Chem. Soc. Faraday Trans.*, 1997, **93**, 1951.
413. C. E. Banks and R. G. Compton, *Analyst*, 2005, **130**, 1232.
414. C. E. Banks and R. G. Compton, *Anal. Sci.*, 2005, **21**, 1263.
415. A. Vasilescu, S. Andreescu, C. Bala, S. C. Litescu, T. Noguer and J.-L. Marty, *Biosens. Bioelectron.*, 2003, **18**, 781.
416. C. R. Raj and S. Behera, *Biosens. Bioelectron.*, 2005, **21**, 949.
417. C. M. Maroneze, L. T. Arenas, R. C. S. Luz, E. V. Benvenuti, R. Landers and Y. Gushikem, *Electrochim. Acta*, 2008, **53**, 4167.
418. M. Zhang, A. Smith and W. Gorski, *Anal. Chem.*, 2004, **76**, 5045.
419. S. Baskar, J.-L. Chang and J.-M. Zen, *Biosens. Bioelectron.*, 2012, **33**, 95.
420. M. Zhou, L. Shang, B. Li, L. Huang and S. Dong, *Biosens. Bioelectron.*, 2008, **24**, 442.
421. J. Zhu, X. Chen and W. Yang, *Sens. Actuators B*, 2010, **150**, 564.
422. L. Wu, X. Zhang and H. Ju, *Anal. Chem.*, 2007, **79**, 453.
423. A. Balamurugan, K.-C. Ho, S.-M. Chen and T.-Y. Huang, *Colloids Surf., A*, 2010, **362**, 1.
424. L. Zhu, J. Zhai, R. Yang, C. Tian and L. Guo, *Biosens. Bioelectron.*, 2007, **22**, 2768.
425. K. C. Honeychurch, J. P. Hart and D. C. Cowell, *Anal. Chim. Acta*, 2001, **431**, 89.
426. K. C. Honeychurch, J. P. Hart and D. C. Cowell, *Electroanalysis*, 2000, **12**, 171.
427. K. C. Honeychurch, J. P. Hart, D. C. Cowell and D. W. M. Arrigan, *Electroanalysis*, 2002, **14**, 177.

428. K. C. Honeychurch, D. M. Hawkins, J. P. Hart and D. C. Cowell, *Talanta*, 2002, **57**, 565.
429. X. Huang, Y. Li, Y. Chen and L. Wang, *Sens. Actuators B*, 2008, **134**, 780.
430. G. Milczarek, *Electroanalysis*, 2008, **20**, 211.
431. R. T. S. Oliveira, G. S. Garbellini, G. R. Salazar-Banda and L. A. Avaca, *Anal. Lett.*, 2007, **40**, 2673.
432. B. R. Kozub, N. V. Rees and R. G. Compton, *Sens. Actuators B*, 2010, **143**, 539.
433. R. Guidelli, F. Pergola and G. Raspi, *Anal. Chem.*, 1972, **44**, 745.
434. B. Pielak and P. K. Wrona, *J. Electrochem. Soc.*, 2002, **149**, E55.
435. N. Spataru, T. N. Rao, D. A. Tryk and A. Fujishima, *J. Electrochem. Soc.*, 2001, **148**, E112.
436. X. Xing and D. Scherson, *Anal. Chem.*, 1988, **60**, 1468.
437. A. Rene, C. Cugnet, D. Hauchard and L. Authier, *Sens. Actuators B*, 2012, **174**, 225.
438. I. Montenegro, M. A. Queiros and J. L. Daschbach, *Microelectrodes: Theory and applications, in: Series E: Applied Sciences*, 1991, **197**.
439. J. Heinze, *Angew. Chem. Int. Ed.*, 1993, **32**, 1268.
440. C. Amatore, *Electrochemistry at ultramicroelectrodes, in: I. Rubinstein (Ed.), Physical Electrochemistry: Principles, Methods and Applications (Chapter 4)*, 1995.
441. R. M. Pemberton, J. Xu, R. Pittson, G. A. Drago, J. Griffiths, S. K. Jackson and J. P. Hart, *Biosens. Bioelectron.*, 2011, **26**, 2448.
442. A. M. Bond and P. A. Lay, *J. Electroanal. Chem. Interfacial Electrochem.*, 1986, **199**, 285.
443. A. M. Bond, K. B. Oldham and C. G. Zoski, *J. Electroanal. Chem. Interfacial Electrochem.*, 1988, **245**, 71.
444. C. Combellas, A. Fuchs and F. Kanoufi, *Anal. Chem.*, 2004, **76**, 3612.

445. A. O. Simm, C. E. Banks, S. Ward-Jones, T. J. Davies, N. S. Lawrence, T. G. J. Jones, L. Jiang and R. G. Compton, *Analyst*, 2005, **130**, 1303.
446. J. P. Metters, R. O. Kadara and C. E. Banks, *Sens. Actuators B*, 2012, **169**, 136.
447. K. C. Honeychurch and J. P. Hart, *Adv. Anal. Chem.*, 2012, **2**, 46.
448. P. N. Bartlett, P. R. Birkin and E. N. K. Wallace, *J. Chem. Soc. Faraday Trans.*, 1997, **93**, 1951.
449. World Health Organisation, *Guidance for Drinking Water Quality*, 1993, Second Ed. Vol. 1, Recommendations, Geneva.
450. J. P. Metters, R. O. Kadara and C. E. Banks, *Analyst*, 2012, **137**, 896.
451. J. P. Hart and S. A. Wring, *TrAC, Trends Anal. Chem.*, 1997, **16**, 89.
452. J. P. Hart and S. A. Wring, *Electroanalysis*, 1994, **6**, 617.
453. M. A. Sirvent, A. Merkoci and S. Alegret, *Sens. Actuators B*, 2000, **69**, 153.
454. A. Morrin, A. J. Killard and M. R. Smyth, *Anal. Lett.*, 2003, **36**, 2021.
455. C. D. Chin, V. Linder and S. K. Sia, *Lab Chip*, 2007, **7**, 41.
456. S. K. Sia, V. Linder, B. A. Parviz, A. Siegel and G. M. Whitesides, *Angew. Chem., Int. Ed.*, 2004, **43**, 498.
457. A. S. Daar, H. Thorsteindottir, D. K. Martin, A. C. Smith, S. Nast and P. A. Singer, *Nat. Genet.*, 2002, **32**, 229.
458. P. Yager, T. Edwards, E. Fu, K. Helton, K. Nelson, M. R. Tam and B. H. Weigl, *Nature*, 2006, **442**, 412.
459. D. Mabey, R. W. Peeling, A. Ustianowski and M. D. Perkins, *Nat. Rev. Microbiol.*, 2004, **2**, 231.
460. R. W. Peeling, K. K. Holmes, D. Mabey and A. Ronald, *Sex. Transm. Infect.*, 2006, **50**, V1.

461. B. V. Chikkaveeraiah, V. Mani, V. Patel, J. S. Gutkind and J. F. Rusling, *Biosens. Bioelectron.*, 2011, **26**, 4477.
462. Y.-L. Yang, M.-C. Chuang, S.-L. Lou and J. Wang, *Analyst*, 2010, **135**, 1230.
463. J. R. Windmiller and J. Wang, *Electroanalysis*, 2012, **24**, In Press.
464. W. Dungchai, O. Chailapakul and C. S. Henry, *Anal. Chem.*, 2009, **81**, 5821.
465. Z. Nie, C. A. Nijhuis, J. Gong, X. Chen, A. Kumachev, A. W. Martinez, M. Narovlyansky and G. M. Whitesides, *Lab Chip*, 2009, **10**, 477.
466. A. W. Martinez, S. T. Phillips, G. M. Whitesides and C. Carrilho, *Anal. Chem.*, 2010, **82**, 3.
467. Z. H. Nie, C. A. Nijhuis, J. L. Gong, X. Chen, A. Kumachev, A. W. Martinez, M. Narovlyansky and G. M. Whitesides, *Lab Chip*, 2010, **10**, 477.
468. H. Liu and R. M. Crooks, *Anal. Chem.*, 2012, **84**, 2528.
469. J. Lankelma, Z. Nie, E. Carrilho and G. M. Whitesides, *Anal. Chem.*, 2012, **84**, 41.
470. M. Novell, M. Parrilla, G. A. Crespo, F. X. Rius and F. J. Andrade, *Anal. Chem.*, 2012, **84**, 4695.
471. L. Gorton, 2002, *Encyclopedia of Electrochemistry*, Wiley-VCH, Weinheim, 67.
472. W. M. Clark, 1972, *Oxidation-Reduction Potentials of Organic Systems*, R. E. Krieger Publishing, Huntington, N.Y.
473. J. Wang, *Electroanalysis*, 2005, **17**, 7.
474. S. D. Sprules, J. P. Hart, S. A. Wring and R. Pittson, *Analyst*, 1994, **119**, 253.
475. A. Vasilescu, T. Noguier, S. Andreescu, C. Calas-Blanchard, C. Bala and J.-L. Marty, *Talanta*, 2003, **59**, 751.
476. *Drinking Water Standards*, 1988, US Department of Health, Education and Welfare, Public Health Service, Washington DC, 1962.

477. J. M. Concon, 1988, *Food Toxicology: Principles and Concepts: Part A*, Marcel Dekker, New York.
478. Y. Wang, E. Laborda and R. G. Compton, *J. Electroanal. Chem.*, 2012, **670**, 56.
479. J.-L. Chang and J.-M. Zen, *Electroanalysis*, 2006, **18**, 941.
480. US Department of Health, 1962, *Drinking Water Standards*, Washington DC, 47.
481. M. Khairy, R. O. Kadara and C. E. Banks, *Anal. Methods*, 2010, **2**, 851.
482. M. Li, Y. Li, D. Li and Y. Long, *Analytica Chimica Acta*, 2011, **734**, 31.
483. A. S. Kumar and J. Zen, *Electroanalysis*, 2002, **14**, 671.
484. K. C. Honeychurch and J. P. Hart, *TrAC, Trends Anal. Chem*, 2003, **22**, 456.
485. A. Heller and B. Feldman, *Chemical Reviews*, 2008, **108**, 2482.
486. M. Schlesinger, *Modern Aspects of Electrochemistry: Applications of Electrochemistry in Medicine*, 2013, **56**, 83.
487. S. Mu, X. Wang, Y. Li, Y. Wang, D. Li and Y. Long, *Analyst*, 2012, **137**, 3220.
488. A. Venkatanarayanan, K. Crowley, E. Lestini, T. E. Keyes, J. F. Rusling and R. J. Forstera, *Biosens Bioelectron*, 2012, **31**, 233.
489. A. Crew, D. Lonsdale, N. Byrd, R. Pittson and J. P. Hart, *Biosens Bioelectron*, 2011, **26**, 2847.
490. F. Tan, J. P. Metters and C. E. Banks, *Sensors and Actuators B: Chemical*, 2013, **181**, 454.
491. J. P. Metters, F. Tan, R. O. Kadara and C. E. Banks, *Anal. Methods*, 2012, **4**, 3140.
492. J. P. Metters, R. O. Kadara and C. E. Banks, *Analyst*, 2013, **138**, 2516.
493. J. P. Metters, R. O. Kadara and C. E. Banks, *Sensors and Actuators B: Chemical*, 2012, **169**, 136.
494. J. P. Metters, F. Tan and C. E. Banks, *J. Solid State Electrochem.*, 2013, In Press.
495. C. K. Tang, A. Vaze and J. F. Rusling, *Lab Chip*, 2012, **12**, 281.

496. Y. Yang, M. Chuang, S. Lou and J. Wang, *Analyst*, 2010, **135**, 1230.
497. K. Malzahn, J. R. Windmiller, G. Valdes-Ramirez, M. J. Shoning and J. Wang, *Analyst*, 2011, **136**, 2912.
498. J. R. Windmiller and J. Wang, *Electroanalysis*, 2013, **25**, 29.
499. J. Cai, K. Cizek, B. Long, K. McAferty, C. G. Campbell, D. R. Allee, B. D. Vogt, J. L. Belle and J. Wang, *Sensors and Actuators B: Chemical*, 2009, **137**, 379.
500. M.-C. Chuang, Y.-L. Yang, T.-A. Tseng, T. Chou, S.-L. Lou and J. Wang, *Talanta*, 2010, **81**, 15.
501. J. P. Metters, S. M. Houssein, D. K. Kampouris and C. E. Banks, *Anal. Methods*, 2013, **5**, 103.
502. R. O. Kadara, N. Jenkinson and C. E. Banks, *Sensors and Actuators B: Chemical*, 2009, **138**, 556.
503. B. J. Seddon, Y. Shao and H. H. Girault, *Electrochim. Acta*, 1994, **39**, 2377.
504. F. Marken, J. C. Eklund and R. G. Compton, *J. Electroanal. Chem.*, 1995, **395**, 335.

RELEVANT PUBLICATIONS ARISING FROM THIS THESIS

1. J. P. Metters, R. O. Kadara and C. E. Banks, *New directions in screen printed electroanalytical sensors: an overview of recent developments*, *Analyst*, 2011, **136**, 1067.

Contribution: Literature review and writing of peer-reviewed review article.

2. J. P. Metters, R. O. Kadara and C. E. Banks, *Electroanalytical sensing of chromium (III) and (VI) utilising gold screen printed macro electrodes*, *Analyst*, 2013, **137**, 896.

Contribution: Fabrication of screen printed sensors, electrochemical measurements, data analysis and writing of peer-reviewed article.

3. J. P. Metters, F. Tan, R. O. Kadara and C. E. Banks, *Platinum screen printed electrodes for the electroanalytical sensing of hydrazine and hydrogen peroxide*, *Analytical Methods*, 2012, **4**, 1272.

Contribution: Fabrication of screen printed sensors, electrochemical measurements, data analysis and writing of peer-reviewed article.

4. J. P. Metters, M. Gomez-Mingot, J. M. Iniesta, R. O. Kadara and C. E. Banks, *The fabrication of novel screen printed single-walled carbon nanotube electrodes: Electroanalytical applications*, *Sensors and Actuators, B*, 2013, **177**, 1043.

Contribution: Fabrication of screen printed sensors, electrochemical measurements, data analysis and writing of peer-reviewed article.

5. J. P. Metters, F. Tan, R. O. Kadara and C. E. Banks, *Electroanalytical properties of screen printed shallow recessed electrodes*, *Analytical Methods*, 2012, **4**, 3140.

Contribution: Design and fabrication of screen printed sensors, microscopy, electrochemical measurements, data analysis and writing of peer-reviewed article.

6. F. Tan, J. P. Metters and C. E. Banks, *Electroanalytical applications of screen printed microelectrode arrays*, *Sensors and Actuators, B*, 2013, **181**, 454.

Contribution: Design and fabrication of screen printed sensors, microscopy, electrochemical measurements, data analysis and writing of peer-reviewed article.

7. J. P. Metters, R. O. Kadara and C. E. Banks, *Electroanalytical properties of screen printed graphite microband electrodes*, *Sensors and Actuators, B*, 201, **169**, 136.
Contribution: Design and fabrication of screen printed sensors, microscopy, electrochemical measurements, data analysis and writing of peer-reviewed article.
8. J. P. Metters, R. O. Kadara and C. E. Banks, *Fabrication of co-planar screen printed microband electrodes*, *Analyst*, 2013, **138**, 2516.
Contribution: Design and fabrication of screen printed sensors, microscopy, electrochemical measurements, data analysis and writing of peer-reviewed article.
9. J. P. Metters, S. M. Houssein, D. K. Kampouris and C. E. Banks, *Paper-based electroanalytical sensing platforms*, *Analytical Methods*, 2013, **5**, 103.
Contribution: Conceptual idea and fabrication of screen printed sensors, microscopy, electrochemical measurements, data analysis and writing of peer-reviewed article.
10. C. W. Foster, J. P. Metters and C. E. Banks, *Ultra flexible paper based electrochemical sensors: Effect of mechanical contortion upon electrochemical performance*, *Electroanalysis*, 2013, Accepted; In Press.
Contribution: Fabrication of screen printed sensors, microscopy, electrochemical measurements, data analysis and writing of peer-reviewed article.

“Arte et labore”